



Department of Chemical Science
INTERNATIONAL PhD IN CHEMICAL SCIENCES
XXXVI Cycle

Alessia Distefano

**Unveiling the biomolecular mechanisms of Alzheimer's
disease: A multi-technical investigation of chemical
factors involved in amyloid β peptide dyshomeostasis.**

PhD Thesis

Tutor: *Prof. Giuseppe Grasso*

PhD Coordinator: *Prof. Salvatore Sortino*

Academic Cycle 2020-2023

Doctor of Philosophy Thesis

International PhD in Chemical Sciences, XXXVI Cycle, 2020-2023

Unveiling the biomolecular mechanisms of Alzheimer's disease: A multi-technical investigation of chemical factors involved in amyloid β peptide dyshomeostasis

ALESSIA DISTEFANO

© ALESSIA DISTEFANO, 2023

UNIVERSITY OF CATANIA, ITALY, 2023

Archived on Open Access Institutional Archive of University of Catania using DSpace open source repository application <http://dspace.unict.it/>

Reviewed and approved by:

Dr Elisa PERONI

Maître de Conférences

Chargée de mission Relations Internationales Dpt Chimie

Equipe de Chimie Biologique - Laboratoire BioCIS

CY Cergy Paris Université

elisa.peroni@cyu.fr

Dr. (PhD) Claudio Iacobucci

Department of Chemical and Physical Sciences, University of L'Aquila, Italy

Martin-Luther-University Halle-Wittenberg (MLU), Institute of Pharmacy, Halle (Saale), Germany

claudio.iacobucci@univaq.it

page left blank intentionally.

*“L’Alzheimer è il male dell’oblio.
È un abisso di ombre che toglie ogni luce”.*

Fabrizio Caramagna

Questa Tesi è dedicata a mio nonno Angelo,
e a tutti coloro che vivono nell’oblio dei ricordi di una vita.

*La ricerca scientifica e la perseveranza
saranno la guida che li riporterà alla luce.*

List of Abbreviations

ACE	Angiotensin-converting Enzyme
AD	Alzheimer's disease
AFM	Atomic Force Microscopy
ALS	Amyotrophic Lateral Sclerosis
Aβ	Amyloid A β peptide
APP	Amyloid Precursor Protein
ATP	Adenosine Triphosphate
Car	Carnosine
CDs	Carbon-dots
CD-COOH	Carbon-dots with COOH-terminal
CD-N	Carbon-dots with NH ₂ -terminal
CID	Collision-induced dissociation cell
CSF	Cerebrospinal Fluid
DLS	Dynamic Light Scattering
ECE	Endothelin-converting Enzyme

FA	Formic Acid
HNE	4-hydroxy-2,3-nonenal
IDE	Insulin-Degrading Enzyme
MMP-9	Matrix metalloproteinase-9
MS	Mass Spectrometry
NEP	Neprilysin
NFTs	Neurofibrillary tangles
NMR	Nuclear Magnetic Resonance
PD	Parkinson's disease
ROS	Reactive Oxygen Species
SPR	Surface Plasmon Resonance
TAT	Trans-Activator of Transcription
THT	Thioflavin T
T1DM	Type I Diabete Mellitus
T2DM	Type II Diabete Mellitus
UPS	Ubiquitin-Proteasomal System

Table of Contents

Abstract.....	1
1. INTRODUCTION	3
1.1 Alzheimer’s disease.....	4
1.2. Aim of this thesis	10
2. Chapter I: Amyloid Catabolism: An In-depth study based on the IDE-insulin model system	13
2.1. AD and T2DM: Exploring the Catabolism Processes of A β and insulin...	14
2.2. Overview of Metalloprotease enzyme: NEP, ECE, ACE, MMP-9.....	15
2.3. Insulin-Degrading Enzyme (IDE).....	16
2.3.1. <i>Structure and Properties</i>	16
2.3.2. <i>Homotropic modulation of IDE activity</i>	18
2.3.3. <i>Heterotropic modulation of IDE activity in AD</i>	21
2.3.4. <i>IDE and the Ubiquitin Proteasome System</i>	22
2.4. Carnosine	23
2.5. Results and Discussions.....	27
2.5.1. <i>Surface Plasmon Resonance (SPR) investigation</i>	30
2.5.1.1 Functionalization of gold sensor chip	30
2.5.1.2. Immobilization of IDE.....	31
2.5.1.3 Immobilization of IDE monomeric variant (R767A).....	32
2.5.1.4. Affinity analysis: The Hill function.....	33
2.5.2 <i>Activator role of Car: A Mass Spectrometry approach</i>	41

2.5.2.1.	Preparation of samples.....	41
2.5.2.2.	HPLC-MS analysis	42
2.6.	Final Remarks	46

3. Chapter II: Amyloid Aggregation: A New Approach Based on CD Biosensors 47

3.1	Amyloid Aggregation Pathway	48
3.1.1.	<i>Aβ peptide aggregation</i>	50
3.1.2.	<i>Insulin and its aggregation pathway</i>	52
3.1.3.	<i>Factors involved in amyloid aggregation</i>	56
3.2.	Results and Discussions	60
3.2.1	<i>Monitoring of insulin aggregation by carbon dots</i>	60
3.2.1.1.	Overview of the biological application of carbon dots.	60
3.2.1.2.	Monitoring of incubated insulin aggregation by Circular Dichroism, DLS, and THT fluorescence maps.....	62
3.2.1.3.	CDs synthesis approach	67
3.2.1.4.	Monitoring of incubated insulin by CD-N fluorescence analysis	69
3.2.2	<i>Isobaric peptides: the case of TAT1-Car series.</i>	73
3.2.2.1.	Solid phase peptide synthesis and RP-HPLC purification.....	75
3.2.2.2.	Mass spectrometry and CD characterization of TAT-peptides.....	78
3.2.2.3.	Synthesis and functionalization of CD-N and CD-COOH.....	83
3.3.	Final Remarks	90

4. Chapter III: Mass spectrometric analysis of Aβ-O₂ and Aβ-O₂-Cu complexes 92

4.1.	Aβ Misfolding: Unravelling Environmental Imbalance.....	93
4.1.1.	<i>Reactive Oxygen Species in AD</i>	93
4.1.2.	<i>Metal unbalance in AD</i>	97

4.1.3. <i>Copper-related damages in AD</i>	100
4.2. Results and Discussions	103
4.2.1. <i>Protonated Aβ peptides</i>	106
4.2.2. <i>Aβ peptides + CuCl₂ complexes</i>	110
4.2.2.1. <i>Aβ₁₋₄₀ + CuCl₂</i>	110
4.2.2.2. <i>Aβ₁₋₁₆ + CuCl₂</i>	114
4.2.2.3. <i>Aβ₁₂₋₂₈ + CuCl₂</i>	116
4.2.2.4. <i>Aβ₂₅₋₃₅ + CuCl₂</i>	118
4.2.2.5. <i>Aβ₂₈₋₃₅ + CuCl₂</i>	121
4.2.3. <i>Aβ peptides + O₂ molecules</i>	123
4.2.4. <i>Aβ peptides + CuCl₂ + O₂ molecules</i>	128
4.3. Final Remarks	132
5. Conclusion and Future perspectives	134
References	136
Appendix Instrumental techniques' overview	153
SPR Theory and Instrumentation	153
Mass Spectrometry	159
Fluorescence Spectroscopy	162
<i>Optical Properties of Carbon Dots</i>	164
Cell viability: Trypan Blue and MTT assays	167
Dynamic Light Scattering	168
Circular Dichroism Spectroscopy	170
Curriculum Vitae	172
List of Publications and Proceedings	174
Acknowledgments	178

Abstract

The spreading of neurodegenerative diseases such as Alzheimer's disease (AD) and the correlated ever-growing medical emergency have directed the research toward a deeper and clearer knowledge of the biochemical mechanisms involved in these diseases.

The downfall of AD is associated with specific features, which include oxidative stress, metal unbalance, and the accumulation and aggregation of a specific protein, the Amyloid β peptide ($A\beta$). In order to deepen and clarify how the above-mentioned factors could influence the onset and the progression of the disease, a multi-technical investigation was applied by means of Surface Plasmon Resonance (SPR), Mass Spectrometry (MS), and Fluorescence techniques combined with supporting techniques such as Circular Dichroism, Dynamic Light Scattering (DLS), and Cell viability assays which provide greater completeness to the experiments described here.

Among the enzymes involved in $A\beta$ homeostasis, Insulin-Degrading Enzyme (IDE) is a highly conserved zinc metallopeptidase capable of catalytically cleaving several substrates, including insulin and $A\beta$, playing a dual role in diabetes and AD.

In this scenario, we have developed a novel SPR method (Chapter I) that allows for the direct measurement of enzyme cooperativity in the binding with insulin in the presence of different IDE activity modulators: carnosine (Car), adenosine triphosphate (ATP), and EDTA. In order to develop and optimize this novel method, insulin was selected as the model system, since it is the most studied and well-established IDE substrate. The results indicate that both positive and negative modulations of IDE activity can be correlated with an increase and a decrease of the measured Hill coefficient, respectively, providing new insights into the mechanism of IDE activity modulation. This preliminary screening will serve as the cornerstone for investigating the IDE- $A\beta$ interaction and assessing the impact of modulators on this interaction through the utilization of the SPR technique.

Peptides such as insulin and $A\beta$ can undergo aggregation pathways, leading to the formation and deposition of amyloid plaques, which are hallmarks of type 2 diabetes mellitus (T2DM) and AD, respectively. However, monitoring the initial phases of this subtle mechanism and identifying the formation of oligomeric species, considered the first toxic species forming before fibril formation begins, are challenging tasks not easily achievable by common analytical techniques. For this reason, in Chapter II, we have demonstrated the possibility of monitoring the early stages of insulin aggregation by the application of synthesized Carbon dots (CDs) providing snapshots of the conformations adopted by insulin, used as a model system. Indeed, the use of insulin as a model system simplifies the analysis, since this peptide is much easier to handle compared to $A\beta$. Once we

have established this methodology, the next phase will involve applying this analysis to the A β -CDs interaction. In addition, CDs were even applied for the detection and identification of isobaric peptides, whose primary sequence is based on the combination of TAT, a cell-penetrating peptide, and Car. Comprehensive fluorescence studies confirm the ability to distinguish isobaric peptides based on the anchoring mode to CDs, which depends on the specific functional groups covering the surface of CDs and on the specific primary sequence of the peptide under analysis.

In addition, the investigation of A β -oxygen adducts (Chapter III) was achieved by the use of a mass spectrometer modified *ad hoc*, allowing for the first time to scrutinize oxygen adducts by the introduction of gases (He, O₂) into the mass spectrometer.

Preliminary results demonstrate the formation of A β ₁₋₄₀-oxygen adducts both in the absence and in the presence of copper ions, whereas no oxygen adducts in the case of A β fragments (A β ₁₋₁₆, A β ₁₂₋₂₈, A β ₂₅₋₃₅, and A β ₂₈₋₃₅) were detected, suggesting the entrapment of O₂ molecules occurs only for the full-length A β peptide. The detection of A β ₁₋₄₀-oxygen adducts is reached thanks to the cooling down effect exerted by helium and oxygen gases, which are directly inserted within the mass spectrometer. Moreover, the mass analysis performed on the A β fragments in the presence of copper ions provides insights into the copper coordination sites within the hydrophilic short A β chains (A β ₁₋₁₆, A β ₁₂₋₂₈), and reveals additional copper binding sites within the A β hydrophobic regions (A β ₂₅₋₃₅, A β ₂₈₋₃₅). This not only sheds light on their involvement in the A β aggregation pathway but also better elucidates the coordination of different A β species with copper ions.

This multi-technical and cross-sectional approach allowed us to explore innovative and unconventional strategies for counteracting AD, examining the same problem from different points of view. These alternative methods can be considered springboards for new analyses that could open up new insights and new therapeutic approaches in the future.

1. INTRODUCTION

Differently from other neurological disorders such as Tetanus, Meningitis, and Poliomyelitis which show a 57% decrease, there is an estimated 66% increase in AD, and other dementias from 2005 to 2030. The estimated death cases for AD is predicted to have a frightful 26% increase by 2030.^[1]

No fewer than 6.2 millions of Americans are estimated to be living with AD in 2021, whose symptoms usually begin after age 60.^[2] The prevalence of AD is higher in women than in men, indeed in the age range 65-69 years the 0.7% are women and the 0.6% are men with a higher discrepancy in age range 85-89 where the 14,2% and 8,8% are respectively women and men who suffer from this disease.^[3] Despite the medical emergency needed for the treatment of this pathology, few countries (less than 20% worldwide) provide a specific budget for the healing of neurological disorders, suggesting an ongoing lack of prioritization, and planning of financial resources for the care of people with neurological disorders globally.^[4]

The development of these diseases is tightly associated with a wrong lifestyle and eating disorders characterized by a diet rich in polyunsaturated fatty acids. For this reason, developing countries where AD has spread are China and Europe (5 million each), USA (2.9 million), India (1.9 million), Japan (1.1 million) and Indonesia (1 million).^[5]

Overall, growing scientific proofs support the principal risk factor for dementia summarized by the 2017 Lancet Commission on dementia prevention, intervention, and care: obesity, depression, low education, diabetes, hearing impairment, smoking, hypertension, physical inactivity, and, above all in the last two years, the low social contact.^[6]

At molecular level, oxidative stress has been implicated in the progression of a number of neurodegenerative diseases, including AD, Parkinson disease (PD), and amyotrophic lateral sclerosis (ALS).^[7]

Timely and accurate diagnosis of neurodegenerative diseases is increasingly necessary nowadays. Although several techniques search A β in AD and α -synuclein in PD, upstream therapies more effective during the early pre-symptomatic or prodromal disease stages are required before the irreversible neurodegeneration occurs.^[8,9]

The early steps of neurodegenerative disease are crucial and the upriver recognition of biomolecules responsible for the onset of the disorders, could hold the relentless race to neurodegenerative decline off.

Due to the urgency of recognizing the earliest stages of the aforementioned diseases, the latest research is devoted to applying new strategies. These strategies include finding new modulators capable of recognizing and modulating the proteins responsible for the pathologies, hindering

amylogenic aggregation in the early stages before the diseases begin, and limiting the levels of external factors (such as heavy metals, ROS overproduction, lipid peroxidation, etc.) that play a pivotal role in A β misfolding.

1.1 Alzheimer's disease

AD is a major neurodegenerative disease with a progressive course and the most frequent cause of dementia in the worldwide population older than 65 (50-70% of all dementia cases).

Patients affected by AD show a deficit in language abilities (i.e., aphasia), a reduced ability to recall over-learned facts, behavioural and personality changes as well as visuospatial and problem solving deficits.^[10] Moreover, amyloid angiopathy, namely deposition of amyloid materials on blood vessel surface of Central Nervous System (CNS), is observed in AD brain after autopsy.^[11] The distribution of neurofibrillary tangle and amyloid plaques is different. Usually, the neurofibrillary tangle spread starts from the hippocampus and other paralimbic structure and then continues up to the prefrontal cortex where are collocated the sensorial area and the executive functions such as planning, decision-making, short-term memory, personality expressions, social behaviour and the control of speech and language. On the contrary, the amyloid plaques tend to form with the basal isocortex (frontal, temporal, occipital) to reach the primary sensorimotor area in a second time.^[12]

AD is classified as a conformational disease due to the misfolding and accumulation of a specific protein, A β peptide, typified by abnormal conformational properties. The term *amyloidosis* refers to a disease in which the misfolding of pathogenic proteins leads to the aggregation of insoluble amyloid fibrils where the initially unstructured proteins constitute a cross- β -sheet system.

The misfolding of proteins such as A β peptide is regulated by the Ubiquitin-Proteasomal System (UPS), the autophagy/endosomal-lysosomal system, and management of protein misfolding by molecular chaperones, which together represent the protein quality control (PQC) center^[13,14]. The main role is to maintain cellular homeostasis and degrade damaged or unwanted cellular components. Intracellularly, autophagy is the first highly conserved cellular process involved into the degradation, recycling and removing of cellular components such as aggregated proteins and damaged organelles^[15]. This process is followed by the UPS which is responsible for the degradation of 80-90% of normal/abnormal/misfolded intracellular protein^[16,17].

The UPS collaborates with three families of ubiquitination-related enzymes: E1 (ubiquitin-activating), E2 (ubiquitin-conjugating), and E3 (ubiquitin-ligating) enzymes. Within neuronal cells, the UPS functions as a significant ATP-dependent proteolytic machinery, playing a crucial role in the advancement of protein-misfolding-related diseases^[13].

The inhibition of proteasome, accumulation of mutant ubiquitin, oxidation of specific deubiquitinating enzymes, and downregulation of E1 and E2 are tightly correlated with the neurodegeneration and AD. This is due to an uncontrolled waste accumulation of misfolded proteins such as A β peptides^[18,19]. Hence, a proper autophagy/UPS processing is crucial to prevent the deposition of misfolded A β peptide.

Until now, findings from numerous foundational, pre-clinical, and clinical investigations have underscored the A β and tau protein as crucial players in the pathophysiology of AD. This stems primarily from their accumulation within distinct histopathological brain abnormalities – A β association with senile plaques and tau with neurofibrillary tangles (NFTs). Moreover, their soluble variants in the brains of AD patients have also been noted to increase.

The causes of AD are unknown, although different hypotheses have been proposed to explain the complex neurodegenerative processes underlying this disease.^[20] The hypothesis with most support among the scientific community is the ‘amyloid cascade hypothesis’, in which the onset of AD is due to an increased formation and deposition of A β ₁₋₄₀ or A β ₁₋₄₂ amyloid peptide.

The origin of A β is from its precursor protein APP (Amyloid Precursor Protein) through a series of sequential proteolytic cleavages. APP is a type I single-pass transmembrane protein with a molecular weight of approximately 110-140 kDa^[21], consisting of three distinct isoforms containing 695, 751, and 770 amino acids^[22,23].

Primarily localized in the endoplasmic reticulum, APP subsequently undergoes N- and O-glycosylation, sulfation, and phosphorylation^[24,25]. Once it reaches the membrane, APP is internalized due to the presence of a signal sequence located at its C-terminal end.

APP is characterized by two distinct proteolytic pathways: *i*) the *non-amyloidogenic* pathway initiated by the α -secretase enzyme, and *ii*) the *amyloidogenic* pathway embarked upon by the β -secretase enzyme (Figure 1). Typically, the *non-amyloidogenic* pathway occurs on the cellular surface where α -secretase enzymes are abundant, whereas the *amyloidogenic* pathway takes place within organelles where β and γ -secretase enzymes operate^[26].

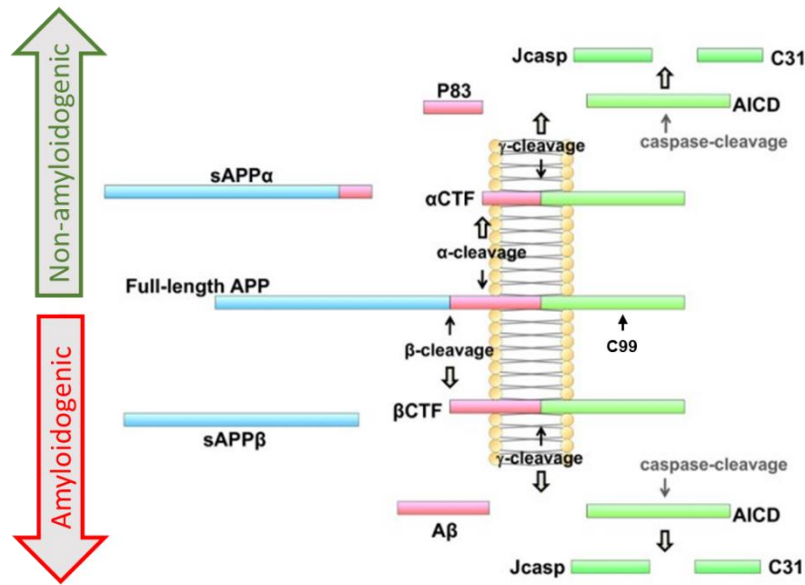


Figure 1 Schematic representation of APP proteolytic pathways: the not-amyloidogenic (top) and the amyloidogenic pathway (bottom). Picture modified from REF^[27] under Creative Commons CC BY 4.0 license; Mol. Brain 2011.

Within the *non-amyloidogenic* pathway, the α -secretase enzyme cuts APP at the 687 amino acid and produces both a soluble fragment (sAPP α) and a membrane bound c-terminal fragment (α CTF). From the action of γ -secretase enzyme, a shorter peptide p83 and the AICD peptide (APP Intra-Cellular Domain) are produced.

On the other hand, within the *amyloidogenic* pathway, the β -secretase enzyme cuts the APP at the 671 amino acid, generating the soluble β fragment (sAPP β) and the C-terminal 99 (C99), which is then processed by the γ -secretase enzyme. The fragmentation of C99 produces the AICD peptide and the A β peptide^[27,28].

Based on the γ -secretase cleavage site, various A β isoforms can occur, ranging in length from 38 to 43 amino acids, where A β_{1-40} is the predominant species. However, although A β_{1-42} appears in lower concentrations, it has garnered greater focus in AD disease research due to its pronounced propensity for aggregation. However, within the brains of AD patients, A β_{1-38} and truncated forms in the N-terminal region, specifically A β_{1-15} , A β_{1-16} , and A β_{1-17} , have also been detected^[29].

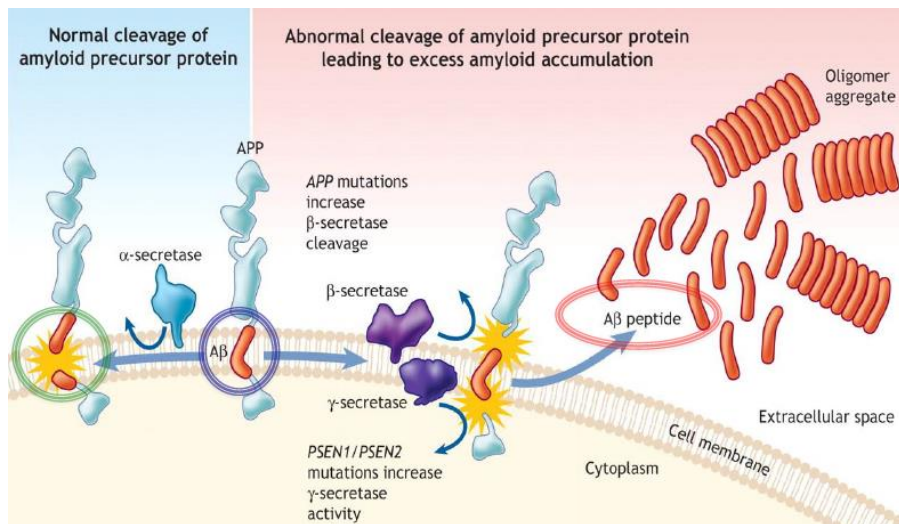


Figure 2 Synthesis of Aβ amyloid peptide via γ and β secretase. Adapted with permission from Ref^[30] published by CMAJ 2008.

APP can undergo a several mutation, one of which is correlated to the presence of specific allelic variants ($\epsilon 2$, $\epsilon 3$ and $\epsilon 4$) of the polymorphic apolipoprotein (ApoE), a plasmatic protein involved in cholesterol transport. Furthermore, the onset of AD is also ascribable to the genetic mutation of PSEN 1 and PSEN 2, two genes belonging to the γ -secretase complex, whose modifications increase the γ -secretase activity (Figure 2)^[12].

According to the amyloid cascade hypothesis, the abnormal extracellular growth of Aβ level in the brain is due to the Aβ aggregation into β -sheet structure, starting from oligomers species and converting later into protofibrils, fibrils, and finally in amyloid plaques. Although the first amylogenic studies identify fibrils as the irreversible step to the formation of amyloid plaques, recently oligomers accumulated in AD patient brains are suggested to be the more toxic species for the cells (Figure 3).

The oligomers and in turn their accumulation could lead to a series of events causing cell dysfunction and death^[31], and in addition, other events such as the intracellular formation of NFTs and the disruption of synaptic functions seem to result from this early and key event.

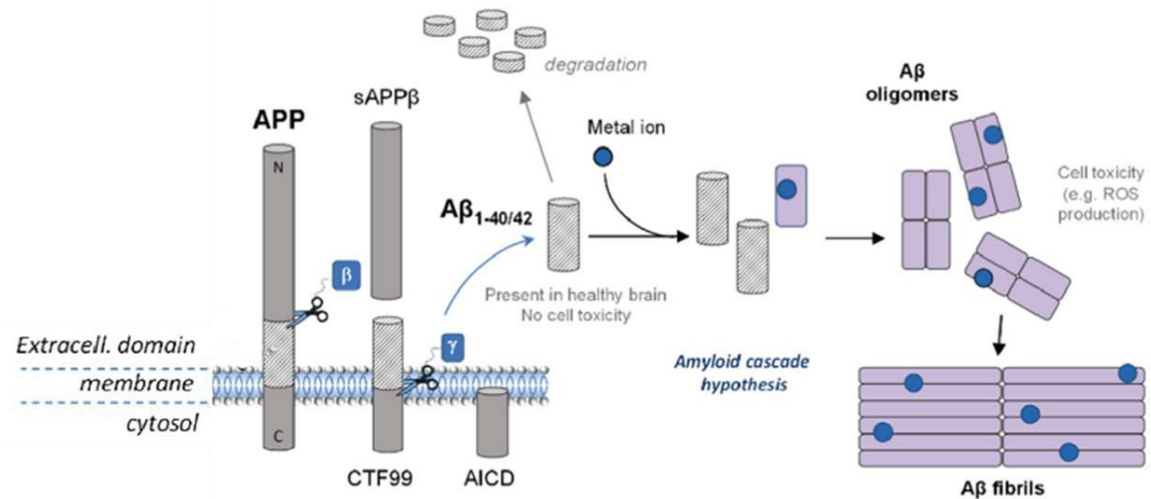


Figure 3 Schematic representation of early steps of amyloid cascade after $A\beta_{1-40/42}$ formation. The present of metal ion promotes the $A\beta$ aggregation. Adapted from Ref^[32] under Creative Commons CC BY 4.0 license; published by Redox Biol. 2018.

Although the formation of oligomers and the subsequent deposition of $A\beta$ fibrils are correlated with the emergence of the longer and amyloidogenic forms of the $A\beta$ peptide, the aggregation process is not strictly linked to the synthesis of the $A\beta$ peptide. Likely, it is more closely associated with uncontrolled levels of $A\beta$ peptide, which in turn trigger dysfunctions and undesired side effects.

Giuffrida et al.^[33] have demonstrated that not only monomers of $A\beta$ (1-42 and 1-40) are present in the brains and Cerebrospinal Fluid (CSF) of normal individuals, but both $A\beta_{1-42}$ and $A\beta_{1-40}$ also exhibit neuroprotective qualities against the excitotoxic death of mature neurons. Specifically, the absence of $A\beta_{1-42}$ leads to a deprivation of trophic support for neurons. The "loss-of-function" hypothesis concerning neuronal death^[33] also considers $A\beta_{1-40}$ as neuroprotective. In fact, their depletion in AD correlates with lower CSF levels of $A\beta_{1-40}$ in patients with mild cognitive impairment, contributing to a more rapid cognitive decline.

Accordingly, the cognitive impairment arising from the formation of oligomers and fibril depositions may not be attributed to the synthesis of $A\beta$ amyloid peptides, but rather to an imbalance of the peptide.

Multiple hypothesis have been linked to the amyloid cascade hypothesis. These theories propose that disturbances in external factors, like metal ions, oxidative stress (ROS production, and lipid oxidation), or issues with peptide breakdown by protease enzymes, can significantly influence the amyloid cascade and regulate the aggregation process following binding with the $A\beta$ peptide.

Among them, the "metal hypothesis" has proved to be the most promising^[34], according to which metal ions such Cu (II) play a crucial role in amyloid aggregation and oxidative stress generation.

Indeed, the metal hypothesis is based on observations wherein the radicalization of copper ions and the deficiency of zinc levels are correlated with oxidative stress, which in turn promotes the precipitation of amyloid fibrils^[35].

The imbalance of A β peptides is also associated with the failure of enzymes responsible for A β peptide catabolism, leading to an excess of the peptide in the case of enzyme deficiency or a reduction of the peptide in the case of enzyme overexpression^[36].

Both impairments contribute to the aggregation of A β peptides, ultimately resulting in the formation of A β plaques, which are a distinctive hallmark in AD.

1.2. Aim of this thesis

As we can gather from all of it, the enormous complexity of AD becomes evident. The intricate network of connections among the various pathways of AD (protein misfolding and aggregation, mutations, failure of proteases enzymes, metal unbalance, oxidative damage, impairment of the PQC system, etc), or their various combinations, can trigger the development of the pathology. This arises from the combination and mutual influence among these systems, making AD a multi-layered system in which each level triggers another, thereby unleashing/developing the pathology.

As a consequence, the strategy adopted was to simplify this high complex system, peeling each level off, focusing on solely individual components, and studying them separately. The key is to shed light on each single aspect of the processes involved into the AD before seeing “*the big picture*”.

In this context, the aim of this thesis is to investigate and disclose some awkward mechanisms engaged in the onset/development/worsening of AD, i.e., the enzymes involved into the amyloid catabolism, the aggregation mechanism, and the A β misfolding owing to the unbalance of some external factors (metals, oxygen).

For the sake of readability and clarity, I have preferred to organize this thesis in three sections, one for each selected pathway involved into AD.

In particular, the first *Chapter I* is focused on the importance of a correct functioning of the enzymes involved in A β peptide and insulin catabolism, namely the metalloproteases. Specifically, the chosen metalloprotease is the IDE, involved into both A β peptide and insulin degradation. For this purpose, I performed SPR investigations on this enzyme to provide a deeper knowledge on the IDE modulation by means of the discovering of new modulators for the enzyme. This was achieved by the application of the Hill function for allosteric enzymes such as IDE, which provides further information on how the presence of modulators might alter the interaction between an enzyme and its substrates. The substrate selected to optimize this novel application was insulin, as it is a well-established IDE enzyme substrate and widely used as a model system.

Given our interest in Car, I conducted SPR and MS analyses on the IDE-insulin interaction in the presence of this dipeptide. The aim was to uncover its role as a modulator by extrapolating the Hill coefficient.

As a result, our interest was funnelled toward ATP since the role of this molecule is still unclear, however, previous studies suggest ATP acts as both activator and inhibitor in the case of smaller and larger substrates respectively. Hence SPR experiments were performed in the presence of this small molecule. Lastly, by being a strong metal-chelating agent, EDTA was used as control system since is a well-known inhibitor of IDE activity.

The development of amyloidogenic aggregates, a characteristic feature of misfolding diseases, stands as a hallmark in pathologies like AD. While much research has been conducted on aggregates formation, a deficiency of comprehensive information concerning the initial stages of this intricate process remains. An example is the insulin peptide, where both conformational changes and impairments serve as potential links between AD and T2DM^[37-39]. In this context, a more comprehensive investigation of the insulin aggregation mechanism could constitute a starting point for a highly sensitive analysis of the early stages of this phenomenon.

To address this gap, **Chapter II** delves into the aggregation of insulin, serving as a model system and whose investigation could set the groundwork for further aggregation studies of further amyloidogenic peptides such as A β . This investigation employs CDs, representing the new frontier of biosensing. The methodology enables the distinct identification of various insulin conformations assumed over time, effectively creating specific fingerprints.

Lastly, the remarkable sensitivity demonstrated by CDs was harnessed to identify and differentiate three synthetic isobaric peptides containing Car within their sequences. These peptides featured Car positioned at three distinct sites. The aim of this study is to prevent Car degradation *in vivo* by inhibiting the action of the carnosinase enzyme.

For the third and last section of this thesis, **Chapter III**, I moved to Université de Bretagne Occidentale (UBO) Brest, France as visiting PhD student under the supervision of Prof. Antony Memboeuf - expert in Mass Spectrometry – for an eight-months research period.

In the Memboeuf's research group, I acquired skills about the employment and handling of an innovative mass spectrometer modified *ad hoc*. This instrument allowed for the direct insertion of gases within the mass spectrometer, which is typically prohibited in normal and common instruments. This modification enabled the investigation of oxygen-A β adducts (with and without CuCl₂), namely A β species coordinating oxygen atoms/molecules, through the insertion of two different gases: *i*) oxygen only, *ii*) helium only, and *iii*) the combination of the two gases.

The cooling effect provided by oxygen, helium, and the combination of the two gases allowed for the preservation of unstable oxygen-A β adducts and their structural identification through MS² analysis. Furthermore, a mass analysis of specific A β fragments was performed in the presence of copper chloride salts to ascertain whether these fragments, once digested by metalloproteases and released in their free form, can participate in copper binding, and initiate unknown secondary reactions.

Here is illustrated a summarized general scheme of aims and objectives of this thesis.

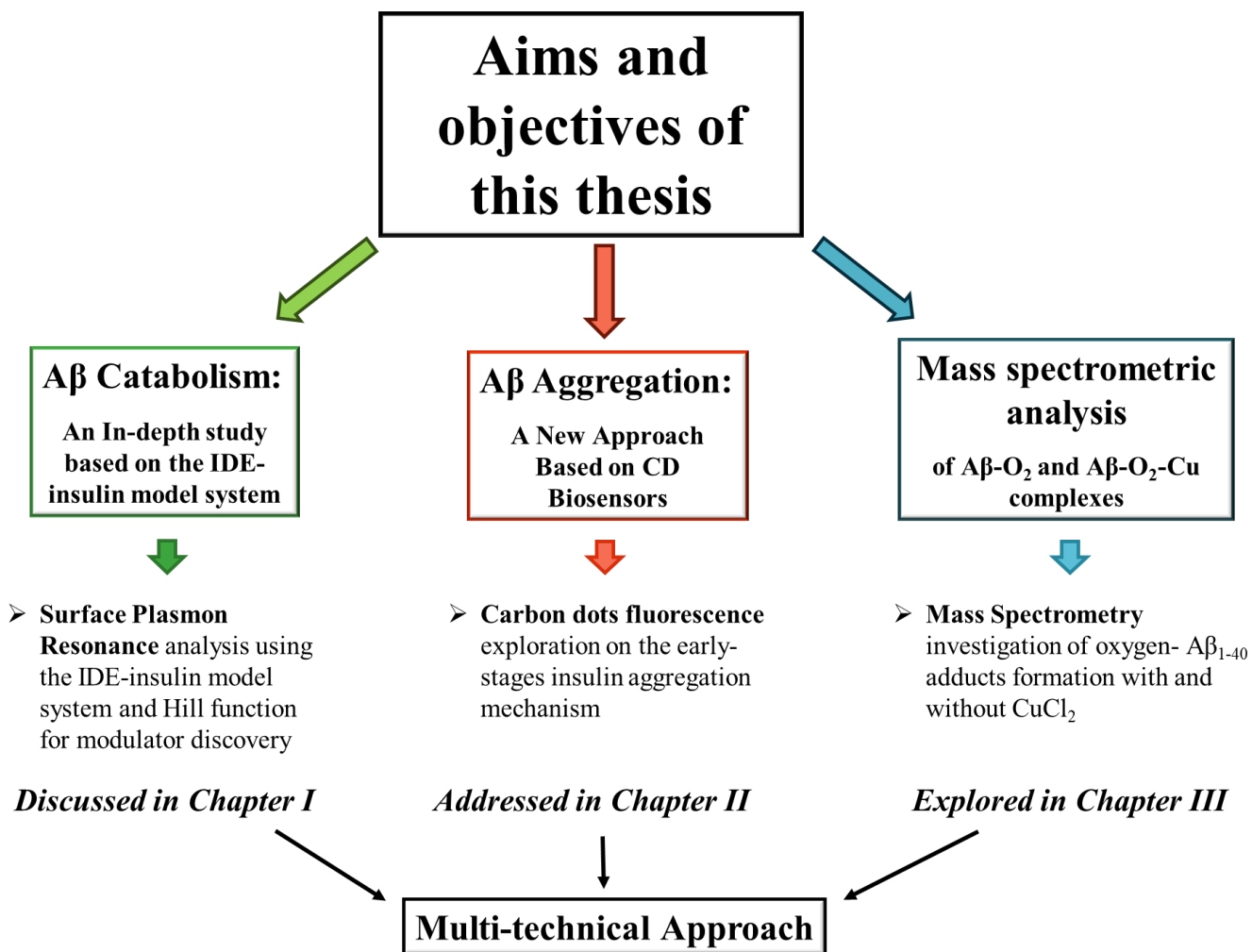


Chart 1 Illustration of Aims and objectives of this thesis.

2. Chapter I

Amyloid Catabolism:

*An In-depth study based on the
IDE-insulin model system.*

2.1. AD and T2DM: Exploring the Catabolism Processes of A β and insulin.

Since the equilibrium between the anabolism and catabolism of peptides determines the steady-state levels of all peptides within a living system, the accumulation of peptides can result from not just heightened production but also reduced breakdown. Research on A β in AD has been predominantly centred around the generation of the neurotoxic peptide and its transformation into fibrils. While the degradation pathway of the A β peptide has often been viewed as marginal and inconsequential, a failure in the proper regulation of A β levels and other amyloid proteins can result in serious consequences. This includes the uncontrolled accumulation of A β , leading to aggregation and the formation of insoluble fibrils. The accumulation of A β amyloid plaques disrupts normal brain function by interfering with cell communication and causing inflammation contributing to the neurodegeneration and cognitive decline observed in AD.

Nowadays, more and more studies have demonstrated the connection between AD and T2DM because both pathologies are prevalent in elderly people and, furthermore, T2DM patients are more prone to develop AD due to the presence of hyperinsulinemia and insulin resistance, characteristic of T2DM, that progressively leads to memory impairment.^[40] One possible link between both pathologies is an impairment of insulin. Insulin is a peptide hormone secreted by the β cells of the pancreatic islet of Langerhans and whose work is to control and regulate blood glucose levels. When a dyshomeostasis of insulin occurs, several disorders may develop such as insulin resistance (elevated insulin level) and T2DM.

T2DM represents 90-95% of all cases of diabetes, and it consists of a high blood glucose level due to increased hepatic glucose production, impaired insulin production by pancreatic β cells, and improper activity of insulin catabolism. What links AD to T2DM is also the role of insulin receptors within the brain. Indeed, insulin receptors not only regulate the glucose levels in the blood but also regulate neuronal differentiation, stem cell, and progenitor cell proliferation, as well as having growth factors properties and own cellular repair mechanisms. As a consequence, several studies have demonstrated that a higher level of insulin in prediabetes, and early T2DM has been associated with damaged cognitive functions. This could indicate that the level of A β peptide might be affected by the amount of insulin in the brain.^[41]

According to these studies, what contributes to the onset of AD and T2DM is not the altered synthesis of A β_{1-42} and insulin respectively but rather their imbalance and dyshomeostasis at cerebral level.

Indeed, the catabolism of A β and insulin intra- and extracellularly is regulated by a family of enzymes known as metalloproteases. For this reason, enzymes such as NEP (neprilysin), IDE, ECE-1

(endothelin converting enzyme 1) ECE-2, ACE (angiotensin-converting enzyme), MMPs (matrix metalloproteinases), PreP (presequence peptidase) and plasmin have been widely studied in the effort to link their malfunctioning to the progress of these pathologies.

2.2. Overview of Metalloprotease enzyme: NEP, ECE, ACE, MMP-9

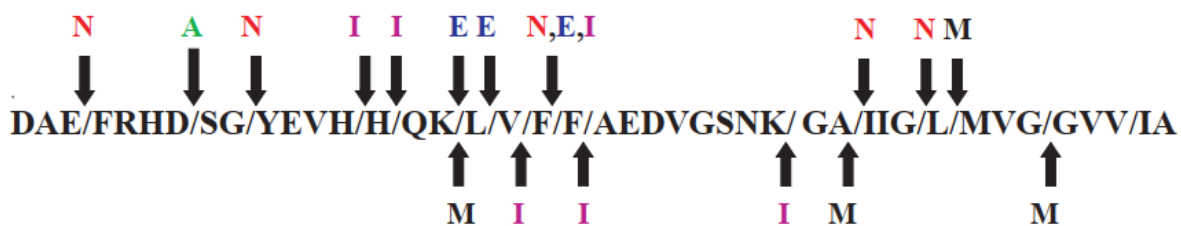


Figure 4 Primary sequence of Aβ₁₋₄₂ peptide. Arrows point out the cleavage sites of NEP (red N); ECE-1 (blue E); ACE (green A); MMP-9 (black M) and IDE (purple I). Figure modified with permission from REF^[42]; published by *Neurochem* 2002.

Metalloproteases are a family of enzymes belonging to the protease group, characterized by the presence of a catalytic site whose mechanism requires the presence of metallic ions to function. Within this “family” we have: NEP, ECE, ACE, MMP-9, and the IDE enzyme extensively studied by our group.

Neprilysin (*NEP*) is a plasma membrane glycoprotein member of the M13 zinc metallopeptidase family. In human, NEP is composed of 750 amino acids with a molecular weight of approximately 90–110-kDa^[43]. Structurally, NEP is composed of a short N-terminal cytoplasmic tail, a membrane-spanning domain, and a large C-terminal extracellular catalytic domain with a HExxH zinc-binding motif^[44,45]. The latter can hydrolyse extracellular oligopeptides with a MW < 5kDa on the amino side of hydrophobic residues, such as Aβ₁₋₄₀ and Aβ₁₋₄₂. Indeed, the cleavage site on the Aβ peptides are between Glu3-Phe4, Gly9-Trp10, Phe19-Phe20, Ala30-Ile31, and Gly33-Leu34^[46] (Figure 4, red N). Furthermore, previous studies have demonstrated capability of NEP to degrade both intracellular and extracellular^[47] oligomeric forms of both Aβ₁₋₄₀ and Aβ₁₋₄₂^[48].

Endothelin-converting enzyme (*ECE*) is a transmembrane metalloprotease responsible for the conversion of Endothelin (ET), a potent vasoconstrictive peptide^[49]. It has two isoforms, i.e., ECE-1 and ECE-2 where the ECE-2 is only 1-2% as much as the more abundant ECE-1^[50-52]. Moreover, only ECE-1 is able to degrade Aβ peptide.

ECE-1 is composed of 758 amino acids^[53] and four isoforms of ECE-1 were identified. ECE-1 can cut A β in the middle of its sequence, namely between Lys16-Leu17, Leu17-Val18, and Phe19-Phe20 (Figure 4, blue E) producing mainly A β ₁₋₁₆, A β ₁₋₁₇, A β ₁₋₁₉, and A β ₂₀₋₄₀ fragments^[54].

Angiotensin-converting enzyme (*ACE*) is a membrane-bound zinc metalloprotease consisting of two isotypes, ACE1 and ACE2^[55]. The main function of this enzyme is to convert angiotensin I to angiotensin II, which is involved in sodium homeostasis and the regulation of blood pressure^[56]. ACE is composed of 732 amino acids^[57] with two proteolytic active domains situated at the N and C terminal respectively^[58]. Although the only cleavage site identified is between Asp7-Ser8 (Figure 4, green A), Hu and coauthors demonstrate ACE's capability to hinder A β aggregation, its deposition, and the subsequent cytotoxic effects of the peptide^[59].

Matrix metalloproteinase (*MMP-9*) is the most widely investigated among MMPs whose main work is to regulate processes involved in inflammation and fibrosis in cardiovascular disease. In human, MMP-9 consists of an NH₂-terminal pro-domain, a COOH-terminal hemopexin-like domain, a linker domain, and a catalytic domain^[60]. The latter comprises two zinc ions, five calcium ions and three repetitions that resemble the type II module found in fibronectin. Of the two zinc ions, only one is coordinated to the cysteine in the pro-domain in order to keep MMP-9 inactive; in fact, the zinc ion is crucial for proteolytic activity^[61]. MMP-9 has several cleavage sites in A β peptide as showed in Fig.4, black M.

2.3. Insulin-Degrading Enzyme (IDE)

2.3.1. Structure and Properties

IDE is a ubiquitous zinc metallopeptidase belonging to the inverzincin family and is present in humans as well as in all eukaryotes and bacteria, showing a highly conserved primary sequence during evolution. Human IDE is synthesized as a single polypeptide of 1019 residues and its principal localization is the cytosol. However, it is possible to find it in other compartments including endosomes, peroxisomes, mitochondria, cell surfaces, and even secreted to the extracellular spaces.^[62-64]

This ubiquitous feature of IDE allows it to carry out its proteolytic function toward insulin since this peptide is never found within the cytosol. Nevertheless, it was proposed that the internalization of insulin from endosome to cytosol occurs involving the acidification of endosome and unfolding of insulin molecules which assist them to pass through the membrane and reach the cytosol.^[65]

Although historically the biological role of IDE has long been associated with its activity in the framework of insulin turnover, many studies have demonstrated the engagement of IDE in the degradation of other substrates such as A β (AD)^[66], glucagon, amylin, and some growth factors. Structurally, the monomeric form of IDE is made up of four equal-sized $\alpha\beta$ domains: two domains constitute the IDE-N (N-terminal portion) whereas the other two represent the IDE-C (C-terminal portion). IDE-N and IDE-C are connected by a 28 amino-acid residue loop (Figure 5).^[67]

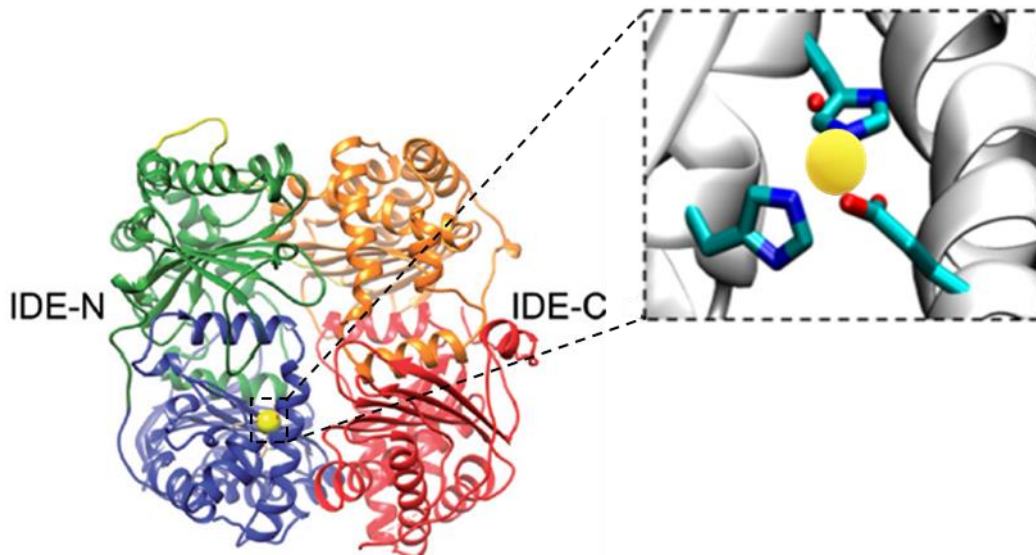


Figure 5 Representation of four IDE structural domains coloured from blue to red going from the N-terminus to the C-terminus. In figure the enlargement illustrates the zinc catalytic chamber. Adapted from Ref^[64] under Creative Commons CC BY 4.0 license; published by Crit. Rev. Biochem. Mol. Biol. 2017.

IDE-N contains the zinc catalytic chamber which can accommodate peptides with a maximum size of 70 amino acids. The active chamber of IDE owns a catalytic tetramer, HxxEHx₇₆E, located inside the domain 1 where two histidine residues (H108 and H112) and two glutamate residues (E189 and E111) coordinate the Zn²⁺ ion. The E111 residue plays a crucial role in catalysis because it activates a catalytic water molecule for the nucleophilic attack necessary for the protein degradation.

IDE-N contains also an exosite, which is approximately 30 Å away from the catalytic site. The exosite is responsible for the allosteric modulation of the enzyme, being the binding location of substrates as well as of small molecules acting as enzyme activity modulators. The binding to the exosite induces a conformational switch on the enzyme structure that promotes the interaction between the catalytic site and the substrate.

However, the allosteric modulation occurs only when IDE is in oligomeric form rather than in monomeric form.^[68] Indeed, the dimeric form is the most thermodynamically stable and can be found in two different conformations: open (active) and closed (inactive) (Figure 6). When a substrate or a modulator binds to the exosite, it induces a structural modification on the enzyme stabilizing the open conformation.^[64,68] This transition is needed to explicate the proteolytic process since in the absence

of a substrate, IDE is preferentially in the closed conformation. The closed conformation is upheld by a “latch” composed by extensive hydrogen bonds which link the two halves of IDE and are involved in the switch from closed to open conformation.

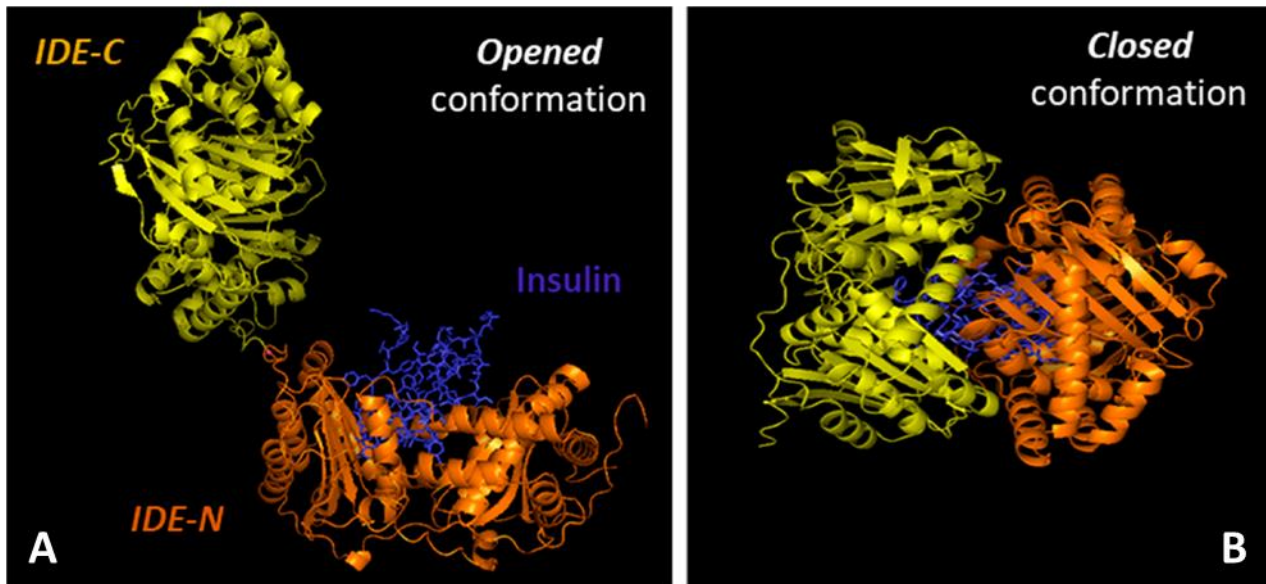


Figure 6 Illustration of IDE binding insulin. **A)** The interaction between IDE and insulin occurs through the binding with IDE-N domain in opened conformation. **B)** Once the binding occurs, IDE assumes the closed conformation in order to carry out the proteolytic action. After digestion and the release of cleavage productions, IDE returns to the opened configuration. Adapted from Ref^[69] under Creative Commons CC BY 4.0 license; published by Biomedicines 2021.

Lastly, two IDE isoforms, 15a and 15b, are both involved in the catabolism of insulin and A β peptide, but with different contributions^[70]. While the 15b isoform is much less efficient at degrading both peptides, the wild-type 15a isoform demonstrates an elevated turnover number, namely the number of substrate molecules that an enzyme can convert into product molecules in a given period of time, for insulin and A β peptide as well^[71].

2.3.2. Homotropic modulation of IDE activity

The allosteric modulation of IDE can occur through two different pathways: homotropic or heterotropic.

The homotropic modulation occurs when the same molecule acts as both substrate and modulator for IDE. This type of modulation is difficult to recognize since it is coupled with conformational changes of the interrelated binding sites. However, this modulation is verified by observing the kinetics profile of wild type IDE which shows a cooperative effect. An example of this modulation occurs in the case of the A β ₁₋₄₀ peptide.^[72]

The presence of a modulator can influence the interaction between IDE and its substrate as well as have an impact on substrate degradation. The interaction between insulin and IDE is notable because it is a crucial starting point of many biological pathways.

When the recognition of insulin occurs (Figure 7), this hormone fits inside the region between the exosite and the catalytic site where the insulin digestion starts. The binding between IDE and insulin is characterized by a high affinity ($\sim 100\text{nM}$) and a rapid cleavage rate ($K_{\text{cat}} \sim 0.5\text{-}2/\text{s}$).

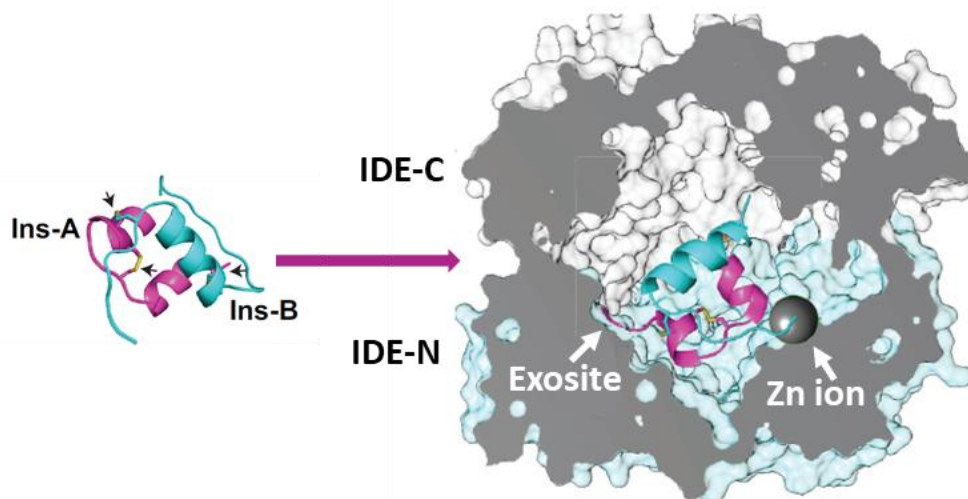


Figure 7 The structure of insulin required for the recognition and the degradation by IDE. In the figure is shown the A and B chain coloured in purple and cyan respectively. The arrows point out the intra and inter-molecular disulfide bonds. On the right side, the binding between insulin and IDE in the middle of exosite and Zn core is displayed. Adapted from Ref^[73] under Creative Commons CC BY 4.0 license; published by eLife 2018.

The main biological task of IDE is the degradation of substrates as insulin and A β peptides, which play a pivotal role in their homeostasis in diabetes and AD respectively since both molecules are essential for the right glucose catabolism, and the protective activity toward mature neurons.

The capability of IDE to promote the proteolytic process lies in the size of the substrate whose sequence cannot exceed the 70 amino acids. Hence, the size and shape of insulin are well-suited for IDE proteolytic activity. However, the flexibility and conformational changes of insulin play a crucial role in its digestion within the active IDE groove. Experimental evidence indicates that insulin undergoes the disruption of an α -helix at the N-terminus of insulin A chain in order to exhibit the hydrophobic residues near the N-terminus of insulin B chain to promote the degradation^[74].

Indeed, the binding of the N-terminus of insulin A chain to the exosite is very crucial for the insulin unfolding because the replacement of a single amino acid, isoleucine instead of alanine, causes the decreased thermodynamic stability of insulin that facilitates the hormone unfolding. The flexible features of insulin allow a tighter anchoring on IDE surface with a high affinity binding^[74].

As explained before, IDE has two conformational states, “open (IDE^o)” and “close (IDE^c)”, both contributing to the complete proteolytic process of insulin, although only IDE^o is suitable for insulin binding. Hence the initial interaction between IDE and insulin implicates the conformational switch

from IDE^c to IDE^o, but once the recognition occurs, the entrapment of insulin within the IDE chamber requires a reversal to IDE^c. When the IDE-insulin complex is formed, IDE seems to cut one of the two sites located on the A chain because these sites are the closest to the catalytic chamber whereas the B chain is sterically hindered by the A chain^[64].

Until this moment and during the insulin unfolding step, the A chain holds tight the IDE-N and IDE-C allowing the holding of the close state of IDE.

As soon as the complete proteolysis occurs, and the other four sites located on the central helix of the B chain are cut, the binding with IDE-N and IDE-C is hindered, inducing the formation of IDE^o and the release of insulin fragments. At the end of the proteolytic process, the closed state is reactivated (Figure 8).

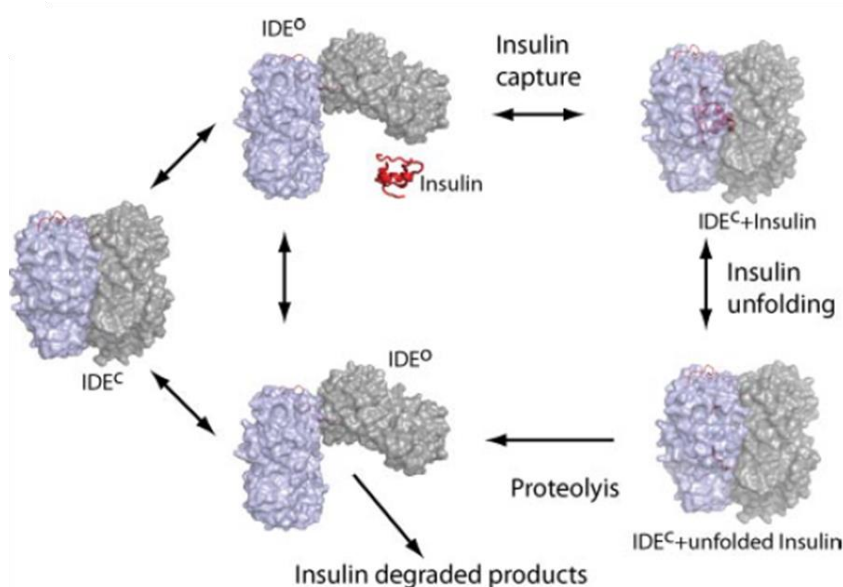


Figure 8 The proteolytic process of insulin. Adapted from Ref^[74] under Creative Commons CC BY 4.0 license; published *Biol. Chem.* 2009.

Accordingly, Grasso et al.^[75] have worked on IDE molecules immobilized on the surface of a gold sensor chip interacting with insulin through a SPR-MS combined experimental approach.

The results suggest that IDE molecules are mainly immobilized in their monomeric form; however, they are equally capable of cleaving insulin, while undergoing a conformational change from the open to the closed conformation.

The A β peptide catabolism by IDE takes place extracellularly such as on the external part of the plasma membrane and in the lumen of the endosomes where this peptide is produced after APP breakdown^[76].

The IDE cleavage sites on the A β peptide include His13-His14, His14-Glu15, Val18-Phe19, Phe19-Phe20, Phe20-Ala21, and Lys28-Gly29, as shown in Fig.4 (purple I)^[42]. Notably, the A β fragments resulting from the digestion, are unable to oligomerize^[77,78]. Therefore, the proper activity of IDE is

essential for the correct degradation of the peptide, playing a crucial role in preventing the formation of β -amyloid plaques.

The $A\beta$ peptide-IDE interaction occurs with both catalytic chamber and the exosite through the formation of a structure stable enough to be detected. Specifically, the stringent interaction arises from the anchoring of fragments 1-3 and 16-22 within IDE, limiting the movement of the amyloid and enhancing the number of interactions^[41,79]. Noteworthy is the slight cooperation displayed by IDE in the $A\beta_{1-40}$ -IDE interaction, where the interaction between this peptide and one IDE catalytic site of one subunit facilitates the cleavage of a second $A\beta_{1-40}$ molecule by another IDE subunit^[80-82].

2.3.3. Heterotropic modulation of IDE activity in AD

The heterotropic modulation is different from the homotropic type since the substrate and the modulator are different in this case. Indeed, the modulator (exogenous molecule) induces a conformational change at the exosite in order to increase or decrease the digestion of substrate at the catalytic site, depending on the type of modulator.

The enhancement or the reduction of the proteolytic activity of IDE is achieved with an exogenous molecule acting as activator or inhibitor, respectively.

A clear example of heterotropic activator for $A\beta$ peptide and insulin is somatostatin, which enhances the degradation of both peptides by IDE at submicromolar concentrations.^[83] In the case of somatostatin, two additional binding pockets were found: one is identified as the “traditional exosite” while the other one, called “secondary exosite”, is much closer to the catalytic site compared to the traditional one^[83].

Of course, *in vivo*, IDE activity regulation might occur also by increasing or decreasing the enzyme expression. As an example, among the natural-originated molecules, curcumin significantly decreases the expression of $A\beta_{1-40}$ and $A\beta_{1-42}$ peptide through the upstream inhibition of β -secretase,^[84,85] whereas regulates the level of the just formed peptide enhancing the IDE expression^[86].

On the contrary, ATP shows an ambiguous behaviour toward the IDE activity. Indeed, although it seems to act as a heterotropic inhibitor for $A\beta$ peptides and insulin at millimolar concentrations^[87,88] showing an allosteric non-competitive inhibitor mechanism, on the other hand it appears to activate IDE cleavage of synthetic^[62] or short peptides.^[72] However, the role of ATP in IDE activity remains unclear because its dual and contradictory action.

Acclaimed IDE inhibitors include EDTA and 6bK. As a potent metal-chelating agent, EDTA is a widely recognized inhibitor of IDE activity. Typically, the dissociation constant (K_d) of a zinc-binding motif falls within the range of 10^{-9} to 10^{-10} M, whereas EDTA binds to zinc with much greater strength with a K_d of approximately 10^{-16} M^[89]. Consequently, EDTA stands as a good competitor

for zinc binding, capable of effectively ripping the zinc ion off from the enzymatic chamber. For this reason, EDTA is often employed as an inhibitor controller^[69,90].

6bK is a member of macrocycle 6b and the selective inhibition of 6bK towards IDE in vitro is \geq 1,000 fold compared to the other metalloproteases. The nature of inhibition displayed by 6bK resides in the position occupied by the macrocycle within the IDE structure. The location is a binding pocket at the interface of IDE domains 1 and 2, which is situated 11 Å away from the catalytic zinc ion. The final structure resulting from the 6bK-IDE interaction, suggests that through engagement with this distant site, the macrocycle obstructs substrate binding and disrupts essential interactions needed to unfold peptides for cleavage.

As well as the proteolytic activity, IDE, in a non-proteolytic manner, is able to hinder the formation of amyloids. This role of IDE has been named “dead end chaperons” and it involves peptides as α -synuclein. Several studies have demonstrated the formation of a stable and irreversible complex between IDE and α -synuclein, which involves the positively charged exosite region of IDE and the negatively charged C-terminus of α -synuclein^[91,92].

The capacity of IDE to preclude the toxic amyloid formation of α -synuclein represents an incisive impact in the onset and in the development of PD.

2.3.4. IDE and the Ubiquitin Proteasome System

Interesting further studies have highlighted a correlation between IDE and the Ubiquitin Proteasome System (UPS) which holds a crucial role in the degradation of abnormal and misfolded proteins. In human organism, this chain reaction called ubiquitination involves three different enzymes (E1, E2, E3) that label the damaged protein with seven Lys residues.

The endpoint of ubiquitination reaction is a ubiquitinated protein that will be recognized by a series of substrate receptors identified by the 19S regulatory particles (RP) of proteasome^[93].

In eukaryotes, the proteasome is composed by a cylinder-shaped multimeric protein complex called 20S catalytic core particle (CP) divided into 28 protein subunits, α and β , and one or two 19S RPs. Indeed, the 20 CP can be single capped 26S (20S + 19S) (Figure 9, panel A) or double capped 30S (20S + 19S + 19S). In the β rings there are three catalytic enzyme β 5, β 2 and β 1 corresponding to chymotrypsin-like activity (ChT-L), trypsin-like activity (T-L) and peptidylglutamyl-peptide hydrolyzing (PGPH)^[94-96].

Sbardella et al.^[97] have highlighted a correlation between IDE and uncapped 20S suggesting a competition with 19S in vitro. According to these studies, IDE binds the free 20S in a bimodal manner inhibiting at (IDE) \leq 30nM and activating at (IDE) \geq 30nM envisaging IDE as a modulator for 20S.

Through the resolution of the crystallographic structure of the 20S proteasome, it is possible to envisage that IDE binds the outer surface of α_3 subunit of 20S proteasome via electrostatic interactions. It is to be noted that α_3 is a critical subunit in mediating the opening of the 20S gate by its N-terminal domain (Figure 9, panel B).

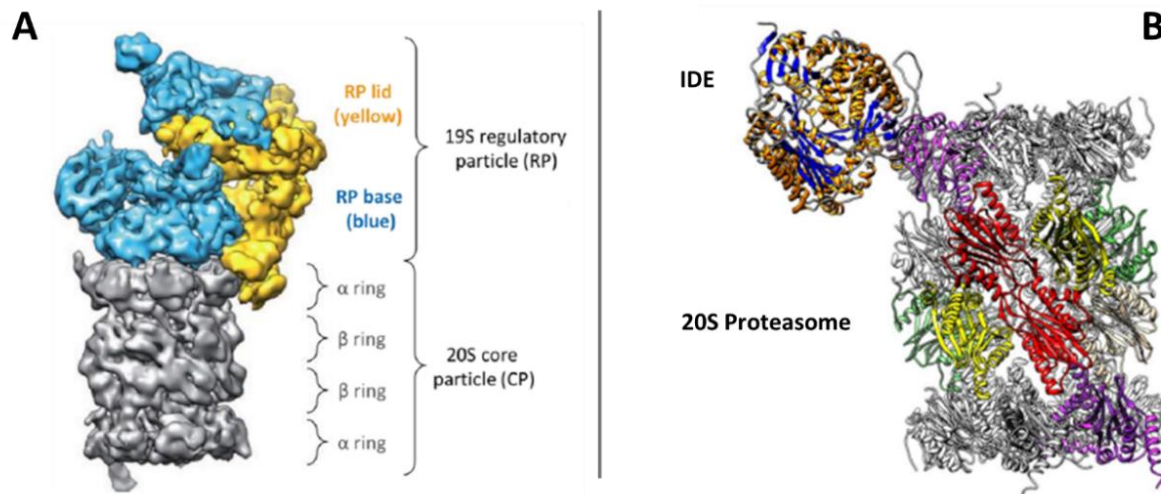


Figure 9 **A)** Structure of 26S (20S+19S) Proteasome. Adapted from Ref^[98] under Creative Commons CC BY 4.0 license; published Nature 2012; **B)** Top-10 best-scoring poses obtained by docking of IDE on 20S Proteasome. Adapted from Ref^[97]; published Cell. Mol. Life Sci. 2018.

2.4. Carnosine

Car was discovered in 1900 by Gulewitsch and is a dipeptide formed by β -alanine and L-histidine (Figure 10).

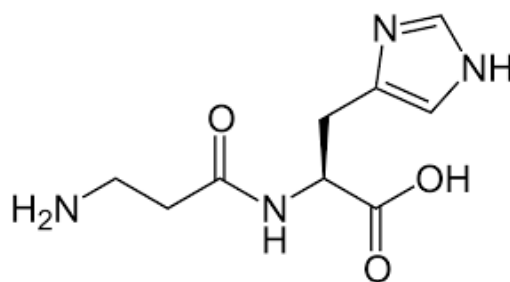


Figure 10 The structure of Car.

The synthesis for the formation of Car starts from two amino acids, β -alanine, and L-histidine used by the Car synthetase enzyme. Mg^{2+} and ATP are also required for the synthesis. Car synthetase is a homotetramer whose gene is located on chromosome 11q13 in humans and codifying for 950 amino acids. Car is widespread over the human body with low millimolar concentrations at brain^[99] levels and high millimolar concentrations in cardiac and skeletal muscles.^[92] It is very soluble in water as it contains three ionizable groups, namely the carboxylic group (pK_a 2.76), the amino group of the β -

alanine (pK_a 9.32), and the nitrogens of the imidazole ring (pK_a 6.72); at physiological pH, Car is normally found in a zwitterionic form. Moreover, Car has two tautomeric forms at the level of imidazole ring existing at neutral pH, where tautomer I is the most prevalent species (75%), tautomer II being energetically less stable than the tautomer I (Figure 11).

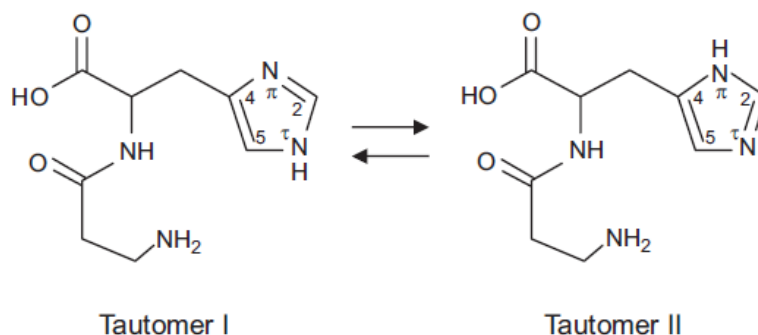


Figure 11 Tautomeric forms of imidazole ring of Car.

Since Car sequence has only two amino acids, it is classified as a small peptide. Nevertheless, it possesses a peptide bond and a stereocenter.

The two known isomeric form of Car that can be isolated and identified according to the Fischer projection are D- and L-Car (Figure 12). As all isomers, both forms share a lot of properties, although the few physical features which distinguish them, have an important effect on the responses of biological systems due to the difference in the stereochemistry of these two small peptides.

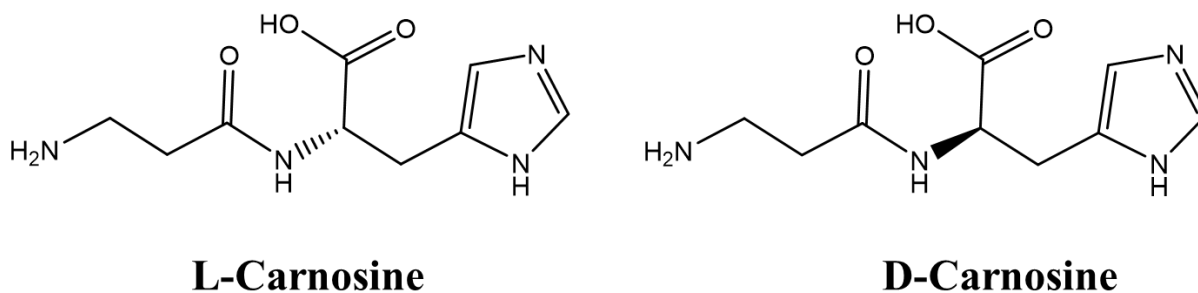


Figure 12 2D Structure of L-Car and D-Car.

One of the well-known differences between them is that only L- Car is endogenous in the human body suggesting the total presence of Car as L form. As a consequence, the latter is strongly decomposed by endogenous enzymes such as serum carnosinase (CN1-CN2), which regulates its homeostasis.^[91] On the contrary, D- Car is not recognized by homeostatic systems making it more resistant to enzymatic decomposition.

Lastly, another crucial property is the ability to act as a ligand of metal ions where the different stereochemistry would seem to play a key role. L- Car can coordinate metal ions such as Cu (II) and

Zn (II)^[100,101], whereas experimental studies have demonstrated the inability of D- Car to exhibit a chelating action.^[102]

Due to the previously mentioned rationale, Car employed in all experiments is L- Car. However, for the sake of simplicity, it will be referred to as just " Car."

Car shows several advantageous properties as an antioxidant, anti-inflammatory, anti-aggregating, and anti-aging activities that make it a key molecule in treatment of neurodegenerative diseases as AD. The toxicity of copper and zinc, and how their dyshomeostasis in the brain causes a key factor in this pathology are well known. Grasso et al. demonstrated that copper ions in both oxidation states inhibit IDE activity toward A β peptides.^[103] This harmful scenario could be overcome thanks to the ability of Car to form a stable dimeric complex with Cu ions or Zn ions through the imidazole ring bond.

Hence, the reduction of the bioavailability of copper and zinc leads to a decrease in the production of ROS species coupled with the ability of Car to scavenge the peroxy radicals at millimolar concentrations.^[104] This antioxidant and scavenging activity of Car was confirmed in numerous studies suggesting that the radical scavenging is due to the L-histidine rather than β -alanine.

Histidine contains an imidazole group responsible for the binding with metals. The presence of the histidine within the majority of metalloproteins, suggests a deeper understanding of the chelate role of this amino acid toward heavy metals. According to Umadevi, the binding of the metal with histidine creates a square planar-like conformation complementing water molecules attached to the metal.^[105]

Conversely, Gorboletova proposes a complex where two histidine attaches each metal ion with three ligands, the imidazole, the NH₂, and COO⁻ assembling as a consequence an octahedral structure. This suggestion is supported by complexes of metal ions with ethylenediaminetetraacetic acid (EDTA)^[106] and diethylenetriaminepentaacetic acid (DTPA).^[107]

Another important feature of Car is the ability to prevent the formation of AGE (Advanced Glycoxidation End-products) and ALE (Advanced Lipoxidation End-products), both involved in aging as well as in the onset of neurodegenerative diseases. Although the overall mechanism is still not well understood, it seems that Car acts through different pathways and is able to quench the reactivity of 4-hydroxy-2,3-nonenal (HNE), the most famous precursor of ALE. Moreover, the inhibitor effect of Car against ALE is to hinder the oxidation of lipids in the first step of ALE synthesis, causing the breakdown of reactive carbonyl species (RCS) (Figure 13, panel A).

On the other hand, Car acts on AGE inducing the break of Schiff base, which is the first product of protein glycation, to obtain the protein and the glucose separately, as well as avoiding the oxidation of glucose and the formation of RCS. Furthermore, Car inhibits the oxidation of Amadori product and conversion in AGE (Figure 13, panel B).

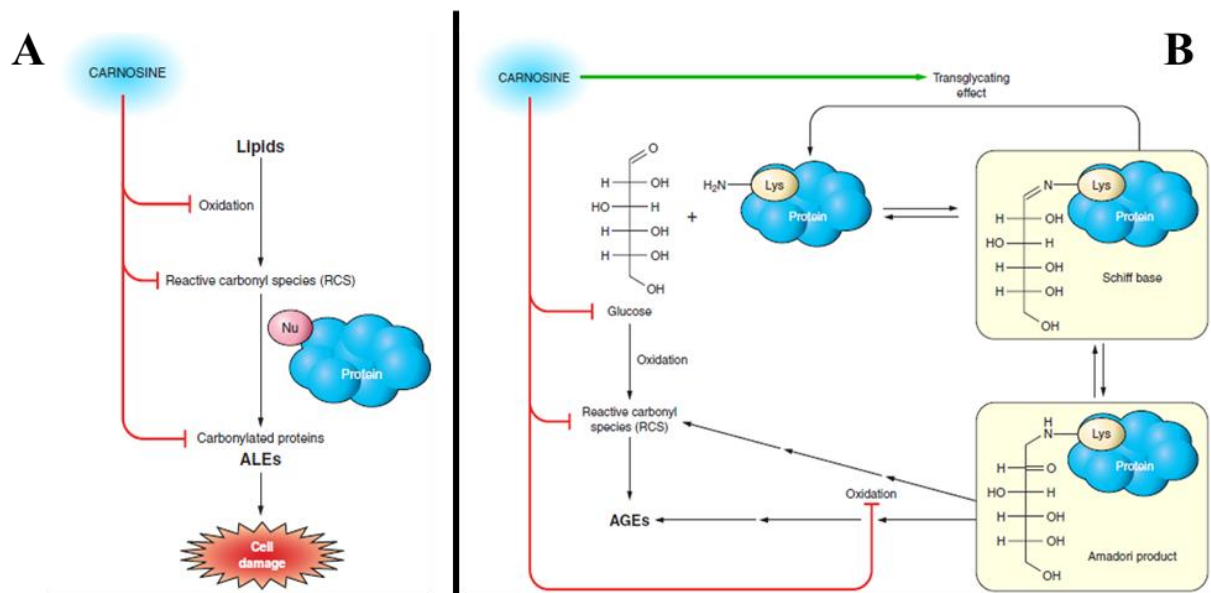


Figure 13 **A)** The antioxidant action of Car toward ALEs. **B)** The four antioxidant pathways of Car to avoid the formation of AGE. Adapted with permission from Ref^[108] published by *Physiol. Rev.* 2013.

All these features could contribute to the regression of AD including the capability of Car to acts as a potential anti-protein-cross-linking agent of A β peptide whose property is ascribed to the imidazole functional group of histidine.^[109]

2.5. Results and Discussions

The catabolism process of A β and insulin represents a critical process for maintaining brain health and proper blood sugar control. Research in this area is ongoing to develop potential therapies for AD. However, the presence of small molecules can play a crucial role in this process by promoting or inhibiting the catalytic activity of metalloproteases that regulate A β and insulin levels in the brain and bloodstream.

Among various modulators, Car stands out due to its numerous properties and ubiquity, becoming an intriguing compound with several potential health benefits. However, the role of this dipeptide in AD is not completely understood, and further investigations are required to gain a more comprehensive understanding of its involvement in the disease.

In this context, the purpose of this chapter is to understand if Car exerts a neuroprotective role through IDE activity modulation in the case of AD. To test this hypothesis, mixed cultures of cortical cells consisting of neurons (35–40%) and glial (astrocytes and microglia; 60–65%) were treated with A β ₁₋₄₂ oligomers for 48h (experiments performed by other research groups from University of Catania).

The monomeric form of lyophilized HFIP-treated A β ₁₋₄₂ was first suspended in DMSO at the final concentration of 5 mM and diluted in ice-cold cell culture medium DMEM/F12 (1:1) at the final concentration of 100 μ M. A β ₁₋₄₂ samples were then incubated at 4 °C for 72 hours and immediately used for the cellular treatment. Primary mixed neuronal cultures were obtained from rats at embryonic day 15 and grown into MEM supplemented with HS (10%), FCS (10%), glutamine (2 mM), and glucose (6 mg/ml). In order to avoid any proliferation of non-neuronal cells, Cytosine-Darabinofuranoside (10 μ M) was added to each dish 5 days after plating and was kept for 3 days before the next change of medium.

The toxicity expressed by mixed cells via trypan blue exclusion assay increases for the cell treated with A β ₁₋₄₂ oligomers (brown block) as compared to the untreated cell (white block) (Figure 14). Conversely, the addition of Car during the incubation leads to a marked reduction in cell toxicity (pink block).

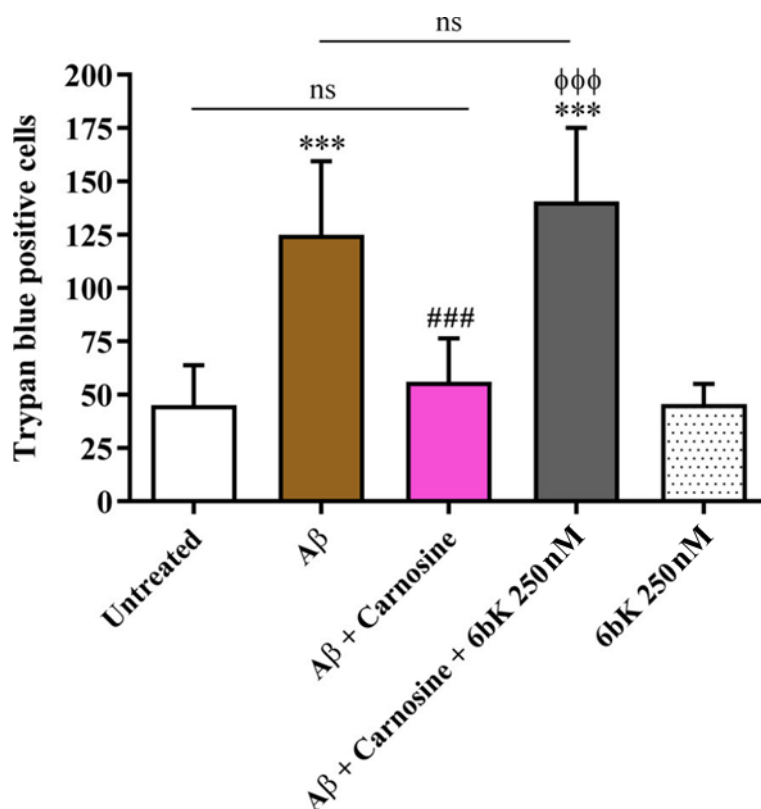


Figure 14 Neuroprotective effects of Car against the toxicity induced by A β_{1-42} oligomers assessed by cell counting after trypan blue staining. Primary mixed neuronal cultures were treated with A β_{1-42} oligomers (1 μ M) for 48 h in the absence (brown block) and in the presence of Car (10mM, pink block). The effect of 6bK pretreatment (1 h; 250 nM) is represented with a dark grey block. Cell counts were performed in three to four random microscopic fields/well. Data are the mean of 7 to 8 determinations. Standard deviations are represented by vertical bars. ***Significantly different from untreated cells, $p < 0.001$, ###significantly different from A β_{1-42} oligomers, $p < 0.001$, φφφsignificantly different from A β_{1-42} oligomers + Car, $p < 0.001$; ns = not significant. Adapted from Ref^[110] under Creative Commons CC BY 4.0 license; published by ACS Chemical Neuroscience 2022.

To verify if the neuroprotective action of Car is mediated by IDE, the highly selective IDE inhibitor 6bK was added to the treatment. Surprisingly, the cell toxicity arises again (dark grey block) suggesting that the selective inhibition of IDE hinders the protective activity showed previously by Car. Moreover, the action of Car is dose-dependent, indeed, the neuroprotective activity enhances as the dipeptide concentration increases^[110].

To underscore the significant role of glial cells in the neuroprotective activity exerted by Car, pure neuronal cultures were subjected to treatment with A β_{1-42} , both in the absence and the presence of Car (experiments performed by other research groups from University of Catania). The cellular viability was assessed using the MTT assay, revealing a notable decrease in cell viability compared to the untreated cells^[110]. The treatment cells were incubated with MTT (0.9 mg/ml final concentration) for 2 hours at 37 °C. As a last step, 200 μ L coming from each type of sample were transferred to a 96-well plate and the absorbance at 569 nm was read using a plate reader (Spectra Max M5, Molecular Devices, Sunnyvale, CA, USA). Untreated neuronal cells were used as controls.

This finding emphasizes the crucial contribution of glial cells in mediating the neuroprotection elicited by Car.

DLS (experiments performed by other research groups from University of Catania) was executed to explore the changes into hydrodynamic diameter (d_h) of IDE in the presence of Car (Figure 15, panel a).

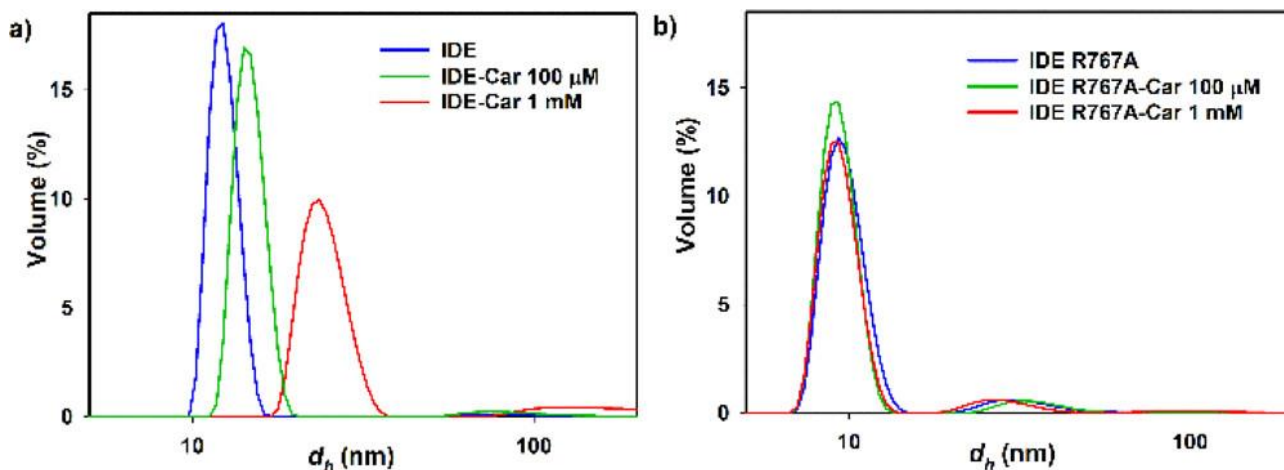


Figure 15 DLS measurements of (a) IDE wild type and (b) IDE R767A in the presence of increasing concentrations of Car. Adapted from Ref^[110] under Creative Commons CC BY 4.0 license; published by ACS Chemical Neuroscience 2022.

The measurements were performed with a Zetasizer Nano ZS (Malvern Instruments Ltd., UK) instrument equipped with a He–Ne laser.

All samples were measured 4-5 times with at least 12 accumulated scans. IDE or IDE R767A (1.3 μ M) was incubated alone or in the presence of Car (0.1 and 1 mM) in Tris buffer (pH 7.4). DLS data were acquired from 25 to 65 $^{\circ}$ C at 2 $^{\circ}$ C intervals with an equilibration time of 180 s.

Usually, d_h of IDE is approximately 12.7 ± 0.9 nm^[72]. However, when the analysis is conducted in the presence of Car, the hydrodynamic diameter of IDE raises as the Car concentration increases. This finding suggests that Car triggers an oligomerization process in IDE.

In contrast, the analysis performed for the IDE R767A monomeric variant both in the absence and in the presence of Car, showed a different scenario (Figure 15, panel b). Indeed, the addition of Car does not change the hydrodynamic diameter of the IDE R767A, which remains unchanged even at higher concentration of the dipeptide.

The IDE R767A is a specific variant of IDE enzyme in which the amino acid arginine (R) at position 767 in the IDE protein is substituted by alanine (A). This replacement results in changes such as the structure of the protein and in a lack of the ability to form dimers, an oligomeric form of the enzyme considered important for the functional modulation of the proteasome and chaperon-like activity^[111].

As a consequence, this result reinforces the hypothesis that Car acts on the IDE oligomerization process. Based on the results obtained through the MTT assay and DLS analysis, it can be inferred that Car not only exerts a neuroprotective function against A β through IDE but that this modulation also affects the oligomeric process of the enzyme by significantly increasing its hydrodynamic diameter in a concentration-dependent manner.

Therefore, in order to understand how Car acts on the IDE activity, two independent techniques, SPR and MS were applied. The aim of both techniques was to scrutinize the activity of IDE, elucidate the molecular and kinetic details based on the IDE and insulin interaction as the chosen model system, and unveil the intricate role of Car within IDE-insulin interaction.

2.5.1. Surface Plasmon Resonance (SPR) investigation.

SPR technique is widely used in the biomedical field for various applications. Based on a quantum optical-electrical phenomenon arising from the interaction of light with the free electrons at the metal surface, this technique allows the real time monitoring of biological phenomena occurring on the surface. Indeed, SPR biosensors can monitor and measure the type of binding occurring between two or more biomolecules over time through changes in the SPR response, a dimensionless parameter derived from the conversion of angle shift. The final outcome is a typical graph called *sensorgram* where kinetics information about biomolecules interactions are collected.

In this context, we employed SPR techniques to explore the influence of Car on the IDE-insulin interaction. By developing a novel experimental method, we monitored the SPR response over time to understand the dynamics of this interaction in the absence and in the presence of Car.

Additional information is provided by the Hill function, which is commonly applied to allosteric enzymes like IDE. This function yields the Hill coefficient, a term directly connected to the degree of cooperativeness exerted by a modulator on the enzyme-substrate interaction, which helps to identify the nature of the modulator.

Thanks to the application of the Hill function, we have uncovered the type of modulation deployed by Car, and we have shed the light on the role of another important modulator for IDE, i.e., ATP.

2.5.1.1 Functionalization of gold sensor chip

The gold sensor chip (SPR 102-Au gold chip. Composition: 50 nm of gold, 2 nm of chromium on glass surface. Dimensions: 20 nm long, 12 nm wide, 0.55 nm thick) was functionalized with the Lomant's reagent in DMSO (Lomant's reagent/DMSO stoichiometric ratio = 2) under a nitrogen

atmosphere for four days.^[112] After four days, the sensor was washed with fresh DMSO, ultrapure water, ethanol and lastly it was dried out with a N₂ flow.

SPR analyses were performed with Bionavis SPR Navi 210A instrument. The system mounts a microfluidic system and two distinct laser with two different wavelengths, 670nm and 750 nm.

2.5.1.2. Immobilization of IDE

The immobilization of IDE was carried out by fluxing a solution of 100nM of IDE in PBS (pH = 7.4) on a functionalized gold sensor chip in parallel configuration (only on the sample channel) at 15 μ L/min for 15 minutes.

The immobilization occurs via peptide bonds between the amino groups of IDE and the carboxylic groups of Lomant's reagent with the release of N-hydroxysuccinimide group. As the amine groups of IDE are widely distributed on the surface exposed to the solvent, this immobilization procedure ensures a layer of enzyme molecules randomly oriented on the surface, so to simulate the same conditions occurring in solution for the other interactions.

Once the immobilization of IDE was reached, a solution of ethanolamine-HCl (1M, pH = 8) was flowed on the sensor twice in serial configuration (both sample and reference channels) at 15 μ L/min for 15 minutes in order to deactivate all the residual active sites on the surface.

In order to evaluate the number of IDE molecules immobilized on the surface, the SPR angle shift due to the enzyme immobilization has been measured and, in our experimental conditions, resulted to be 0.201 ± 0.029 deg. Noteworthy, as a rule of thumb, if a wavelength of 670nm is employed, 1 ng mm⁻² of immobilized adsorbate corresponds to a signal of about 1000 RU SPR angle shift. For our instrument (Bionavis SPR Navi 210A) 1 mdeg SPR angle shift corresponds to 8.0 resonance unit (RU), therefore 201 mdeg is equal to 1608 RU. Hence the ng deposited on mm² corresponding to 1.608 ng.

According to the gold sensor chip used, the real portion of surface where the immobilization occurs is 12 mm². As a result, the ng deposited on 12mm² corresponds to 19.312 ng and the number of IDE molecules immobilized onto the examined surface is 8.243×10^{11} molecules cm⁻². This number is obtained by dividing the molecular weight of IDE and multiplied by the Avogadro's number.

Moreover, the adlayer thickness (d) of IDE was calculated from the following equation 1:

$$d(cm) = \frac{\theta(\text{molecules/cm}^2)}{N(\text{molecules/cm}^2)} \quad (1)$$

where θ corresponds to 8.243×10^{11} molecules cm^{-2} and N is the bulk number density of the adsorbate. This latter is obtained by dividing the bulk density of adsorbate ρ ($\rho = 1.30 \text{ g cm}^{-3}$)^[75] and the Avogadro's number multiplied by the molecular weight.

Thus, considering the previous formula, the IDE adlayer thickness (d) is $1.30 \pm 0.18 \text{ nm}$.

In order to minimize the aspecific interactions between insulin molecules and the reference channel, a Bovine Serum Albumin (BSA) solution ($100 \mu\text{M}$) was flowed on the sensor in parallel configuration (only on the reference channel) at $30 \mu\text{L}/\text{min}$ for 7 minutes of injection.

Although the wider blocking agent used for activated ester groups is ethanolamine, a further treatment of the sensor with a BSA solution guarantees a more thorough deactivation of the reference channel surface^[113,114] and allows a comparable height between the sample and the reference channel, avoiding the problems due to a different homogeneity of the two channels.

In Fig.16 the immobilization steps of the IDE and BSA on sample and reference channel are reported respectively. The results are monitored by SPR.

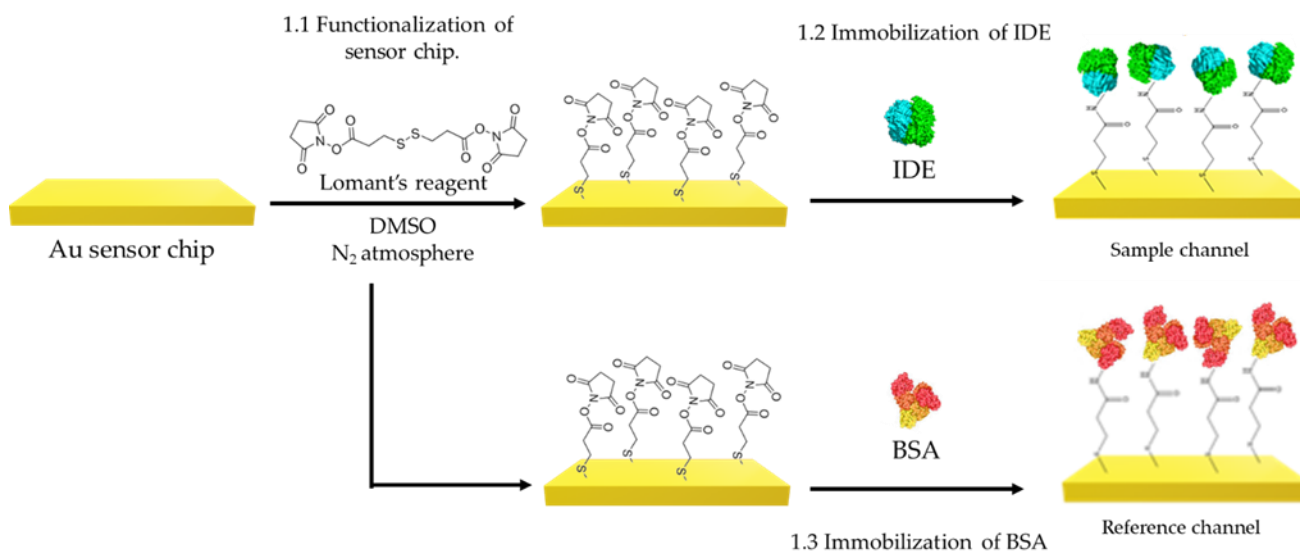


Figure 16 Schematic refiguration of both immobilization step of IDE on the sample channel and the BSA on the reference channel.

2.5.1.3 Immobilization of IDE monomeric variant (R767A)

The same procedure was applied for the immobilization of IDE monomeric variant: a solution of IDE R767A (50 nM) was fluxed onto the sample channel. The SPR angle shift reached was 0.205 therefore the value of θ corresponds to 1.01×10^{11} molecules cm^{-2} , and assuming that the bulk density of adsorbate ρ ($\rho = 1.30 \text{ g cm}^{-3}$) is the same for the monomeric variant, the IDE R767A adlayer thickness (d) resulted to be $1.30 \pm 0.18 \text{ nm}$.

2.5.1.4. Affinity analysis: The Hill function

Human insulin in PBS buffer at five different concentrations (500nM; 2.5 μ M; 5 μ M; 10 μ M; 20 μ M) were prepared as serial dilutions starting from the insulin stock solution at concentration of 0.2mM. All solutions were flowed onto the surface in serial configuration at 30 μ L/min for 7 minutes of injection time and 15 minutes of post-wait time. During this latter step, the fluxing of running buffer (PBS) allows the removal of the insulin molecules from the surface after the interaction with IDE (Figure 17, panel a).

Reported results are obtained by subtracting the signal from the reference channel containing BSA. The investigation of the interaction between immobilized IDE and insulin solutions was carried out in the absence and in the presence of different IDE activity modulators, Car, ATP and EDTA, at various concentrations in PBS buffer (Figure 17, panel b). Four sets of measurements composed by five samples with the different insulin concentrations have been carried out. For each set, the used concentrations of Car, ATP, and EDTA were kept constant. EDTA is used as an inhibitor control for IDE activity.

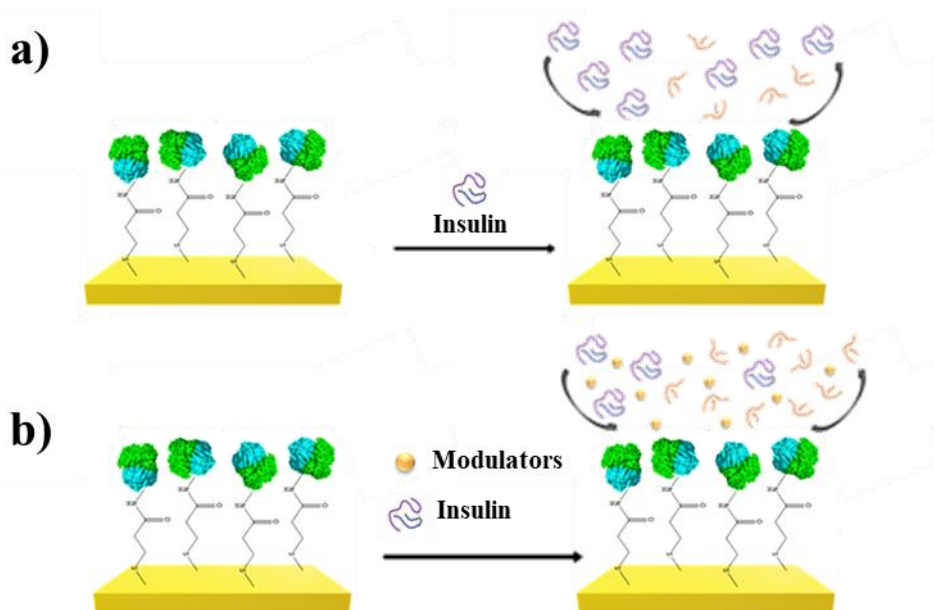


Figure 17 Schematic representation of interaction step between the IDE immobilized on the surface and **a)** insulin, and **b)** insulin with the three modulator analysed separately.

Lastly, in case of IDE R767, the interactions with only insulin and in presence of Car at two different concentrations (100 μ M; 1mM) were also scrutinised. Both set of measures (Table 1, set 6 and 7) were analysed with five different insulin concentrations, and the results were compared to the insulin-IDE system. In details, the compositions of samples with the various IDE modulators are reported in table 1.

	[Car]	[Insulin]				
Set 1	100μM	20 μ M	10 μ M	5 μ M	2.5 μ M	500nM
Set 2	1mM	20 μ M	10 μ M	5 μ M	2.5 μ M	500nM

	[ATP]	[Insulin]				
Set 3	100μM	20 μ M	10 μ M	5 μ M	2.5 μ M	500nM
Set 4	1mM	20 μ M	10 μ M	5 μ M	2.5 μ M	500nM

	[EDTA]	[Insulin]				
Set 5	100μM	20 μ M	10 μ M	5 μ M	2.5 μ M	500nM

	[Car]	[Insulin] (IDE R767A)				
Set 6	100μM	20 μ M	10 μ M	5 μ M	2.5 μ M	500nM
Set 7	1mM	20 μ M	10 μ M	5 μ M	2.5 μ M	500nM

Table 1 Composition of the solutions used in sets of experiments performed to investigate the interaction between IDE and insulin in the presence of different Car concentrations (set 1 and set 2), in presence of different ATP concentrations (set 3 and set 4), and EDTA at the concentration of 100 μ M (set 5). In addition, the composition of solutions used for the interaction between IDE R767A-insulin in presence of Car is also reported (set 6 and set 7).

SPR is an experimental technique based on an optical phenomenon occurring on a gold surface where the interaction between an analyte and a ligand immobilized on the surface produces a change in the system refractive index^[75,115,116] providing information about the type of interaction obtained.

A typical SPR curve is characterized by the presence of three phases: association, dissociation, and the steady-state (Figure 18). The latter is representative of the equilibrium state reached during the interaction between the analyte and the ligand. All sensograms exhibit a positive SPR response, which increases with the increase of insulin concentration.

Although our SPR system allows working with a wide range in solution concentrations (10^{-9} - 10^{-1} M), all the three IDE activity modulators chosen, namely ATP, Car, and EDTA, are small molecules, whose direct interaction with the enzyme is not detectable. However, the effect of modulators on the IDE-insulin interaction is well observed.

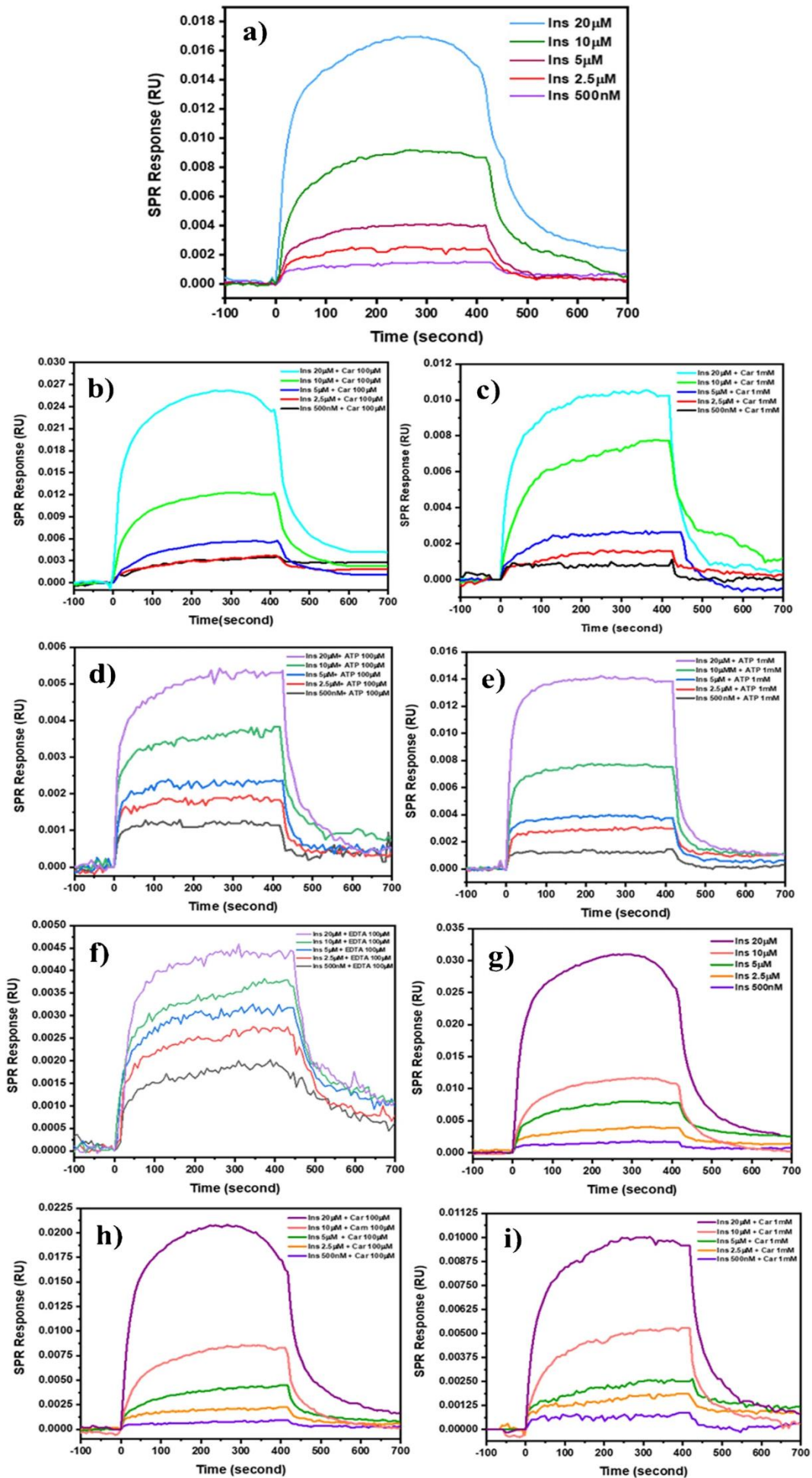


Figure 18 SPR sensorgrams ($\lambda = 670 \text{ nm}$) have been obtained after subtraction of the signal obtained from the reference channel with immobilized BSA (see text). Sensorgrams of IDE - insulin (500nM; 2.5 μM ; 5 μM ; 10 μM ; 20 μM) obtained from **a**) averaging three curves of IDE-insulin measurements; in the presence of **b**) Car 100 μM ; **c**) Car 1mM; **d**) ATP 100 μM ; **e**) ATP 1mM, **f**) EDTA 100 μM ; using IDE R767A in: **g**) the absence and in the presence of **h**) Car 100 μM ; **i**) Car 1mM. Adapted from Ref^[110] under Creative Commons CC BY 4.0 license; published by ACS Chemical Neuroscience 2022.

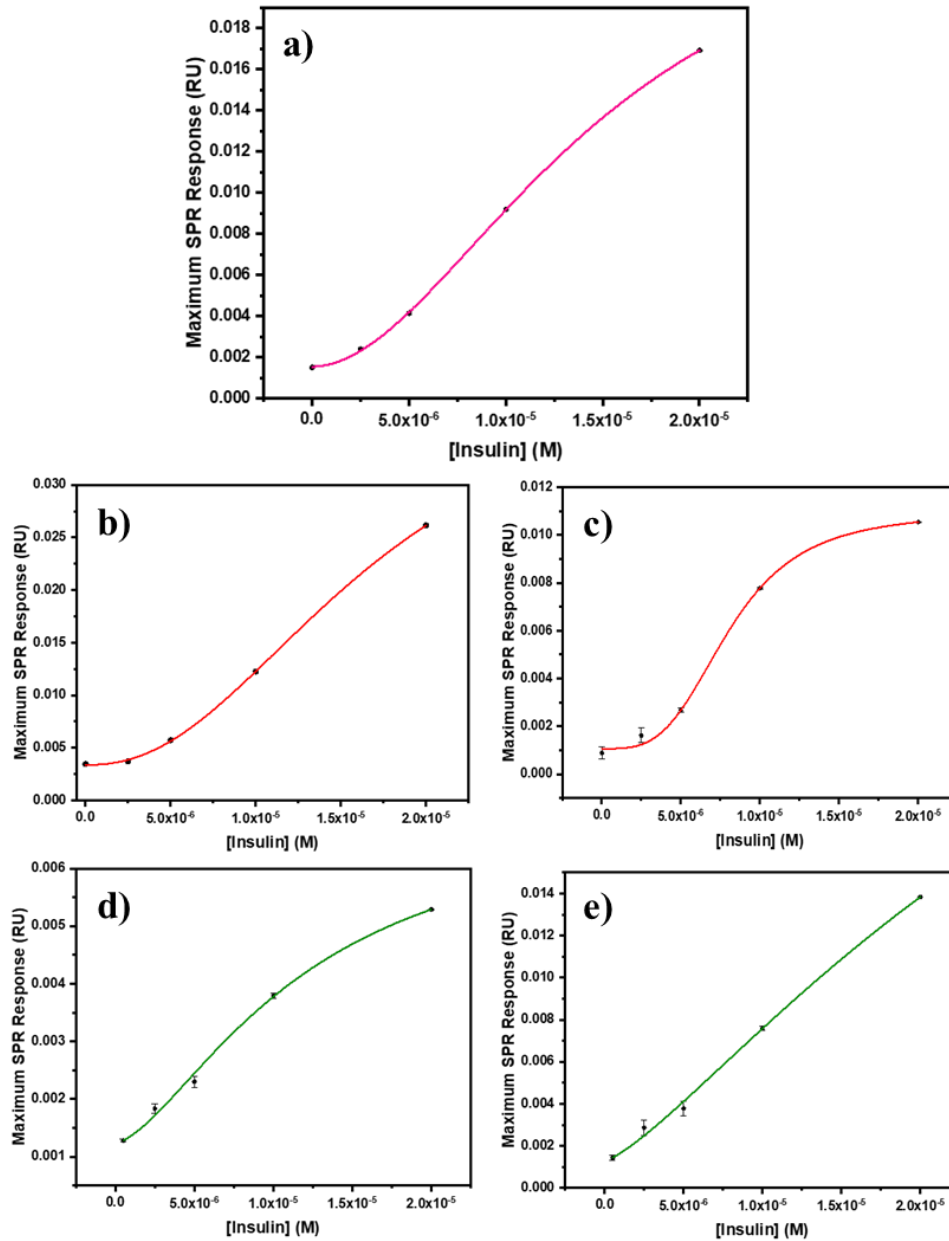
The purpose of this work is to examine the IDE-insulin interaction with and without the three modulators, obtaining the Hill coefficient values in the case of Car, ATP and EDTA, a well-known irreversible inhibitor for the IDE activity.

In this context, the most interesting part of the curve is the “flat zone”, located between 300 and 420s, which represents the equilibrium reached between insulin and IDE molecules immobilized on the surface (the steady-state phase) and corresponds to the maximum SPR response reached for a specific concentration of insulin during the interaction with the enzyme. The SPR response is not dependent on the enzyme activity, as it rather depends on the binding between the biomolecules and how the modulators affect such binding. Indeed, although insulin is also degraded by the enzyme, the solution replenishment guaranteed by the high flow rate used during the experiment (30 $\mu\text{L}/\text{min}$) ensures the establishment of an equilibrium state between immobilized IDE and not-degraded insulin (steady-state part of the SPR sensorgram). Nevertheless, in the case of high insulin concentrations, the steady-state part of some curves is followed by a lowering in the SPR signal (see the curves obtained for Figure 18 a, b, g e h). This phenomenon is explainable considering the ability of IDE not only to interact with insulin but also to degrade the hormone in catalytic manner.^[75] Indeed, although at the flow rate used during the experiment (30 $\mu\text{L}/\text{min}$) a fresh insulin solution is constantly supplied to the flow cell, it is well possible that the produced insulin fragments just released from the enzyme and still very close to the surface could bind IDE, as normally occurs in static IDE-insulin solutions. In such a situation, having the insulin fragments a much lower molecular weight, a lower SPR signal would be produced, justifying the abovementioned trend, which is indeed observed only at very high insulin concentration. As a support of this hypothesis, when EDTA is used (Figure 18 f), even the highest insulin concentration does not produce such a trend, as in this case the strong inhibition of the enzyme hinders the formation of insulin fragments and the occurring of such an unusual sensorgram shape.

The maximum SPR response extrapolated from the steady state of each curves (Figure 18) were plotted versus the insulin concentrations and the data points were fitted with the Hill’s binding model function employed in the Origin software. All the curves reported in Fig.18 were plotted with the following equation (2):

$$Y = Y_0 + (Y_{MAX} - Y_0) \cdot \frac{X^n}{K^n + X^n} \quad (2)$$

Y is the maximum $\Delta\theta$ SPR(RMAX), X is the insulin concentration, n and K are, respectively, the Hill coefficient and the Michaelis-Menten constant. Equation (2) is also employed for the analysis of IDE R767A-insulin interaction without (Figure 19, g) and with the presence of Car (Figure 19, h, i).



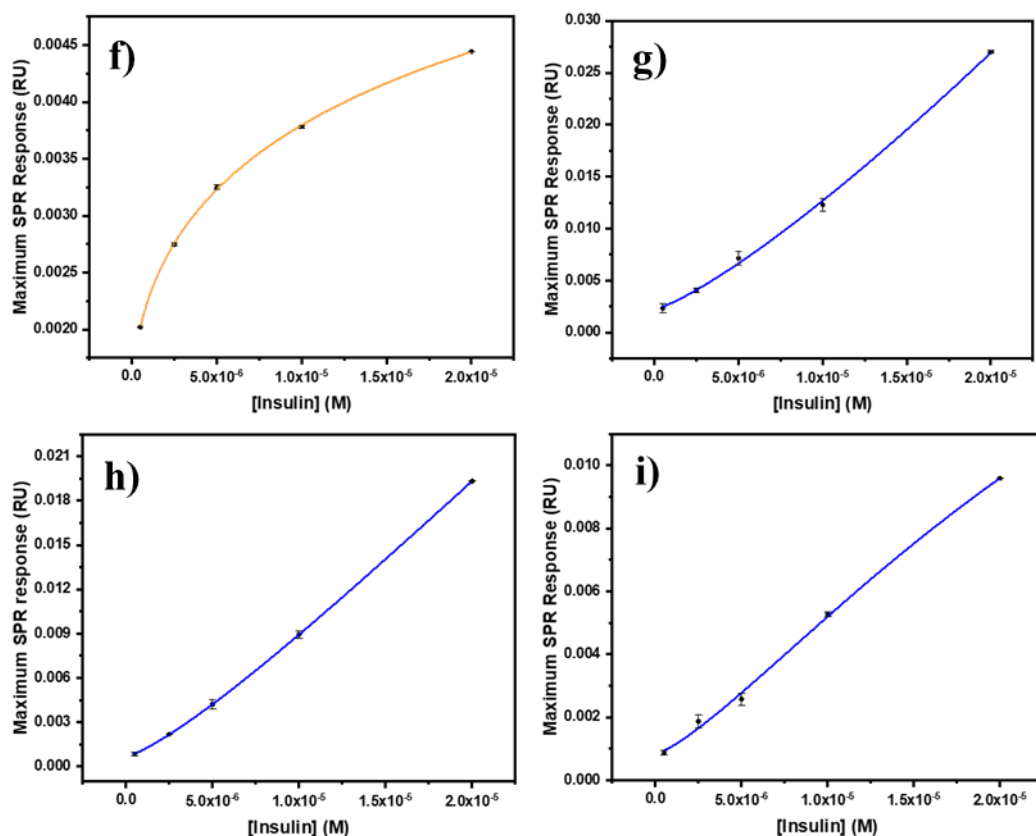


Figure 19 Experimental data extrapolated from the experimental SPR curves (Figure 18) have been fitted by using equation (2) as described in the text: IDE-insulin: (a) in the absence or in the presence of Car (b) 100 μM , (c) 1 mM, (d) ATP 100 μM , (e) ATP 1mM, (f) EDTA 100 μM ; using IDE R767A (g) in the absence or in the presence of Car (h) 100 μM and (i) 1mM. Adapted from Ref^[110] under Creative Commons CC BY 4.0 license; published by ACS Chemical Neuroscience 2022.

Solution	n	K_D (mol·L ⁻¹)	R^2
IDE – insulin	1.89 ± 0.11	$1.52 \cdot 10^{-5}$	0.9999
IDE - insulin + Car 100 μM	2.26 ± 0.21	$1.70 \cdot 10^{-5}$	0.9998
IDE - insulin + Car 1mM	3.36 ± 0.65	$8.09 \cdot 10^{-6}$	0.9977
IDE - insulin + ATP 100 μM	1.56 ± 0.38	$1.18 \cdot 10^{-5}$	0.9998
IDE - insulin + ATP 1mM	1.30 ± 0.43	$3.53 \cdot 10^{-5}$	0.9998
IDE – insulin + EDTA 100 μM	0.53 ± 0.19	$3.85 \cdot 10^{-5}$	0.9998
IDE R767A - insulin	1.24 ± 0.04	$2.66 \cdot 10^{-1}$	0.9987
IDE R767A - insulin + Car 100 μM	1.25 ± 0.02	$1.25 \cdot 10^{-4}$	0.9993

IDE R767A - insulin + Car 1mM	1.31± 0.53	3.50·10 ⁻⁵	0.9980
--	------------	-----------------------	--------

Table 2 The n (dimensionless quantity) and K_D (mol·L⁻¹) values obtained by fitting the curves for the IDE-insulin interactions with and without Car, ATP, and EDTA respectively as well as the IDE R767A-insulin with and without Car. The R-square is also reported in the last column^[117].

The n and K_D values obtained from the processing of Hill functions for all interactions are reported in Table 2.

The Hill coefficient is a crucial parameter in the study of ligand-receptor interactions and reflects the degree of cooperativeness of the substrate with the available binding sites. Cooperativity is a biomolecular phenomenon involving the interaction between receptors and ligands, and it is strictly tied to the concept of allosteric regulation; indeed, it can be positive or negative depending on the type of allosteric modulation occurring. Positive cooperativity arises when a higher affinity site of the receptor binds with the ligand after another binding site has already been occupied with a lower affinity; on the contrary, negative cooperativity is observed when the binding of a second molecule is hindered by the previous one.

Since both of them are typical for allosteric enzyme and the type of modulation has an impact on the affinity between the enzyme and the substrate, the Hill coefficient is also considered a measure of this affinity. Therefore, this value can give three different results depending on the type of interaction occurring: the $n= 1$ describes a non-cooperative binding in which the affinity of the enzyme for substrates does not depend on the real binding between enzyme and substrate, whereas an $n> 1$ and $n < 1$ apply for a positive and negative cooperative binding, respectively.

According with previous enzyme activity studies, the value of n is 2 when IDE interacts with insulin, showing a positive allosteric mechanism.^[68,118] The latter suggests that the binding of the substrate induces a conformational change of the enzyme, enhancing the formation of its more active dimeric form.

Current analytical techniques normally applied to obtain the cooperativity of the enzyme action are all based on activity measurements, hindering the possibility to both studying the allosteric mechanisms with inactive forms of the enzyme and giving information about allosteric mechanism. Contrarily, the SPR technique allows the study of biomolecular interactions and of the allosteric mechanism without being affected by the activity of the enzyme batch used.

Indeed, the Hill coefficient could be influenced by the activity of the enzyme and in addition, in case of a strong inhibition such as EDTA for IDE, the loss of activity hinders the possibility to study the allosteric mechanism. This is dodged with the use of SPR technique, where each type of interaction is hypothetically explored.

The n value obtained for the IDE-insulin interaction (shown in table 2) is equal to 1.89 in line with abovementioned values for the same interaction. The presence of Car increases the Hill coefficient in a concentration dependent manner, suggesting a positive allosteric modulation for IDE, which affects enzyme oligomerization and cooperativity.

The same behaviour is not detected in the case of IDE R767A, where the K_D value measured for the interaction with insulin in absence of any modulators ($2.66 \cdot 10^{-1}$) indicates a much lower affinity of the mutated IDE in comparison to the wild-type enzyme. Indeed, equilibrium constant K_D is represented in $\text{mol} \cdot \text{L}^{-1}$ and corresponds to the ratio of the off- and on-rates. K_D is defined as the ratio between the dissociation rate of ligand-analyte interaction (off-rate or dissociation constant K_d) and the association rate of the complex formation (on-rate or association constant K_a). A lower K_D value indicates a stronger binding affinity between the ligand and receptor, while a higher K_D value indicates a weaker binding affinity.

This aspect highlights the crucial relevance of the enzyme oligomerization and the correct functioning of IDE. Indeed, once Car is added to IDE R767A solution, the presence of the dipeptide induces, albeit weak, an increment of n value suggesting a milder affinity gain to insulin for the enzyme. Although the impossibility of IDE R767A to be allosterically modulated by the dipeptide, the measured Hill coefficient value of 1.2 indicates that a very slight cooperativity might occur. This result can be explained by considering that IDE R767A has been reported to be only “mostly” monomeric and could partially retain some allosteric modulations.

On the other hand, the presence of ATP induces a concentration-dependent decrease of the n value, and for ATP 1 mM a lower affinity of IDE for insulin is obtained, as demonstrated by the higher K_D values in this case. These results are a further confirmation of the inhibitory role of ATP toward the larger substrates for IDE.^[62,72,88]

Finally, the presence of EDTA lowers the Hill coefficient to a value smaller than 1, demonstrating a negative allosteric regulation of this molecule, which seems also to be able to lower the enzyme affinity for insulin (a higher K_D value is obtained also in this case).

Therefore, this innovative and direct method has allowed to unveil the activator role adopted by Car towards the IDE-insulin interaction, whereas the results obtained with ATP support the hypothesis of its inhibitory role towards the interaction between IDE and a large-sized substrate like insulin^[87,119-121].

2.5.2 Activator role of Car: A Mass Spectrometry approach

In order to investigate the involvement of Car on the IDE activity, I carried out HPLC coupled to MS analysis of different solutions of insulin at different concentrations with an increasing amount of Car (100 μ M, and 1 mM) and considering five incubation times.

The purpose of this section is to provide a deeper understanding of the role of Car activator within the IDE-insulin interaction by focusing on the insulin catabolic processes carried out by IDE.

2.5.2.1. Preparation of samples.

The enzymatic digestion of Human insulin was performed in according to this method: a solution of insulin (20 μ M) was incubated with IDE (180nM) in PBS buffer solution (pH 7.3) at 37°C inside a controlled temperature incubator. The experiment was monitored over the time taking six aliquots in the range of: 0, 10, 45, 60 and 180 minutes.

This latter set (Set 1) of measures was repeated twice in presence of Car 100 μ M (Set 2) and 1mM (Set 3). Indeed, a solution of Car has been incubated with insulin (20 μ M) and IDE (180 μ M) to attain a final solution of 100 μ M and 1mM.

Notably, the composition of sample is elucidated in Table 3 below:

		<i>Incubation time</i>				
<i>Set 1</i>	IDE 180nM	<i>0 min</i>	<i>10min</i>	<i>45 min</i>	<i>60 min</i>	<i>180 min</i>
	Insulin 20μM					
<i>Set 2</i>	IDE 180nM	<i>0 min</i>	<i>10min</i>	<i>45 min</i>	<i>60 min</i>	<i>180 min</i>
	Insulin 20μM Car 100μM					
<i>Set 3</i>	IDE 180nM	<i>0 min</i>	<i>10min</i>	<i>45 min</i>	<i>60 min</i>	<i>180 min</i>
	Insulin 20μM Car 1mM					

Table 3 *Incubation time of the solutions used in three set of measures performed to examine the kinetic degradation of insulin by IDE.*

Lastly, 10 μ L of 10%TFA was added for each sample in order to turn off the IDE activity. The TFA concentration in aliquots is 0.2%.

2.5.2.2. HPLC-MS analysis

The kinetic degradation of insulin and the analysis of its fragments have been obtained through the use of HPLC-coupled MS (Finnigan LCQ Deca XP Max LC / MSn, Thermo Electron Corporation, USA). The mobile phase consists in a mixture of high purity water (Milli-Q Element Ultrapure Water) and high purity acetonitrile (CH₃CN). Moreover, the mobile phase was degassed for 30 minutes. TFA was added to both solvents until it reached a concentration of 0.05%. The use of TFA is crucial in Chromatography because it is used as an ion-pairing agent allowing the suppression of the rejection of residual silanols of the stationary phase. This hinders nonspecific interactions between the analytes and the stationary phase.^[122]

During the analysis, the chromatographic column was kept at a temperature of 34°C, with a workflow of 250 µL/min and each experiment run last 40 min with a starting waste of time of 18 minutes to avoid the ions accumulation on the ESI source.

The instrument is equipped with an ESI source and an ion trap analyser, capable of scanning a m/z range from 15 to 4000 Uma with a nominal resolution of 10000 Normal Unit mass scan. The following method was applied to the ESI source, to optimize the quality of the acquired spectra: applied spray voltage was set at 4.8 kV, the capillary was kept at 300 ° C and 44 V, nitrogen gas flow was set at 8 (arb) during the whole duration of the analyses.

According to previously works, insulin is the ultimate substrate of IDE and the preferred cleavage sites are well known (Figure 20, panel a).

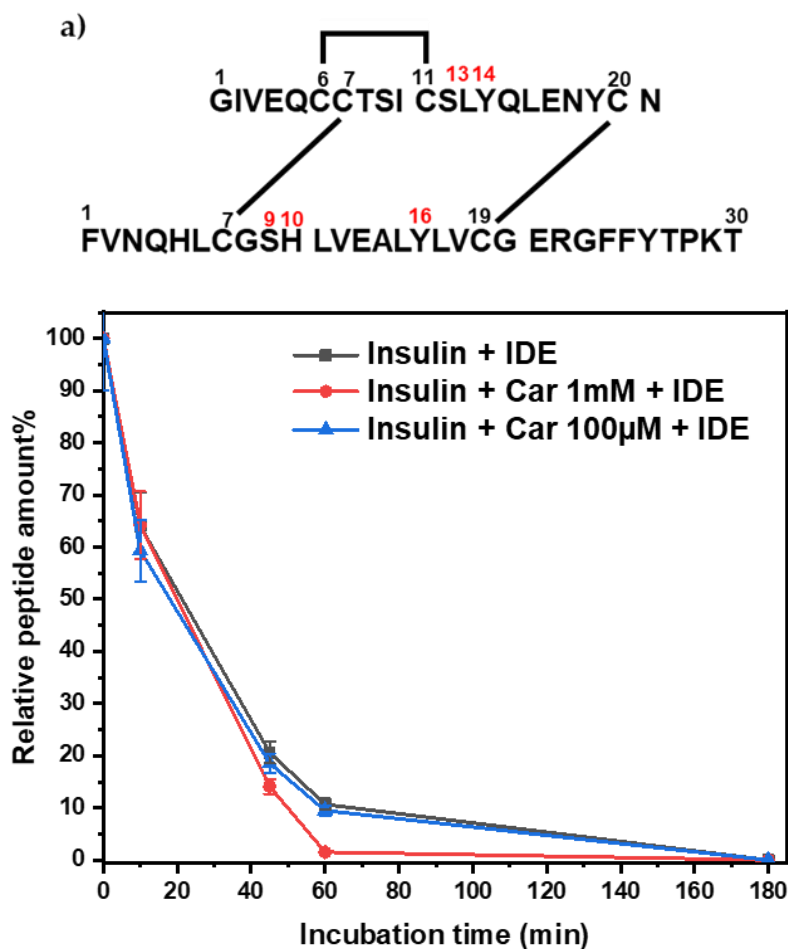


Figure 20 a) Primary sequence of insulin. The numbers in red point out the known cleavage sites of IDE during the insulin digestion; **b)** Normalized peak of insulin per incubation time. The \pm (error bars, 10%) for the three measurements are shown in figure. Adapted from Ref^[10] under Creative Commons CC BY 4.0 license; published by ACS Chemical Neuroscience 2022.

The relative amount of molecular peak corresponding to the insulin signal for each set of measures, was followed over the time considering the incubation times chosen. In Fig. 20 panel b, we report the intensity (in percentage) of the peak of insulin that is expressed as normalized area, as shown in equation 3:

$$\text{Normalized area} = \frac{\text{Area insulin } t}{\text{Area Tot}} \cdot 100 \quad (3)$$

where the Area insulin t is the area of the peak of insulin per incubation time and Area tot is the sum of all peaks per incubation time (0 min; 10min; 45min; 60min; 180min).

The relative amount of insulin treated with IDE, decreases in accordance with the literature and the presence of Car affects the rate of degradation of the substrate.

Therefore, it is visible a measurable activation of IDE depending on the Car concentration, in particular the insulin digestion increases when Car has a concentration of 1mM.

In order to know if Car influences not only the degradation rate of insulin but also the cleavage sites, the fragments obtained after the insulin digestion were measured with HPLC-MS and followed over the time. The normalized area of fragments derived from the insulin degradation, was obtained dividing each area of fragments by total area per incubation time (0 min; 10min; 45min; 60min; 180min). A summary of fragments obtained from insulin digestion is shown in Table 4.

<i>Fragments Pattern</i>			
A-B fragment	Retention time range (min)	Experimental peak (m/z)	Calculated peak (m/z)
[A (1-14) B (1-16)] ⁺³	28.76 - 28.83	1117.80	1117.80
[A (14-21) B (10-30)] ⁺³	28.21 – 28.43	1163.35	1163.40
[A (1-13) B (1-9)] ⁺²	26.98 – 27.24	1179.08	1179.80
[A (1-13) B (1-10)] ⁺²	26.58 – 26.78	1246.98	1248.90
[A (1-14) B (1-9)] ⁺²	27.38 – 27.52	1259.70	1261.40

Table 4 Summary of MS analysis of IDE-degraded insulin fragments per three sets of measures.

In Fig. 21, the histograms of fragments are showed for the three sets of measurements, insulin+IDE, insulin + Car 100 μ M+IDE and insulin + Car 1mM+IDE.

Comparing the system of insulin+IDE with the other two carried out in presence of Car, it is possible to understand that Car does not generate new cleavage sites but rather it increases only the rate by which these fragments are formed.

Finally, certain fragments display a formation trend resembling a bell curve, where they exhibit a distinct peak that does not coincide with the maximum incubation time. Indeed, unlike the m/z 1179.08 and m/z 1246.98 whose growth increases over the time, the m/z 1259.70 and m/z 1163.35 fragments reach a maximum formation and then decrease. The reason is due to the ability of IDE to degrade this fragments once they are produced during the insulin digestion suggesting that these fragments are in turn other substrates of IDE. As a result, the mass analysis reaffirms the role of Car as an activator of IDE activity, a role initially uncovered by SPR investigation through a higher Hill coefficient.

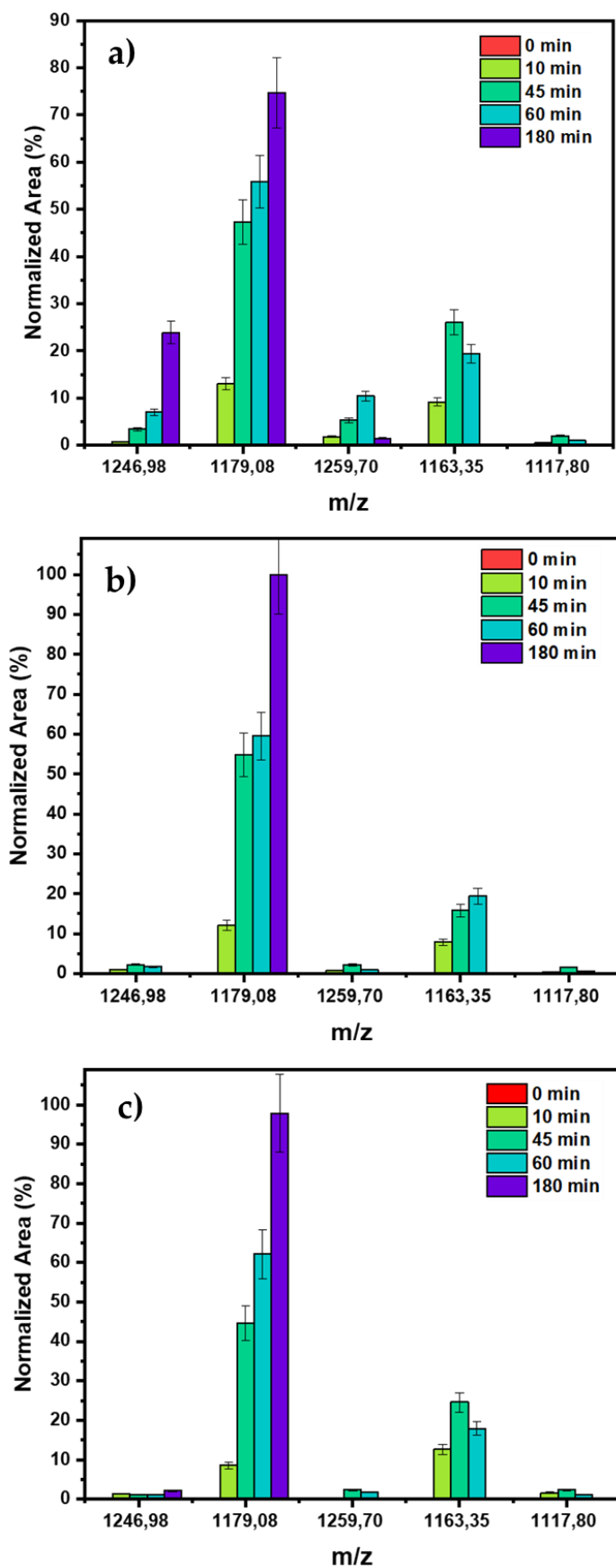


Figure 21 The percentage of normalized peak areas for the fragments after insulin digestion for the three sets **a)** insulin-IDE; **b)** insulin + Car 100 μ M + IDE; **c)** insulin + Car 1mM + IDE. The \pm (error bars, 10%) for the five fragments are shown in figure. Adapted from Ref^[110] under Creative Commons CC BY 4.0 license; published by ACS Chemical Neuroscience 2022.

2.6. Final Remarks

The purpose of Chapter I was to unveil the role of Car in relation to IDE activity based on the chosen model system of IDE-insulin. Additionally, it aimed to explore new potential modulators of the IDE enzyme through the application of novel methods that allow for the easy identification of the nature of modulators without being influenced by the activity of the enzyme batch used.

For the first time, the Hill function, commonly used for allosteric enzymes such as IDE, was determined through SPR measurements and then correlated with the maximum SPR response achieved during steady-state conditions. This correlation facilitated the extraction of essential affinity information between the enzyme immobilized on the surface (IDE in our case) and a substrate acting as an analyte (insulin in our case). This affinity information provided insights into the level of cooperativity between the enzyme and substrate, being IDE an allosteric enzyme. This cooperativity is tightly correlated with the Hill coefficient, and, in this manner, it becomes possible to investigate the type of cooperativity occurring between the enzyme and the substrate.

Subsequently, the same experiment was conducted in the presence of three small molecules: *i*) a potential activator, Car; *ii*) a possible inhibitor, ATP; and *iii*) a well-known irreversible inhibitor, EDTA, employed as a control.

Through the application of the Hill function, it was determined that the positive enzyme activity modulator, Car, increases the n value for the IDE-insulin interaction, while both ATP and EDTA decrease the n value, respectively. These results revealed the activator and inhibitor roles of Car and ATP, respectively, through the extrapolation of the Hill coefficient via real-time monitoring of the modulator's effect on the enzyme-substrate interaction.

The research involved optimizing sensor functionalization and IDE immobilization for effective analysis. Sensorgrams analysis revealed significant involvement of Car in this interaction, leading to conformational changes and heightened cooperativity, particularly at higher Car levels.

HPLC-MS experiments demonstrated that Car enhanced insulin degradation by IDE in a concentration-dependent manner. This effect was seen without generating new cleavage sites.

Therefore, the combination of the SPR technique and HPLC-MS experiments has proven to be a valuable tool for investigating the role of Car in the IDE-insulin interaction, laying the groundwork for further investigations. This could involve substituting A β for insulin and investigating how these modulators can impact the A β -IDE interaction. This will be achieved by integrating the Hill function, a key component of SPR techniques, with kinetic studies using MS analysis. The coalition of these two approaches could be considered a springboard for new analysis that could open up new insights and new therapeutic approaches in the future.

3. Chapter II

*Amyloid Aggregation:
A new approach based on CD
biosensors.*

3.1 Amyloid Aggregation Pathway

Amyloid aggregation is a biological process wherein proteins that are intrinsically disordered or misfolded come together and assemble into atypical insoluble structures known as amyloid fibrils or plaques. The formation of fibrils and the deposition of plaques are a hallmark of many human diseases such as AD, PD, ALS, systemic amyloidosis, and frontotemporal dementia^[123].

Nowadays, around 50 disorders are influenced by the misfolding of proteins and their subsequent conversion into aggregates^[124]. Specifically, this mechanism contributes to the progression of pathologies, which is linked to the impairment of the functions of the involved proteins, the generation of toxic intermediates, and the loss of cognitive functions^[125–131].

This pathological mechanism is associated with disparate factors including ageing in AD and an unhealthy lifestyle in T2DM, which currently affects over 300 million individuals^[132].

To gain a deeper understanding of this complex and not yet fully comprehended mechanism, it is crucial to both explore the nature and properties of each state involved and define the thermodynamic and kinetic aspects that lead to pathogenic behaviours^[124,125].

The thermodynamically driven force is the free energy surface, which relies on several weak interactions, including electrostatic interactions, hydrogen bonds, dispersion forces, and interactions with solvent molecules that underlie the hydrophobic effect. Although the functional native state possesses a local free energy minimum at physiological concentrations, the self-assembly of the native state into aggregates leads to protein species with even lower local free energy, rendering this process thermodynamically favoured^[133,134].

Kinetically, the process can be explained by plotting the fraction of fibril mass versus time (Figure 22, panel a). The most widely accepted theory involves the conversion of monomers into oligomers first and then into fibrils, through the formation of nucleation and growth centers^[135,136].

Although early studies primarily concentrated on fibril formation, the current focus has shifted to intermediate soluble oligomers. These oligomers, which are inherently misfolded under normal physiological conditions, have become the main subject of interest due to their potential toxicity.

Fig.22, panel a, illustrates how soluble monomers self-assemble during the initial *lag phase* to create disordered, benign soluble oligomers (BO). Over time, these oligomers transform into toxic oligomers (TO) with a partially β -sheet structure. The *growth phase* is characterized by an exponential curve. The slope of this curve depends on the number of monomers added to the toxic oligomers, stabilizing them, and creating nucleation centers. These nucleation centers represent the rate-limiting step of the process. Lastly, the *plateau phase* represents the formation of mature amyloid fibrils highly stable^[136–140]. Fig.22, panel b, simplifies the mechanism explained above.

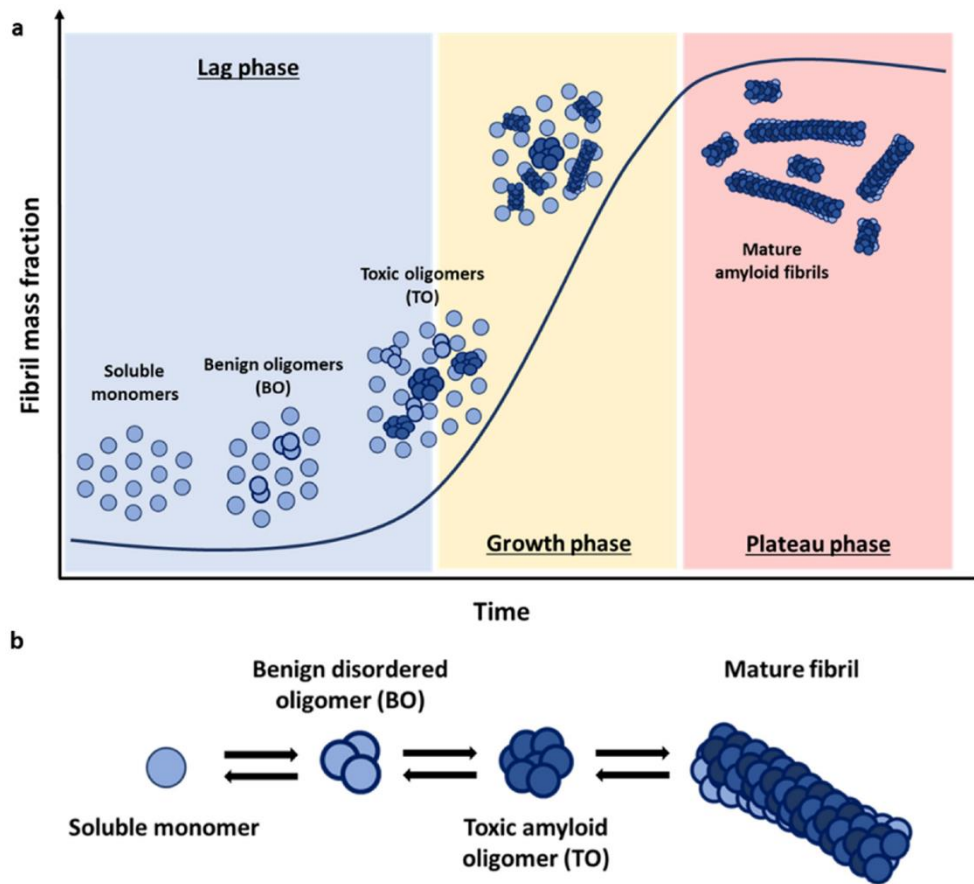


Figure 22 a) Schematic representation of the kinetic process of amyloid formation shown as the fraction of fibril mass over time. b) Simplified reconfiguration of the main structural states of protein species present during the fibril formation process: monomers, benign oligomers, toxic oligomers, and fibrils. Adapted from Ref^[140] under Creative Commons CC BY 4.0 license; published by Biophysica 2022.

The conversion from monomers to fibrils involves structural changes from mostly α -helical folds typical of native states to the β -sheet structures of the fibrils. Amyloid fibrils appear as unbranched filamentous structures under Atomic Force Microscopy (AFM)^[141], while X-ray fibre diffraction studies confirm the cross- β -sheet core of this filament, where β -strands effectively come together to create uninterrupted hydrogen-bonded β -sheets extending along the length of the fibril^[142,143].

Comprehending the aggregation process and the various intermediate protein assemblies that manifest from the very early stages, such as the small oligomers and protofibrils, up until the emergence of fibrils and amyloid plaques, and elucidating their role and contribution to the development of the disease, remains of paramount importance.

Regarding this issue, in this chapter, we will take a deeper look at the aggregation processes of the A β peptide and insulin related to AD and T2DM, respectively.

3.1.1. $A\beta$ peptide aggregation

Being an amyloid disease, the progressive aggregation of the $A\beta$ peptide from soluble monomers to insoluble fibrils is believed to be directly associated with the onset of the disease. Specifically, both the $A\beta_{1-40}$ and the more toxic $A\beta_{1-42}$ peptide are prone to aggregation due to their high hydrophobic content^[144].

The $A\beta$ aggregation pathways involves several structural states of protein species including monomers, dimers, oligomers, protofibrils, fibrils, and amyloid plaque (Figure 23). As explained before for the general mechanism, the progression of $A\beta$ aggregation involves a series of intricate steps, starting from primary nucleation phase leading to the insurgence of disordered oligomers. These oligomers then develop into nuclei capable of further growth^[145]. Subsequently, these nuclei elongate into fibrillar assemblies, which in turn facilitate the creation of new nuclei through a feedback loop referred to as secondary nucleation. This secondary nucleation process is responsible for the proliferation and expansion of the aggregated species^[146].

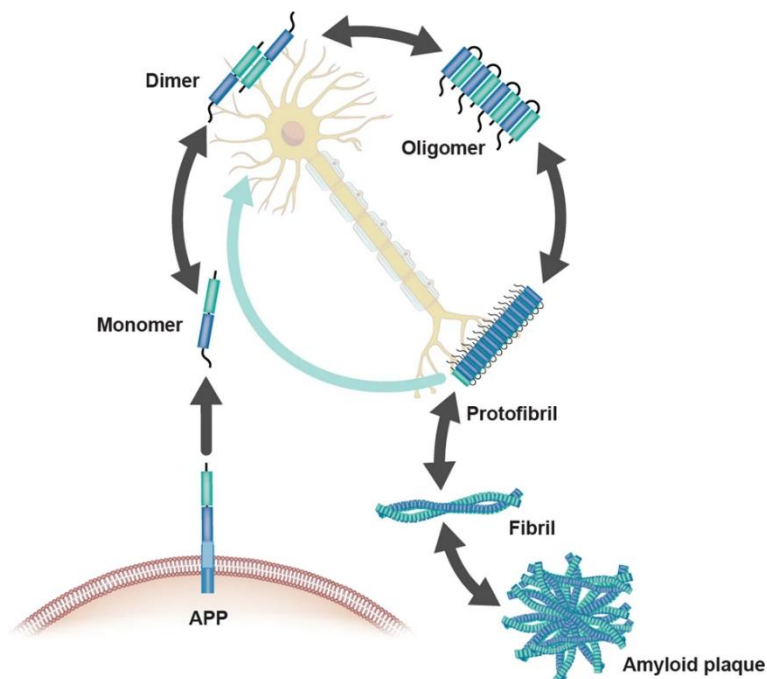


Figure 23 Schematic refiguration of the $A\beta$ aggregation pathway. The aggregation states include monomers, dimers, oligomers, protofibril, fibril and amyloid plaques. Adapted from Ref^[147] under Creative Commons CC BY 4.0 license; published by *Mol. Psychiatry* 2021.

The $A\beta$ monomers predominantly have α -helical and random coil structures, depending on the amino acidic sequence. As an example, while $A\beta_{1-28}$ folds into a predominately α -helical structure^[148] and $A\beta_{1-39}$ has the tendency to preserve the random-coil conformation, the $A\beta_{1-42}$ is more prone to adopt the β -sheet conformation^[149]. Indeed, the sequence of the peptide is a crucial factor in the conformation adopted by $A\beta$ peptides. The amphipathic character of the $A\beta$ allows to divide the peptide sequence in two regions: the N-terminal hydrophilic segment exposed extracellularly and the

C-terminal segment whose high hydrophobic nature locates this portion within the transmembrane helix of APP^[150]. In physiological conditions, A β monomers participate in neuronal cytoprotective pathways and maintain correct intracellular signalling and synaptic functions^[151].

Differently to the past, the current general knowledge identifies *oligomers* more cytotoxic than insoluble A β fibrils^[152–155]. Circular dichroism, infrared spectroscopy and hydrogen deuterium exchange analysis indicate that A β oligomers show an extended β -sheet structure^[156]. The size of the oligomers has an impact on their aggregation fate. Indeed, smaller oligomers appear to be more toxic than larger ones^[157,158], and compact oligomers are less implicated in the aggregation process compared to extended conformations due to their metastable nature^[159]. The types of oligomers that A β can form vary from smaller ones like dimers, trimers and tetramers to larger ones including pentamers, hexamers and so on^[160]. The cytotoxicity of A β oligomers is correlated to *i*) the inhibition of electrophysiological mechanism of synaptic plasticity, *ii*) enhancement of the long term depression (LTD) at low to sub-nanomolar concentration^[161,162], *iii*) reduction in the expression of memory-related receptors, and *iv*) induction of synaptic deterioration in hippocampal neurons cultures^[163].

The process of converting from oligomers to fibrils remains unclear, and even more challenging is the real-time, step-by-step detection of oligomers along the aggregation pathway. Indeed, currently, the focus is entirely directed towards the development of new and sensitive oligomers detection systems^[164–167], and furthermore, in their distinction from protofibril formation.

Protofibrils are considered the precursor of mature fibrils and accumulate in glial cells; they are relatively flexible with a size ranging from 75 to 200 nm^[153]. Their binding to some dyes like Congo red and Thioflavin T (THT) indicates a high β -sheet content^[168]. They can fast convert into fibrils through sedimentation of small amount of preformed fibrils. Moreover, numerous studies have demonstrated the neurotoxic effect exerted by protofibrils^[169,170]. Indeed, protofibrils inhibit the long-term hippocampal (LTP)-mediated synaptic plasticity, impair cognitive functions and learning processes^[171].

The *fibrils* of A β peptide have been defined as “*highly insoluble, structurally organized, thermodynamically stable, filamentous protein aggregates for the repeating units of β -sheets aligned perpendicular to the fibre axis, with a distinctive X-ray diffraction pattern (cross- β) similar to crystalline silk and consistent with high β -sheet content*”^[61]. The quaternary structure of fibrils consists of an S-shaped cross-section formed by arranging two or three protofibrils into a left-handed superhelix^[172].

Usually, under physiological conditions, proteins are metastable in their native state and the conversion to the more stable amyloid state is prevented by the presence of high free energy

barriers^[173]. However, in AD, specific brain micro-environmental conditions and the abundance of a variety of poorly soluble proteins seems to promote the fibrils formation^[174].

The final step of this process is the formation of *plaques*, which are not inherently neurotoxic, but whose deposition can disrupt signalling pathways, impair synaptic transmission, leading to an increase of cognitive decline and other neurological symptoms^[175].

3.1.2. *Insulin and its aggregation pathway*

Among amyloid diseases, T2DM is classified as such^[176] due to the involvement of amyloid formation by islet amyloid polypeptide (IAPP, or amylin) and insulin^[177]. This contributes to the dysfunction of pancreatic β -cells, the deposition of abnormal aggregates, alteration of glucose transport, and eventual cell death^[178,179].

Insulin is a peptide hormone synthesized in the pancreatic β -cells of the islets of Langerhans^[180]. It is a highly conservative protein with two chains: A and B composed of 21 and 30 amino acids respectively (Figure 24). The two chains are held together by two inter-chain disulfide bridges, one between the cysteine moiety of A7 and B7 residues, and the other between A20 and B19 residues. Additionally, an intra-chain disulfide bond A6-A11 and a hydrophobic core that enables the folding of the structure are present in the A chain.

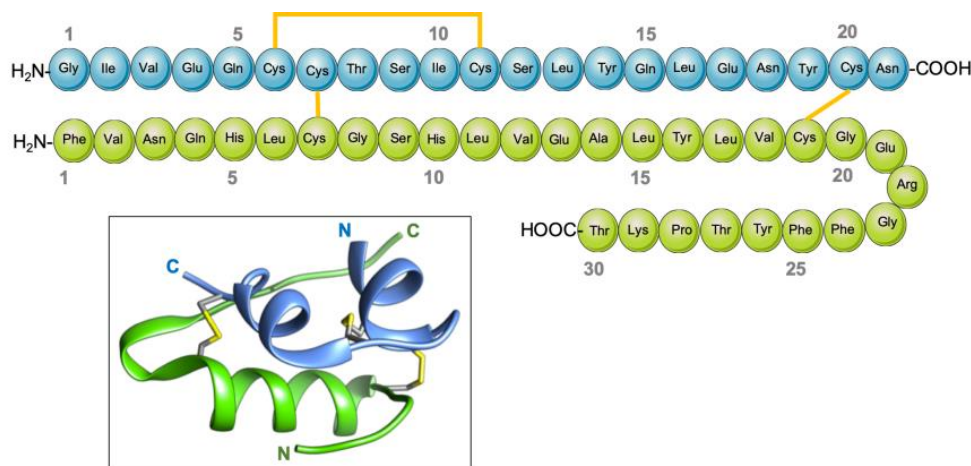


Figure 24 *Insulin primary sequence with the A chain in blue and B chain in green. The three disulfide bridge are highlight in yellow. The 3D insulin monomer is depicted in the insert. Adapted from Ref^[181] under Creative Commons CC BY 4.0 license; published Biomed. Res. Ther. 2021.*

Firstly, insulin is synthesized as proinsulin, and subsequently, it undergoes a maturation process in the endoplasmic reticulum, during which it is converted into proinsulin. It is then stored in the Golgi apparatus as a hexameric zinc-calcium complex. The final step of insulin synthesis is completed by the removal of the C-peptide (31 amino acids) present in the proinsulin, carried out by trypsin-like

peptide and carboxypeptidase-like enzyme^[182]. Currently, the C-peptide levels present in the body is a discriminating factor for distinguish T2DM from type I diabete mellitus (T1DM)^[183].

Although insulin can exist as hexamers, tetramers or dimers^[184], its functional form is the monomer. After binding with specific receptors, it can fulfil several cellular functions.

The main role of insulin is the regulation of glucose metabolism. It is secreted in response to a postprandial increase in blood glucose concentration. Its aim is to maintain proper glucose levels, which typically range between 4 and 7 mM,^[185] facilitating glucose uptake into cells. Any alteration in insulin levels and/or in its native form can lead to complications such as hyperinsulinemia and T2DM.^[186] As a hormone, insulin operates through the binding with the insulin receptor (IR), which is a heterotetrameric transmembrane protein with tyrosine kinase activity^[187]. The dysfunction of this receptor, in addition to the impairment of insulin, is a connection between AD and T2DM. The insulin signalling pathway involves a series of GTPases which, among other functions, increase the concentration of the glucose transports (GLUT) on the cell surface. One of the most crucial transporter is Glucose Transporter type 4 (GLUT4), and insulin, by modulating translocation of the latter, helps in carbohydrate metabolism by facilitating glucose diffusion into fat and muscle cells^[188,189].

In addition to the regulation of glucose metabolism, insulin is involved in phospholipid metabolism^[190] and urea circle^[189]. It is responsible for the synthesis and the storage of fatty acid into liver^[190], and promotes cell proliferation^[191] in connective and musculoskeletal tissue by binding to the insulin growth factor receptor (IGF).

Differently from healthy individuals, where the primary role of insulin is the management of blood glucose level, in diabetic patients, the body either does not produce enough insulin or cannot properly use the one produced. As a result, these patients undergo repeated subcutaneous insulin injections to maintain the physiological blood glucose levels. However, many patients experience the local formation of insulin aggregates beneath the skin due to these injections^[192–195]. Such insulin deposits have been observed for recombinant human insulin through both analysis with Congo red birefringence^[196] and THT^[197], a well-known amyloid marker. Moreover, two recent studies have brought attention to progressive insulin-derived amyloidosis in individuals diagnosed with T2DM^[195,198]. In addition, the insulin aggregation presents a challenge in commercial environments due to the massive amount of insulin used^[188].

Hence, insulin aggregation is a global issue, and its reduction or prevention at the early stages is imperative. Because insulin is a straightforward, extensively researched, and easily attainable protein, it has additionally been utilized as a model system for investigating amyloidosis. In this perspective,

the specific and selective detection of insulin oligomers at the early stages before the fibrils formation started is of paramount importance and interest.

While the active form of insulin required for glucose binding and uptake is the monomer, insulin typically exists as a hexamer consisting of three dimers held together by two zinc ions^[199,200]. When these three dimers dissociate, monomers are formed (Figure 25).

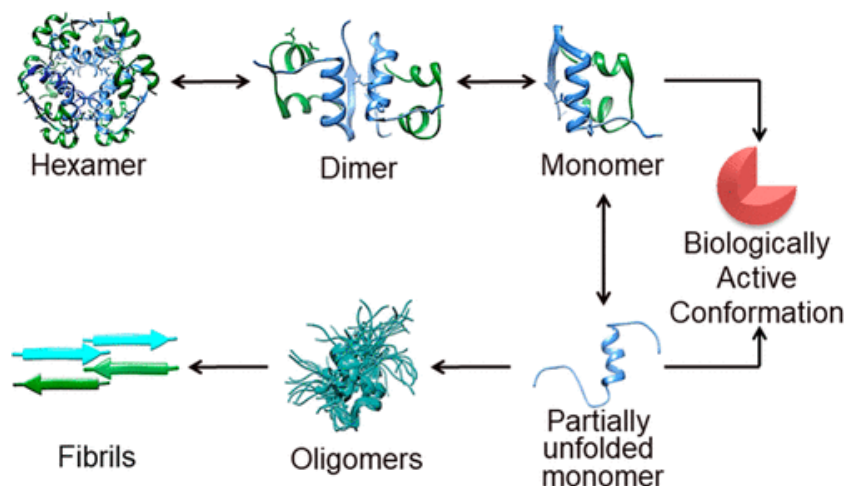


Figure 25 Schematic illustration of insulin aggregation pathway. Adapted from Ref^[201] under Creative Commons CC by 4.0 license; published by ACS bio med Chem Au 2022 .

However, under conditions that favour fibrillation (such as pH changes, high temperature, or contact with hydrophobic surfaces), insulin undergoes partial unfolding, resulting in partially unfolded monomers. These monomers then aggregate, forming a nucleus that elongates to create a fibrillary amyloid structure^[201].

The driving forces for nucleus formation and insulin are both hydrogen bonding and hydrophobic interactions, which involve several residuals belonging to both insulin chains including LeuA13, TyrA14, and GluA17 from the insulin A-chain, and PheB1, ValB2, GluB13, GlnB4, AlaB14, LeuB17, ValB18, CysB19, and GlyB20 from the insulin B-chain^[202].

The kinetic of insulin aggregation is characterized by a *lag phase* during which hexamers convert into monomeric forms, leading to the formation of nuclei, which are characteristic of *the nucleation phase*. Indeed, the rate-limiting step consists of the conversion of monomers into nuclei. However, once this step is surpassed, the transition from oligomers to fibrils is thermodynamically favoured. This is followed by a *growth phase*, where the generation of oligomers before and protofibrils afterward paves the way for the creation of mature fibrils (Figure 26). The formation of fibrillary amyloid structures represents the absolute minimum of the entire free energy landscape^[203,204].

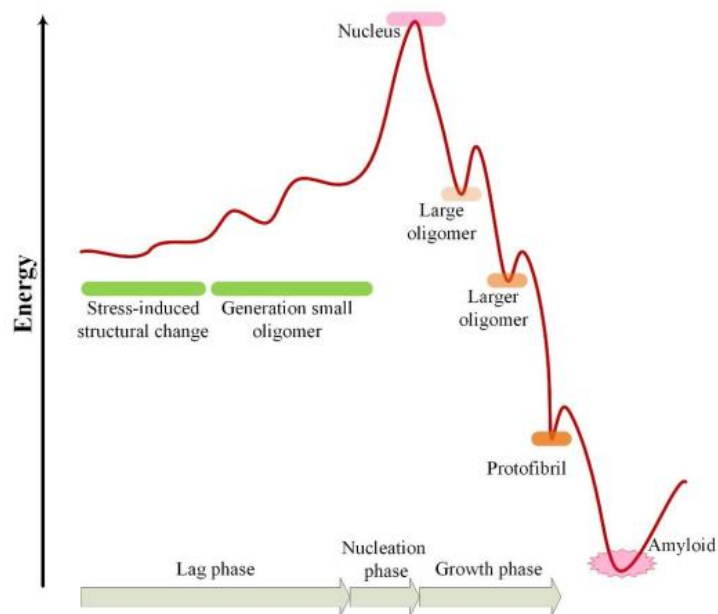


Figure 26 Energetic landscape from insulin monomer to fibril. Adapted with permission from Ref^[205]; published by *Chem. Commun.* 2020.

The ultimate steps of the insulin aggregation pathways were thoroughly explored. Such an example, cryo-electron microscopy has revealed the left-handed arrangement of the twists around protofilaments (the precursors of the mature flat and twisted fibrils)^[206] while the protofilaments arrange themselves into constituting β -strands. Moreover, the protofilament surface not involved in aggregation, can interact with free monomers in no-disrupting manner. The intra- and inter-chain disulfide bonds are crucial in the fibril packaging. Specifically, while the inter-chain ones facilitate the parallel running direction of the strands, the intra-chain bonds cause a bulge in one of the sheets^[207].

Instead, oligomers possess a helical structure, in which two helical oligomers intertwine to form protofibrils with an average diameter of 100 Å. According to Vestergaard et al.^[208], helical oligomers interacting with other oligomers facilitate the elongation of protofibrils, promoting the formation of mature fibrils. In support of this, Selivanova et al.^[209] proposed that the formation of fibrils occurs as a result of oligomers diminishing. Specifically, ring-like oligomers, composed of hexamers which in turn are formed by monomers, constitute the building block of fibrils.

Therefore, the role adopted by oligomers within the insulin aggregation pathway represents both a triggering factor in the progression and worsening of the disease, and, at the same time, a turning point that may slow down fibril formation and consequently amyloid deposition in diabetic patients, affecting proper blood glucose metabolism.

3.1.3. Factors involved in amyloid aggregation.

The aggregation pathway of A β peptides, insulin and, in general, for all other amyloidogenic proteins may be influenced by some external factors. In particular, the A β peptide and insulin misfolding can inhibit or enhance the formation of fibrils and plaques.

A large number of experimental parameters capable to affect protein aggregation, including metals, temperature, pH, natural or synthetic molecules such as cyclic compounds, peptides, cyclodextrins, and nanoparticles have been investigated.

Metals such as zinc and copper are considered multifactorial agents because they are involved in *i*) A β and insulin aggregation pathway, *ii*) oxidation mechanisms, and *iii*) alteration of their primary sequence. For instance, in insulin aggregation, Zn²⁺, Cu²⁺, and Fe²⁺ ions induce the formation of large aggregates at natural pH with a molecular weight ranging between 10⁵ and 2·10⁵ Da^[210]. Indeed, in the presence of Cu²⁺ ions, the precipitation of particles is visible within 4 hours. Otherwise, in the absence of this metal, the aggregates are visible only after 3-4 days^[201].

The effect of zinc ions on insulin aggregation is quite different because they induce the formation and stabilization of hexamers, opening a new off-pathway. This is due to the coordination with the histidine residue (His10) in the B-chain, which promotes the formation of insulin hexamers at concentrations above 0.01M zinc-insulin^[211]. However, the pH value plays a crucial role in this mechanism. At pH values greater than 4, insulin demonstrates the ability to form complexes with zinc^[212].

Conversely, under lower pH conditions, the protonation of HisB10 residues inhibits zinc coordination, resulting in insulin heightened inclination for aggregation^[201]. Therefore, the aggregation of insulin can occur through the dissociation of the hexameric zinc-insulin structure and consequent transformation into the dimeric form.

Based on this, the earliest strategy to inhibit insulin aggregation was the addition of zinc ions to facilitate the self-association of insulin into hexameric forms, stabilizing them and reducing their propensity to fibrillate^[213,214]. However, hexameric forms of insulin show a decrease in the biological activity of this hormone peptide^[201].

In AD, Zn²⁺ ions can bind to A β peptides, leading to the formation of oligomers and suppressing both A β ₁₋₄₀ and A β ₁₋₄₂ fibrillization in a dose-dependent manner. ThT analysis revealed that the removal of Zn²⁺ ions through the addition of EDTA restores the process of amyloid fibril formation in accordance with a classic nucleation-dependent pattern^[215].

The formation of fibrils is hindered by a competitive pathway that involves the formation of amorphous aggregates. The addition of Cu²⁺ ions induces the formation of A β amorphous aggregates

from fibrils^[216,217], depending on the experimental temperature and pH. AFM results confirmed the fibrous morphology of A β , while CD analysis tracked the aggregation rate of A β as the temperature increased^[218]. However, subsequent analyses have shown that Cu²⁺ ions modulates aggregation of A β ₁₋₄₂ by enhancing interactions between peptide molecules^[219]. However, although the mechanism through which copper participates in the aggregation process of A β is still unclear, there is a general consensus whereby, depending on the protein/ion ratio, the aggregation is driven toward amorphous or fibrillar structures^[220,221].

High temperature and *low pH* are the optimal conditions for promoting amyloid aggregation. Particularly, high temperatures (above 50°C) lead to the breakages of salt bridges, hydrogen, and disulfide bonds within insulin structure. These conditions are necessary for the initiating of the early stages of fibrillation processes^[222]. Conversely, pH does not impact the tertiary structure of insulin^[223] but it does significantly affect its oligomerization state. This is exemplified in the case of zinc-insulin oligomers, where the protonation of HisB10 plays a pivotal role^[224].

Among *cyclic compounds*, polyphenols are natural antioxidants^[225,226], anti-aging agents^[227], inhibitors of cancer growth^[228], present in many foods, and regularly assumed by humans with the diet. In addition, polyphenols are used as inhibitors in A β and insulin aggregation mechanisms. Indeed, the inhibitory effect exerted by polyphenols involves either the binding and the stabilization of native amyloid states or the binding to mature fibrils and their disruption. In the case of insulin, it entails the binding to partially unfolded insulin molecules, preventing nuclei formation, and subsequent fibrillation^[205]. As an example, curcumin, a spice derived from the rhizome of *Curcuma longa*, can act as the anti-aggregating agent and as potent inhibitor of A β amyloid formation^[229], prion protein^[230], insulin^[231], and more. Looking at the insulin fibrillation, curcumin can interact at various insulin states such as the lag phase, inhibiting the formation of β -structures^[231].

Regarding the interaction between A β -curcumin, curcumin acts by inhibiting the formation of toxic oligomers through the π - π stacking interactions between the aromatic rings of curcumin and the aromatic side chains of His, Tyr and Phe residues. This interaction subsequently contributes to the reduction of β -sheet content in the A β dimer^[232]. On the other hand, even non-cyclic compounds such as osmolytes and peptides/proteins can prevent amyloid aggregation. The physiological effects of betaine and citrulline, two osmolytes, include the charge distribution changing in which, by masking hydrophobic portion on insulin surfaces avoid the hydrophobic collapse typically in fibrils formation^[233].

Synthetic and designed *peptides/proteins* were envisioned to encompass several inhibitors mechanism, including π - π stacking interactions typically found in cyclic compound, to show

selective and efficient inhibitor actions. For instance, two synthetic peptides, KR7 (KPWWPRR) and NK9 (NIVNVSLVK) stand for inhibitors in insulin aggregation^[234,235]. In particular, NK9 owning β -sheet breaker amino acids, can inhibit insulin nucleation, resulting in a reduction of fibrils formation and a decrease in cytotoxicity.

Derived from the A β protein, the two peptides KLVFFA and LPFFD have also been studied for their potential inhibitory effects on A β aggregation, with KLVFF displaying a lower binding affinity than LPFFD. Both peptides interfere with oligomerization by stabilizing the monomer state of A β ₁₋₄₀ hindering the fibrillation^[236-238].

Supramolecular moieties such as *cyclodextrins*, particularly β -cyclodextrins, have shown to inhibit insulin aggregation and A β aggregation as well. The mechanism of action, demonstrated by cyclodextrins in insulin aggregation, involves breaking down mature fibrils and transforming them into smaller, non-toxic species through the encapsulation of Tyr residues to prevent fibrillation^[239]. In the case of AD, HP- β -cyclodextrin inhibits A β fibrillation in a concentration manner^[240]. The inhibitory capability is exerted through interactions occurring at the hydrophobic residues of A β in two β -strands and the N-terminal tail. Additionally, the inner hydrophobic cavity of HP- β -cyclodextrin serves as an active site for A β inhibition.

Being biocompatible, small, easy to functionalize on their surfaces, with a tunable electrical charge, and high surface-to-volume ratio, *nanoparticles* are widely used in biotechnology. The general mechanism involves the stabilization of partially unfolded proteins and the disintegration of preformed fibrils. The coverage of the nanoparticles surface with hydrophobic molecules decrease the fibrillation rates at the early stages of the A β ₁₋₄₀ aggregation^[241,242].

In addition, in recent years, carbon-based nanoparticles known as carbon dots (CDs) have gained popularity in various research areas due to their numerous properties. In this context, the electrostatic interaction occurring between insulin and CDs serves as the driving force behind the inhibition of insulin aggregation^[243]. Therefore, the presence of CDs hinders human insulin fibrillation.

The below table summarized the effects exerted by the aforementioned factors (Table 5).

Factors	A β aggregation	Insulin aggregation
Copper	↑	↑
Zinc	↓	↓

Hight Temperature



Low pH



Cyclic Compounds



Peptides



Cyclodextrins



Nanoparticles



Table 5 *List of factors involved in A β and insulin fibrillation. The arrows indicate the promotion (in red) or the hindrance (in green) of fibrils production.*

3.2. Results and Discussions

Amyloid peptide aggregation refers to the tendency of some peptides to clump together and form insoluble fibril aggregates. These aggregates are a hallmark feature of various neurodegenerative diseases, including AD^[244], PD^[245], and Huntington's disease^[246].

Usually, a correct peptide folding and/or no modification on the peptide sequence can minimize the formation of these aggregates and ideally avoid the onset of the pathology. However, the unbalance of some crucial factors can trigger chain reactions that involve the peptide misfolding and in turn the beginning of the disease.

Although the research on the exact mechanisms underlying the formation of fibrils is still ongoing, the early stages were recognized to play a pivotal and awkward role in the onset and progression of the pathology^[244].

Insulin aggregation has been widely studied by the use of several techniques such as electrophoresis^[247] and small-angle X-ray^[248], in order to identify the mechanism with which this peptide is deposited on the arterial wall of T2DM patients. Indeed, insulin provides a model system being a classical amyloidogenic protein. However, these techniques are able to monitor the final stages of insulin aggregation without providing any information on the start steps of this mechanism. The issue is overcome by the use of functionalized CDs whose fluorescence gives a specific outcome depending on the conformation adopted by the peptide over time^[249]. The strength is to modulate CDs properties by changing the chemical groups at their surface.

3.2.1 Monitoring of insulin aggregation by carbon dots

3.2.1.1. Overview of the biological application of carbon dots.

CDs are fluorescence carbon material with a diameter below 10 nm^[250,251]. Thanks to their fluorescence properties, biocompatibility, low cytotoxicity, easy engineering, eco-friendly, and low cost, CDs are designed to be a new generation of biosensors better than metal-based quantum dots^[252]. Biosensors are devices used to analyse organic and inorganic compounds in living organism and they are composed by three component *i)* a detector, *ii)* a converter, and *iii)* a signal producer^[253]. The main part for a biosensor is the detector which usually composed of biological receptors such as cell sensors, enzymatic sensor etc. Instead, CDs play the role of converter which transform information into useful signal. Actually, in the most sensing devices, CDs assume the role of both detector and converter thanks to the possibility to modify the functional groups present on their surface, and accordingly, become more sensitive to specific biomolecules.

The power of the new generation of biosensors is the combination of the latter with nanotechnology, where several advantages including real-time analysis, label-free detection, high-throughput screening^[254] are optimized. Compared to the traditional methods, CDs offer numerous advantages, making them the optimal choice for biosensors. These advantages include: *i*) unique photoluminescence (PL) across a broad spectrum, ranging from visible to near-infrared (NIR), *ii*) chemical inactivity and excellent PL stability, ensuring reliable and long-lasting performance, and *iii*) environmental friendliness and non-toxicity to organisms. In contrast, many metal-based nanomaterials contain harmful metals and are prone to degradation. Additionally, the CDs surface features multiple functional groups that can be easily modified, thereby altering their fluorescence properties.

For this reason, CDs are employed in several applications such as in biosensor field, drug delivery, cancer theranostics, bioimaging and disease detections (Figure 27).

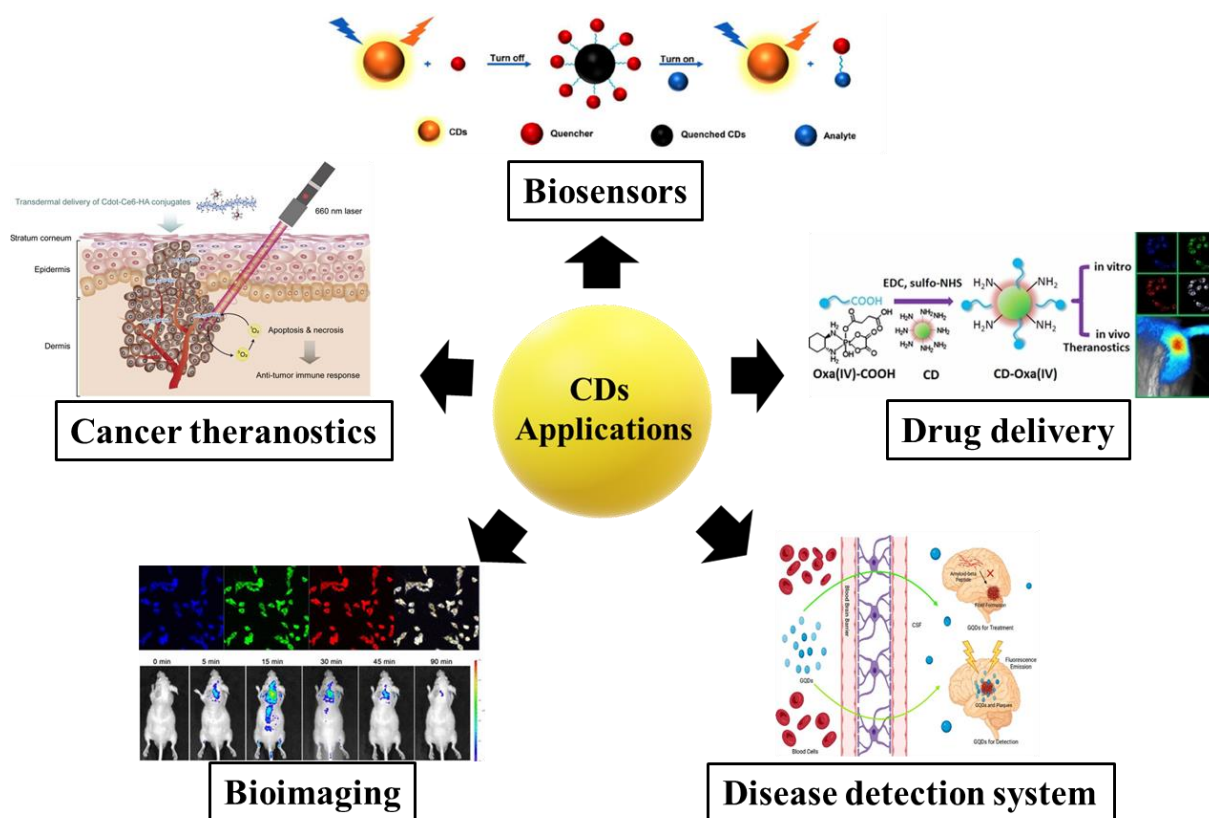


Figure 27 Summary of CDs application in biological field. Figure is reproduced with permission from Ref^[255] published by American Chemical Society Sensors 2020, from Ref^[256] published by Acta Biomateriala 2015, from Ref^[257] published by Advanced Materials 2014, from Ref^[258] published by Carbon Letters 2022, from Ref^[259] published by American Chemical Society Nano 2015.

As biosensors, CDs can detect the presence of a target enzyme following an *on-off-on* strategy^[260]. Here, the starting point is the formation of a specific CD-substrate complex, whose CDs fluorescence

is quenched. The addition of the specific target enzyme restores the fluorescence of CDs, and the degree of fluorescence recovery is proportional to the concentration of target enzyme.

CD-based antigen-antibody optical sensors take advantages of the strong interaction between the two biomolecules, so that this type of binding is widespread in SPR-base immunoassay for the detection of sample trace in biological fluids^[261,262]. Indeed, by monitoring the CDs fluorescence, the presence and the concentration of antigen can be determined. This promising devices are useful for the detection of biomarkers in human blood^[263]. In this field, the detection of cancer biomarker micro-RNA is achievable because of the high affinity between CDs and DNA through the π - π stacking or electrostatic interaction^[264].

CDs offer a significant advantage due to their compact size, enabling deep tissue penetration, which proves highly valuable for cancer theranostics. Beack et al.^[256], demonstrate that CDs – chlorine e6 – hyaluronate (Cdot-Ce6-HA) conjugates could generate singlet oxygen in aqueous solution compared to the free porphyrinoid Ce6, playing a significant anti-tumor effect in the photodynamic therapy (PDT) of melanoma skin cancer.

In the same manner, CDs covalently combined with oxaliplatin^[257] provide a target drug release into the cancer cell, significantly enhancing treatment selectivity and efficacy—a crucial requirement for such therapeutic treatments.

The CDs capability to cross the blood-brain barrier (BBB) is helpful for therapy design against neurological diseases. Once CDs cross the BBB, they can inhibit the fibril formation and exhibit neuroprotective activities, countering the deposition of brain plaques effectively^[258]. Lastly, owing to low toxicity and high biocompatibility, CDs are widely used in bioimaging for cancer treatment in living organism. Zheng et al.^[259] synthesized CDs by pyrolysis of D-glucose and L-aspartic acid for the identification of glioma site in targeting tissue. The strong fluorescence signal obtained in case of cerebral tumour than normal cells, indicate that CDs can be a targeting agent for non-invasive glioma diagnosis.

In light of the astonishing properties possessed by CDs, we have employed CDs as biosensors to detect and differentiate subtle conformational changes in insulin, chosen as a model system for the development of this innovative application, that manifest during the early stages of pathology. Their exceptional characteristics make CDs an ideal choice for this critical application.

3.2.1.2. Monitoring of incubated insulin aggregation by Circular Dichroism, DLS, and THT fluorescence maps.

In order to study the insulin aggregation changes, 1 mM of insulin solution prepared in PBS buffer pH 1.6 (137 mM NaCl, 2.7 mM KCl, HCl, and 10 mM phosphate buffer) was firstly filtered through

a 0.2- μm pore nylon filter and then incubated at 60°C. In the experiment involving ZnSO_4 , the salt was added until a final concentration of 1mM was reached.

The insulin aggregation was firstly explored by the use of common techniques such as Circular Dichroism, DLS and THT fluorescence, which usually they are addressed to this type of study.

The Circular Dichroism analysis (experiments performed by other research groups from University of Catania) was performed preparing a working solution (3 μM in PBS) at room condition from a mother solution where insulin was kept under fibrillation at 60°C. The measurements were acquired by the use of a spectropolarimeter (JASCO J-715) equipped with a 1-cm path-length cell. The insulin fibrillation process was followed over time analyzing incubation points at 0 min–45 min–90 min–135 min–195 min–255 min–375 min–495 min, and 24 h (Figure 28, panel a).

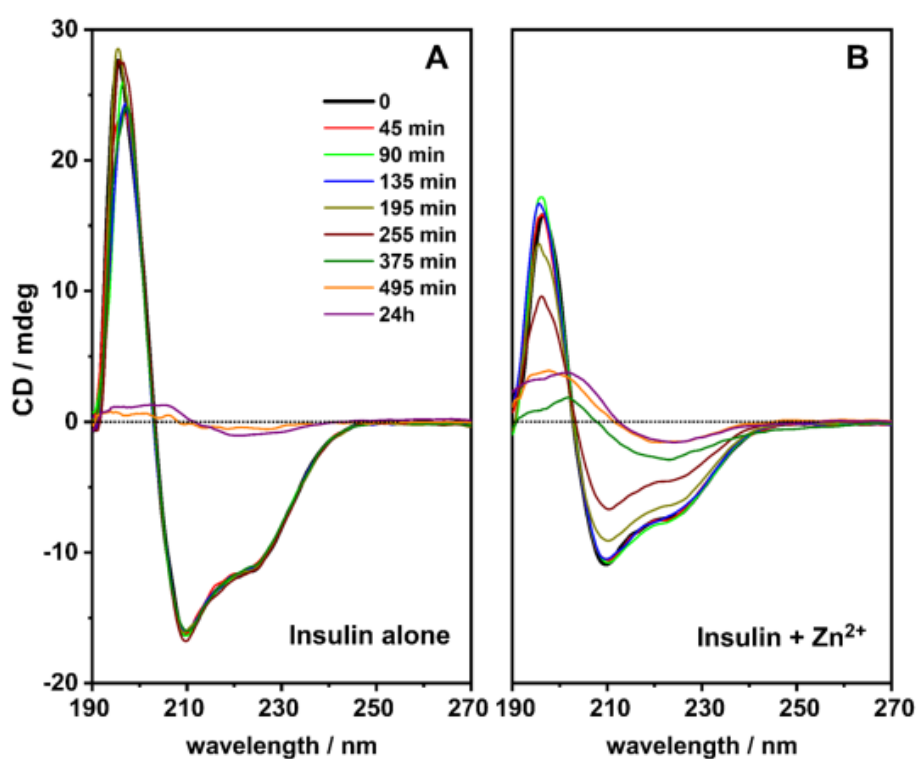


Figure 28 Dichroic spectra during the incubation of **a)** insulin alone, and **b)** in the presence of zinc ions. The insulin concentration is 3 μM and the $\text{pH} = 3.5$. In presence of zinc, the ratio $[\text{insulin}]/[\text{Zn}^{2+}]$ is 1:1. Adapted from Ref^[249] under Creative Commons CC BY 4.0 license; published by Analytical and Bioanalytical Chemistry 2023.

The native insulin structure is predominantly twisted in α -helix, however during fibrillation it develops into β -turn, going via a partially folded intermediate. Multidimensional Nuclear Magnetic Resonance (NMR) studies, indeed, demonstrate the conversion from a native insulin monomer toward fibrils formation via a putative partial fold^[265].

Accordingly, Circular Dichroism analysis shows two relative minimums at 222 nm and 208 nm, namely $n \rightarrow \pi^*$ and $\pi^* \rightarrow \pi$ transitions respectively, typical for an α -helix conformation (Figure 28, panel a). However, no changes are shown until 6h of incubation, when a typical β -sheet conformation appears, characterized by a negative band at 218 nm and a positive band at 195 nm as well.

The same trend is even noticed with the addition of zinc sulfate salt. Zinc²⁺ ions are known to be coordinated by insulin hexamers, which protect insulin from fibrillation process opening a new off-pathway^[266].

For this experiment, ZnSO₄ salt was added to the same insulin solutions to attain a final concentration of 1mM, and dichroic spectra were acquired at the same incubation times chosen for the previous experiment. The dichroic spectrum (Figure 28, panel b) displayed both the complete α -helix (until 2h) and the β -sheet stably reached at 495min and unchanged until 24h.

However, differently to the insulin alone experiment, here the presence of zinc induces a gradual conformational change from the α -helix to the β -sheet over time. While this technique is effective in detecting significant peptide alterations, it may not be suitable for detecting subtle conformational variations that occur within the initial 2-3 hours of incubation.

In addition to Circular Dichroism analysis, DLS experiments (experiments performed by other research groups from University of Catania) were executed at 25°C both on 100 μ M insulin alone PBS buffer pH 1.6 (137 mM NaCl, 2.7 mM KCl, HCl and 10 mM phosphate buffer) diluted from the aggregating solution at different incubation times, and on the insulin-zinc solution. Experiments were performed at 25°C with a Zetasizer Nano ZS (Malvern Instruments Ltd., UK) instrument equipped with a He–Ne laser. Both resulting spectra are shown in Fig.29.

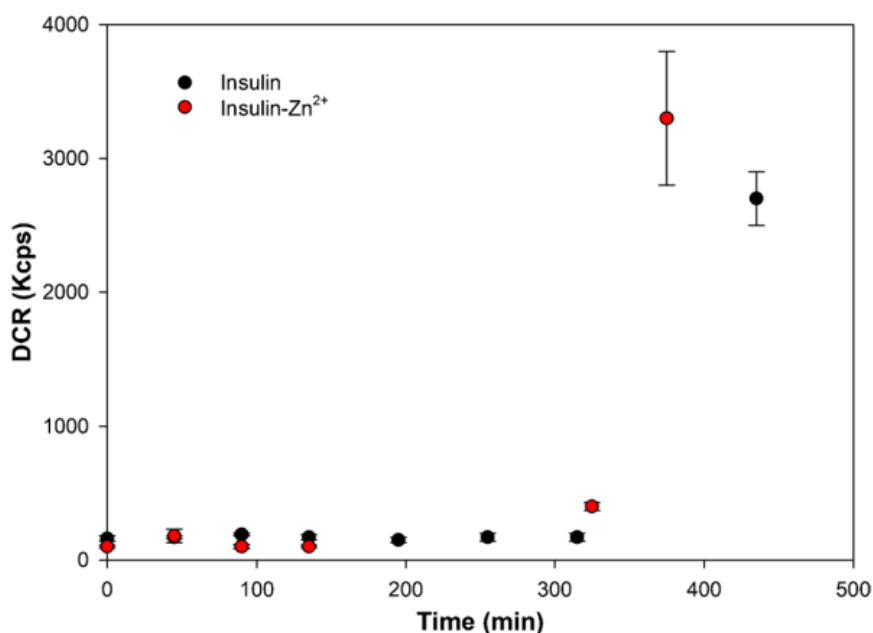


Figure 29 The scattering intensity, denoted by the derived count rate (DCR), vs time for insulin sample in the presence (red spots) and in the absence (black spots) of Zn²⁺. Experiments performed at 25°C with a Zetasizer Nano ZS instrument equipped with a He–Ne laser. The angle of the scattering light used for size determination was 173°. Sample analysis was based on water viscosity (0.88 mPa s) and refractive index (1.33) at 25 °C. All samples were measured 4–5 times with 10–15 accumulated scans. Error bars show standard deviations. Adapted from Ref^[249] under Creative Commons CC BY 4.0 license; published by Analytical and Bioanalytical Chemistry 2023.

DLS measurements were performed on disposable micro cuvettes by using optimal measurement times and laser attenuation settings. The angle of the scattering light used for size determination was 173°. Sample analysis was based on water viscosity (0.88 mPa·s) and refractive index (1.33) at 25 °C. All samples were measured 4–5 times with 10–15 accumulated scans.

The derived count rate (DCR) expresses the diffuse signal intensity and allows to compare different samples with each other. Higher DCR value is an indication of *i*) high concentration of sample or *ii*) larger particles or *iii*) both cases.

In both experiments (with and without zinc ions) the DCR value remains constant until 5h, however, once this threshold is reached, the DCR value starts to increase, indicating the occurrence of an aggregation process. Interestingly, the presence of zinc ions accelerates this aggregation process.

Hence, DLS technique provides some valuable insights into the insulin aggregation kinetic, but it still remains blind to the first changes occurring at the early stages of this complex mechanism.

The conversion into β -sheet conformation is typical in amyloidogenic peptides and usually is observed by ThT fluorescence.

ThT dye is widely used for the recognition and quantification of amylogenic fibrils, and it was the first technique earmarked for the monitoring of aggregation kinetics in real time^[80]. The mechanism adopted by the ThT is to intercalate within grooves created by β -sheet quaternary structure; here, a strongly increase of ThT fluorescence is observed as compared with the free ThT in an aqueous environment whose fluorescence is very weak.

Therefore, ThT experiments were performed for following insulin fibrillation by fluorescence maps in the absence (Figure 30) and in the presence (Figure 31) of ZnSO₄ salt. The working sample was prepared from incubated insulin solution at 60°C and analysed at each time of incubation. Each maps shows the insulin conformational change over time since the maps are obtained from the subtraction of ThT fluorescence curves at several excitation wavelengths from the ThT-insulin fluorescence curves performed at the same excitation wavelengths.

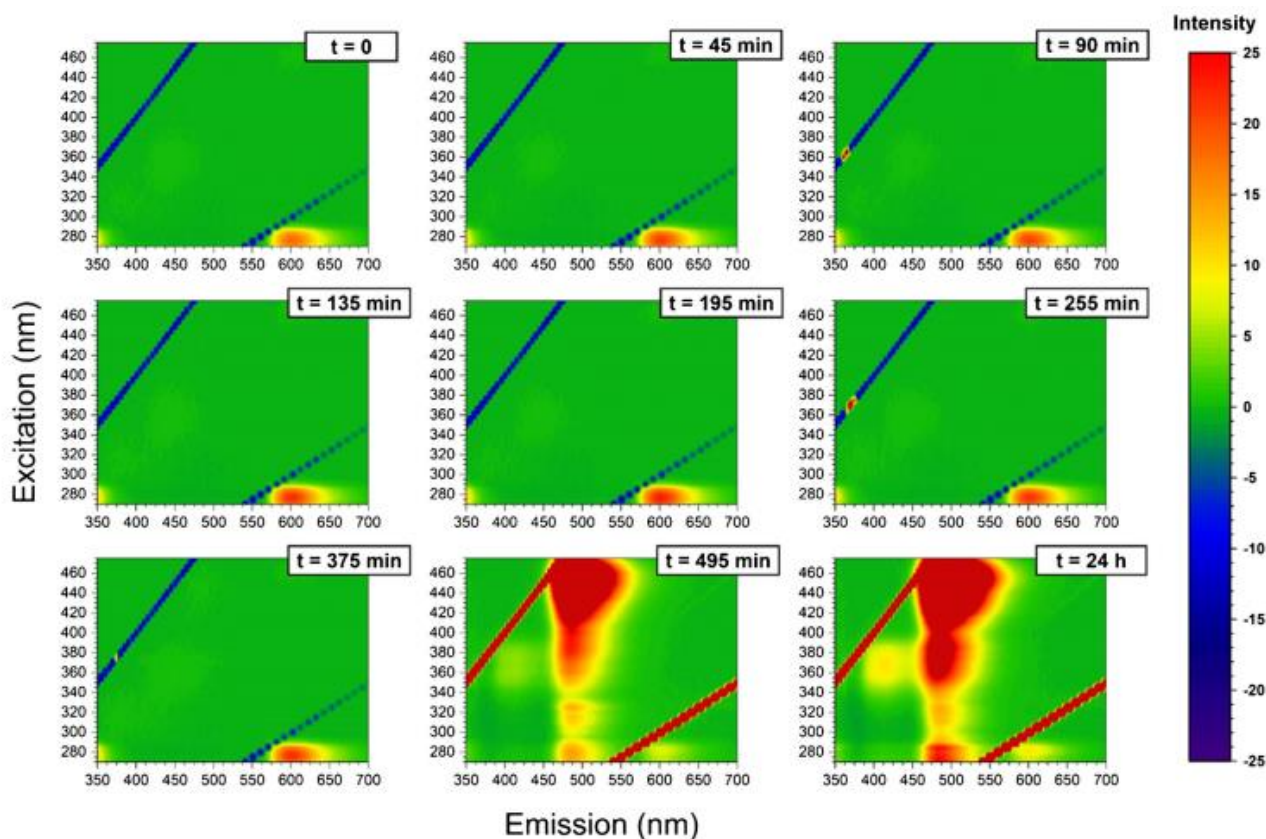


Figure 30 3D fluorescence variation maps of 20- μM ThT solution mixture with insulin (20 μM). The solution was analysed at 0 min-45 min -90 min -135 min -195 min -255 min -375 min -495 min and 24h incubation time (1-mM solution of insulin at 60 °C). Fluorescence set up parameters are excitation range 270–475 nm; emission range 350–700 nm; excitation increment 5 nm; excitation/emission slit width 3 nm/3 nm; sampling interval 2 nm. Adapted from Ref^[249] under Creative Commons CC BY 4.0 license; published by Analytical and Bioanalytical Chemistry 2023.

Based on Fig. 30, a noteworthy observation can be made regarding a substantial change occurring at 495 minutes, potentially indicating the onset of fibril formation. Additionally, this change persists unchanged for the next 24 hours. Moreover, no notable modifications are observed before 495 min. The capability of zinc ions to promote oligomeric species such as hexamers is shown in Fig.31. The results show similar maps except at the time 375 min where a minor occurrence of β -sheet formation is observed. This finding highlights that the formation of insulin hexamers acts as an obstacle to fibril formation.

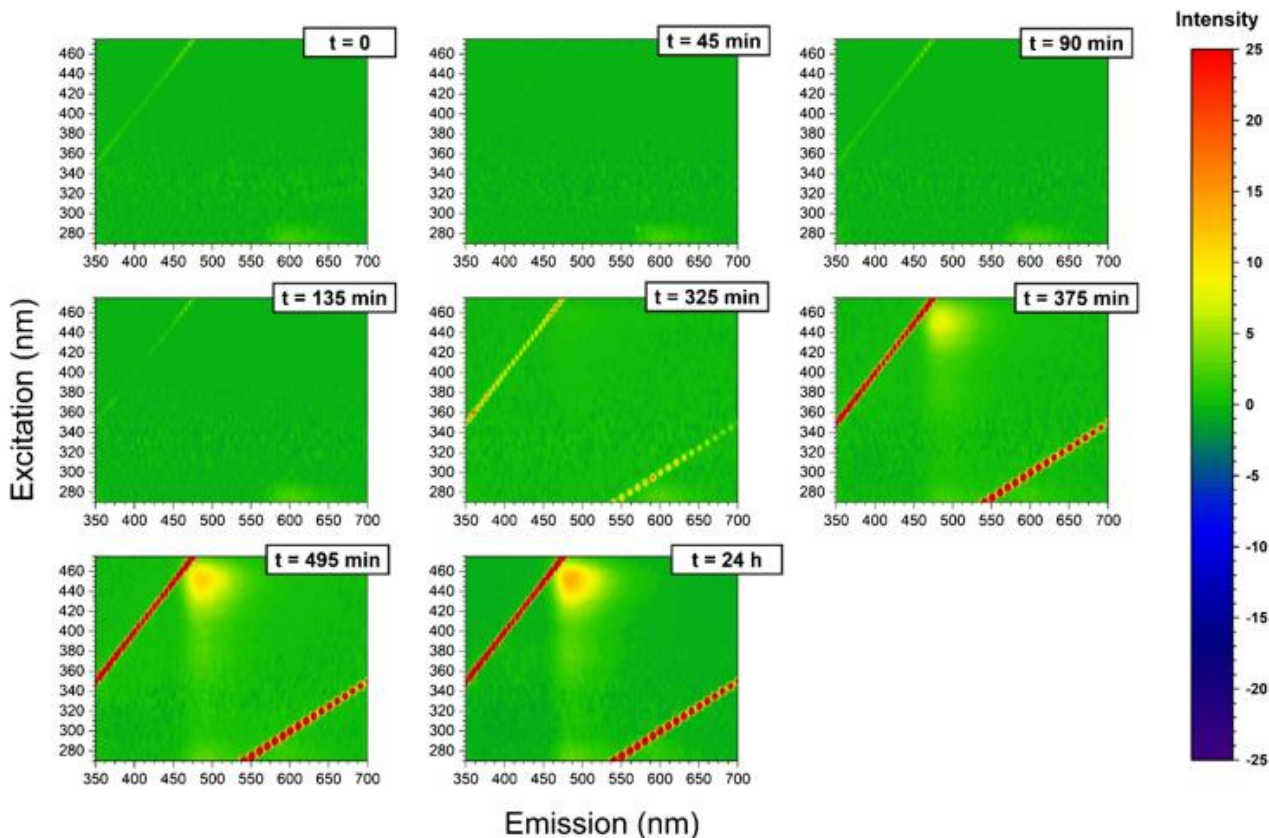


Figure 31 3D fluorescence variation maps of 20- μM ThT solution mixture with insulin (20 μM) in presence of zinc. The solution was analysed at 0 min-45 min -90 min -135 min -195 min -255 min -375 min -495 min and 24h incubation time (1-mM solution of insulin and 1mM ZnSO_4 solution at 60 $^\circ\text{C}$). Fluorescence set up parameters are excitation range 270–475 nm; emission range 350–700 nm; excitation increment 5 nm; excitation/emission slit width 3 nm/3 nm; sampling interval 2 nm. Adapted from Ref^[249] under Creative Commons CC BY 4.0 license; published by Analytical and Bioanalytical Chemistry 2023.

Hence, all the techniques employed to investigate the insulin aggregation process, both in the absence and in the presence of zinc ions, confirm the formation of fibrils after 4-5 hours after the incubation begins. However, these techniques fail to provide insights into the initial stages of this process, specifically the subtle conformational changes that take place during the early stages of the mechanism.

This gap is overcome by the use of CDs as a biosensor and by the possibility to modulate their fluorescence properties, which, as we will see hereafter, depend on both the type of functional group covering the surface of CDs and the primary sequence and conformation assumed by the peptide during the binding.

3.2.1.3. CDs synthesis approach

Usually, two different strategies of synthesis are adopted for CDs preparation *i)* top down and *ii)* bottom up approaches. In the first one, CDs are obtained from graphene oxide, graphite, carbon fibers, carbon nanotubes, and carbogenic solid via chemical or physical peel process^[267,268]. Whereas the

second method consists in polymerization and consecutive dehydrogenation of small molecules such as citric acid, saccharide, and amino acids^[269].

For our aim, we have prepared a family of CDs called CD-N by thermally decomposing citric acid and urea, where the surface is mainly covered by amino groups. The choice to use CD-N was motivated by an in-depth study of the mechanism underlying the binding between the peptide and CDs, as will be discussed in the following section (see Section 3.2.2.). This study revealed that CD-Ns exhibit high sensitivity, making them more efficient in distinguishing isobaric peptides. Scheme of CD-N synthesis is shown in Fig.32, panel a.

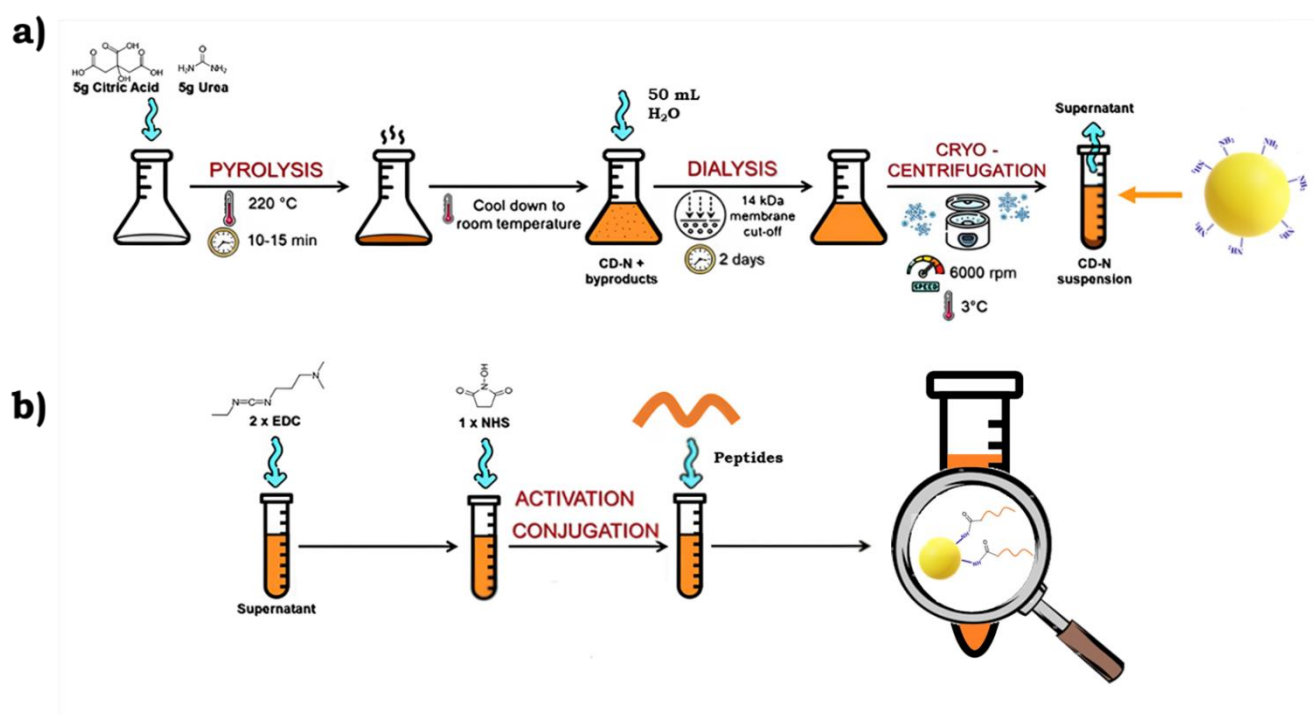


Figure 32 a) Scheme of CD-N synthesis procedure, and b) CD-N functionalization and insulin covalent conjugation. . Adapted from REF^[249] under Creative Commons CC BY 4.0 license; published by Analytical and Bioanalytical Chemistry 2023.

In particular, 5g of citric acid and 5g of urea were added together and undergone to pyrolysis process at 220°C for 10-15 min until both powders reach the consistency and colour of “caramel”. This step represents the citric acid decomposition followed by the CO₂ production.

Once this paste reached the room temperature, 50 mL of water were added. Here we have both the production of CD-N and the formation of other soluble by-products obtained by the urea thermal decomposition, which represent contaminants to be eliminated.^[270]

For this reason, dialysis was used as diffusion based separation process with a 14kDa membrane cut-off in order to obtain a suspension as clean as possible. Dialysis ends when the dialyzed water no longer fluoresces, i.e., after about 2 days, and then a cryo-centrifugation at 3 °C, at 6000 rpm for 1 h

is performed. The resulting supernatant solution corresponds to the final solution where the obtained CD-N, previously powdered by rotavapor, were analysed and characterized by AFM, FT-IR and elemental composition analysis^[249]. Latter analyses indicate that these CD-Ns are predominantly coated with amino groups on their surface.

To determine the optimal concentration of our CD-N, I diluted a specific amount of CD-N powder in water using various dilution factors. Subsequently, I analysed the resulting solutions through fluorescence measurements.

The fluorescence intensity of CD-N is dependent on its concentration in the solution. When the concentration is excessively high, the proximity between each CDs becomes too close, leading to a quenching phenomenon. On the other hand, if the concentration is too low, the fluorescence diminishes due to an excessively high dilution factor^[271].

For our purpose, a concentration of 0.0096 mg/ml in PBS (at pH 1.6) gives the maximum fluorescence value.

3.2.1.4. Monitoring of incubated insulin by CD-N fluorescence analysis

In order to monitor the insulin aggregation step by step, the addition of EDC (1-ethyl-3-(3-dimethylaminopropyl)-carbodiimide hydrochloride) and NHS (N-hydroxy succinimide) as powder (50mM and 25mM final concentration, respectively, to have a molar ratio 2:1 EDC: NHS) mainly allow the covalent binding between the activated COOH group of insulin and the terminal NH₂ group covering the CD-N surface (Figure 32, panel b). Working insulin solutions were incubated at the following time points: 0 minutes, 45 minutes, 90 minutes, 135 minutes, 195 minutes, 255 minutes, 375 minutes, 495 minutes, and 24 hours. The final concentration of working insulin was 20 μM. The system was consequently subjected to fluorescence analysis.

The resulting analysis is the creation of several fluorescence maps obtained from the subtraction of activated CD-N fluorescence curves at several excitation wavelengths on the incubated insulin-CD-N fluorescence curves performed at the same excitation wavelengths (Figure 33).

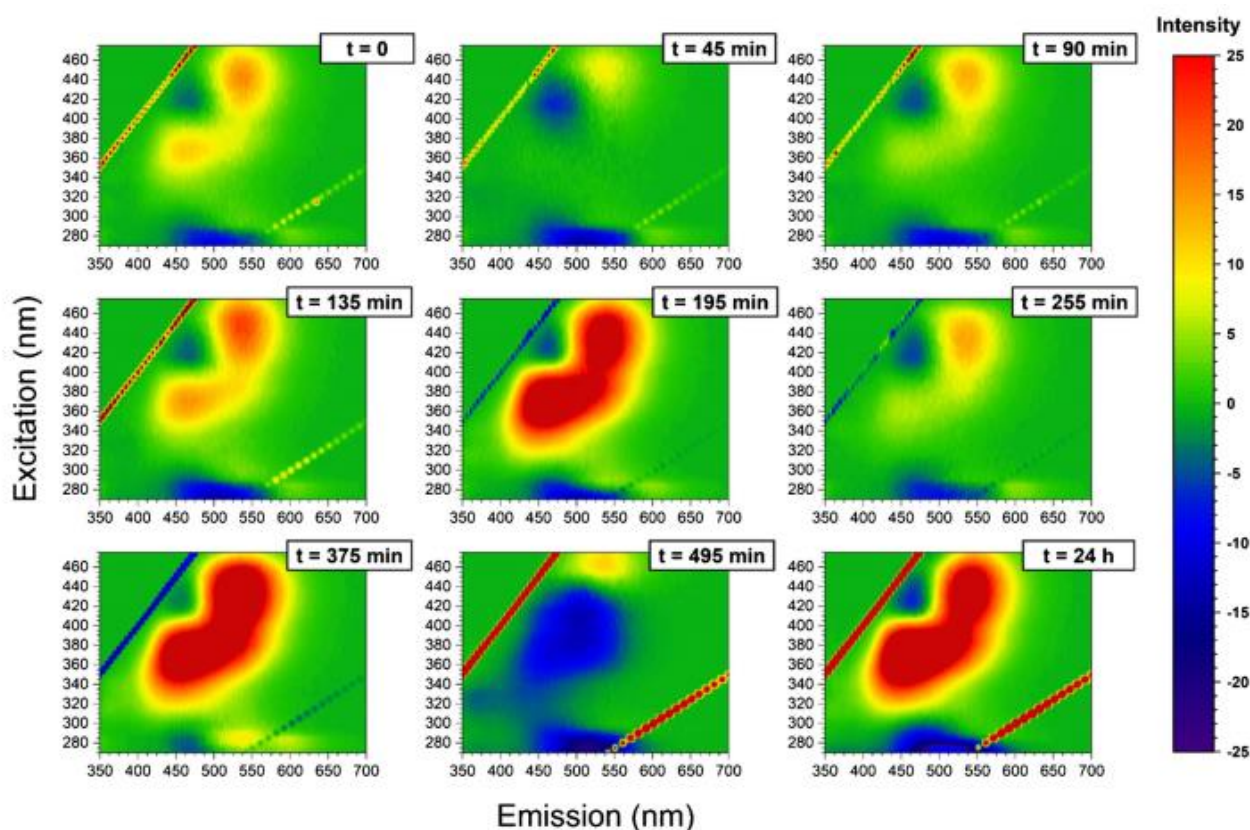


Figure 33 3D fluorescence variation maps of 0.0096 mg/ml CD solution coupled with insulin (20 μ M) at several incubation time. Fluorescence set up parameters are excitation range 270–475 nm; emission range 350–700 nm; excitation increment 5 nm; excitation/emission slit width 3 nm/3 nm; sampling interval 2 nm. Adapted from Ref^[249] under Creative Commons CC BY 4.0 license; published by Analytical and Bioanalytical Chemistry 2023.

Fig.33 shows the insulin conformational change occurring over time and in particular these changes are visible before the 375 min; a feature does not present in the case of the THT analysis (Figure 30). Therefore, the CD-N fluorescence is more sensitive than the THT fluorescence analysis. This phenomenon can be attributed to variations on the CD-N surface since the covalent conjugation of insulin to CD-N leads to notable changes in the fluorescence properties of CD-N. Indeed, to play a crucial role in the CDs fluorescence changing are the COOH groups of insulin which in turn are activated by the EDC and NHS (activators) present within solution and allowing a covalent binding between activated COOH groups of insulin and NH₂ of CD-N whose are in the majority. This behaviour will be further observed in the case of isobaric peptides (see section 3.2.2), where the single COOH group within the peptide sequence, determines the directionality and selectivity of the binding between the peptide and CD-N.

As a consequence, the different exposure of the insulin COOH groups to the solvent and their steric availability for the coupling reaction alters the fluorescence properties of CD-N, giving rise to a change in the variation maps that is dependent to every change of insulin conformation and/or oligomerization (Figure 33).

The steric availability for the coupling reaction is thus directly influenced by protein folding and oligomerization, rather than just on the formation of amyloid- β sheets. From Fig. 33 it is possible to see that the exposure of carboxyl groups in insulin molecules to the solvent is very similar for the three time points taken at 195 min, 375 min and 24 h. This demonstrates that changes in the conformation of insulin occur gradually, well before the detection of fibril formation by ThT after 375 minutes of incubation.

Interestingly, insulin molecules appear to alter the exposure of their carboxyl groups to the solvent and, consequently, their steric arrangement on the CD surface, resulting in the different fluorescence observed around 195 minutes of incubation in our experimental conditions. These changes, likely caused by the formation of oligomeric species, remain undetectable by ThT detection, which is sensitive only to amyloid fibrils. Indeed, it is worth mentioning that at all incubation time, an equilibrium between the monomeric and oligomeric insulin species cannot be excluded^[265]. The latter is confirmed from fluorescence maps (Figure 33). In fact, the shift from monomers to fibrils is hindered by the presence of oligomers, like hexamers, as clearly observed in the fluorescence variation maps at 255 minutes and 495 minutes that are similar to the ones observed at shorter times of incubation. Moreover, their fluorescence values decrease compared to those at 195min, 375min and 24h. Hence, the formation of fibrils is preceded by several crucial steps, including the aggregation of prefibrillar species, the disruption of oligomeric structures, and the unfolding of insulin molecules. This mechanism is strongly evidenced in Fig.34, where the presence of zinc ions promotes the formation of oligomers and decreases the hormone fibrillation. Fluorescence maps were obtained from the subtraction of activated CD-N fluorescence curves at several excitation wavelengths on the incubated insulin-CD-N + Zn^{2+} fluorescence curves performed at the same excitation wavelengths (Figure 34).

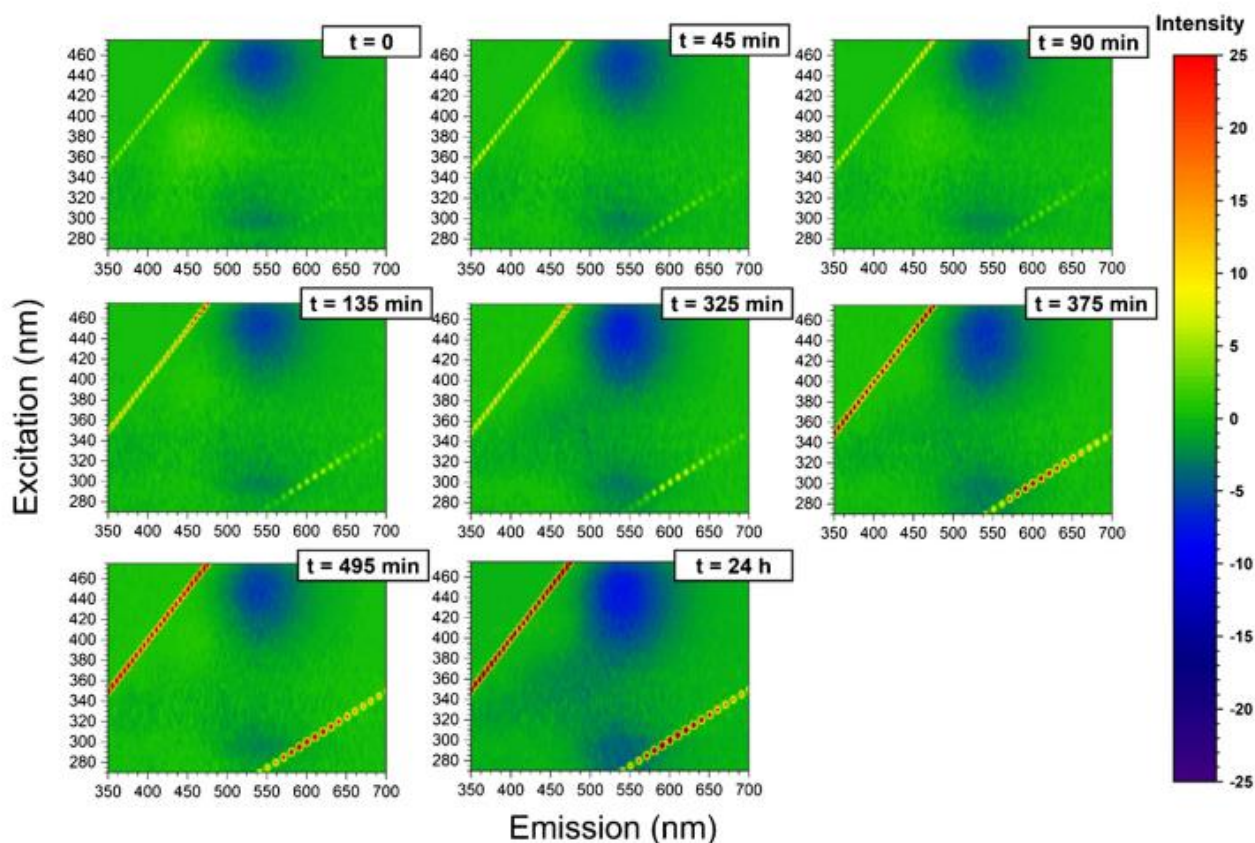


Figure 34 3D fluorescence variation maps of 0.0096 mg/ml CD solution coupled with insulin (20 μ M) in the presence of Zn²⁺ ions at several incubation time. Fluorescence set up parameters are excitation range 270–475 nm; emission range 350–700 nm; excitation increment 5 nm; excitation/emission slit width 3 nm/3 nm; sampling interval 2 nm. Adapted from Ref^[249] under Creative Commons CC BY 4.0 license; published by Analytical and Bioanalytical Chemistry 2023.

The decrease of fluorescence, observed even at very long incubation time, suggests the preferential formation of oligomers species in presence of metal during the insulin incubation with the opening of an additional off-pathway^[266].

In light of these results, fluorescence properties of CD-N provide a deep insight into the early-stage insulin aggregation, and CDs fluorescence turns out to be a promising tool to monitor protein aggregation mechanism.

Unlike other explored techniques such as Circular Dichroism, DLS and THT fluorescence, which are blind to discern insulin conformation changes before β -sheet formation, CD-N fluorescence offers a unique advantage. CD-N fluorescence enables to take a snapshot of the insulin aggregation state at a specific moment without compromising the peptide conformation.

Indeed, the addition of CD-N to the incubated insulin solution does not alter the insulin state. However, if CD-N is added during the insulin incubation process, it interferes with the genuine insulin conformation, thus disrupting the correct peptide aggregation mechanism^[249]. Moreover, each fluorescence map becomes a fingerprinting for the identification of that specific conformation

adopted by insulin. This innovative and easy method can be applied to all amylogenic peptides involved in aggregation processes, including the A β peptide.

The utilization of CD-N as biosensors in insulin conformation/aggregation mechanisms serves as a steppingstone for exploring similar aggregation mechanisms in misfolding pathologies. This is attributed to the remarkable properties exhibited by CD-N, including its sensitivity, biocompatibility, and low cytotoxicity. These advantageous characteristics make CD-N an excellent candidate for probing various aggregation processes in biological systems.

In the next section, we will delve into a comprehensive exploration of how the fluorescence properties of CDs are influenced through covalent binding with peptides, showcasing their remarkable sensitivity.

3.2.2 Isobaric peptides: the case of TAT1-Car series.

Among the various properties exhibited by CDs, their exceptional sensitivity enables their usefulness in numerous applications within the field of biosensing. This feature is associated with the capacity to modify functional groups on the surface of CDs. The attachment of peptides^[275,276] and proteins^[277,278] to CDs influences the fluorescent responses observed in CDs-peptides systems. However, the underlying mechanism of this interaction remains in part unclear^[279,280].

To exploit the inherent sensitivity of CDs, already observed in the binding between insulin and CD-N and, in the meantime, fulfil this knowledge gap, innovative CDs-peptide systems were designed. The purpose of this work was design CDs-peptide systems to more thoroughly understand how the fluorescence properties of CDs can be influenced by specific amino acid sequences and orientation of the attached peptide. CDs have been widely used as fluorescent probing in different fields including biological systems, as explained above. The enhancement/activation (turn-on) and quenching (turn-off) of CDs fluorescence can have enormous potential and development in biosensing. In fact, changes in the optical properties of CDs may be attributed to alterations on the CDs surface. These alterations can result from chemical processes that modify the functional groups present on the surface and/or from the binding of various molecules, such as peptides, environmental species, vitamins, etc^[281]. Indeed, a specific amino acid sequence and/or conformation of the peptide (as previously observed in the study of insulin and CD-N) can play a pivotal role in binding specificity and, in turn, influence sensitivity to changes in CD-N fluorescence.

In this scenario, Pandit et al.^[282] synthesized water-soluble emissive CDs through the pyrolysis of citric acid in the presence of various amino acids under hydrothermal conditions for the application of an array-based protein sensing system. The covered surface of CDs with selected amino acids provides a selective and highly specific detection of hemoglobin, cytochrome C, chymotrypsin, β -

glucanase, and xylanase by collecting ΔI (I-I0) fluorescence values, namely the observed fluorescence intensity after (I) and before (I0) the addition of the protein analytes, respectively.

Although nature is abundant in various chemical entities, including isomeric and isobaric species, their detection and differentiation using CDs, as well as variations in the fluorescence of CDs in the presence of isomeric species or isobaric peptides, have not yet been documented in scientific literature.

In this context, four isobaric peptides, synthesized at CY Cergy Paris University in France, were combined with two different type of CDs (CD-N and CD-COOH, namely with COOH terminal) whose fluorescence variation was followed by 3D fluorescence maps.

Peptides chosen for this aim are *i*) TAT1 derived from Trans-Activator of Transcription (TAT) protein and *ii*) the three isobaric peptides, i.e., peptides with same chemical formula but different amino acid sequences, designed to have the TAT1 sequence and the Car as well.

TAT is a protein that is encoded by the TAT gene in human immunodeficiency virus 1 (HIV). Its role is to dramatically increase the level of transcription of the HIV genes through before the binding to cellular factors, and then promote their phosphorylation^[283].

A shorter basic portion of HIV-1 TAT (TAT1) (sequence shown in Figure 35 as red dashed line) was found to prevent cognitive deficits and mortality in animal models of AD. Indeed, proteasome stimulation by TAT1 increases the turnover of APP and β secretase whose effect is a decrease of β -amyloid levels^[284,285]. TAT sequence is composed by 86 amino acids; however, the basic domain (TAT1) is enclosed between the 48th and the 59th amino acids whose sequence is GRKKRRQRRRPS (Figure 35).

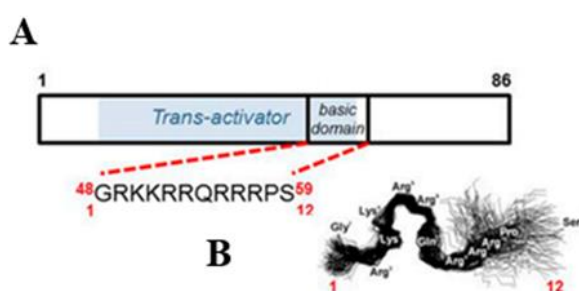


Figure 35 **A)** HIV-1 TAT protein sequence with the domain required for transactivation (blue) and the TAT1 short basic region (red dashed line). **B)** Proposed TAT1 conformation from molecular dynamics simulation. The result suggests the formation of two turn. Adapted from Ref^[284] under Creative Commons CC BY 4.0 license; published by *Molecules* 2020.

The presence of 6 arginine and 2 lysine residues gives the basic behaviour of TAT, moreover, because of this high arginine content, various homopolymers of arginine have also been investigated to study the mechanism of cell penetration showed by TAT^[286].

Indeed, thanks to this skill, TAT peptide is classified as a cell penetrating peptide, which can facilitate drugs, proteins and small molecules selective entrance into the cell through a membrane translocation mechanism^[287,288]. The entrance mechanism is influenced by the physiochemical properties of cargo, i.e., a carrier system comprising TAT and the designated molecule for transportation. The physicochemical properties of the cargo include the portion exposed to the aqueous environment, the folding of the cargo, and the specific molecule attached to the TAT peptide.

Ferrari et al.^[289] design a specific cargo where TAT peptide was fused to the glutathione S-transferase (GST) tag protein at the N-terminal end, and to the green fluorescent protein (GFP) reporter protein at the C-terminal. The synthesized cargo was tested in live HeLa and CHO cells in order to unravel the intracellular mechanism occurring.

Results demonstrated that the internalization process exploits a caveolar-mediated pathway, which, in turn, is influenced by the design of the cargo. Hence, the physiochemical properties and the position assumed by the molecule within the TAT sequence, significantly influence its biological characteristics, particularly the cell-penetrating mechanism.

In this context, our purpose was to design TAT1-cargo system in which the peptide is covalently coupled to Car peptide.

In human, Car is mainly degraded by carnosinase-1 (CN1) which is secreted from the liver to the serum. The Car degradation by CN1 is a serious problem concerning the cellular uptake of the dipeptide. Indeed, lower levels of Car, resulting in a higher CN1 activity, represent a “high-risk” for patient affected by T2DM. Moreover, a deficiency in Car levels is associated with impaired glucose mechanisms^[290]. As a consequence, Car represents a critical protective factor in diabetic patients.

Accordingly, the covalently coupling of TAT1 peptide with Car has a dual aim, i.e., *i*) the protection of Car in order to avoid its degradation *in vivo*, and *ii*) understand if the addition of Car in three different positions of TAT1 sequence can have a side effect on the cell-penetrating mechanism. Specifically, Car was added both to the N-terminal, C-terminal and in the middle of TAT1 sequence as well.

3.2.2.1. Solid phase peptide synthesis and RP-HPLC purification

Peptides were synthesized using microwave assisted solid phase peptide synthesis performed on a Liberty Blue Microwave Automated Peptide Synthesizer (CEM Corporation, Matthews, NC, USA), following the standard protocols for Fmoc/tBu strategy (0.1 mmol scale). Fmoc-deprotection cycles are respectively of 15 s (75 °C, 155 W) and 30 s (90 °C, 30 W). The synthesis was performed at CY Cergy Paris University (France).

The synthesized peptides have the following sequences (Figure 36): 1)GRKKRRQRRRPS (TAT1); 2)GRKKRRQRRRPS- β Ala-H (TAT1-Car); 3) β Ala-H-GRKKRRQRRRPS (Car-TAT1); 4)GRKKRRQ- β Ala-H-RRRPS (T-Car-T).

Couplings of Arg residues are performed in 1500 s (25 °C, 0 W) and 300 s (75 °C, 30 W). Couplings of His are performed in 240 s (50 °C, 35 W). Couplings of other residues are performed in 15 s (90 °C, 170 W) and 110 s (90°C, 30 W). After Fmoc deprotection of the last amino acid, the resin was washed with CH₂Cl₂ (10-mL) and dried. Peptide cleavage (4 h at room temperature) from the resin and deprotection of the amino acid side chains were performed with a TFA/H₂O/TIS (95:2.5:2.5 v/v/v) solution. The resin was then washed with TFA, and the filtrate partially evaporated.

(Waters Acquity UPLC coupled to a Waters 3100 ESI-SQD MS) supplied with a Luna Omega PS C18 (1.6 μm 2.1 x 50 mm) column at 35 °C at 0.6 mL/min with solvent systems A (0.1% TFA in H_2O) and B (0.1% TFA in CH_3CN). Data were acquired and processed using MassLynx software (Waters, Milford, MA, USA). All the peptides were obtained with a purity $\geq 90\%$.

3.2.2.2. Mass spectrometry and CD characterization of TAT-peptides.

To distinguish the isobaric peptides (TAT1-Car, Car-TAT1, and T-Car-T) (Figure 36), and the TAT peptide as well, MSMS (Thermo Scientific LCQ-DECA ion trap mass spectrometer) analysis were performed (Figure 37). The instrument is equipped with an ESI ion source operating in MS and MS/MS positive ion mode under the following conditions: capillary temperature 220 °C, sheath gas 10a.u.; source voltage 3.5 kV and capillary voltage 18 V. The MS/MS analysis was performed as follows: *i*) full-scan MS in the m/z range 100–2000; *ii*) Isolation width: 2; *iii*) MS/MS analysis of with normalized collision energy: 17–27 a.u. and activation Q: 0.250. Mass calibration was made using a standard mixture of caffeine (Mr. 194.1 Da), MRFA peptide (Mr. 524.6 Da), and Ultramark (Mr. 1621 Da).

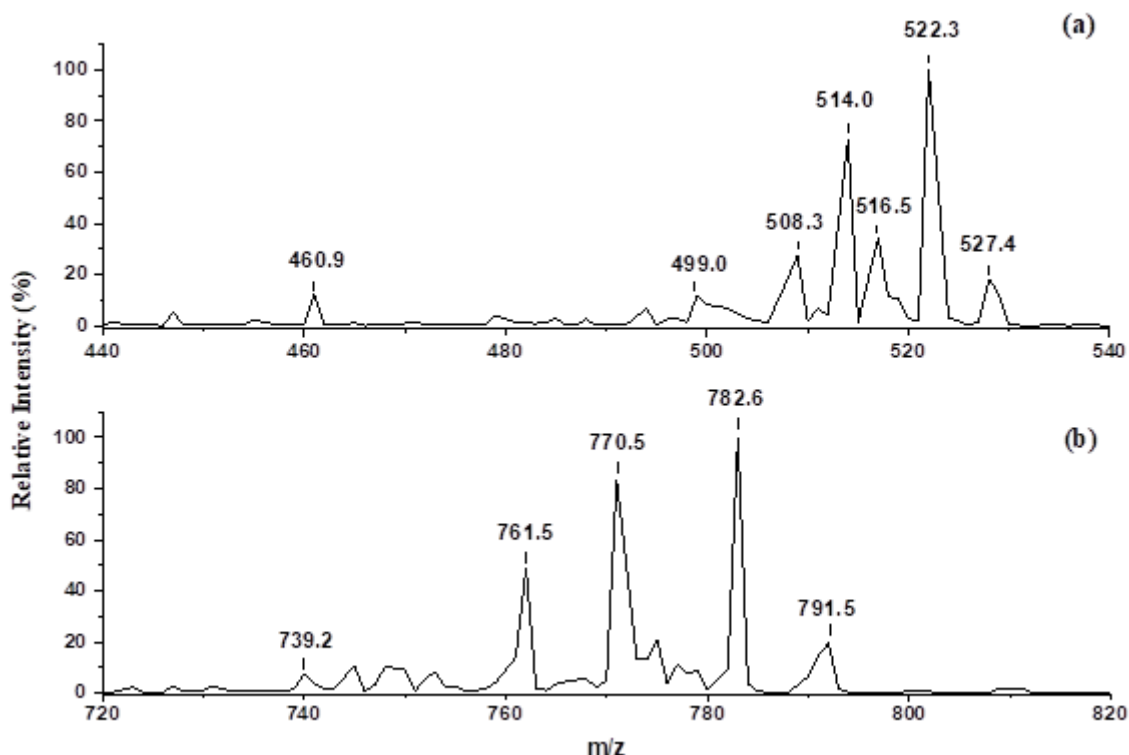


Figure 37 MSMS spectra of TAT1 (MW 1580.0 u.m.a.) for the **a**) triply charged peak at m/z 527.4, $CID = 17$ a.u., and **b**) the doubly charged peak at m/z 791.5, $CID = 22$ a.u. Adapted from Ref^[274]; published by Journal of Colloid and Interface Science 2022.

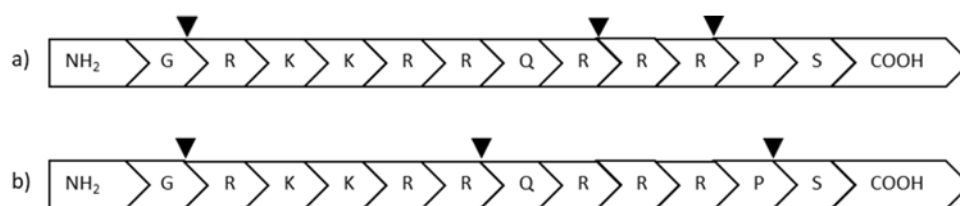


Figure 38 The TAT1 sequence and the observed cleavage sites for **a)** triply charged peak at m/z 527.4; and **b)** doubly charged at m/z 791.5. Adapted from Ref^[274]; published by Journal of Colloid and Interface Science 2022.

Peptides	Exp Mass (m/z)	Theor Mass (m/z)	Structure	Ion type	Relative Intensity (%)
m/z 527.4	527.4	527.7	[GRKKRRQRRRPS + 3H] ³⁺	PI	18.3
	522.3	522.0	[GRKKRRQRRRPS - NH ₃ + 3H] ³⁺	PI	100.0
	516.5	516.6	[GRKKRRQRRRPS - H ₂ O + 3H] ³⁺	PI	34.8
	514.0	515.3	[RRPS + H] ⁺	y ₄	73.2
	508.3	507.97	[RKKRRQRRRPS + 3H] ³⁺	y ₁₁	27.7
	499.0	498.3	[RRPS + H] ⁺	z ₄	11.2
	460.9	460.6	[GRKKRRQRRR + 3H] ³⁺	b ₁₀	12.4
m/z 791.5	791.5	791.5	[GRKKRRQRRRPS + 2H] ²⁺	PI	20.0
	782.6	782.5	[GRKKRR + H] ⁺	b ₆	100.0
	770.5	770.9	[RKKRRQRRRPS + H ₂ O + 2H] ²⁺	y ₁₁	83.5
	761.5	761.9	[RKKRRQRRRPS + 2H] ²⁺	y ₁₁	48.8
	739.2	738.5	[GRKKRRQRRR + 2H] ²⁺	b ₁₁	7.6

Table 6 List peaks for triply and doubly charged peaks at m/z 527.4 and m/z 791.5 respectively. In the table are shown the experimental mass, the theoretical mass, the structure proposed, the ion type, and the relative intensity for each peak.

The MSMS analysis for both peaks shows the neutral loss of both water molecule and the amino group for the triply and the doubly charged peaks. Furthermore, the fragmentation of the peaks at m/z 527.4 and m/z 791.5 reveals *b* and *y* preferred cleavage sites, but they are not in the same position. Indeed, as shown in Table 6, the peak at m/z 527.4 exhibits cleavage sites at 4th and 10th positions, whereas the cleavage site occurring for the peak at m/z 791.5 is located at 6th position. However, both peaks share the same *y*₁₁ cleavage site. Moreover, although the collision energies used are very similar (17 a.u. for the doubly charged peak, and 22 a.u. for the triply charged peak), the identity of the most intense peak detected in both cases is different. Indeed, while the most intense peak for the triply charged is the parent ion with the neutral loss of the NH₃ group, the doubly charged peak exhibits the [GRKKRR + H]⁺ species as the most intense peak, suggesting that the cut at 6th position is favourite.

The three isobaric peptides (TAT1-Car, Car-TAT1, and T-Car-T) were undergone to the MSMS analysis, whose results, i.e., the cleavage sites within the three structures, and the assignment of the fragment ions are shown in Fig.39, Fig.40, and Table 7 respectively.

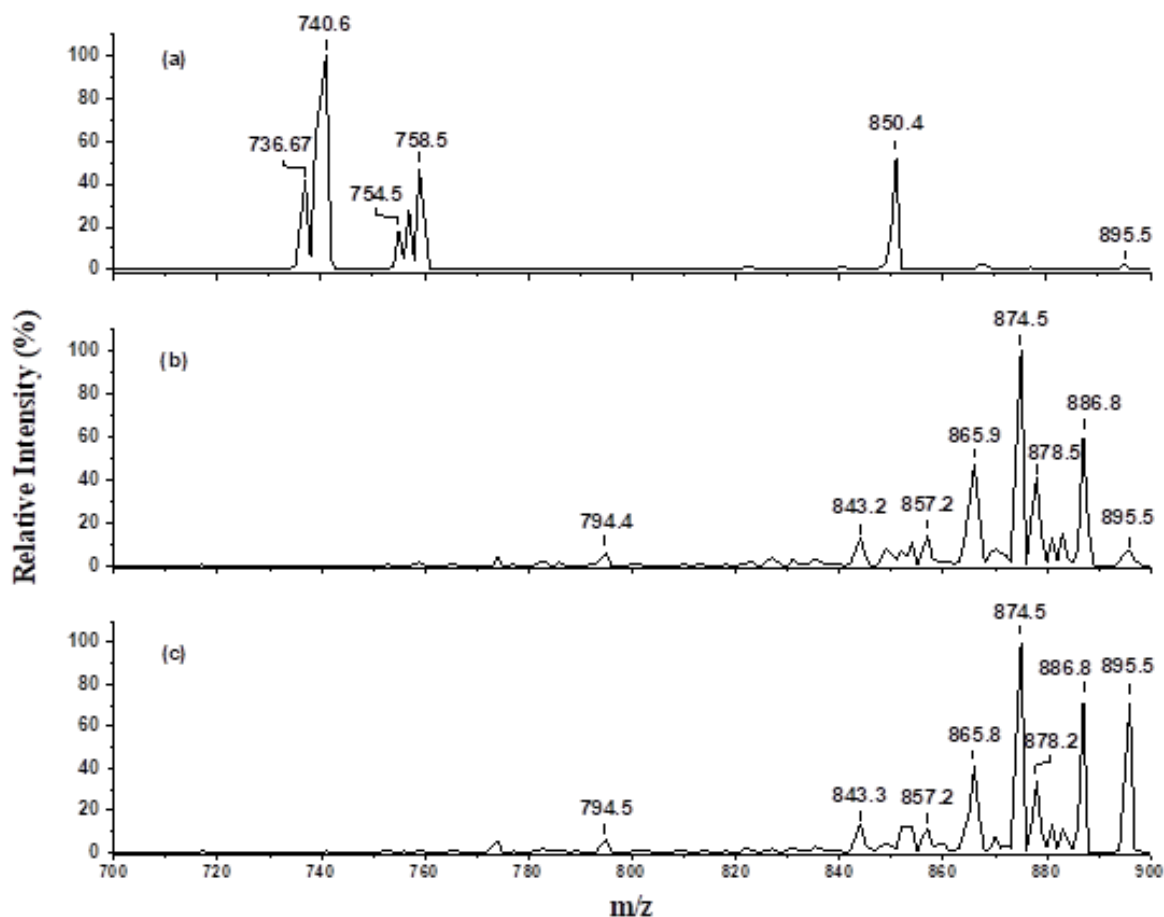


Figure 39 MSMS spectra for the doubly charged at m/z 895.5 of **a)** TAT1-Car (CID at 22 a.u.), **b)** Car-TAT1 (CID at 27 a.u.), and **c)** T-Car-T (CID at 25 a.u.). Adapted from Ref^[274]; published by Journal of Colloid and Interface Science 2022.

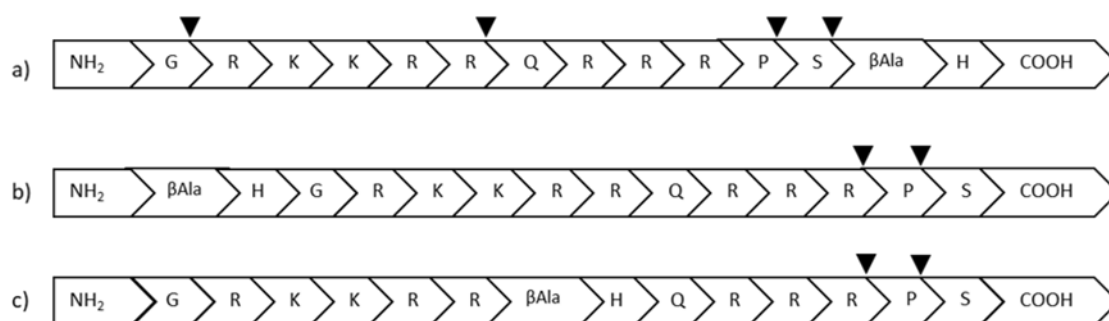


Figure 40 The primary sequence and the observed cleavage sites of doubly charged peak at m/z 895.5 of **a)** TAT1-Car **b)** Car-TAT1, and **c)** T-Car-T. Adapted from Ref^[274]; published by Journal of Colloid and Interface Science 2022.

Peptides	Exp Mass (m/z)	Theor Mass (m/z)	Structure	Ion type	Relative Intensity (%)
TAT1-Car	895.5	895.5	[GRKKRRQRRRPS-βA-H + 2H] ²⁺	PI	3.0
	850.4	851.5	[RKKRRQRRRPS-βA-H - H ₂ O + 2H] ²⁺	z ₁₃	52.1
	758.5	760.5	[GRKKRRQRRRPS - NH ₃ + 2H] ²⁺	a ₁₂	46.7
	754.5	754.5	[GRKKRR + H] ⁺	a ₆	18.1
	740.6	739.0	[GRKKRRQRRRP + 2H] ²⁺	b ₁₁	100
Car-TAT1	895.5	895.5	[βA-HGRKKRRQRRRPS + 2H] ²⁺	PI	8.1
	886.8	886.5	[βA-HGRKKRRQRRRPS - H ₂ O + 2H] ²⁺	PI	59.7
	878.5	878.5	[βA-HGRKKRRQRRRPS - OH - NH ₂ + 2H] ²⁺	PI	41.5
	874.5	873.5	[βA-HGRKKRRQRRRP + 2 Na] ²⁺	c ₁₃	100.0
	865.9	866.0	[βA-HGRKKRRQRRRP + 2 Na] ²⁺	b ₁₃	47.5
	851.4	851.5	[βA-HGRKKRRQRRRP + 2H] ²⁺	c ₁₃	14.2
	843.2	843.0	[βA-HGRKKRRQRRRP + 2H] ²⁺	b ₁₃	13.1
	794.4	794.0	[βA-HGRKKRRQRRR + 2H] ²⁺	b ₁₂	5.9
T-Car-T	895.5	895.5	[GRKKRR-βA-HQRRRPS + 2H] ²⁺	PI	71.7
	886.9	886.5	[GRKKRR-βA-HQRRRPS - H ₂ O + 2H] ²⁺	PI	72.2
	878.2	878.5	[GRKKRR-βA-HQRRRPS - OH - NH ₂ + 2H] ²⁺	PI	34.0
	874.5	873.5	[GRKKRR-βA-HQRRRP + 2 Na] ²⁺	c ₁₃	100.0
	865.8	866.0	[GRKKRR-βA-HQRRRP + 2 Na] ²⁺	b ₁₃	40.6
	851.4	851.5	[GRKKRR-βA-HQRRRP + 2H] ²⁺	c ₁₃	11.7
	843.3	843.0	[GRKKRR-βA-HQRRRP + 2H] ²⁺	b ₁₃	13.7
	794.5	794.5	[GRKKRR-βA-HQRRR + 2H] ²⁺	b ₁₂	6.2

Table 7 List peaks for doubly charged peak at m/z 895.5 for the three isobaric peptides. In the table are shown the experimental mass, the theoretical mass, the structure proposed, the ion type, and the relative intensity for each peak.

Interestingly, when Car is located at the COOH terminus (TAT1-Car), the Car moiety is lost during the fragmentation. However, in the cases of Car-TAT1 and T-Car-T, the fragmentation does not result in Car shedding. Instead, both peptides tend to lose their Ser and Pro residues at the COOH terminus. Consequently, the MSMS spectra of Car-TAT1 and T-Car-T appear identical, making it impossible to distinguish them through MSMS experiments.

Furthermore, the collision energy used for the three isobaric peptides is higher than the collision energy applied for the original TAT1 peptide. Nevertheless, TAT1-Car and T-Car-T peptides seem to be more resistant to the fragmentation in comparison with the Car-TAT1 peptide, where the fragments, resulting from cleavage in the middle of the peptide sequence, were detected.

Such a behaviour could depend on the different conformation assumed by the three isobaric peptides. Indeed, diverse non-covalent interactions within the chain of the peptide can affect the final peptides conformation in the aqueous environment.

For this reason, to validate our hypothesis, we conducted Circular Dichroism analysis (experiments performed by other research group from University of Catania) on the three isobaric peptides, along with the original TAT1 peptide. All peptides stock solutions were prepared by dissolving the proper amount of the solid in ultrapure water to reach a final concentration of 0.25 mM (pH solution: 3.5). Then, the solutions of each peptide (5 μ M) were obtained from the corresponding stock solution by diluting in ultrapure water. After the dilution, the pH increased to about 5.0–5.5. Since the peptide-CDs systems were investigated at pH = 4.5, we adjusted the pH value of each solution to 4.5. A JASCO J-715 spectropolarimeter equipped with a 1-cm path-length cell was used for all Circular Dichroism measurements. All Circular Dichroism measurements are shown in Fig.41:

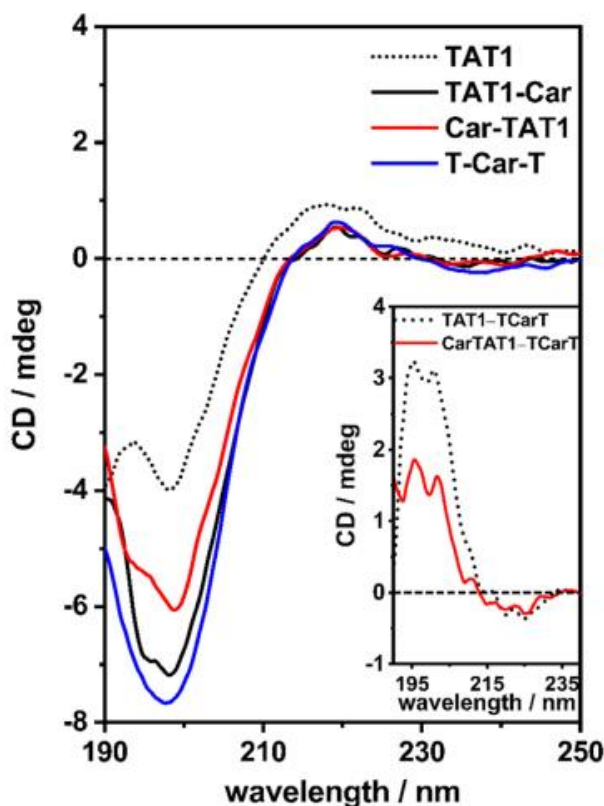


Figure 41 Circular dichroism spectra for TAT1 peptide and its Car-derivatives in aqueous solution at room temperature. The peptide concentration is 5 μ M and the pH = 4.5. In the inset, the Circular Dichroism spectra's arithmetic differences are reported: (TAT1) - (T-Car-T), black dotted plot; (Car-TAT1) - (T-Car-T), red solid plot. Adapted from Ref^[274]; published by Journal of Colloid and Interface Science 2022.

The dichroic spectra of all peptides displayed Cotton effects ascribable to a random coil conformation. In fact, as reported in Fig.41, the negative circular signal just below 200nm, the positive band at 218 nm and the very weak negative band at 235 nm are characteristic of such conformation. Thus, the circular dichroism spectrum of the T-Car-T peptide (Figure 41, blue curve) is completely in accordance with a random coil arrangement.

On the other hand, the dichroic spectra of TAT1, TAT1-Car, and Car-TAT1 peptides, point out slight differences in respect to the T-Car-T peptide, taken as a reference. Since the concentration of the analyzed peptides is equal in all experiments (= 5 μ M), these dichroic variations may be related to distinct conformational changes.

The arithmetic difference between the CD spectra of TAT1 with T-Car-T (black dotted plot within the inset-Figure 41) shows a mixed CD signal of β -sheet and β -turn conformations, characterized by a negative band at about 216 nm, a positive one near 195 nm (β -sheet), a negative band near 225 nm and a strong positive transition between 200 nm and 205 nm (β -turn). Therefore, this result indicates that TAT1 adopts a partial arrangement in β -conformations, which is entirely lost when Car is inserted in the middle of the TAT1 peptide.

Similar behaviour is observed for Car-TAT1 peptide. Indeed, the arithmetic difference between the CD spectra of Car-TAT1 with T-Car-T suggest that Car-TAT1 adopts principally a random coil conformation, however, the presence of a short portion of β -sheet conformation cannot be excluded (red solid plot).

Lastly, no change in the arithmetic difference between the CD spectra of TAT1-Car with T-Car-T were detected, indicating that TAT1-Car mainly adopts a random coil conformation.

Therefore, the CD analysis provided insights into how the position of Car along the TAT-1 chain can influence the final peptide conformation, giving an important suggestion for the experiment with CDs.

3.2.2.3. Synthesis and functionalization of CD-N and CD-COOH

In order to achieve our purpose and allow the discrimination of the three isobaric peptides, each peptides were tested with two different types of CDs, i.e., *i*) amino-rich (CD-N), and *ii*) carboxyl rich (CD-COOH) CDs.

The experiments start from the synthesis of both CDs carried out in the same manner explained previously (see the 3.2.1.3 section), however, the formation of CD-COOH foresees the pyrolysis of only citric acid. After the synthesis is completed, the coupling agents (in a 2:1 ratio of EDC/NHS) and the three isobaric peptides, along with TAT1 at a final concentration of 0.4 mg/mL, are introduced to both types of CDs (both CD-COOH and CD-N). Thereafter, all resulting samples were undergone

to the fluorescence analysis in order to extrapolate the fluorescence variation maps (Figure 42 and 45 for CD-COOH and CD-N fluorescence maps respectively).

All the fluorescence maps are obtained from the subtraction of activated CD-COOH or activated CD-N fluorescence curves at specific excitation wavelengths to peptides conjugated with CD-COOH and CD-N fluorescence curves respectively.

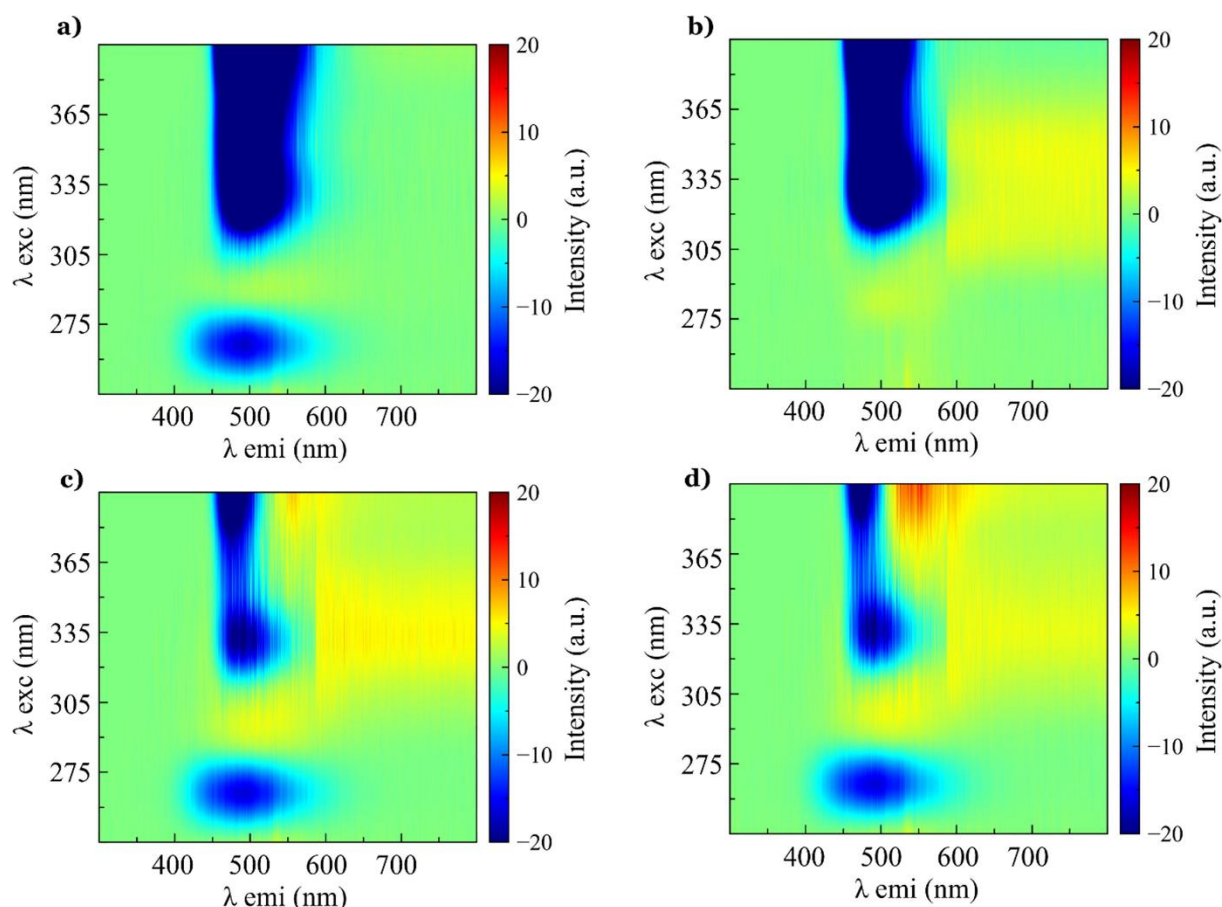


Figure 42 Fluorescence variation maps of **a)** TAT1-Car, **b)** TAT1, **c)** Car-TAT1, and **d)** T-Car-T. The concentration of all peptides is 0.4mg/mL. All maps are obtained by the subtraction of the activated CD-COOH fluorescence curves on the peptides conjugated with CD-COOH fluorescence curves. Adapted from Ref^[274]; published by Journal of Colloid and Interface Science 2022.

Upon observing the four fluorescence maps, it becomes evident that there are no discernible differences among them, highlighting the impossibility of distinguishing the isobaric peptides using CD-COOH. This is due to a multiple combination of binding manners occurring between peptides and the carboxyl groups present on CD-COOH surfaces.

Indeed, the coupling occurs between the COOH groups of the CDs, and the three reacting amino groups present in the peptide sequences. In this manner, since multiple linkages within the same peptide can occur, the peptides anchoring to the surface of CD-COOH will be random and lack preferential directionality. Hence, this marked disordered coverage occurring indiscriminately for

each peptide gives similar fluorescence responses caused by a strong similarity of the average chemical environment for the three isobaric peptides.

This behaviour is strongly evident in Fig.43, where the fluorescence variation maps of several TAT1-Car concentrations are reported.

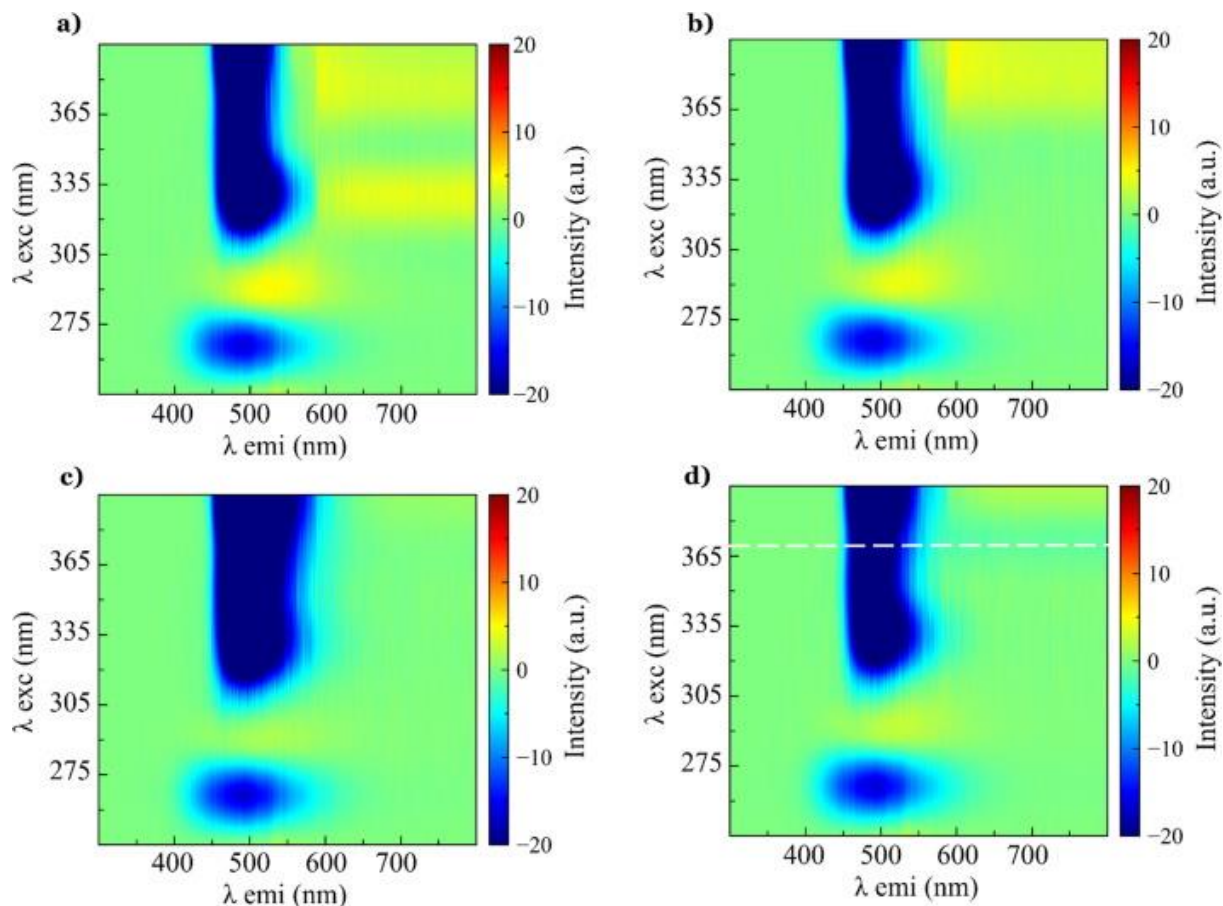


Figure 43 Fluorescence variation maps of TAT1-Car, at different concentration, namely **a)** 0.2 **b)** 0.3, **c)** 0.4, and **d)** 0.8 mg/mL. All maps are obtained by the subtraction of the activated CD-COOH fluorescence curves on the peptides conjugated with CD-COOH fluorescence curves. Adapted from Ref^[274]; published by *Journal of Colloid and Interface Science* 2022.

As observed previously, no differences in term of peptide concentration were detected. This is clearly explained by the plotting of ΔI (defined as the difference in fluorescence intensity between TAT1-Car at different concentrations and the activated CD-COOH) extrapolated from each fluorescence maps versus the emission wavelength (Figure 44, panel a) under an excitation wavelength of 370nm (indicated by the white dotted line in Figure 43). Besides (Figure 44, panel b), the ΔI trend extrapolated for each TAT1-Car concentration under emission wavelength of 450 nm versus the polypeptide concentration is reported.

Both fluorescence variations, shown in Fig. 44 panel a, and especially the ΔI trend illustrated in panel b, highlight a complete flat trend of fluorescence variation. This observation can be rationalized by considering that the saturation of the CD-COOH surface by TAT1-Car is already reached at very low peptide concentrations.

This phenomenon is due to the presence of three binding sites available in the peptide sequence: the two Lys side chains and the NH₂ in N-terminus position.

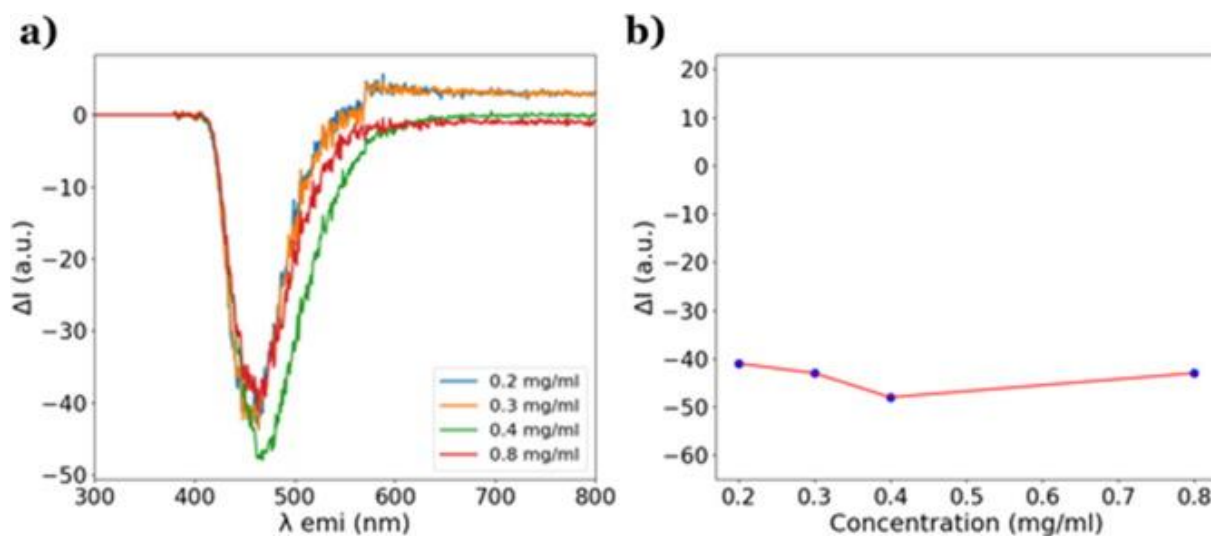


Figure 44 a) Carboxyl-rich CD TAT1-Car fluorescence variations, at different peptide concentrations, as labelled in picture, under excitation wavelength of 370 nm; b) ΔI trend as the concentration of TAT1-Car changes under emission wavelength of 450 nm. Adapted from Ref^[274]; published by Journal of Colloid and Interface Science 2022.

A different situation is observed in the case of CD-N, whose fluorescence maps for the three isobaric peptide and TAT1 are shown in Fig.45:

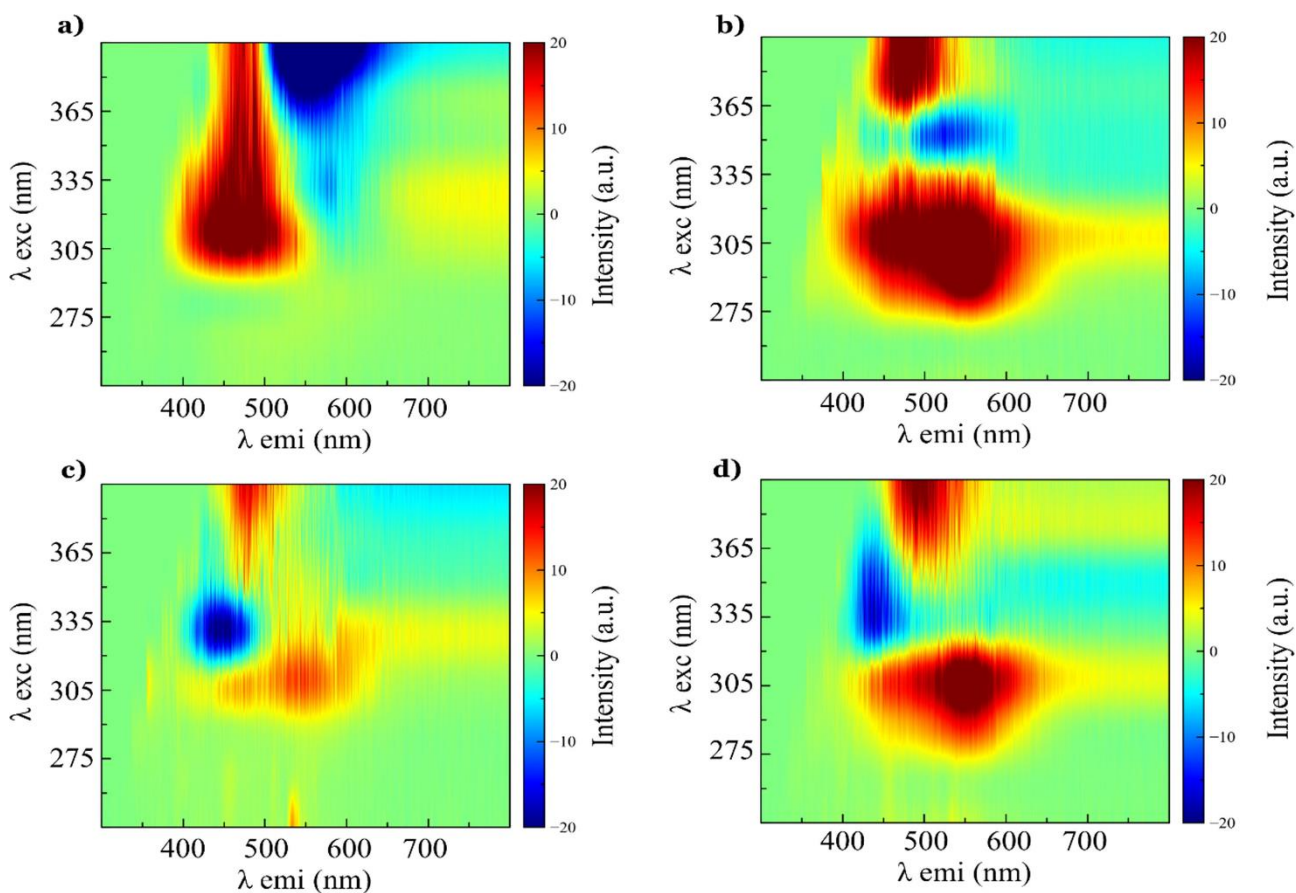


Figure 45 Fluorescence variation maps of a) TAT1-Car, b) TAT1, c) Car-TAT1, and d) T-Car-T. The concentration of all peptides is 0.4mg/mL. All maps are obtained by the subtraction of the activated CD-N fluorescence curves on the CD-N-peptide fluorescence curves. Adapted from Ref^[274]; published by Journal of Colloid and Interface Science 2022.

The results reveal four distinct fluorescence maps. Although each map shares the same positive and negative variation zone, the intensity of these zone differs between them. This discrepancy is a result of a singular binding opportunity, arising from the existence of a single COOH group positioned at the C-terminus of the peptide chain. These outcomes open up the possibility of distinguishing isobaric peptide by the use of amino rich CDs since their fluorescence depends on the nature of the peptide covalently attached to the CD-N surface. Moreover, each fluorescence map becomes a fingerprinting for the identification of that specific peptide.

In addition, the fluorescence varying maps for TAT1-Car at different concentrations are displayed in Fig.46.

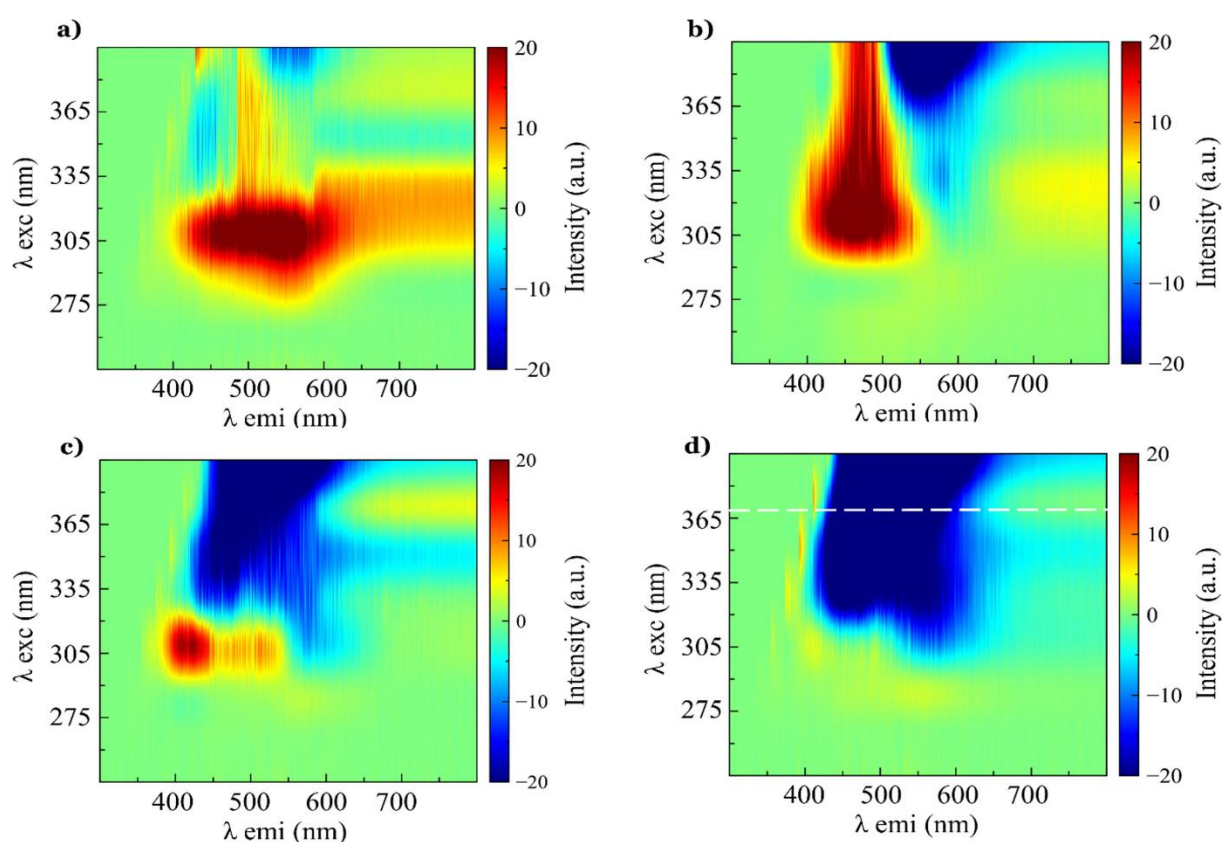


Figure 46 Fluorescence variation maps of TAT1-Car, at different concentration, namely **a)** 0.2, **b)** 0.4, **c)** 0.8, and **d)** 1.4 mg/mL. All maps are obtained by the subtraction of the activated CD-N fluorescence curves on the CD-N-peptide fluorescence curves. Adapted from Ref^[274]; published by *Journal of Colloid and Interface Science* 2022.

In contrast to the fluorescence varying maps of TAT1-Car at different concentration (Figure 43), the distinctions among all the fluorescence maps are remarkably evident in this case. Indeed, upon careful examination of the fluorescence maps labelled from *a* to *d*, the fluorescence of this CDs exhibits a quenching effect due to the increasing concentration of the peptide covering the CD-N surface. To confirm this experimental evidence, the fluorescence intensity variation ΔI (defined as the difference in fluorescence intensity between TAT1-Car at different concentrations and the activated CD-N)

trend was plotted versus the emission wavelength (Figure 47) under a specific excitation wavelength of 370 nm (indicated by the white dotted line in Figure 46).

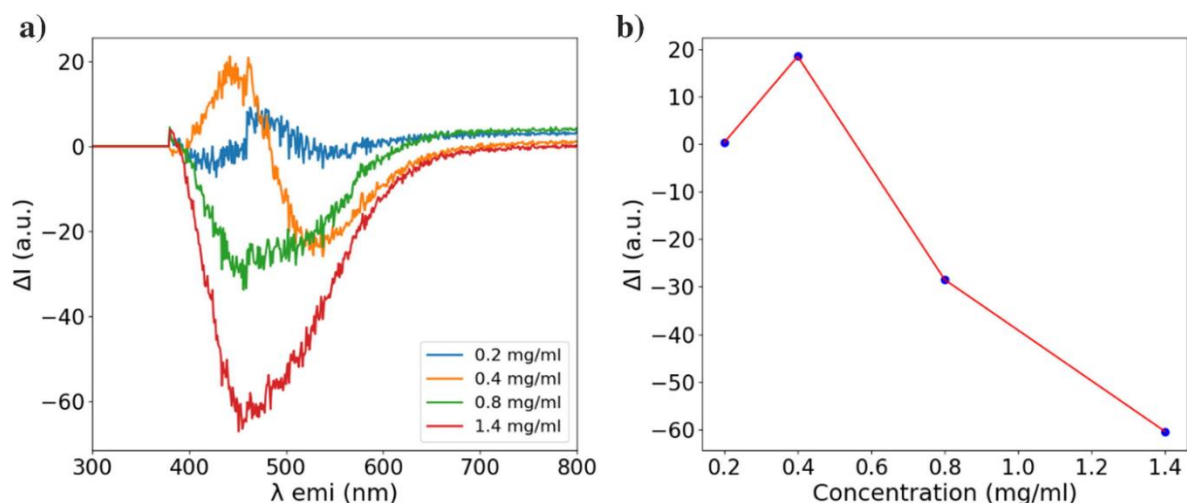


Figure 47 a) TAT1-Car-CD-N fluorescence variations, at different peptide concentrations, as labelled in picture, under excitation wavelength of 370 nm; b) ΔI trend as the concentration of TAT1-Car changes under emission wavelength of 450 nm. Adapted from Ref²⁷⁴; published by Journal of Colloid and Interface Science 2022.

Unlike the ΔI observed for the carboxyl-rich CD TAT1-Car where no variation was revealed, here the different TAT1-Car concentrations induce a clear fluorescence shift from *i*) a positive fluorescence changes for 0.2 and 0.4 mg/mL samples, to *ii*) a negative fluorescence variation for the higher TAT1-Car concentration (0.8 and 1.4 mg/mL).

This phenomenon (more evident in Figure 47, panel b) can be elucidated by considering the varying molar ratio between CD-N and peptide as their concentrations varies. Indeed, at low peptide concentration, there are still many NH_2 free on the CD surface, so an increase in peptide concentration results in an increase of the CD-N fluorescence (see point 0.4 mg/mL in figure 47, panel b). On the contrary, beyond a certain threshold, an increase in peptide concentration leads to excessive surface coverage, subsequently causing a quenched effect (see point 0.8 mg/mL and 1.4 mg/mL in Figure 47, panel b).

Therefore, the utilization of CD-N enables us to differentiate isobaric peptides. This capability is due to an ordered anchoring between peptides and CDs. The key distinction lies in the directionality of the $-\text{COOH}$ groups present in the peptide when bind the NH_2 group of CDs, compared to the indiscriminate peptides anchoring to CD-COOH. Hence, the findings imply that variations in the chemical properties of the CDs surface influence the binding mechanism observed. In particular, when the anchoring of the peptide occurs tidily through their $-\text{COOH}$ terminal group as in the case of CD-N, the method of fluorescence maps is very useful to discern isobaric peptides. Otherwise, the random attached of the peptides through their multiple $-\text{NH}_2$ moieties present in the peptides chain reveals the impossibility to distinguish isobaric peptides, even at very low concentration values. The

remarkable findings and the exceptional sensitivity exhibited by CDs open up exciting possibilities for their application as a novel tool to discern isobaric peptides that are indistinguishable by MS analysis.

3.3. Final Remarks

The potentiality of CDs as biosensor was widely explored within Chapter II.

CDs have gained relevant attention due to their unique fluorescence properties, adaptable for a wide range of several applications.

The covalent chemical modification of the surface of CDs enables a specific modulation of their fluorescence properties, tailored to the type of modification applied. This, combined with their biocompatibility, positions CDs as promising biosensors in the disease field.

Firstly, CDs were employed to monitor the aggregation of insulin over time, in which its ease of handling made insulin a model system for implementing this innovative biosensing system that will be adopted for the study of A β aggregation. Unlike DLS and THT fluorescence, which are very useful for detecting amyloid aggregates typical of the last stages of aggregation processes, CDs provide insight into the early stages of fibrillation processes where oligomers formation initiates the production of toxic species.

The results yield fluorescence maps which represent a real time snapshot of the conformation adopted by insulin at that specific moment. Noteworthy, the process of fibril formation is preceded by a series of critical stages, encompassing the aggregation of prefibrillar entities, the disintegration of oligomeric structures, and the unfolding of insulin molecules.

Conversely, the addition of zinc ions inhibits the formation of fibrils; however, it induces the formation of large oligomeric species, confirming the inhibitory role of this metal in insulin aggregation.

Secondly, CDs were used to identify and differentiate isobaric peptides with structures based on the TAT sequence. Techniques like MS have been unable to distinguish such isobaric peptides.

However, the covalent binding of these peptides to CD surfaces yields fluorescence maps that are a fingerprinting of each isobaric peptide, allowing the discrimination.

Nonetheless, this outcome was not achieved in all cases. In fact, the type of functionalization carried out on the CDs played a pivotal role in discerning these peptides. While the COOH-coated surface failed to distinguish the peptides, CDs with amino-rich functionalities have proven to be helpful in peptide discrimination. This is due to the unique COOH group on the peptide, which imparts a specific directionality in the binding process. Indeed, the ordered anchoring demonstrated by CD-N, as opposed to the much more randomized situation occurring with CD-COOH, was crucial for peptide identification and distinction. It also played a significant role in the future development of a highly sensitive biosensor.

Hence, the chemical neighbourhood sensitiveness shown by the fluorescence properties of CDs, joined to their increasingly widespread application in biotechnology, make them a powerful tool for the development of new strategies for sensing and/or preventing protein misfolding.

4. Chapter III:

*Mass spectrometric analysis of
A β -O₂ and A β -O₂-Cu complexes*

4.1. A β Misfolding: Unravelling Environmental Imbalance

The structure of proteins is intricately linked to their functionality. When proteins achieve proper folding, they can effectively carry out their intended biological functions^[291]. However, any incorrect folding of proteins, known as misfolding, can lead to alterations in the sequence of the protein or disruptions in its molecular interactions. This can subsequently result in improper protein functions and the build-up of misfolded protein deposits. Consequently, the presence of misfolded proteins arises when a specific protein follows an incorrect folding pathway or becomes trapped within an energy-minimizing funnel. This process often occurs spontaneously^[292]. The accumulation in the brain of misfolded proteins and the resulting disruption of cellular processes contribute to the development and progression of diseases.

Indeed, the emergence of misfolded protein lead to modification of biological processes such as the impairment of synaptic function, uncontrolled release of neurotransmitters, active cellular stress response like the oxidative stress pathways, and induce inflammatory response^[293,294].

In turn, the propensity of proteins to misfold is extremely affected by several factors ranging from genetic mutations to the imbalance of biological levels of environmental factors present in the disease. The pathologies associated with the accumulation of misfolded proteins are called *amyloidosis* including AD, in which A β peptide misfolding is strongly correlated with the alteration of some factors present in the AD environment^[295].

Among the factors that enhance the misfolding and aggregation of A β peptide, the production of reactive oxygen species (ROS) and the imbalance of metals such as copper and zinc play a decisive role.

Hereinafter, the detailed exploration of the involvement of ROS and metals in A β misfolding are explored.

4.1.1. Reactive Oxygen Species in AD

Oxidative stress is the result of an unruly production of ROS as hydroxyl radicals, nitric oxide, and superoxide species paired to a low antioxidant level of superoxide dismutase (SOD), glutathione peroxidase and glutathione reductase present in the hippocampus^[296].

Under physiological conditions, ROS are normally produced within the cell, and their role as mediators in several signalling pathways has been demonstrated^[297,298]. Moderate or low intracellular levels of ROS are correlated with the activation of survival, growth, proliferation, and cellular migration processes. However, high levels of ROS can damage cellular structures and activate the apoptosis signalling pathway^[299].

The primary source of intracellular ROS is the electron transport chain. It has been estimated that 1-2% of molecular oxygen is not fully converted into water; instead, it is partially reduced to superoxide anion ($O_2^{\bullet-}$). This production occurs at the level of complex I and III of the chain. Subsequently, this superoxide anion can be converted into hydrogen peroxide (H_2O_2) first and then into the hydroxyl radical (OH^{\bullet}) (Figure 48)^[300].

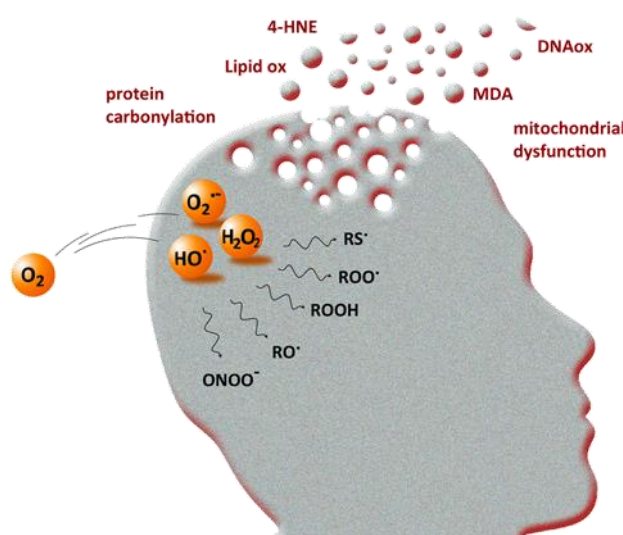


Figure 48 Graphical representation depicting the generation of ROS from oxygen molecules. Adapted from Ref^[300] under Creative Commons CC BY 4.0 license; published by *Int. J. Mol. Sci.* 2019.

However, although there are several pathways to produce ROS, a further origin of ROS is the reaction of molecular oxygen with the redox active metal iron and copper via the Fenton and Haber-Weiss reactions.^[32,42,216] Both reactions are metal-catalyzed in which, for example, the interaction between H_2O_2 and Fe^{2+} induces the generation of hydroxyl radicals (OH^{\bullet}) and hydroxide ions (OH^-)^[300,301]. In mitochondria, both $O_2^{\bullet-}$ and H_2O_2 take part in redox signalling^[302], but their production increases dramatically under oxidative stress conditions.

Indeed, the imbalance between the production of ROS and the ability of the body natural antioxidant defences to neutralize them are the building block of oxidative stress. Factors such as environmental pollutants, unhealthy diets, smoking, radiation, and certain diseases can increase the production of ROS and contribute to oxidative stress^[303–305].

Oxidative stress is associated with a range of health conditions, including neurodegenerative diseases, cardiovascular diseases, cancer, and aging. It can damage cellular structures and biomolecules, leading to inflammation, cell dysfunction, and even cell death. Antioxidants, which are molecules that neutralize ROS, are crucial in mitigating oxidative stress^[304,306–308].

Three enzymes are considered endogenous antioxidant systems: the Superoxide Dismutase (SOD), the Catalases (Cat), and Glutathione Peroxidase (GPx).

SOD is one of the most efficient enzymes and catalyses the conversion of $O_2^{\bullet-}$ into O_2 and H_2O_2 through a dismutase reaction. In humans, three different isoforms have been identified: SOD1, cytosolic copper complex isoform; SOD2, a manganese complex localized at mitochondrial level, and SOD3, an extracellular copper-zinc complex isoform^[309].

In the reaction catalyzed by Cat, the conversion of H_2O_2 into O_2 and water takes place within peroxisomes^[310]. Lastly, GPx is responsible for removing H_2O_2 , especially under low levels of oxidative stress. Its function is to convert H_2O_2 into an organic peroxide (ROOH), to water or alcohol (R-OH), through the use of glutathione (GSH) as a reducing agent. Under physiological conditions, this tripeptide composed of cysteine-glycine-glutamate is present in the reduced form in nucleus, cytosol, and mitochondria. However, under oxidative stress conditions, its oxidized form (GSSG) increases. Indeed, variations in the GSH/GSSG ratio serve as an indicator of oxidative stress status^[311,312].

Several evidence has highlighted the importance of oxidative stress, along with its linked mitochondrial dysfunction, in neurodegeneration, particularly in the pathogenesis of AD.

Neurons are more exposed to oxidative reactions due to their high consumption of oxygen molecules (approximately 20-30% of the oxygen consumed within the organism), resulting in a subsequent high production of ROS. Indeed, it is believed that in the neurons of individuals with AD, catalase activity decreases, leading to an increase in the SOD/Cat ratio^[313,314].

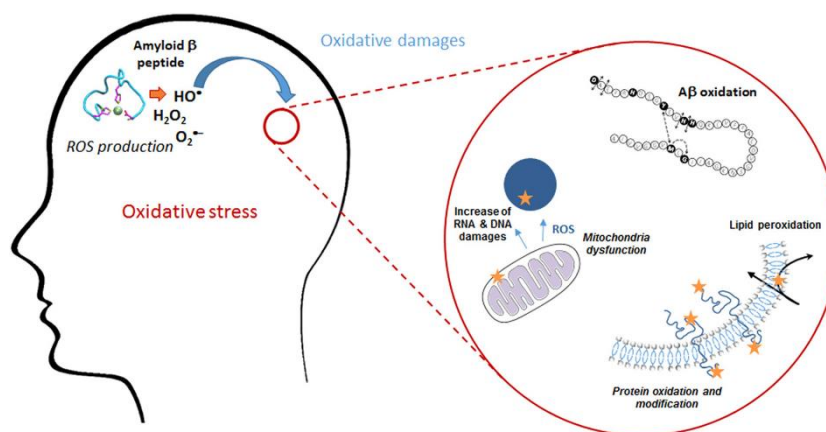


Figure 49 Illustration of oxidative damage pathways affecting the β -amyloid peptide due to the production of ROS. Adapted from Ref^[315] under Creative Commons CC BY 4.0 license; published by Antioxidants 2023.

In the presence of metal-catalyzed ROS production, the $A\beta$ peptide undergoes oxidative damages including lipid peroxidation, DNA damages and oxidation of some amino acid residues within $A\beta$ peptide primary sequence (Figure 49). The oxidation of amino acids such as cysteine, methionine, arginine, histidine, lysine, phenylalanine, tryptophan, and tyrosine alters intrachain interactions, destabilizing the native $A\beta$ conformation^[316].

The DNA damage includes the augmentation of the levels of oxidized bases, i.e., 8-oxo-2-dehydroguanine, 8-hydroxyadenine, 5-hydroxyuracil in temporal, parietal and frontal lobes^[317].

Moreover, an increase of 8-hydroxyadenine levels within hippocampus of subjects affected by AD and a DNA damage in peripheral blood cells in AD patients^[318] have been detected.

Several studies in normal old mice have demonstrated an increase of copper and iron levels in brain tissue,^[319,320] as well as in human amyloid deposits in AD-affected brains.^[321,322] The neuronal cell loss in AD could be attributed to the capacity of copper to cross the blood-brain barrier and interact with A β ₁₋₄₂ peptide causing the unbalanced production of ROS. This is due to the presence of histidine residues at positions 6, 13, and 14, which form a structural complex that allows A β ₁₋₄₂ to coordinate with metal ions.^[7,323]

Proteins, nucleic acids, and lipids are the primary targets for oxidative actions of ROS and stand in biomarkers of oxidative stress^[152]. Lipids are more susceptible to oxidation through ROS reactions compared to nucleic acids and proteins due to the presence of unsaturated sites in carbon-carbon double bonds.

Indeed, a further evidence of oxidative stress is the oxidation of unsaturated lipids, known as a sensitive marker of oxidative stress. The peroxidation occurs on the double bond of poly-unsaturated fatty acid (PUFA) by radicals in order to generate highly reactive lipid peroxy radicals and start a chain reaction. The final result is the production of HNE or 4-hydroxy-hexanal (HHE), depending on which PUFA is oxidated. This process spontaneously and readily modifies the three His residues of A β by Michael addition. As a consequence, this increases the hydrophobicity of A β , its affinity for lipid membranes, and the tendency for unmodified A β to form amyloid fibrils at low concentrations.^[324]

Indeed, an increase in HNE levels have been reported in brain portions where histopathologic alterations of AD, such as hippocampus, are typically found^[325]. Next to lipid peroxidation, the nitration process leads to nitrosative stress. This stress is triggered by the reaction of proteins with peroxynitrite (ONOO⁻, resulting from the reaction of superoxide radicals with nitric oxide). The outcome is a heightened vulnerability of brain proteins to proteasomal degradation^[326].

The accumulation of advanced glycation end products in the brain (AGEs), associated with the Maillard reaction, is an indicator of aging. Moreover, both AGEs and Maillard reaction are both implicated in the development and worsening of age-related disease including atherosclerosis, diabetes mellitus, and AD^[327-329]. AGEs are the final products obtained through a cascade reaction, including dehydration, oxidation, and cyclization, in which sugars react with proteins or lipids without the control of an enzyme^[330]. Moreover, in vitro analyses exhibited that AGE-modified A β promotes rapid aggregation^[331].

Unlike oxidative stress hypothesis, the mitochondrial hypothesis concerns that inherent dysfunction of mitochondria, being responsible for energy production, is a direct implication in the onset of AD. This dysfunction would occur in the early stages of the pathology^[332].

This hypothesis is based on the idea that mitochondria can alter the energy production and the Ca^{2+} homeostasis within cells. Imbalances in Ca^{2+} levels are a hallmark of neurodegenerative diseases, including AD. The $\text{A}\beta$ peptide is able of inducing the release of Ca^{2+} from endoplasmic reticulum, thereby increasing intracellular calcium levels. When the Ca^{2+} concentration in cytosol increases^[333], a portion of it is stored within mitochondrial matrix through an active transport. The Ca^{2+} overload leads to disruptions in ionic equilibrium, production of ROS, reduction of membrane potential and ATP synthesis, and $\text{A}\beta$ aggregation^[334], along with the activation of amyloidogenic pathway^[335].

4.1.2. Metal unbalance in AD

Heavy metals have undertaken a dramatic role in society today. The human body is a complicated system of storing and managing opportunely the amount of metal traces, which we swallow every day with food. Usually, the metals are transported from the stomach into cells throughout the bloodstream and excreted once the cell levels are sufficient or overloaded. When this mechanism fails, abnormal and dangerous levels of metals can develop, causing metals imbalances, where the most common are elevated copper and depressed zinc.

Normally there are 2-4 gr of Zn^{2+} located principally in the brain, kidney, muscle, liver, and bones. Zn^{2+} appears also as the unique metal in all enzyme classes, as IDE, with the highest concentrations in the eyes and prostate, in blood plasma. Furthermore, zinc is bound and transported by albumin and transferrin; this richness makes Zn^{2+} the second most abundant transition metal in the organism after iron.^[336] The third place is occupied by copper with only 75-100 milligrams in the organism. It is present in every tissue, stored mainly in the liver but it is possible found fewer amounts in the heart, brain muscles and the kidney.^[337]

Due to the helplessness of our body in the appropriate storage of both metals, daily consumption of copper and zinc is required to maintain a correct steady state. A huge variety of food contains zinc and copper such as oysters, seafood, red meat, nuts, cereals, and sunflower seeds. Zn is also present in beans, grains, and lamb whereas copper is taken by dark green leafy vegetables, green olives, avocados, dried legumes, chocolate, cocoa, and black pepper as well.^[338]

Zinc is involved in numerous biological mechanisms and about 10% of human proteins can hypothetically bind, traffic, and transport this metal. The role of zinc in the human body includes the antioxidant property by protecting sulfhydryl groups of proteins against free radical attack and it can

act as an antimicrobial agent even at low concentrations. Recently, zinc has been identified as neuroprotective nutrient against SARS-CoV-2. Specifically, zinc has been administered as therapy for SARS-CoV-2 infections for the following reasons: *i*) the anti-inflammatory activity of Zn^{2+} triggered by COVID-19, *ii*) the antiviral activity of this metal on various pathogens including, coronaviruses, and *iii*) the capacity of Zn^{2+} to regulate the competitive equilibrium between the host and the invading pathogens^[339].

Copper plays an important role in our metabolism, because it allows the opportune enzymes functions and it is indispensable for maintaining the strength of skin, blood vessel, and connective tissue^[340]. Copper is absorbed in the gut and transported to the liver by the binding with albumin, in particular, a membrane transporter 1-CMT1 carries copper inside the cell where it is bound to metallothioneins and sent to trans-Golgi network. Here, the release of copper into the liver is ascribable to ATP7A enzyme. Mutation in copper transports and ATP7A leads to Wilson's disease and Menkes disease respectively.^[341]

Copper can act as both antioxidant and pro-oxidant depending on the coordination site. Indeed, in case of copper homeostasis failure, free or loosely bound copper concentrations can increase, catalysing ROS production^[342]. The unrestrained production of ROS can damage cells and contributes to the development of health problem and diseases. When copper behaves as a pro-oxidant, the growth of ROS promotes the development of AD.

The generation of free radicals is strictly correlated to the involvement of redox-active trace metal as the case of Cu^+/Cu^{2+} redox couple, where the reduction of Cu^{2+} to Cu^+ can alter the breakable oxidative equilibrium occurring in mitochondria. In particular, Cu^{2+} in the presence of superoxide anion radical can be reduced to Cu^+ ($Cu^{2+} + O_2^{\bullet-} \rightarrow Cu^+ + O_2$) which in turn can catalyze the formation of reactive hydroxyl radicals through the decomposition of hydrogen peroxide via the above-mentioned Fenton reaction ($Cu^+ + H_2O_2 \rightarrow Cu^{2+} + OH^{\bullet} + OH^-$). In AD, the interaction between Cu^{2+} -A β is associated with the metal reduction to Cu^+ and with the unavoidable generation of hydroxyl radical by the decomposition of hydrogen peroxide^[343].

Contrarily, zinc is unable to participate in oxidation-reduction reactions due to its inherent redox-inert nature. Zinc deficiency has been correlated with an increased level of oxidative damage, including lipid, protein, and DNA oxidation.^[344]

In human body, a multitude of metalloproteins exists, enzyme and transporters in which metals are necessary for a correct function. Moreover, they are essential for regulation of the neuronal activity in synapses^[345].

In several diseases such as AD, copper and zinc are so extensively involved that the *metal hypothesis* has been proposed, suggesting that both metals, especially copper, are at least partially responsible

for the onset of the disease. However, the involvement of both metals in AD is not simply correlated to the increase, but rather to the breakdown of the zinc and copper homeostasis mechanism. In particular, the levels of Cu and Zn can be increased up to threefold in AD in comparison to the typical levels observed in healthy brains^[343]. Therefore, it is crucial to understand the types of interaction between A β and the metals and the species formed consequently.

Zn and Cu are found in amyloid plaques in relatively high and even submillimolar concentration (1mM and 400 μ M respectively)^[346]. According to Isothermal Titration Calorimetry (ITC)^[347] and NMR studies^[348,349], the hydrophilic fragment (N-terminus) containing the first 16 amino acids of A β peptides (A β ₁₋₁₆) takes part in the interaction with metals, whereas the hydrophobic part (C-terminus) is less involved in copper and zinc coordination. The A β ₁₋₁₆ fragment contains potential donor sites: Asp1 (NH₂, CO, COO⁻), Ala2 (CO), Glu3, Glu11 (COO⁻), Asp7 (COO⁻), His6, His13, His14 (Imidazole ring), and amidyl from the peptide backbone. Moreover, in vitro, the nature of the binding and the resulting conformational changes of A β ₁₋₁₆ upon Cu²⁺ binding exhibit pH and incubation time dependence^[350].

Although the binding between zinc and A β is not yet fully established, the widely accepted view supports a 1:1 coordination between the metal and the peptide^[351]. Zn²⁺ ions bound to the peptide throughout the imidazole ring of His6 and either His13 or His14 in addition to the carboxylate group of Glu11, Asp1, Glu3 or Asp7 (Figure 50). Moreover, affinity constants in the range of 10⁵ M⁻¹ have been confirmed through ITC and competition studies, allowing the zinc-A β interaction in vivo^[347,352].

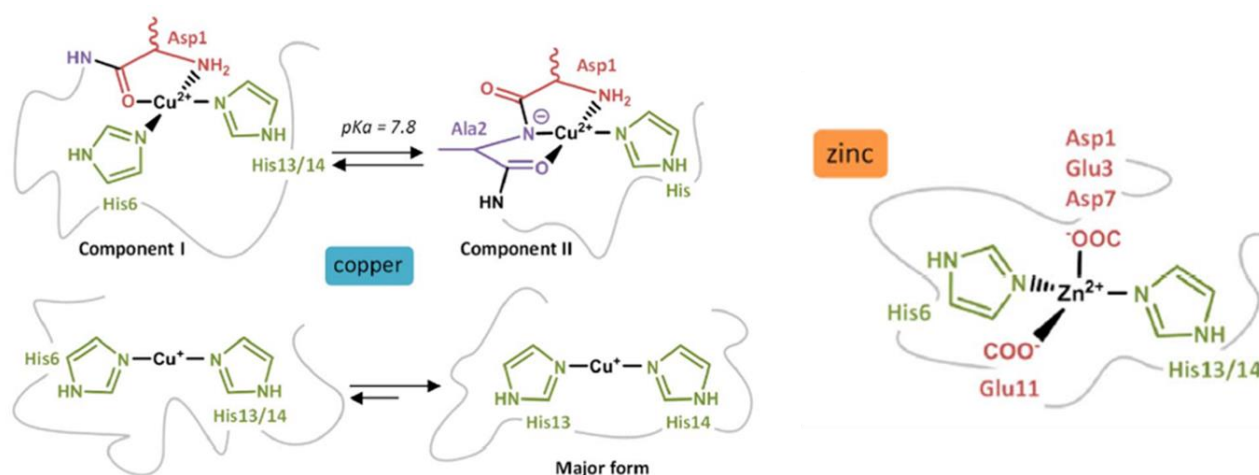


Figure 50 Schematic illustration of copper (Cu²⁺, Cu⁺) and zinc coordination with A β peptide. In the figure are shown the amino acids involved in the metal-peptide binding. Adapted from Ref^[32] under Creative Commons CC BY 4.0 license; published by Redox Biol. 2018.

The Cu²⁺- A β complex was studied for years, and the general agreement proposes two binding modes called component I and II observed around the physiological pH value (Figure 50). For component I,

Cu^{2+} is bound to the NH_2 terminus and the CO of Asp1 and to the imidazole ring of His6 and either His13 or His 14 assembling a square planar structure^[307,353–356]. Conversely, component II considers the NH_2 of Asp1, the amidyl function of Asp1-Ala2, the carbonyl group of Ala2, and the imidazole ring of one His residues binding to the Cu^{2+} ^[353–355].

Competitive studies, including ITC and potentiometry analysis, have reported a Cu(II) affinity constant in the 10^9 M^{-1} range^[357]. These results demonstrate a high affinity between copper and $\text{A}\beta$, significantly greater than the corresponding zinc- $\text{A}\beta$ interaction.

The Cu^+ coordination with $\text{A}\beta$ has been investigated more recently than the oxidated copper form and NMR studies^[358] have shown the crucial implication of histidine residues involved in the coordination with the metal. Accordingly, the two models proposed suggest a linear binding of histidine residues to the metal with a dynamic exchange between His6, His13, and His14 and an equilibrium between the His dyad and the His triad for Cu^+ coordination (Figure 50).

4.1.3. Copper-related damages in AD

Due to this strong affinity towards the $\text{A}\beta$ peptide and its inherent toxicity, copper is a “time bomb” implicated in multiple AD pathways, and its imbalance is responsible for different damages. These damages include oxidative stress, protein misfolding, disruption of cellular homeostasis, and many others which can contribute to the progression of neurodegenerative disorders such as AD (Figure 51).

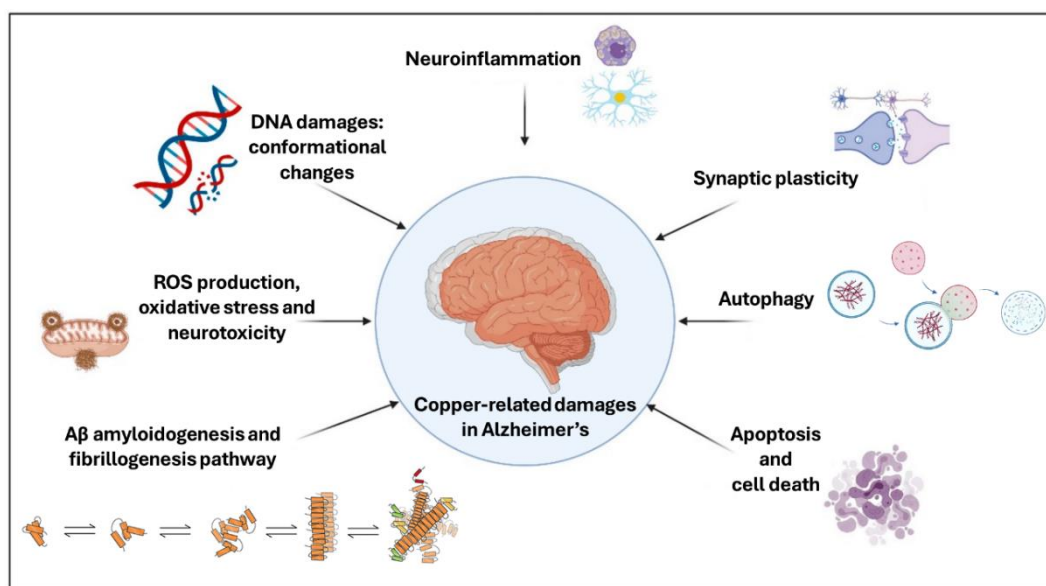


Figure 51 Comprehensive insight into the impact of copper ion in AD. Figure modified by REF^[359] under Creative Commons CC BY 4.0 license; published by Int. J. Mol. Sci. 2021.

Although copper serves as a cofactor in numerous enzyme, its perturbation is associated with the oxidative damage to DNA through the accumulation of copper in heterochromatin regions, leading to intracellular neurotoxicity^[360,361]. Moreover, the redox properties of copper induce neuronal dysfunction, impair biological functions, and cell death, contributing to the onset of neurodegeneration^[341]. UV, Circular Dichroism, and fluorescence analysis^[362] have revealed copper binding to the anionic phosphate ions of DNA backbone^[363], followed by its intercalation in DNA bases, inducing the loss of conformation. Indeed, copper exhibits high affinity towards guanine^[364] and cytosine^[365] of DNA, competing with hydrogen bonds.

These results demonstrate the ability of copper to promote a conformational change in the DNA structures within chromatin and highlight its involvement in DNA damage in various neurological disorders.

The primary toxic effect of copper is linked to the A β /Cu²⁺ complexes formation which drive and modulate the final end of the aggregation process^[220,221], as discussed in the previous chapter (see the paragraph 3.1.3.). The interaction between A β peptides and copper ions is characterized by a high affinity^[216,249,357]. Notably, the binding with Cu²⁺ ions stimulates the formation of dityrosine-linked β -amyloid dimers. The presence of these metal ions leads to a structural shift from a parallel arrangement to an anti-parallel conformation^[366-369]. Moreover, this process is regulated by the specific binding site occupied by copper^[219]. The observations made through in vitro studies are further confirmed by the lack of neurotoxicity observed in mutant dimers. In these mutants, the substitution of tyrosine10 with alanine prevents the induction of dityrosine cross-links^[370].

Moreover, AD brain tissues and the cortices of transgenic animals with severe brain damage have exhibited an elevated capacity for binding with Cu²⁺ ions^[371,372].

Beside the A β aggregation and the well-known ROS production triggered by copper, the direct consequences of this toxic mechanism include the loss of synaptic plasticity, neurotoxicity, autophagy, and apoptosis^[373]. Moreover, A β deposition within senile plaques, and NFTs, intricately linked to the aforementioned toxic process, show significant susceptibility to homeostatic influence of copper^[374].

Lu et al.^[375] demonstrated that disordered copper metabolism is associated with the hippocampal neuronal apoptosis induced by copper and a decrease in neuronal vitality. The experiments unveiled that copper exposure incites oxidative stress, promoting the apoptosis of HT22 murine hippocampal neuronal cell. The mechanism involves the hindrance of protein phosphorylation, while on the other hand, it promotes ROS production and lipid peroxidation.

Copper involvement in synaptic plasticity is highly complex due to its multifaceted action. Several studies have demonstrated that Cu²⁺ inhibits long-term potentiation (LTP) in cultured mouse

hippocampal slices and rat hippocampus^[376,377]. Synaptic plasticity is closely related to long-term potentiation (LTP) since LTP is a significant mechanism through which synaptic plasticity occurs. Furthermore, copper is tightly linked to the neurotransmitter release within the synaptic cleft^[378]. In fact, copper can influence the function of glutamate receptors, which are fundamental for synaptic transmission. Copper can also modulate the activity of NMDA (N-Methyl-D-Aspartate) receptors, which are important for LTP^[379].

Although the involvement of copper in autophagy mechanism is still under discussion, the production of ROS by copper seems to induce dysfunction of autophagy in the hippocampus of AD^[342]. Recently, it has been observed that copper can influence the function of proteins involved in autophagy and lysosomal metabolism. Xue et al.^[380] demonstrated that copper can trigger the onset of the autophagy through multiple mechanisms. Moreover, the presence of copper leads to an increase in MAP1LC3 levels and the activation of the TFEB transcription factor, contributing to the formation of autophagosomes and autolysosomes, respectively^[380].

4.2. Results and Discussions

The imbalance of metals, such as copper, plays a crucial role in the worsening and development of AD. While most studies primarily investigate how copper affects the misfolding of the complete A β ₁₋₄₀ or A β ₁₋₄₂ sequences due to their critical role in the disease, smaller fragments resulting from enzymatic digestion by metalloproteases could also be candidates for copper interactions. The aforementioned metalloproteases feature cleavage sites along the amino acid sequence of the full length A β (see section 2.2), leading to the generation of smaller fragments. However, our understanding of the biological functions and interactions with metals of these fragments remains limited. Therefore, an analysis is required to determine whether these fragments, once in their free form, can participate in copper binding and trigger unexplored secondary reactions.

On the other hand, the generation of ROS and their oxidative mechanisms, occurring within both normal biological pathways and pathological contexts such as AD, have been thoroughly investigated. However, the discovery of oxygen-adducts, namely A β species coordinating oxygen atoms/molecules, is of paramount importance for achieving a deeper knowledge of the upstream redox mechanism occurring before molecular oxygen converts into ROS redox mechanism in AD and other neurodegenerative^[315,381,382].

How and if O₂ molecules bind A β is not known, and the understanding of such possible binding could give an insight into the A β oxidation mechanism occurring in the brain^[152,383].

However, the direct binding of oxygen with A β is a challenging task by using common analytical techniques. Usually, oxidative processes involving A β peptide consider H₂O₂ as oxidant agent^[384] in aqueous solution. In this manner, the presence of specific solvents and salts surely affects and compromises the identification of the basic chemical processes at the base of A β oxidation. This issue can be overcome by the use of gas reactions coupled with MS, so that the compounds produced in the gas phase can be analysed in their intactness, without the presence of contaminants. In spite of the huge advantages characterizing this technique, common mass spectrometers are not equipped with the insertion of other gases beyond argon in the collision-induced dissociation (CID) cell or in other compartments present in the instrument. Therefore, the direct use of gaseous oxygen molecules, necessary for our aim, is not possible.

The hindrance is overpassed by means of a mass spectrometer modified *ad hoc*, belonging to Université de Bretagne Occidentale, where the formation of oxygen-adducts has been investigated in the gas phase.

Indeed, the introduction of oxygen molecules in the hexapole could allow the formation of oxygen adducts, which in turn can be isolated and fragmented in CID cell through the use of argon gas for the structural analysis.

In Fig.52, the scheme of the modified mass spectrometer is described in detail.

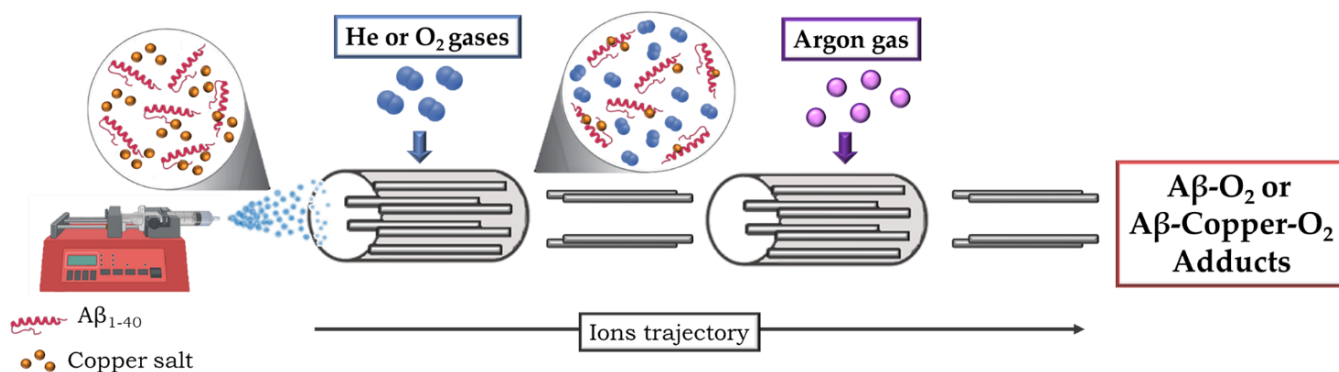


Figure 52 Scheme of the modified mass spectrometer.

MS experiments were performed on a home-modified Quattro II (Figure 52, Waters/Micromass, Manchester, UK) equipped with a Z-electrospray source (ESI, Waters, Manchester, UK) working in positive ion mode. All experiments were carried out exploring different cone and extractor voltages in order to improve the signal obtained in the wide range of m/z 700-1500. However, in order to properly compare the signals in all four experiments, a tight combination of cone and extractor voltages were chosen. Indeed, the source parameters were fixed as follow: capillary 3.2 kV, cone 20-40 V, extractor 5 V, source temperature $90^\circ C$, desolvation temperature $130^\circ C$, HM1/LM1 resolution 14 and HM2/LM2 resolution 12 for MS1 and MS2 analysis respectively. Ion Energy 1 and Ion Energy 2 were 5 and 10 according to the calibration of the instrument by means of using horse heart myoglobin specifically prepared for mass calibration from m/z 600 up to m/z 2000. This standardized approach allowed reliable and consistent results for all experiments, facilitating an effective comparison of signals in the specified m/z range. The focusing of the fragment ions from the first quadrupole to the second quadrupole through the CID was made possible by an appropriate voltage applied to various internal lenses (identified as 6, 7 and 8 in the software). The fragmentation of isolated ions occurred in the CID cell by collision with argon gas at the approximate pressure of $2.5 \cdot 10^{-3}$ mbar, whereas the oxygen gas and helium gas inlet were set up in the hexapole with a pressure of $4-4.5 \cdot 10^5$ mbar and approximately $3 \cdot 10^5$ respectively. Indeed, the innovation of this modified mass spectrometer, compared to the common mass spectrometers, is the possibility to directly insert some gases such as oxygen and helium. Pressures are specified as uncorrected gauge reading (no correction factors applied due to the nature of gas). As there is no pressure gauge in the H0 transfer cell where He and O_2 are inserted, we report the pressure indicated in the high vacuum quadrupole region namely

“Analyser” (close to the first quadrupole). The pressure modulation of both O₂, He, and Ar, was obtained manually through flow-control of valves characterizing the entwined system which joins the O₂, He, and Ar tanks with the hexapole and CID cell respectively.

The MS2 analysis of the A β ₁₋₄₀ (Figure 58), the A β fragments (Figure 60, 62, 64, and 66) with copper chloride complexes, as well the proof of A β structures proposed (Figure 54, and 56) were performed with ESI-HRMS SYNAPT XS, whose instrumental scheme is shown in Fig.53.

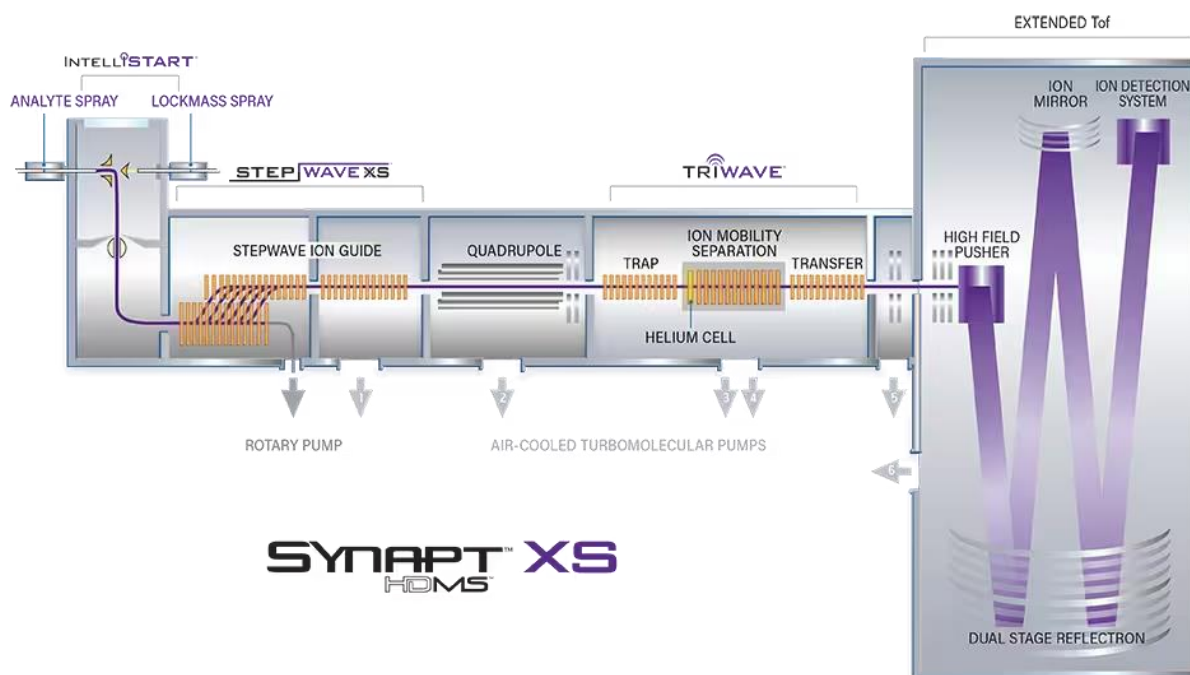


Figure 53 Scheme of Synapt XS HDMS mass spectrometer from Waters. The instrument is equipped with ESI for the analyte and the standard, ion guide, source nozzle, sampling cone, Quadrupole, collision cell, transfer lenses, pulse system, ion mirror, detector, TOF analyser, double-stage reflectron, and vacuum pumps.

The Synapt XS HDMS quadrupole-time of flight (Q-TOF) mass spectrometer is equipped with an ESI source for both the analyte and the standard spray (from Waters, Milford MA, USA), and two analyzers, i.e., a quadrupole and an extended TOF arranged before and after the ion mobility respectively. After ionization of the solution to be analyzed in the ESI source, a portion of the generated ions is captured by a sampling cone and then guided through an ion optic system with a discontinuous design that allows the elimination of neutral species (uncharged) under a vacuum of 10⁻³ mbar. Subsequently, the ions pass through a quadrupole, where the high vacuum is approximately 10⁻⁶ mbar, and they are sorted based on their m/z ratio before entering the CID cell where helium is injected at a specific pressure. It is at this moment that the ions fragment. To calibrate the analyser across the entire spectral range, a solution of sodium formiate is used, which, during ionization in the source, forms various adducts with sodium (singly charged).

For the presented study, a measurement was conducted after calibration and following experiments at the end of the day, in order to compare the theoretical and experimental values of m/z and deduce

the level of precision. Finally, instrumental optimization before spectrum acquisition aims to achieve optimal sensitivity.

In this context, the purpose of this chapter includes: *i*) investigating the formation of copper complexes with both the full-length $A\beta_{1-40}$ and selected fragments ($A\beta_{1-16}$, $A\beta_{12-28}$, $A\beta_{25-35}$, and $A\beta_{28-35}$) (section 4.2.2), exploring the potential formation of oxygen adducts with all $A\beta$ peptides *ii*) in the absence (section 4.2.3), and *iii*) in the presence of copper chloride salts (section 4.2.4).

4.2.1. Protonated $A\beta$ peptides.

The analysis of $A\beta_{1-40}$, 1 μ M in acetonitrile/water 1:1 + 0.1% formic acid (FA), was investigated in MS1 and the resulting spectrum and the list of peaks are shown in Fig. 54 and Table 8 respectively:

a) $^1\text{DAEFRHDSGYEVHHQKLVFFAEDVGSNKGAIIGLMVGGVV}^{40}$

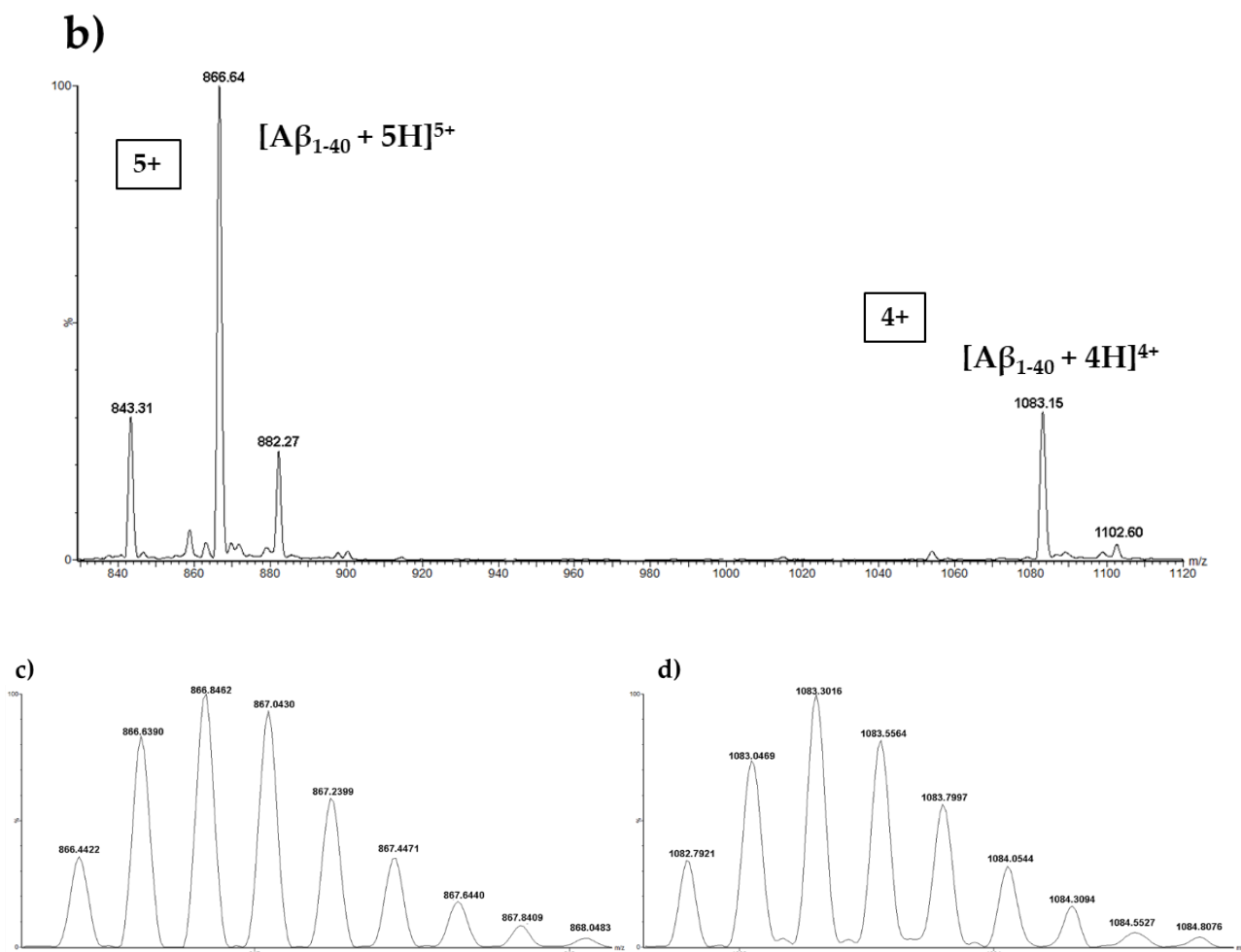


Figure 54 a) $A\beta_{1-40}$ primary sequence, b) $A\beta_{1-40}$ peptide mass spectrum acquired in positive mode. The setup source parameters are capillary 3.2kV, cone 40V, extractor 5V. Flow rate 10 μ l/min. c) ESI-HRMS SYNAPT XS analysis of $[A\beta_{1-40} + 5H]^{5+}$ and d) $[A\beta_{1-40} + 4H]^{4+}$ proton ions.

Exp. Mass (m/z)	Theor. Mass (m/z)	Intensity (arb.u.)	Structure
843.31	843.42	$2.69 \cdot 10^7$	$[\text{A}\beta_{1-39}+5\text{H}]^{5+}$
866.64	866.83	$8.82 \cdot 10^7$	$[\text{A}\beta_{1-40}+5\text{H}]^{5+}$
882.27	882.54	$2.05 \cdot 10^7$	$[\text{A}\beta_{1-40}+\text{DMSO}+5\text{H}]^{5+}$
1083.15	1083.29	$2.77 \cdot 10^7$	$[\text{A}\beta_{1-40}+4\text{H}]^{4+}$

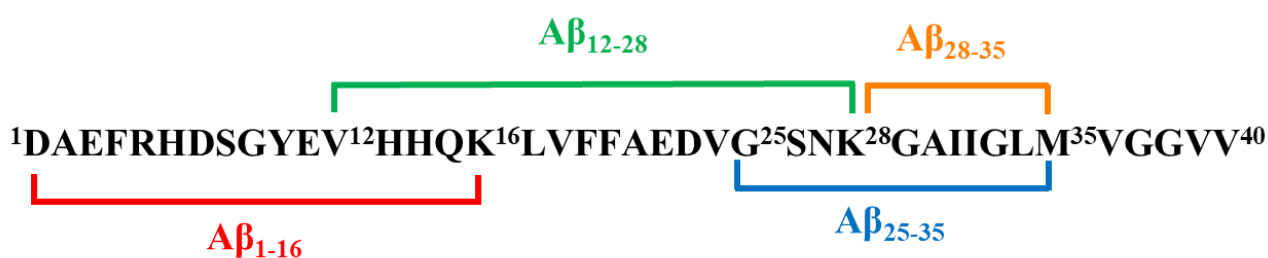
Table 8 List peaks $\text{A}\beta_{1-40}$ proton ions. In the table are shown the experimental mass (from Quattro II analysis), the theoretical mass, the intensity and the structure proposed for each peak.

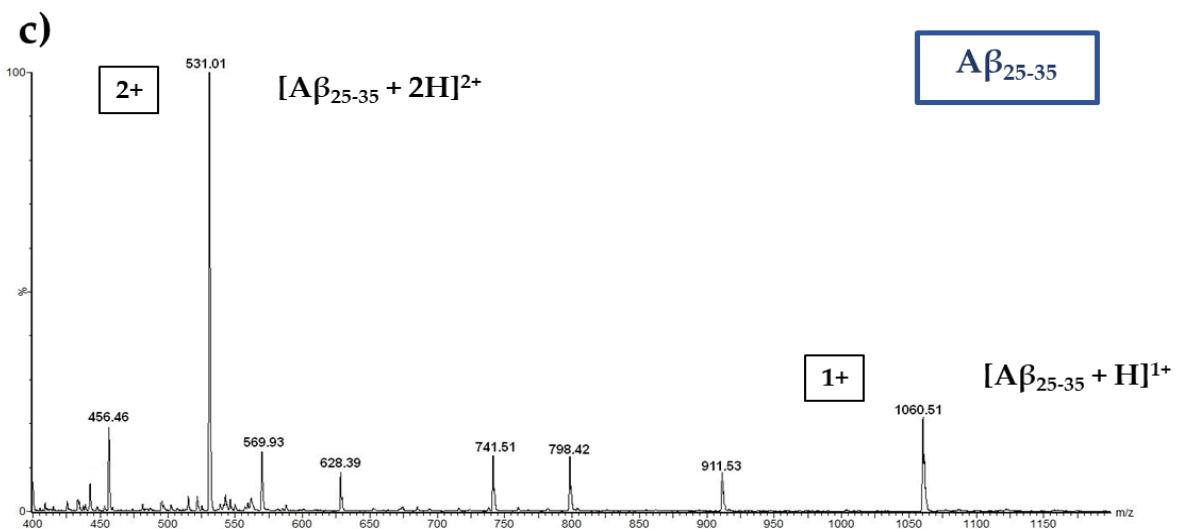
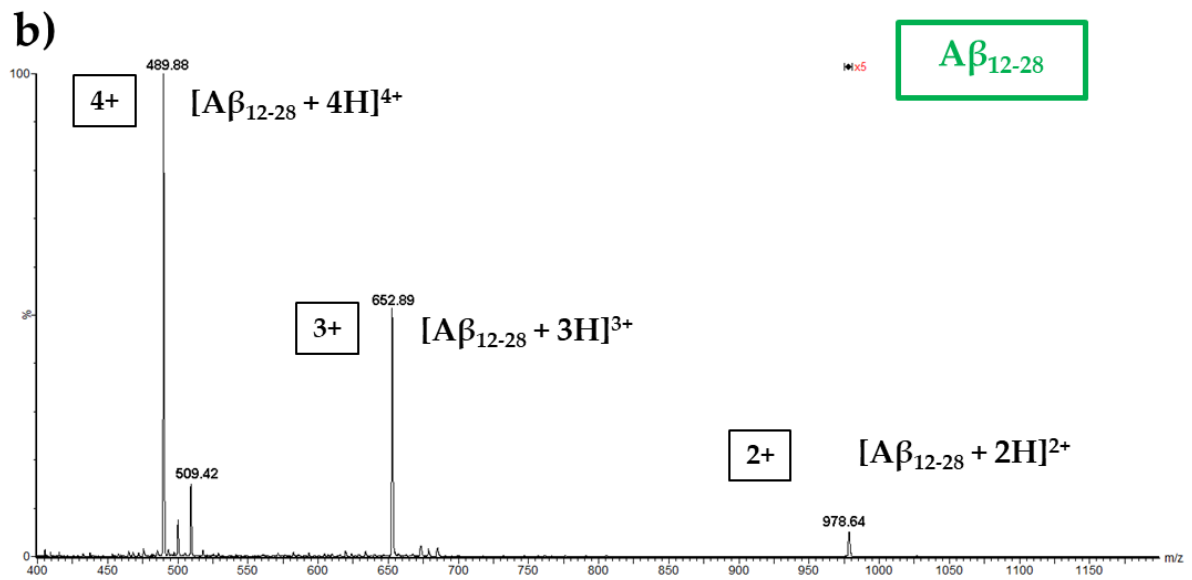
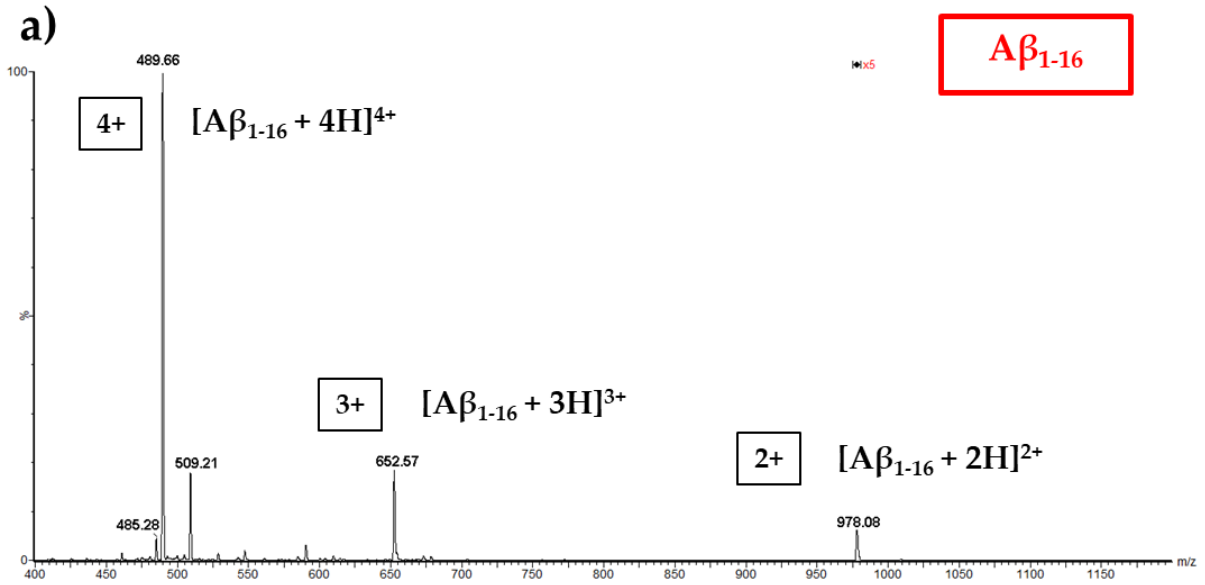
Sample was injected with a syringe pump (flow rate 10 $\mu\text{l}/\text{min}$) by electrospray ionization set in positive mode and the MS analysis was conducted as follows: capillary 3.2kV, cone 40V, extractor 5V, source and desolvation temperature 90°C and 130°C respectively.

The MS analysis shows peaks at m/z 866.64 and m/z 1083.15, the protonated compound of $[\text{A}\beta_{1-40} + 5\text{H}]^{5+}$ and $[\text{A}\beta_{1-40} + 4\text{H}]^{4+}$ respectively, the m/z 843.31 assigned to the $[\text{A}\beta_{1-39}+5\text{H}]^{5+}$ due to an impurity of the purchased sample. Lastly, the m/z 882.27 is ascribable to the DMSO adduct being this organic compound used for the preparation of $\text{A}\beta_{1-40}$ mother solution.

The structure of $[\text{A}\beta_{1-40} + 5\text{H}]^{5+}$ and $[\text{A}\beta_{1-40} + 4\text{H}]^{4+}$ were both confirmed by ESI-HRMS SYNAPT XS analysis (see Figure 54, panel c and d).

The MS analysis of $\text{A}\beta$ fragments $\text{A}\beta_{1-16}$, $\text{A}\beta_{12-28}$, $\text{A}\beta_{25-35}$, and $\text{A}\beta_{28-35}$ was conducted in the same manner of the $\text{A}\beta_{1-40}$ mass analysis, except for the concentration, which was of 5 μM in acetonitrile/water 1:1 + 0.1% FA. The resulting compound for each fragments are shown below:





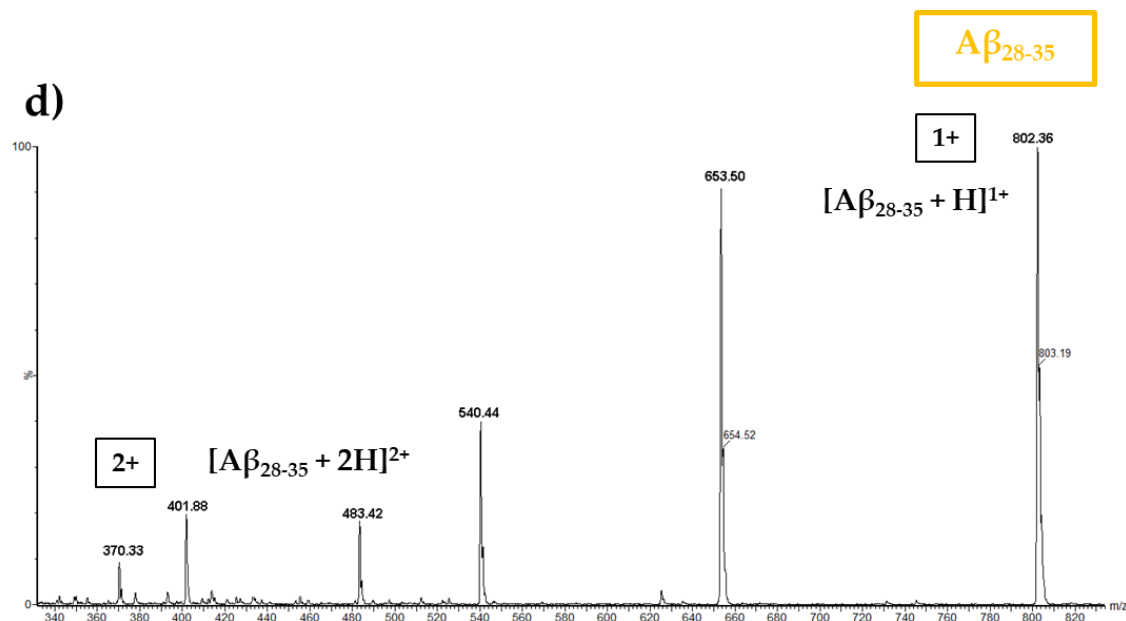


Figure 55 MS analysis of **a)** $A\beta_{1-16}$ (source parameters: capillary 3.2kV, cone 40V, extractor 5V); **b)** $A\beta_{12-28}$ (source parameters: capillary 3.2kV, cone 20V, extractor 5V) **c)** $A\beta_{25-35}$ (source parameters: capillary 3.2kV, cone 40V, extractor 5V); and **d)** $A\beta_{28-35}$ (source parameters: capillary 3.2kV, cone 40V, extractor 5V). All MS spectra were acquired with Quattro I and a flow rate of 10 μ l/min. In **a)** the peak at m/z 978.08 and **b)** the peak at m/z 978.64 are both magnified x5.

	Exp. Mass (m/z)	Theor. Mass (m/z)	Intensity (arb.u.)	Structure
$A\beta_{1-16}$	485.28	485.22	$6.15 \cdot 10^6$	$[A\beta_{1-16} - H_2O + 4H]^{4+}$
	489.66	489.72	$1.38 \cdot 10^8$	$[A\beta_{1-16} + 4H]^{4+}$
	509.21	509.23	$2.57 \cdot 10^7$	$[A\beta_{1-16} + DMSO + 4H]^{4+}$
	652.57	652.59	$2.59 \cdot 10^7$	$[A\beta_{1-16} + 3H]^{3+}$
	978.08	978.30	$1.74 \cdot 10^6$	$[A\beta_{1-16} + 2H]^{2+}$
$A\beta_{12-28}$	489.88	489.76	$9.39 \cdot 10^6$	$[A\beta_{12-28} + 4H]^{4+}$
	509.42	509.29	$1.41 \cdot 10^6$	$[A\beta_{12-28} + DMSO + 4H]^{4+}$
	652.89	652.63	$4.83 \cdot 10^6$	$[A\beta_{12-28} + 3H]^{3+}$
	978.64	978.40	$1.01 \cdot 10^5$	$[A\beta_{12-28} + 2H]^{2+}$
$A\beta_{25-35}$	456.46	456.38	$4.11 \cdot 10^6$	$[A\beta_{25-34} + 2H]^{2+}$
	531.01	530.94	$2.07 \cdot 10^7$	$[A\beta_{25-35} + 2H]^{2+}$
	569.93	569.98	$2.81 \cdot 10^6$	$[A\beta_{25-35} + DMSO + 2H]^{2+}$
	628.39	628.34	$1.83 \cdot 10^6$	$[A\beta_{25-31} + H]^+$
	741.51	741.43	$2.74 \cdot 10^6$	$[A\beta_{25-32} + H]^+$
	798.42	798.45	$2.60 \cdot 10^6$	$[A\beta_{25-33} + H]^+$
	911.53	911.53	$1.84 \cdot 10^6$	$[A\beta_{25-34} + H]^+$
	1060.51	1060.58	$4.47 \cdot 10^6$	$[A\beta_{25-35} + H]^+$

Aβ₂₈₋₃₅	370.33	370.25	2.37·10 ⁶	[A β ₂₈₋₃₁ + H] ⁺
	401.88	401.86	4.66·10 ⁶	[A β ₂₈₋₃₅ + 2H] ²⁺
	483.42	483.33	4.34·10 ⁶	[A β ₂₈₋₃₂ + H] ⁺
	540.44	540.35	9.57·10 ⁶	[A β ₂₈₋₃₃ + H] ⁺
	653.50	653.43	2.18·10 ⁷	[A β ₂₈₋₃₄ + H] ⁺
	802.36	802.49	2.37·10 ⁷	[A β ₂₈₋₃₅ + H] ⁺

Table 9 List peaks A β fragments proton ions. In the table are shown the experimental mass (from Quattro II analysis), the theoretical mass, the intensity and the structure proposed for each peak.

The MS analysis of A β ₁₋₁₆ and A β ₁₂₋₂₈ reveals the formation of several protonated compound up to 4 charges instead of the A β ₂₅₋₃₅ and A β ₂₈₋₃₅ fragments where the maximum accommodated charge is 2. This is due to the different peptide sequences, which have a different protonation capability. Lastly, other shorter fragments of the A β ₂₅₋₃₅ and A β ₂₈₋₃₅ peptides are also present as impurities in the investigated samples.

4.2.2. A β peptides + CuCl₂ complexes.

4.2.2.1. A β ₁₋₄₀ + CuCl₂

The interaction between the various A β fragments with copper chloride salt was investigated by ESI-Triple Quad (Quattro II). For this purpose, a solution of CuCl₂ was added to A β ₁₋₄₀ with a molar ratio of 3:1 (CuCl₂: A β) in acetonitrile/water (1:1) and 1%FA and the resulting solution was immediately analysed. The resulting spectrum and peaks list obtained from MS1 analysis are reported in Fig.56 (panel a) and have been assigned as reported in Table 10. Additionally, the assignment was confirmed through high-resolution analysis using ESI-HRMS SYNAPT XS (Fig. 56b and 56c).

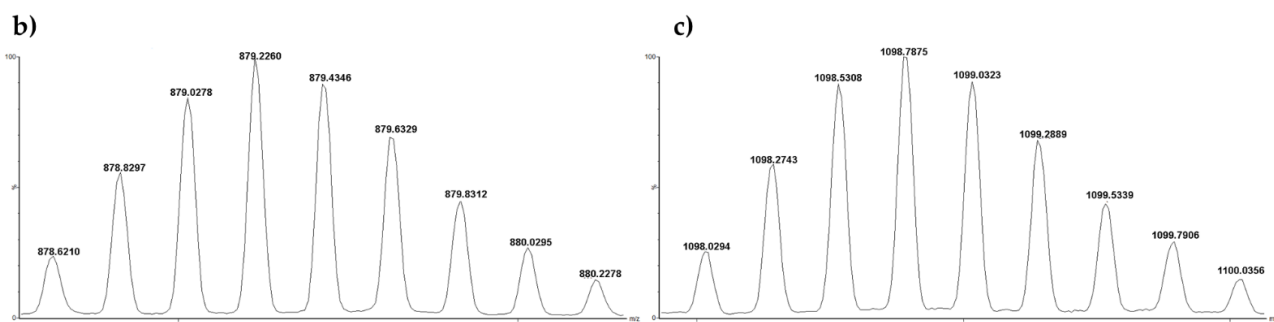
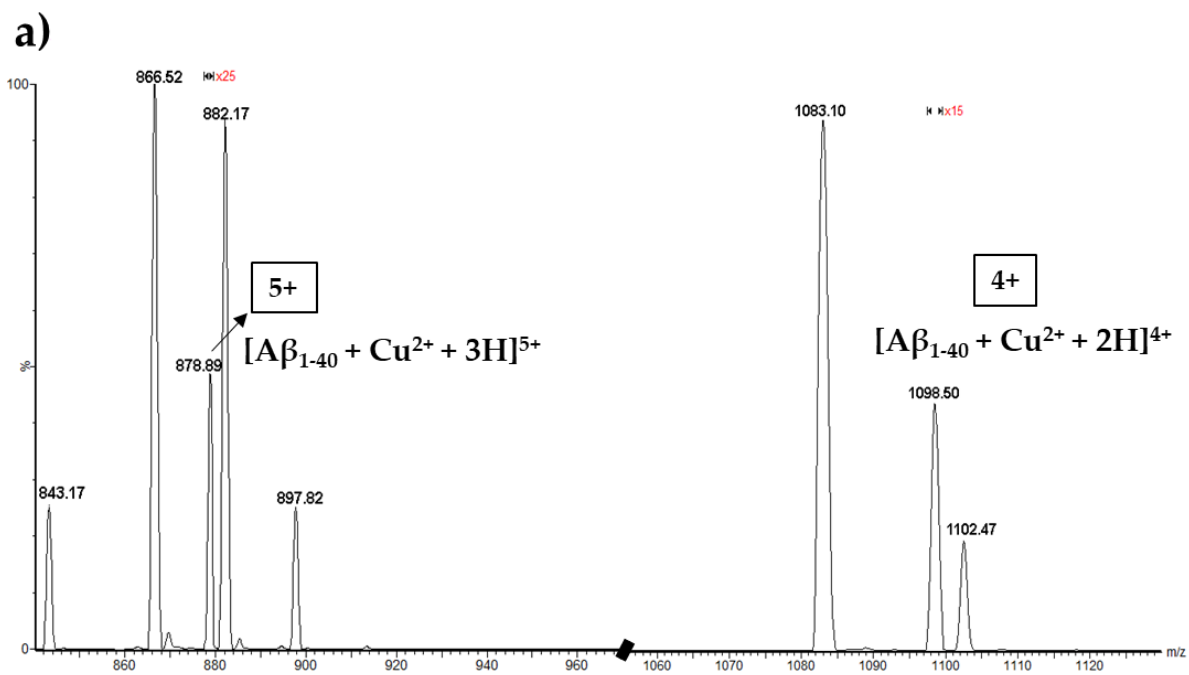


Figure 56 a) $A\beta_{1-40} + CuCl_2$ mass spectrum acquired in positive mode. The setup source parameters are capillary 3.2kV, cone 40V, extractor 5V. Flow rate 10 μ l/min. Peaks at m/z 878.89 and m/z 1098.50 are magnified x25 and x15 respectively. b) ESI-HRMS SYNAPT XS analysis of $[A\beta_{1-40} + Cu^{2+} + 3H]^{5+}$ and c) $[A\beta_{1-40} + Cu^{2+} + 2H]^{4+}$ proton ions.

Exp. Mass (m/z)	Theor. Mass (m/z)	Intensity (arb.u.)	Structure
878.89	879.22	$2.29 \cdot 10^5$	$[A\beta_{1-40} + Cu^{2+} + 3H]^{5+}$
1098.50	1098.77	$1.46 \cdot 10^5$	$[A\beta_{1-40} + Cu^{2+} + 2H]^{4+}$

Table 10 List peaks $A\beta_{1-40} + CuCl_2$. In the table are shown the experimental mass (from Quattro II analysis), the theoretical mass, the intensity and the structure proposed for each peak.

As showed above, under these conditions, $A\beta_{1-40}$ can form Cu^{2+} complexes through the coordination with one copper atom forming $[A\beta_{1-40} + Cu^{2+} + 3H]^{5+}$ and $[A\beta_{1-40} + Cu^{2+} + 2H]^{4+}$ for 5+ and 4+ charges respectively. However, repeating the experiment and analysing the sample after more than 2h of

incubation at room temperature, we can observe the rising of $[A\beta_{1-40} + 2Cu^{2+} + H]^{5+}$ and $[A\beta_{1-40} + 2Cu^{2+}]^{4+}$ corresponding to the coordination of 2 copper atoms with the $A\beta_{1-40}$ peptide. This suggests that by changing the incubation time, different species can be observed. Moreover, while 2 hours are needed to observe the bis-copper species in acidic conditions, only few minutes are sufficient at physiological pH.

This interesting result is explained by considering the competition between the H proton (from FA) and the copper ions. Indeed, the addition of FA obstacles the complexation of the second copper ion by $A\beta_{1-40}$. However, the addition of FA increases the stability of all peaks allowing an easier analysis. Table 11 and Fig. 57 show a detailed comparison of the MS results obtained at acidic and neutral conditions.

Theor. Mass (m/z)	Intensity (+1%FA) (arb.u.)	Intensity (no FA) (arb.u.)	Structure
866.84	$1.18 \cdot 10^7$	$6.19 \cdot 10^5$	$[A\beta_{1-40} + 5H]^{5+}$
879.22	$2.29 \cdot 10^5$	$4.10 \cdot 10^5$	$[A\beta_{1-40} + Cu^{2+} + 3H]^{5+}$
1083.29	$4.68 \cdot 10^6$	$1.24 \cdot 10^6$	$[A\beta_{1-40} + 4H]^{4+}$
1098.77	$1.46 \cdot 10^5$	$1.72 \cdot 10^6$	$[A\beta_{1-40} + Cu^{2+} + 2H]^{4+}$

Table 11 List peaks of $A\beta_{1-40}$ peptide with and without the addition of FA. In the table are shown the experimental mass (from Quattro II analysis), the theoretical mass, the intensity and the structure proposed for each peak. The setup sources for both experiments are i) capillary 3.2kV, cone 25V, and extractor 5V (with FA) and ii) Setup source parameters are capillary 3.2kV, cone 40V and extractor 5V (without FA). The resolution and the multiplier for both experiments are 14 and 700 respectively.

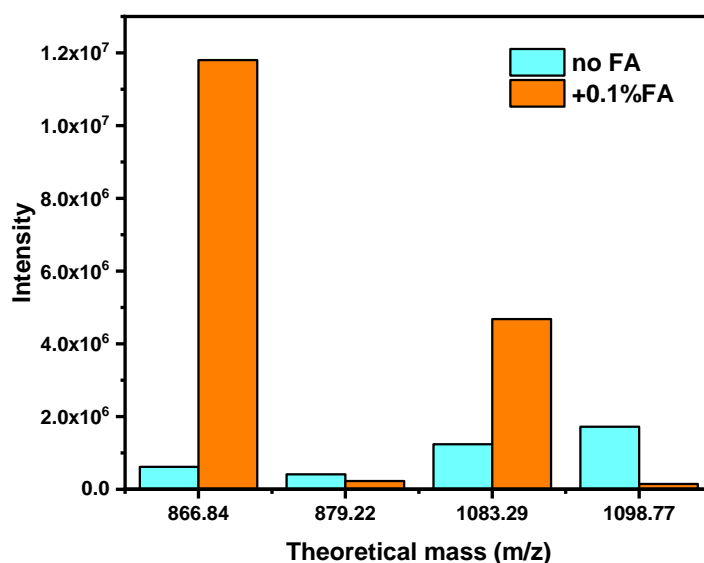


Figure 57 Histogram of $A\beta_{1-40}$ -copper complexes without Fa (in turquoise) and with the 0.1% FA (orange)

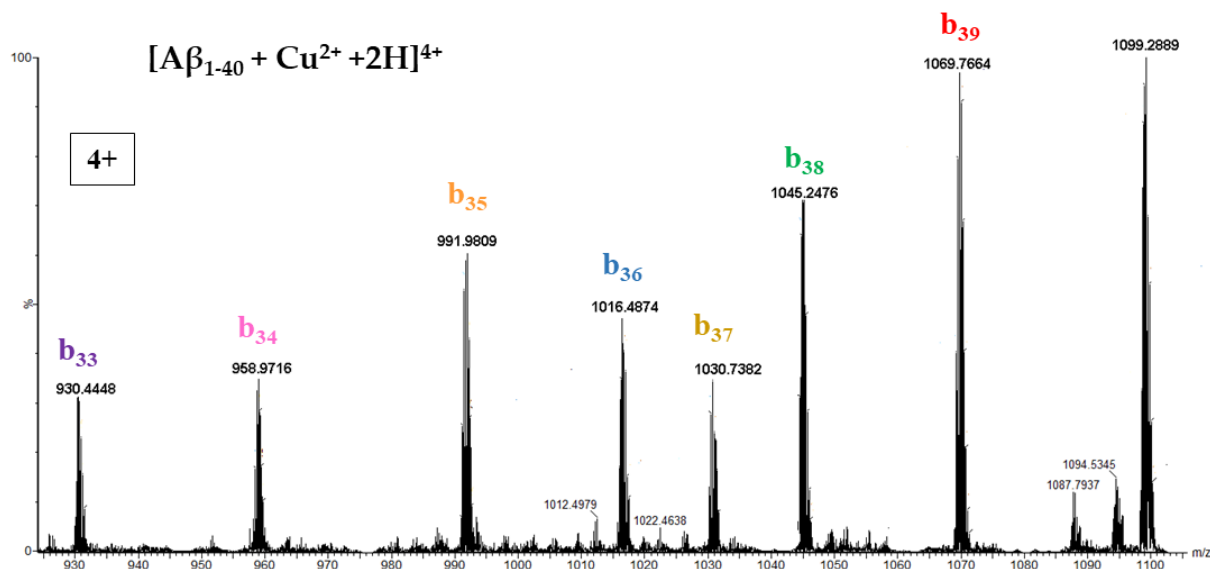


Figure 58 MS2 of $[A\beta_{1-40} + Cu^{2+} + 2H]^{4+}$. The setup parameters (ESI-HRMS SYNAPT XS) are capillary 3kV, cone 70V, source offset 5V, Source temperature 150°C, Desolvation Temperature 200°C, Cone Gas Flow 70.0 L/Hr, Desolvation Gas Flow 500.0 L/Hr, and Nebuliser Gas Flow 5.5 Bar.

The MS2 analysis of $[A\beta_{1-40} + Cu^{2+} + 2H]^{4+}$ (Figure 58, peaks list displayed in Table 12) reveals that the peptide fragmentation mainly occurs on the hydrophobic side, where cleavages from the 39th to the 33rd amino acid are observed. All product ions are Cu^{2+} complexes whose assignments, confirmed by ESI-HRMS SYNAPT XS analysis, are m/z 1069.7664 ($[A\beta_{1-39} + Cu^{2+} + 2H]^{4+}$), m/z 1045.2476 ($[A\beta_{1-38} + Cu^{2+} + 2H]^{4+}$), m/z 1030.7382 ($[A\beta_{1-37} + Cu^{2+} + 2H]^{4+}$), m/z 1016.4874 ($[A\beta_{1-36} + Cu^{2+} + 2H]^{4+}$), m/z 991.9809 ($[A\beta_{1-35} + Cu^{2+} + 2H]^{4+}$), m/z 958.9716 ($[A\beta_{1-34} + Cu^{2+} + 2H]^{4+}$), and m/z 930.4448 ($[A\beta_{1-33} + Cu^{2+} + 2H]^{4+}$).

This result confirms the copper propensity to be located in the first 30 aa, where the strongest coordination with the side chains of His, Arg, Lys and N-terminal amine function takes place.

Exp. Mass (m/z)	Cleavage	Structure
1069.7664	b_{39}^{++++}	$[A\beta_{1-39} + Cu^{2+} + 2H]^{4+}$
1045.2476	b_{38}^{++++}	$[A\beta_{1-38} + Cu^{2+} + 2H]^{4+}$
1030.7382	b_{37}^{++++}	$[A\beta_{1-37} + Cu^{2+} + 2H]^{4+}$
1016.4874	b_{36}^{++++}	$[A\beta_{1-36} + Cu^{2+} + 2H]^{4+}$
991.9809	b_{35}^{++++}	$[A\beta_{1-35} + Cu^{2+} + 2H]^{4+}$
958.9716	b_{34}^{++++}	$[A\beta_{1-34} + Cu^{2+} + 2H]^{4+}$
930.4448	b_{33}^{++++}	$[A\beta_{1-33} + Cu^{2+} + 2H]^{4+}$

Table 12 List peaks of $[A\beta_{1-40} + Cu^{2+} + 2H]^{4+}$ product ions. In the table are shown the experimental mass from ESI-HRMS SYNAPT XS analysis, the cleavage site, and both structures proposed for each peak.

4.2.2.2. $A\beta_{1-16} + CuCl_2$

The $A\beta$ fragment corresponding to the first 16th amino acid has been analysed in the presence of copper chloride salt. The solution was prepared from a stock solution of $A\beta_{1-16}$ in DMSO, added with a solution of $CuCl_2$ to attain a final concentration of $5\mu M$ of $A\beta_{1-16}$ and $15\mu M$ of $CuCl_2$ (molar ratio of 1:3) in acetonitrile/water (1:1) and 1%FA. The resulting solution was immediately analysed. The $A\beta_{1-16} + CuCl_2$ mass spectrum was acquired with an ESI-Triple Quad (Quattro II) (Figure 59), and the list of experimental $A\beta_{1-16}$ -Cu complexes peaks are shown in Table 13 with their assignment.

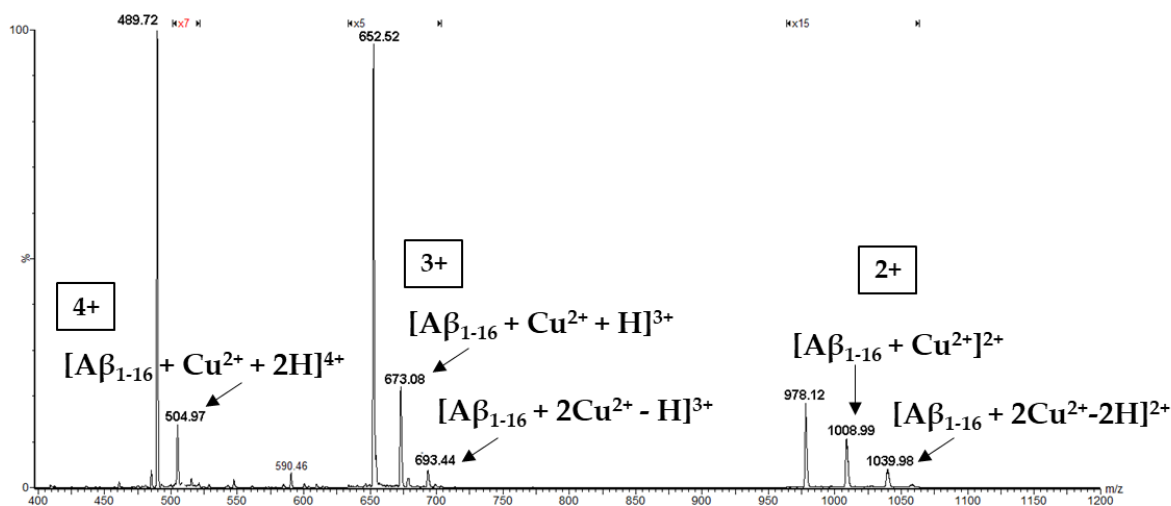


Figure 59 $A\beta_{1-16} + CuCl_2$ mass spectrum acquired in positive mode. The setup source parameters are capillary 3.2kV, cone 40V, extractor 5V. Flow rate 10 μ l/min. The peak at m/z 504.97 is magnified $\times 7$, peaks at m/z 652.52, m/z 673.08, m/z 693.44 are magnified $\times 5$, and peaks at m/z 978.12, m/z 1008.99, m/z 1039.98 are magnified $\times 15$.

Exp. Mass (m/z)	Theor. Mass (m/z)	Intensity (arb.u.)	Structure
504.97	505.06	$2.61 \cdot 10^6$	$[A\beta_{1-16} + Cu^{2+} + 2H]^{4+}$
673.08	673.08	$5.84 \cdot 10^6$	$[A\beta_{1-16} + Cu^{2+} + H]^{3+}$
693.44	693.50	$1.00 \cdot 10^6$	$[A\beta_{1-16} + 2Cu^{2+} - H]^{3+}$
1008.99	1009.04	$9.36 \cdot 10^5$	$[A\beta_{1-16} + Cu^{2+}]^{2+}$
1039.98	1039.90	$3.52 \cdot 10^5$	$[A\beta_{1-16} + 2Cu^{2+} - 2H]^{2+}$

Table 13 List peaks $A\beta_{1-16} + CuCl_2$. In the table are shown the experimental mass (from Quattro II analysis), the theoretical mass, the intensity and the structure proposed for each peak.

The hydrophilicity of this portion of the peptide guarantees to catch both protons and copper ions for complex formation, indeed, the MS spectrum shows the formation of several $A\beta_{1-16}$ -Cu complexes at 4, 3 and 2 charges. In addition, complexes with two copper ions have been observed for the 3rd and 2nd charges, i.e., m/z 693.44 ($[A\beta_{1-16} + 2Cu^{2+} - H]^{3+}$) and m/z 1039.98 ($[A\beta_{1-16} + 2Cu^{2+} - 2H]^{2+}$) respectively.

The MS2 of $[A\beta_{1-16} + 2Cu^{2+} - H]^{3+}$ (Figure 60) was analysed by means of ESI-HRMS SYNAPT XS in order to identify the copper site inside the $A\beta_{1-16}$ structure. The analysis shows preferred *b* cleavages (m/z 685.2272 b_{11}^{++} cut, m/z 510.6638 b_8^{++} cut, m/z 467.1459 b_7^{++} cut and, m/z 409.1369 b_6^{++} cut) in the middle of the primary sequence, followed by an a_6 cut with the loss of CO group (m/z 395.1389) and a c_9 cut (m/z 547.6872). Moreover, an uncommon x cut (m/z 350.0630) in the end of the sequence was also observed.

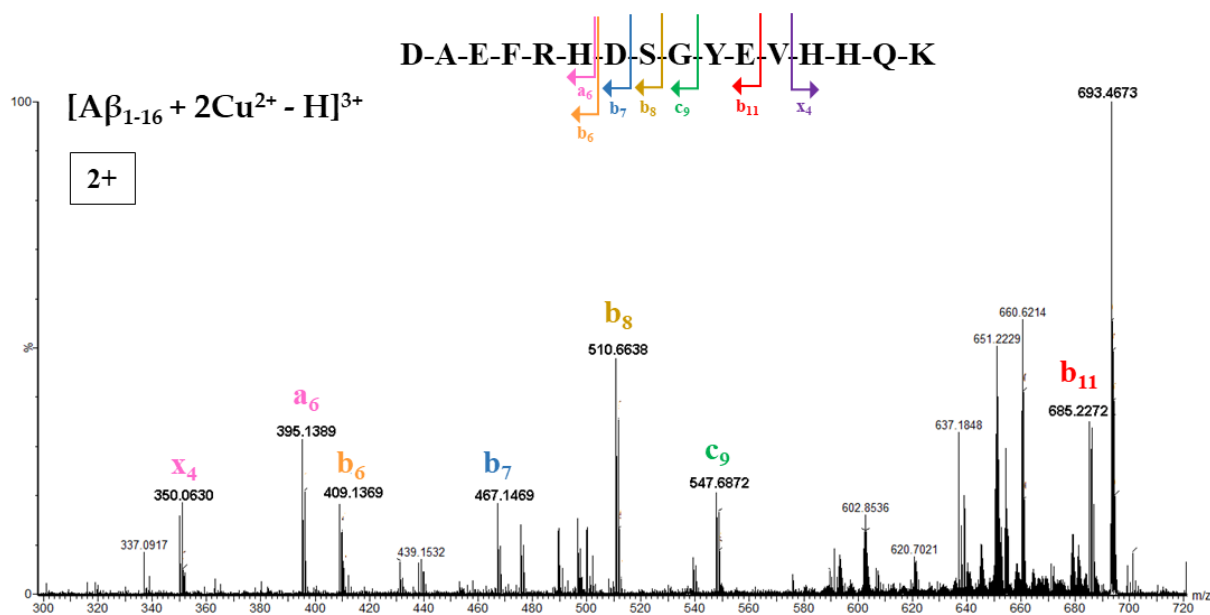


Figure 60 MS2 of $[A\beta_{1-16} + 2Cu^{2+} - H]^{3+}$. The setup parameters (ESI-HRMS SYNAPT XS) are capillary 3kV, cone 30V, source offset 5V, Source temperature 100°C, Desolvation Temperature 130°C, Cone Gas Flow 70.0 L/Hr, Desolvation Gas Flow 500.0 L/Hr, and Nebuliser Gas Flow 5.5 Bar.

The high resolution of ESI-HRMS SYNAPT XS allows us to assess the *i*) type of cleavage occurring, *ii*) total charge of the compound formed and, *iii*) number of copper ions present in the complex. Although we cannot know the exact mechanism occurring during the complex formation, we can hypothesize the assignment for each product ions where both homolytic and heterolytic cleavages can be considered. In the first case, a radical compound is formed, and we can consider the formation of an organometallic compound, otherwise a simple coordination between the specific $A\beta$ site and the copper ion occurs.

Exp. Mass (m/z)	Cleavage	Structure
685.2272	b_{11}^{++}	$[A\beta_{1-11} + Cu^+ + H^+]^{2+}$
547.5872	c_9^{++}	$[A\beta_{1-9} + Cu^+ + H^+]^{2+}$
510.6638	b_8^{++}	$[A\beta_{1-8} + Cu^{2+} - H]^{2+}$
467.1469	b_7^{++}	$[A\beta_{1-7} + Cu^{2+} - H]^{2+}$
409.1369	b_6^{++}	$[A\beta_{1-6} + Cu^{2+}]^{2+}$

395.1389	a_6^{++}	$[(A\beta_{1-6} - CO) + Cu^{2+}]^{2+}$
350.0630	x_4^{++}	$[A\beta_{13-16} + Cu^{2+} + Cu^+ - H^+]^{2+}$ or $[A\beta_{13-16} + 2Cu^+ - H^+]^{2+}$

Table 14 List peaks of $[A\beta_{1-16} + 2Cu^{2+} - H]^{3+}$ product ions. In the table are shown the experimental mass from ESI-HRMS SYNAPT XS analysis, the cleavage site, and the structure proposed for each peak.

Unlike the *a*, *b*, and *c* cleavage sites, which display only one copper ion in the complexes, the x_4^{++} cleavage shows a short fragment where two copper ions seem to be caught by the peptide. Despite the peculiarity of the formed complex, the structure was confirmed comparing the experimental isotopic pattern with the theoretical one of the structures hypothesized.

4.2.2.3. $A\beta_{12-28} + CuCl_2$

The interaction between the $A\beta_{12-28}$ fragment and the copper ions was explored adding a solution of $CuCl_2$ to the $A\beta_{12-28}$ to attain a final molar ratio of 3:1 in acetonitrile/water (1:1) and 1%FA and the resulting solution was investigated by ESI-Triple Quad (Quattro II).

The MS spectrum shown in Fig.61 displays the binding of Cu^{2+} to $A\beta_{12-28}$, producing species with several charges and with one or even two copper ions as for $[A\beta_{12-28} + 2Cu^{2+} - H]^{3+}$ (m/z 693.49) and $[A\beta_{12-28} + 2Cu^{2+} - 2H]^{2+}$ (m/z 1039.98) (Table 15).

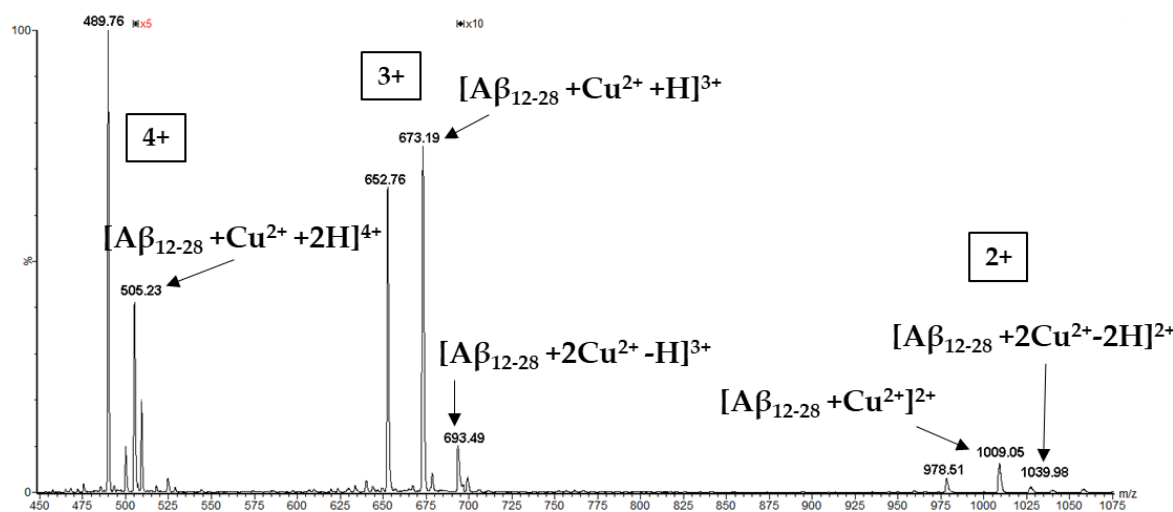


Figure 61 $A\beta_{12-28} + CuCl_2$ mass spectrum acquired in positive mode. The setup source parameters are capillary 3.2kV, cone 20V, extractor 5V. Peaks at m/z 505.23 and m/z 693.49 are magnified $\times 5$ and $\times 10$ respectively.

Exp. Mass (m/z)	Theor. Mass (m/z)	Intensity (arb.u.)	Structure
505.23	505.13	$1.25 \cdot 10^6$	$[A\beta_{12-28} + Cu^{2+} + 2H]^{4+}$
673.19	673.13	$1.14 \cdot 10^7$	$[A\beta_{12-28} + Cu^{2+} + H]^{3+}$

693.49	693.66	$1.53 \cdot 10^5$	$[\text{A}\beta_{12-28} + 2\text{Cu}^{2+} - \text{H}]^{3+}$
1009.05	1009.15	$9.51 \cdot 10^5$	$[\text{A}\beta_{12-28} + \text{Cu}^{2+}]^{2+}$
1039.98	1039.97	$7.26 \cdot 10^4$	$[\text{A}\beta_{12-28} + 2\text{Cu}^{2+} - 2\text{H}]^{2+}$

Table 15 List peaks $\text{A}\beta_{12-28} + \text{CuCl}_2$. In the table are shown the experimental mass (from Quattro II analysis), the theoretical mass, the intensity, and the structure proposed for each peak. Flow rate 10 $\mu\text{l}/\text{min}$.

A similar behaviour was found for the $\text{A}\beta_{1-16}\text{-CuCl}_2$ complexes. This is due to a partial hydrophilic nature of the $\text{A}\beta_{12-28}$ primary sequence, which is more prompt to catch more than one copper ion.

In order to localize the binding site of copper in the $\text{A}\beta_{12-28}$ sequence, the MS2 of the $[\text{A}\beta_{12-28} + \text{Cu}^{2+} + \text{H}]^{3+}$ compound was analysed by ESI-HRMS SYNAPT XS (Figure 62). The product ions obtained by the fragmentation of $[\text{A}\beta_{12-28} + \text{Cu}^{2+} + \text{H}]^{3+}$ are reported in Table 16.

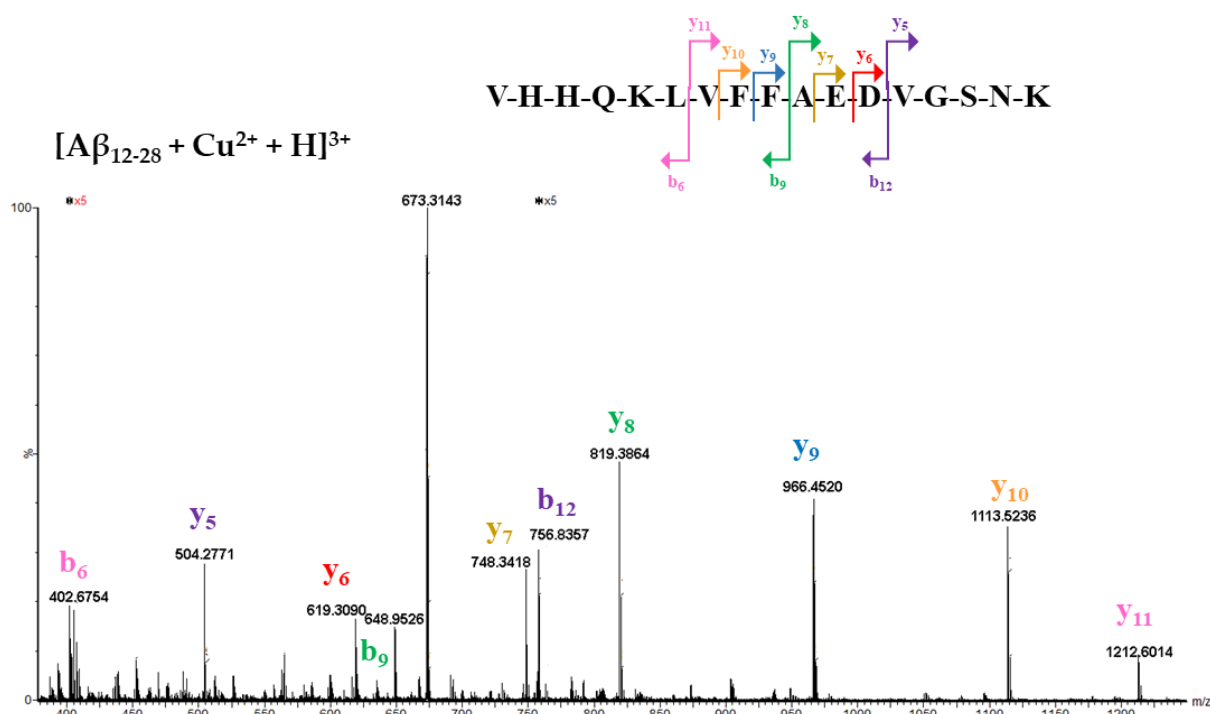


Figure 62 MS2 of $[\text{A}\beta_{12-28} + \text{Cu}^{2+} + \text{H}]^{3+}$. The setup parameters (ESI-HRMS SYNAPT XS) are capillary 3kV, cone 30V, source offset 5V, Source temperature 100°C, Desolvation Temperature 130°C, Cone Gas Flow 70.0 L/Hr, Desolvation Gas Flow 500.0 L/Hr, and Nebuliser Gas Flow 5.5 Bar. Peaks at m/z 402.6754 and m/z 756.8357 are both magnified $\times 5$.

Exp. Mass (m/z)	Cleavage	Structure
504.2771	y_5^+	$[\text{A}\beta_{24-28} + \text{H}]^+$
756.8357	b_{12}^{++}	$[\text{A}\beta_{12-23} + \text{Cu}^{2+}]^{2+}$
619.3090	y_6^+	$[\text{A}\beta_{23-28} + \text{H}]^+$
748.3418	y_7^+	$[\text{A}\beta_{22-28} + \text{H}]^+$

819.3854	y_8^+	$[A\beta_{21-28} + H^+]^+$
634.8063	b_9^{++}	$[A\beta_{12-20} + Cu^{2+}]^{2+}$
966.4520	y_9^+	$[A\beta_{20-28} + H^+]^+$
1113.5236	y_{10}^+	$[A\beta_{19-28} + H^+]^+$
1212.6014	y_{11}^+	$[A\beta_{18-28} + H^+]^+$
402.6754	b_6^{++}	$[A\beta_{12-17} + Cu^{2+} - H\cdot]^{2+}$
648.9526	x_{16}^{+++} or $C_4H_{10}N$ loss	$[A\beta_{13-28} + Cu^{2+} + H^+]^{3+}$ $[(A\beta_{13-28} - C_4H_{10}N) + Cu^{2+} + H^+]^{3+}$

Table 16 List peaks of $[A\beta_{12-28} + Cu^{2+} + H]^{3+}$ product ions. In the table are shown the experimental mass from ESI-HRMS SYNAPT XS analysis, the cleavage site, and the structure proposed for each peak.

The analysis shows progressive y cleavages with the production of singly-charged species of the middle section of the peptide. In the case of y_5 (m/z 504.2771, $[A\beta_{24-28} + H^+]^+$), y_8 (m/z 819.3854, $[A\beta_{21-28} + H^+]^+$) and y_{11} (m/z 1212.6014, $[A\beta_{18-28} + H^+]^+$) cleavages, complementary NH_2 -fragments were also found, namely the b_{12} (m/z 756.8357, $[A\beta_{12-23} + Cu^{2+}]^{2+}$), b_9 (m/z 634.8063, $[A\beta_{12-20} + Cu^{2+}]^{2+}$) and b_6 (m/z 402.6754, $[A\beta_{12-17} + Cu^{2+} - H\cdot]^{2+}$) respectively.

The structures proposed for each peak, confirmed by the comparison between the experimental isotopic pattern with the theoretical one, suggest a clean charge separation between the protonated portion and the section binding the copper ion, except for the shorter fragment (b_6) where a homolytic cleavage seems to occur.

Moreover, according to the type of fragments produced, the copper-binding site is located in the first 6 amino acids as confirmed by the compound $[A\beta_{12-17} + Cu^{2+} - H\cdot]^{2+}$ (b_6). This could be associated with the hydrophilic amino acids collocated in the first peptide sequence and with the presence of histidine residues (in the 13th and 14th position) which are well-known copper binding sites because of the imidazole group.

Lastly, the m/z 648.9526 corresponds to the Δ loss of 72 Da which could be either the production of an x_{16}^{+++} fragment ($[A\beta_{13-28} + Cu^{2+} + H^+]^{3+}$) or the loss of $C_4H_{10}N$ from the side chain of the lysine residue in 16th or 28th position.

4.2.2.4. $A\beta_{25-35} + CuCl_2$

For MS analysis of $A\beta_{25-35}$ -Cu, a defined aliquot of copper chloride salt was added to a solution of $A\beta_{25-35}$ peptide to achieve a final concentration of 15 μ M and 5 μ M respectively (3:1 in acetonitrile/water (1:1) and 1%FA).

The final solution was immediately analysed and injected with a syringe pump into the ESI source for the acquisition of the MS spectrum by ESI-Triple Quad (Quattro II). The MS spectrum and $A\beta_{25-35}$ -Cu complexes formed are displayed in Fig.63 and Table 17.

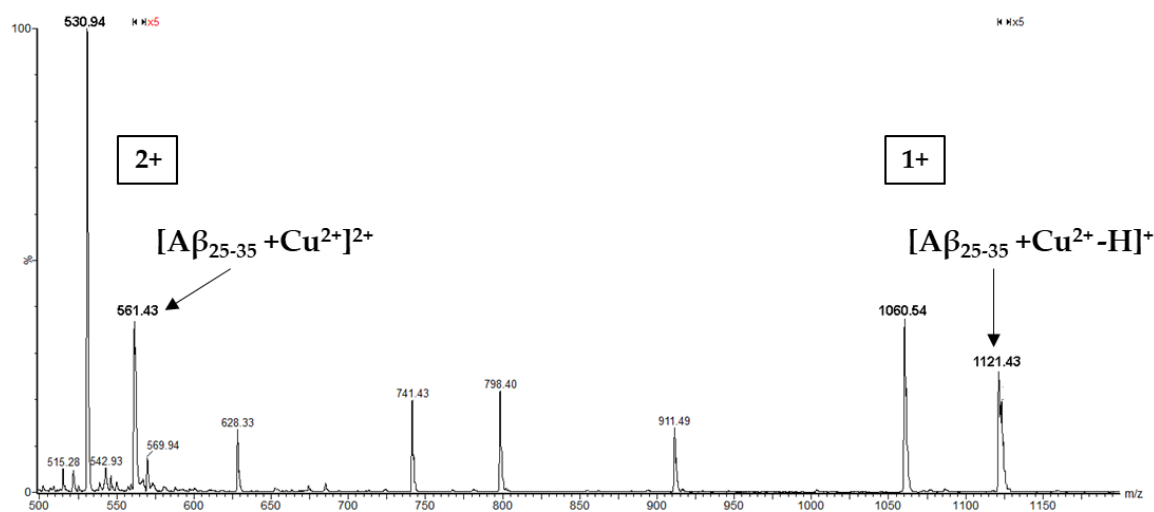


Figure 63 $A\beta_{25-35} + CuCl_2$ mass spectrum acquired in positive mode. The setup source parameters are capillary 3.2kV, cone 40V, extractor 5V. Flow rate 10 μ l/min. Peaks at m/z 561.43 and m/z 1121.43 are both magnified x5.

Exp. Mass (m/z)	Theor. Mass (m/z)	Intensity (arb.u.)	Structure
561.43	561.43	$1.23 \cdot 10^6$	$[A\beta_{25-35} + Cu^{2+}]^{2+}$
1121.43	1121.50	$8.71 \cdot 10^5$	$[A\beta_{25-35} + Cu^{2+} - H]^+$

Table 17 List peaks $A\beta_{25-35} + CuCl_2$. In the table are shown the experimental mass (from Quattro II analysis), the theoretical mass, the intensity, and the structure proposed for each peak.

The MS spectrum shows the formation of two copper complexes: m/z 561.43 and m/z 1121.43 corresponding to the $[A\beta_{25-35} + Cu^{2+}]^{2+}$ and $[A\beta_{25-35} + Cu^{2+} - H]^+$ compound respectively. The MS2 analysis of the latter was acquired, by the use of ESI-HRMS SYNAPT XS (Figure 64), in order to identify the portion of the peptide responsible of the copper ion binding. The resulting product ions, obtained from the $[A\beta_{25-35} + Cu^{2+} - H]^+$ fragmentation, are listed in Table 18.

The peaks observed in the mass spectrum reveal a preponderance of *b* cleavages followed by *a* cleavages characterized by the loss of a CO group. All peaks are singly positive charged and are assigned to a copper-peptide complex. The latter is confirmed by the comparison between the experimental isotopic patterns and the theoretical ones, which both show the typical shape of a copper-based complex.

Indeed, the neutral loss between two close peaks corresponds to the sequential loss of amino acids and the survey of the copper complex on the NH_2 -peptide side.

The formation of the shorter fragment, the b_4 $[\text{A}\beta_{25-28} + \text{Cu}^{2+} - \text{H}]^+$ related to the sequence glycine-serine-asparagine-lysine, suggests the copper arrangement in the first four amino acids. This is supported by the presence of the lysine residue and the other close NH_2 group that play a crucial role in the coordination with copper.

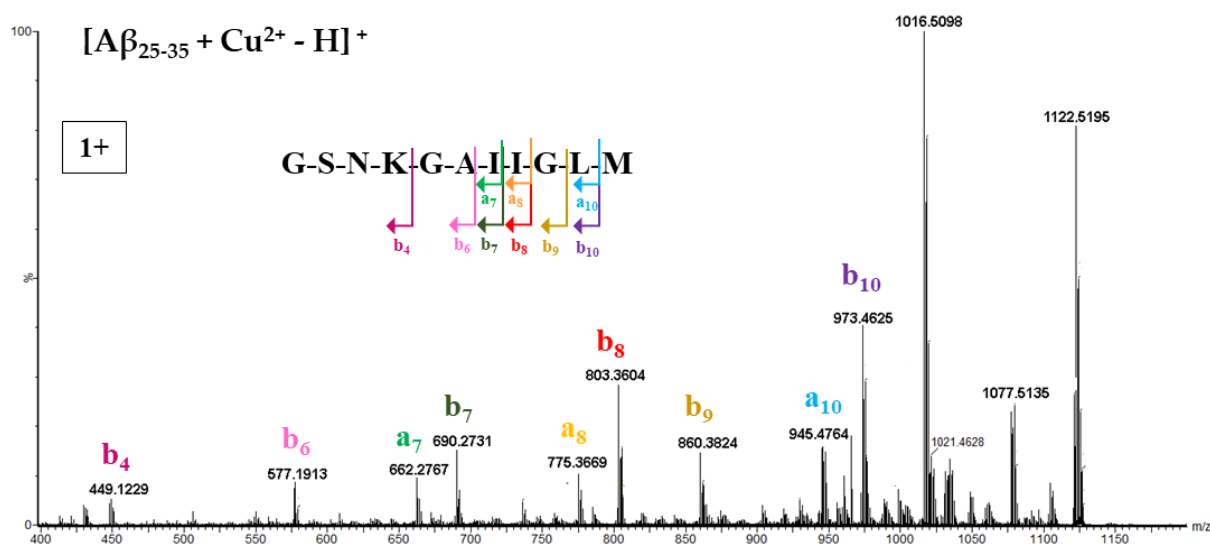


Figure 64 MS2 of $[\text{A}\beta_{25-35} + \text{Cu}^{2+} - \text{H}]^+$. The setup parameters (ESI-HRMS SYNAPT XS) are capillary 3.5kV, cone 100V, source offset 5V, Source temperature 100°C, Desolvation Temperature 130°C, Cone Gas Flow 100.0 L/Hr, Desolvation Gas Flow 600.0 L/Hr, and Nebuliser Gas Flow 4.7 Bar.

Lastly, the peaks at m/z 1077.5135 and m/z 1016.5098 are not correlated to cleavages of the principal chain of the peptide, but rather to the loss of organic molecules, such as the CO_2 loss for the m/z 1077.5135. In case of m/z 1016.5098, the neutral loss of 106 Da is assigned to either $\text{C}_3\text{H}_6\text{O}_2\text{S}$ or $\text{C}_4\text{H}_{10}\text{OS}$. However, the $\Delta m/z$ calculated between the $\text{C}_3\text{H}_6\text{O}_2\text{S}$ theoretical m/z or $\text{C}_4\text{H}_{10}\text{OS}$ theoretical m/z and the experimental peaks are not the same ($\Delta m/z = 0.0144$ and $\Delta m/z = 0.0508$ for $\text{C}_3\text{H}_6\text{O}_2\text{S}$ and $\text{C}_4\text{H}_{10}\text{OS}$ respectively) and indicate the $\text{C}_3\text{H}_6\text{O}_2\text{S}$ loss more probable than the $\text{C}_4\text{H}_{10}\text{OS}$ one. Nevertheless, both choices are notable and would consider a rearrangement of the methionine residue as a consequence of the fragmentation.

Exp. Mass (m/z)	Cleavage	Structure
1077.5135	CO_2 loss	$[(\text{A}\beta_{25-35} - \text{CO}_2) + \text{Cu}^{2+} - \text{H}]^+$
1016.5098	$\text{C}_3\text{H}_6\text{O}_2\text{S}$ loss	$[(\text{A}\beta_{25-35} - \text{C}_3\text{H}_6\text{O}_2) + \text{Cu}^{2+} - \text{H}]^+$
	$\text{C}_4\text{H}_{10}\text{OS}$ loss	$[(\text{A}\beta_{25-35} - \text{C}_4\text{H}_{10}\text{OS}) + \text{Cu}^{2+} - \text{H}]^+$
973.4625	b_{10}^+	$[\text{A}\beta_{25-34} + \text{Cu}^{2+} - \text{H}]^+$
945.4764	a_{10}^+	$[(\text{A}\beta_{25-34} - \text{CO}_2) + \text{Cu}^{2+} - \text{H}]^+$
860.3824	b_9^+	$[\text{A}\beta_{25-33} + \text{Cu}^{2+} - \text{H}]^+$

803.3604	b_8^+	$[\text{A}\beta_{25-32} + \text{Cu}^{2+} - \text{H}]^+$
775.3669	a_8^+	$[(\text{A}\beta_{25-32} - \text{CO}_2) + \text{Cu}^{2+} - \text{H}]^+$
690.2731	b_7^+	$[\text{A}\beta_{25-31} + \text{Cu}^{2+} - \text{H}]^+$
662.2767	a_7^+	$[(\text{A}\beta_{25-31} - \text{CO}_2) + \text{Cu}^{2+} - \text{H}]^+$
577.1913	b_6^+	$[\text{A}\beta_{25-30} + \text{Cu}^{2+} - \text{H}]^+$
449.1229	b_4^+	$[\text{A}\beta_{25-28} + \text{Cu}^{2+} - \text{H}]^+$

Table 18 List peaks of $[\text{A}\beta_{25-35} + \text{Cu}^{2+} - \text{H}]^+$ product ions. In the table are shown the experimental mass from ESI-HRMS SYNAPT XS analysis, the cleavage site, and both structures proposed for each peak.

4.2.2.5. $\text{A}\beta_{28-35} + \text{CuCl}_2$

As for the previous $\text{A}\beta$ fragments, even the shorter $\text{A}\beta_{28-35}$, localized in the hydrophobic region of the $\text{A}\beta_{1-40}$ peptide, was added with copper chloride salt. Indeed, in order to investigate the interaction between this peptide portion and the metal, a solution made up of $\text{A}\beta_{28-35}$ (5 μM) and CuCl_2 (15 μM) (3:1 in acetonitrile/water (1:1) and 1%FA) was directly injected into the ESI source for the acquisition of the MS spectrum by ESI-Triple Quad (Quattro II).

The resulting MS spectrum (Figure 65) and the analysis of the peaks (Table 19) are shown below.

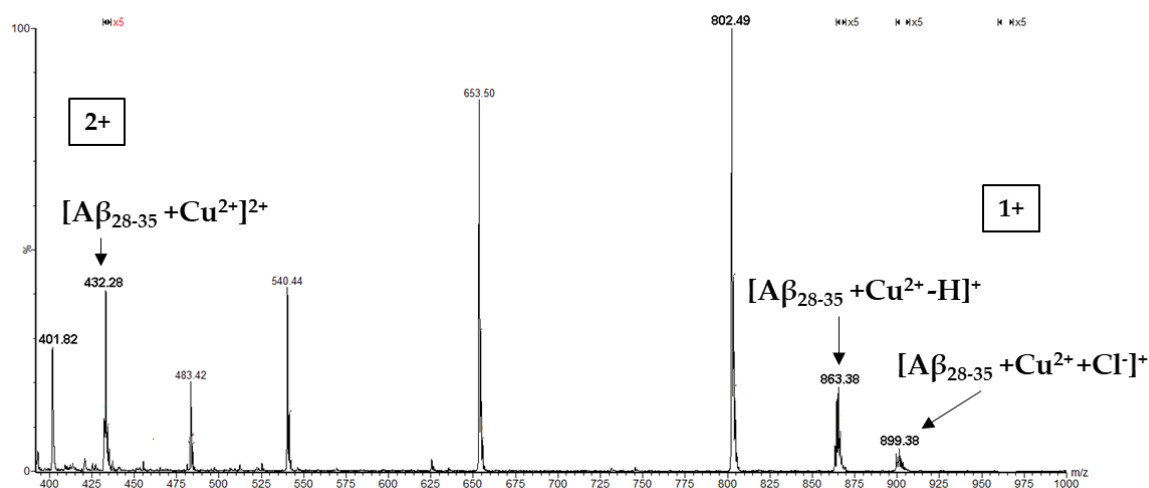


Figure 65 $\text{A}\beta_{28-35} + \text{CuCl}_2$ mass spectrum acquired in positive mode. The setup source parameters are capillary 3.2kV, cone 40V, extractor 5V. Flow rate 10 $\mu\text{l}/\text{min}$. Peaks at m/z 432.28, m/z 863.38 and m/z 899.38 are all magnified x5.

The MS spectrum reports the formation of three copper complexes: m/z 432.28, m/z 863.38, and m/z 899.38 corresponding to the $[\text{A}\beta_{28-35} + \text{Cu}^{2+}]^{2+}$, $[\text{A}\beta_{28-35} + \text{Cu}^{2+} - \text{H}]^+$, and the $[\text{A}\beta_{28-35} + \text{Cu}^{2+} - \text{Cl}]^+$, compound respectively.

Exp. Mass (m/z)	Theor. Mass (m/z)	Intensity (arb.u.)	Structure
432.28	432.26	$9.60 \cdot 10^5$	$[\text{A}\beta_{28-35} + \text{Cu}^{2+}]^{2+}$
863.38	863.40	$6.69 \cdot 10^5$	$[\text{A}\beta_{28-35} + \text{Cu}^{2+} - \text{H}]^+$
899.38	899.38	$1.17 \cdot 10^5$	$[\text{A}\beta_{28-35} + \text{Cu}^{2+} + \text{Cl}]^+$

Table 19 List peaks $\text{A}\beta_{28-35} + \text{CuCl}_2$. In the table are shown the experimental mass (from Quattro II analysis), the theoretical mass, the intensity and the structure proposed for each peak.

In order to localize the copper-binding site inside the $\text{A}\beta$ peptide (28-35) sequence, the MS2 analysis of the $[\text{A}\beta_{28-35} + \text{Cu}^{2+} - \text{H}]^+$ was acquired, by the use of ESI-HRMS SYNAPT XS (Figure 66). The resulting fragments are exposed in Table 20.

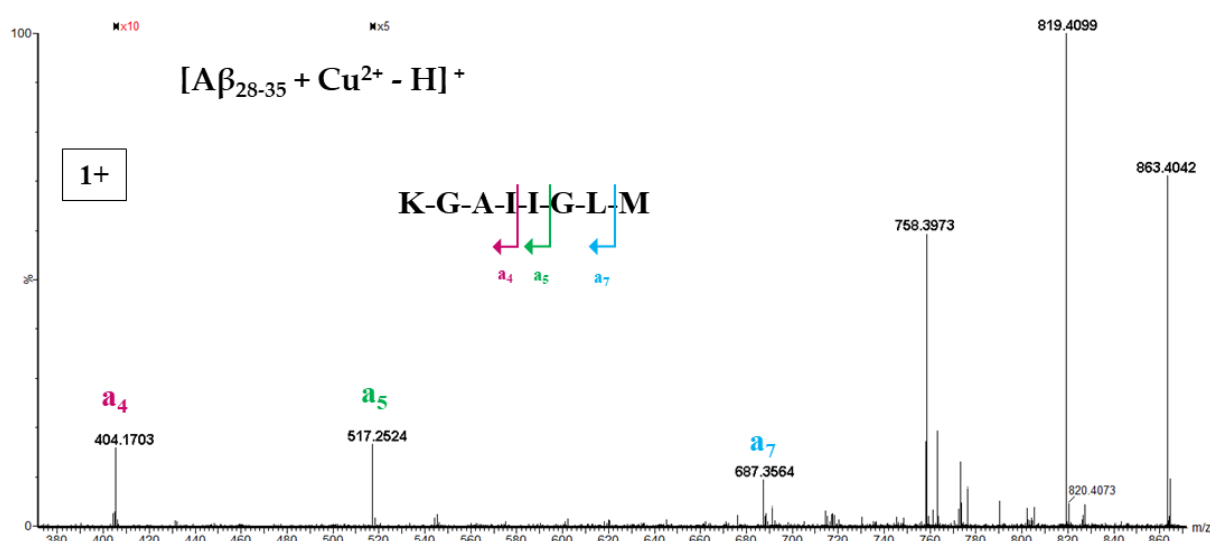


Figure 66 MS2 of $[\text{A}\beta_{28-35} + \text{Cu}^{2+} - \text{H}]^+$. The setup parameters (ESI-HRMS SYNAPT XS) are capillary 3.5kV, cone 80V, source offset 10V, Source temperature 100°C, Desolvation Temperature 130°C, Cone Gas Flow 70.0 L/Hr, Desolvation Gas Flow 500.0 L/Hr, and Nebuliser Gas Flow 5.5 Bar. Peaks at m/z 404.1703, and m/z 517.2524 are magnified x10 and x5 respectively.

Exp. Mass (m/z)	Cleavage	Structure
819.4099	CO_2 loss	$[(\text{A}\beta_{28-35} - \text{CO}_2) + \text{Cu}^{2+} - \text{H}]^+$
758.3973	$\text{C}_3\text{H}_6\text{O}_2\text{S}$ loss	$[(\text{A}\beta_{28-35} - \text{C}_3\text{H}_6\text{O}_2) + \text{Cu}^{2+} - \text{H}]^+$
	$\text{C}_4\text{H}_{10}\text{OS}$ loss	$[(\text{A}\beta_{28-35} - \text{C}_4\text{H}_{10}\text{OS}) + \text{Cu}^{2+} - \text{H}]^+$
687.3564	a_7^+	$[(\text{A}\beta_{28-34} - \text{CO}_2) + \text{Cu}^{2+} - \text{H}]^+$
517.2524	a_5^+	$[(\text{A}\beta_{28-32} - \text{CO}_2) + \text{Cu}^{2+} - \text{H}]^+$
404.1703	a_4^+	$[(\text{A}\beta_{28-31} - \text{CO}_2) + \text{Cu}^{2+} - \text{H}]^+$

Table 20 List peaks of $[\text{A}\beta_{28-35} + \text{Cu}^{2+} - \text{H}]^+$ product ions. In the table are shown the experimental mass from ESI-HRMS SYNAPT XS analysis, the cleavage site, and both structures proposed for each peak.

Differently from the A β peptide (25-35), here the type of cleavage observed is *a*, i.e., between methionine and leucine (a_7^+), between isoleucine and glycine (a_5^+), and between the two isoleucine (a_4^+). These series of cleavages appear even in the fragmentation of $[\text{A}\beta_{28-35} + \text{Cu}^{2+} - \text{H}]^+$ and they correspond to the b_{10}^+ , b_8^+ , and b_7^+ respectively.

An analogy between the A β_{25-35} and A β_{28-35} is the same neutral loss observed for the peaks at m/z 758.3973 (A β_{28-35}) and the peak at m/z 1016.5098 belonging to the A β_{25-35} peptide. Indeed, even in this case, the loss of either C₃H₆O₂S or C₄H₁₀OS were considered. The $\Delta m/z$ calculated for the loss of C₃H₆O₂S clearly lower ($\Delta m/z = 0.0017$) than the $\Delta m/z$ calculated for the loss of C₄H₁₀OS ($\Delta m/z = -0.0347$), makes the loss of C₃H₆O₂S more probable.

The presence of the short a_4^+ fragment, a copper-based complex, indicates that copper ions can bind even to this portion of the A β peptide. Comparing this fragment with the shorter one of the A β_{25-35} , the two peptides have in common the lysine in position 28. This confirms the key role of this amino acid in the coordination with copper ion.

4.2.3. A β peptides + O₂ molecules.

In order to investigate the interaction between amyloid peptides and the oxygen molecules, each peptide fragment (A β_{1-16} , A β_{12-28} , A β_{25-35} , and A β_{28-35}) as well as A β_{1-40} , were analyzed after being ionized and mixed in the gas phase with oxygen molecules.

The innovation of this technique is the ability to explore this type of interaction by the introduction of oxygen gas in one or more sections located before the mass analyser.

The experimental set up foresaw the introduction of oxygen molecules in the hexapole H0, where these molecules can interact with the sample coming from the source.

The analysis of A β_{1-40} with oxygen molecules was performed by preparing a solution A β_{1-40} (1 μ M) in acetonitrile/water (1:1) and 1%FA and exposed to the oxygen gas (at $4 \cdot 10^{-5}$ mbar) inserted in the (H0) 2. The resulting MS spectrum is shown in Fig.67.

By comparing the protonated MS spectrum of A β_{1-40} (Figure 54) with the MS spectrum of A $\beta_{1-40} + \text{O}_2$ (Figure 67), it is clear that a new peak at m/z 1107.60 ($I = 2.26 \cdot 10^5$ arb.u.) appears in the latter case.

Indeed, the assignment for this peak is hypothesized to be $[\text{A}\beta_{1-40} + 3\text{O}_2 + 4\text{H}]^{4+}$, considering the entrapment of three molecules of oxygen inside the folded A β_{1-40} (theoretical peak for this structure is at m/z 1107.43). Although the value of the peak is slightly shifted ($\Delta m/z = 0.17$) as compared to the value of the theoretical peak of the structure proposed (Figure 68), the mass deviation is congruous with the instrument calibration (see Figure 68).

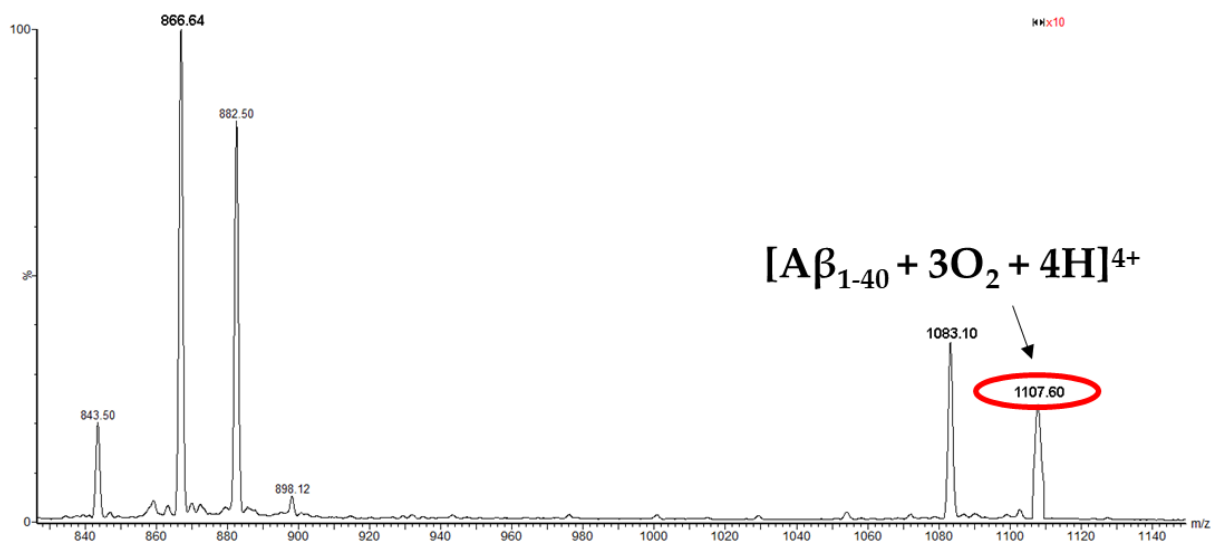


Figure 67 $A\beta_{1-40} + O_2$ mass spectrum acquired in positive mode. The setup source parameters are capillary 3.2kV, cone 40V, extractor 5V. Flow rate 10 μ l/min. Peaks at m/z 1107.60 is magnified x10.

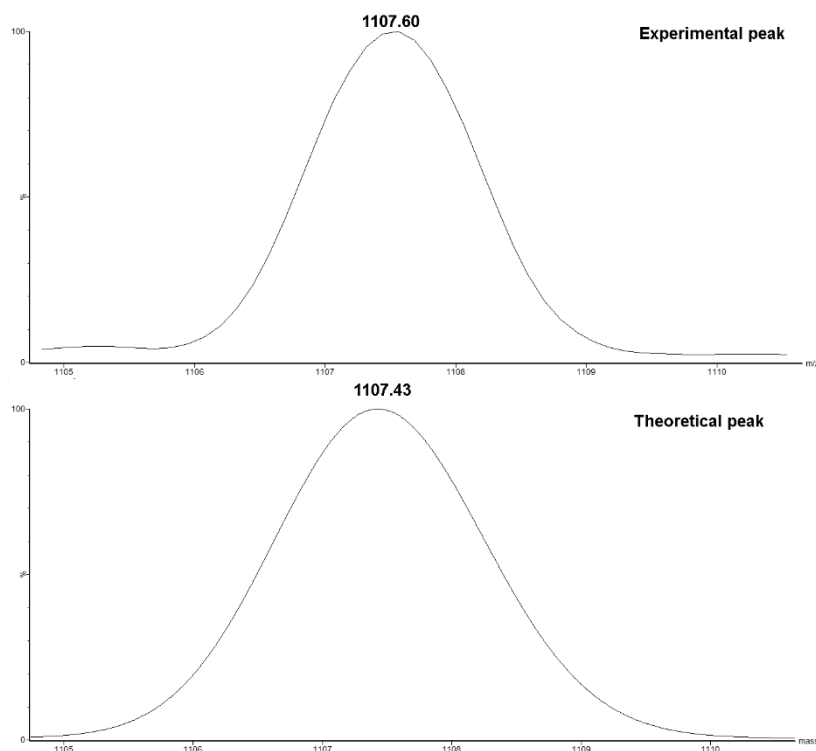


Figure 68 Comparison between the experimental and the theoretical peak. At the top the experimental mass spectrum, and at the bottom the peak of the structure proposed.

Actually, the real proof of the presence of oxygen molecules into the peptide structure is given by the MS2 of the $[A\beta_{1-40} + 3O_2 + 4H]^{4+}$. The MS2 spectrum and the list of product ions are shown in Fig. 69 and Table 21 respectively.

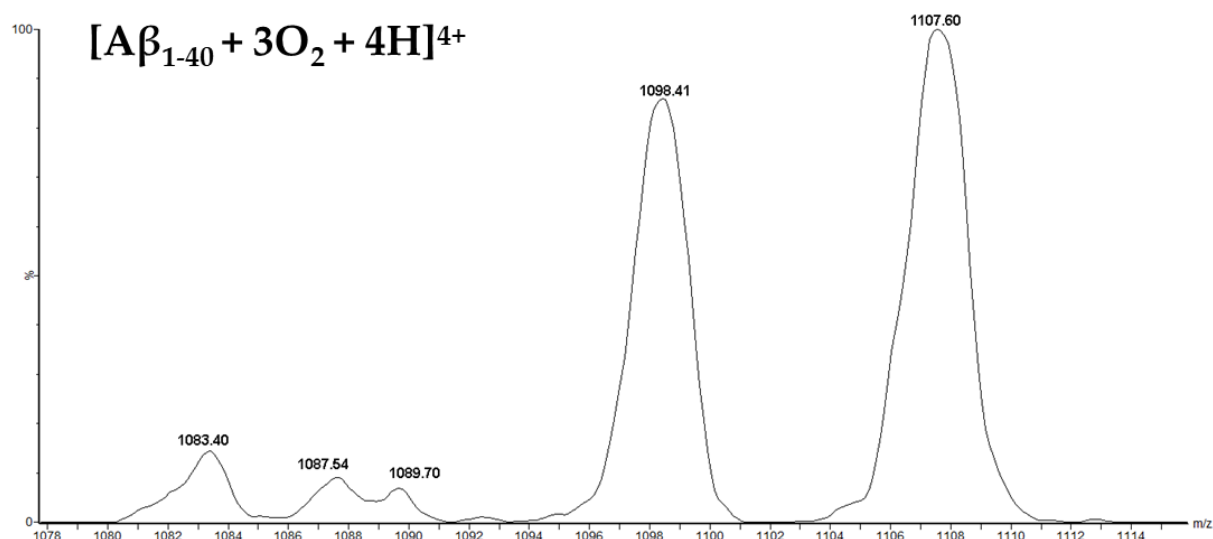


Figure 69 MS2 of $[A\beta_{1-40} + 3O_2 + 4H]^{4+}$. The setup source parameters are capillary 3.2kV, cone 40V, extractor 5V. Flow rate $10\mu\text{L}/\text{min}$. Acquired with ESI- Quattro II. $P_{\text{Arg}} = 2.6 \cdot 10^{-3}$ mbar.

Measured mass (m/z)	Proposed structure
1098.41	$[A\beta_{1-40} + 2O_2 + 4H]^{4+}$
1089.70	$[(A\beta_{1-40} + O_2 - C_3H_6NO) + 2O_2 + 4H]^{4+}$
1087.54	$[(A\beta_{1-40} - C_4H_4N_2) + 3O_2 + 4H]^{4+}$
1083.40	$[A\beta_{1-40} + 4H]^{4+}$

Table 21 Proposed structures for the product ions from the peak at m/z 1107.60 after MS/MS experiments (precursor ions assigned to $[A\beta_{1-40} + 3O_2 + 4H]^{4+}$). Source parameters were the same for all experiments: capillary 3.2 kV, cone 40 V, extractor 5 V, flow rate $10\mu\text{L}\cdot\text{min}^{-1}$.

All the peaks coming from the fragmentation of $[A\beta_{1-40} + 3O_2 + 4H]^{4+}$ have or release oxygen molecules. Moreover, this compound does not fragment anymore and leaves the last fragment produced intact, namely the protonated form of $A\beta_{1-40}$ ($[A\beta_{1-40} + 4H]^{4+}$).

The peak at m/z 1107.60 is formed during the interaction between $[A\beta_{1-40} + 4H]^{4+}$ and O_2 molecules. Interestingly, the peaks at m/z 1089.70 and m/z 1087.54 could be assigned only considering the losses of C_3H_6NO and $C_4H_4N_4$ molecules respectively. In the case of $C_4H_4N_4$ neutral loss, it may result from the deletion of the aromatic moiety after the rearrangement of methylimidazole from histidine residues. Concerning the loss of C_3H_6NO , it can be attributed to the existence of an oxidative process occurring in the $A\beta_{1-40}$ arrangement owing to the presence of oxygen molecules.

To determine if both losses are only related to an oxidation process occurring in $[A\beta_{1-40} + 3O_2 + 4H]^{4+}$, we performed the MS2 of $[A\beta_{1-40} + 4H]^{4+}$ (Figure 70).

Upon observing the MS2 of $[A\beta_{1-40} + 4H]^{4+}$ (Figure 70), we do not see a peak corresponding to the neutral loss of C_3H_6NO (equal to 72.04 Da), and to the neutral loss of $C_4H_4N_4$ (equal to 108.12 Da) (indicated by the empty red square in Figure 70 – no peaks in this range are present).

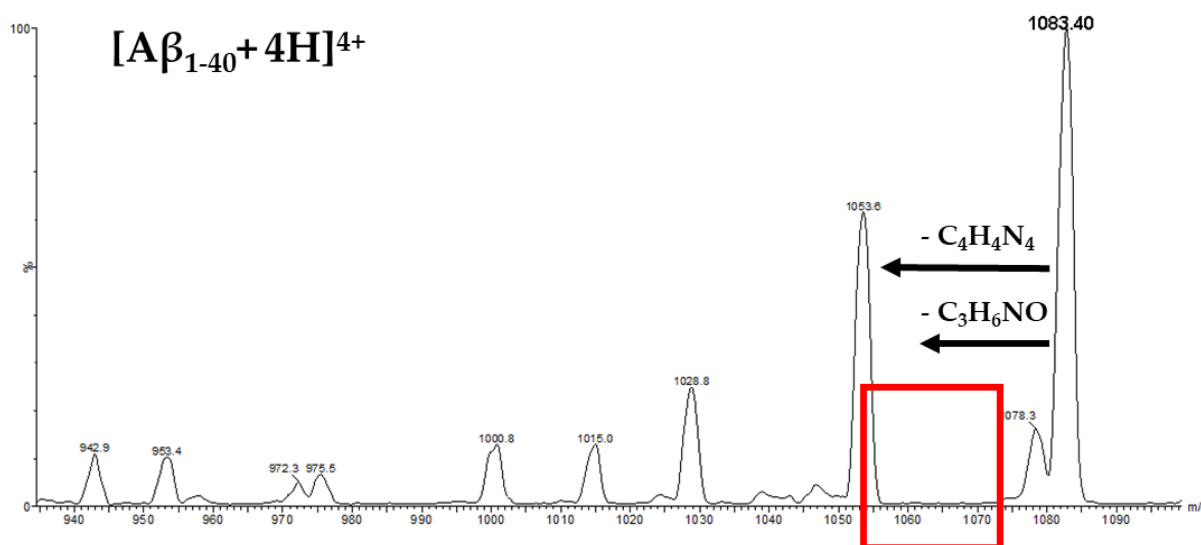


Figure 70 MS2 of $[A\beta_{1-40} + 4H]^{4+}$. The setup source parameters are capillary 3.2kV, cone 40V, extractor 5V. Flow rate 10 μ l/min. Acquired with ESI- Quattro II. $P_{Arg} = 2.6 \cdot 10^{-3}$ mbar.

Therefore, both losses seems to be typical of $[A\beta_{1-40} + 3O_2 + 4H]^{4+}$ fragmentation and entails that a chemical oxidation process occurring in $A\beta_{1-40}$.

In order to understand where the formation of $[A\beta_{1-40} + 3O_2 + 4H]^{4+}$ come from, several experiments with and without the insert of oxygen gas were performed. Indeed, two additional experiments were performed *i*) Helium in (H0) 1, and *ii*) Helium in (H0) 1 with O₂ in (H0) 2 at a pressure of $3.21 \cdot 10^5$ mbar and $4 \cdot 10^5$ mbar respectively (the pressure gauge is located at the end of (H0) 1 section, so in case of two gases, one in (H0) 1 and one in (H0) 2, the measured pressure is the sum of both gases). Helium is one of the smallest gas and is inert. Being inert, helium is relatively safe to use and does not react with any of the molecules inside the mass spectrometer, so it is a useful carrier gas. The analysis of *i*) and *ii*) experiments reveals the appearance of $[A\beta_{1-40} + 3O_2 + 4H]^{4+}$ even without the introduction of oxygen gas.

This crucial information suggests that this compound ($[A\beta_{1-40} + 3O_2 + 4H]^{4+}$) is formed in solution and not in the gas phase. However, without the introduction of oxygen and/or helium gases into the mass spectrometer, the detection of this compound cannot occur, due to the inherent instability of the compound. Indeed, the helium and oxygen's effect is to cool down the energy stored by the $[A\beta_{1-40} + 3O_2 + 4H]^{4+}$ inhibiting the fragmentation of this species before it can reach the detector.

In MS, the cooling down effect refers to the phenomenon where ions experience a decrease in kinetic energy, leading to a reduction in their velocity and subsequent cooling. This effect is particularly relevant in techniques such as CID or collisional activation, which are used for fragmentation studies.

By cooling down the ions, their internal energy decreases, leading to more controlled and specific fragmentation pathways. This allows for a clearer and more detailed understanding of the structure and composition of ions. Indeed, it has been shown that large use of He pressure can strongly decrease internal energy of ions stored^[385]. In the case of FT-ICR instruments, a very short pulse of He gas is also used as the ions enter the ICR cell in order to slow them down, decrease the size of ion cloud and increase the trapping efficiency^[386].

Hence, both oxygen and helium gases fulfil the role of carrier and stabilizing gas for the detection of unstable molecules; this is further supported by the increase in the intensity of DMSO adducts peaks. Indeed, when the helium and/or oxygen gas are inserted into the mass spectrometer, the intensity of DMSO adducts peaks arises, thus becoming a controller for the detection of metastable compounds. In Table 22 are shown the intensities of the $[A\beta_{1-40} + 3O_2 + 4H]^{4+}$ peak for all three experiments performed.

This result highlights a marked cooling down effect for helium gas as compared to oxygen gas.

Experiment	m/z 1107.60 Intensity/arb.u.	Pressure/ mbar
$A\beta_{1-40} + O_2$	$2.26 \cdot 10^5$	$P_{O_2} = 4 \cdot 10^{-5}$
$A\beta_{1-40} + He$	$2.45 \cdot 10^5$	$P_{He} = 3.21 \cdot 10^{-5}$
$A\beta_{1-40} + He + O_2$	$2.17 \cdot 10^5$	$P_{He+O_2} = 4.2 \cdot 10^{-5}$

Table 22 Intensities of $[A\beta_{1-40} + 3O_2 + 4H]^{4+}$ from ESI- Quattro II for the three experiments performed and the pressure for each gas introduced. Set up source parameters are the same for all of three experiments (are capillary 3.2kV, cone 40V, extractor 5V, flow rate $10 \mu\text{L} \cdot \text{min}^{-1}$).

Lastly, each experiment previously executed (only O_2 in (H0) 2, only He in (H0) 1, or both in (H0) 1 and 2) was also performed for all four $A\beta_{1-40}$ fragments ($A\beta_{1-16}$, $A\beta_{12-28}$, $A\beta_{25-35}$, and $A\beta_{28-35}$). Samples were prepared as follows: $5\mu\text{M}$ of peptide in acetonitrile/ water 1:1 and 0.1% of FA, and each one was handled with *i*) O_2 in (H0) 2, *ii*) helium in (H0) 1, and *iii*) helium in (H0) 1 with O_2 in (H0) 2 at a total pressure not higher than $4-4.5 \cdot 10^5$ mbar.

Interestingly, the MS spectra of all peptides, even in the presence of the gases before detection, do not display the presence of oxygen adducts, whereas they show DMSO adducts whose intensity increases as compared to the same pristine samples. This reinforces the hypothesis of the role assumed by the gases in stabilizing metastable compounds already present in solution and lowering their energy. At the same time the increase of DMSO adducts intensity suggests that no oxygen adducts produced by the shorter $A\beta$ fragments were formed in solution, otherwise the intensity of these peaks should have increased by the introduction of gases into the instrument.

As a consequence, all four A β ₁₋₄₀ fragments are not capable to catch oxygen molecules from the aqueous environment. This means that the formation of the peptide-oxygen adducts is peculiar for A β ₁₋₄₀, which is capable to accommodate and tightly coordinate oxygen molecules inside its structure. This is probably correlated to the specific A β ₁₋₄₀ structure, where two helical domains and a type I β -turn, with a hinge between the 25th – 27th amino acids^[160] are present, whereas A β ₁₋₁₆, A β ₁₂₋₂₈, A β ₂₅₋₃₅, and A β ₂₈₋₃₅ peptide chains do not have such a peculiar conformation because of their shorter chain length.

4.2.4. A β peptides + CuCl₂ + O₂ molecules.

The purpose of the last series of experiments was the interaction between A β peptides with copper and oxygen molecules when the latter is introduced into the mass spectrometer. The amyloid peptides chosen for the analysis were: the A β ₁₋₄₀ peptide, the A β ₁₋₁₆, and A β ₂₅₋₃₅ fragments for the hydrophilic and hydrophobic peptide sections respectively.

The MS spectrum of A β ₁₋₄₀ peptide + CuCl₂ + O₂ (Figure 71) was obtained by analyzing a solution of this peptide (5 μ M) and copper chloride (15 μ M) (3:1) in acetonitrile/water (1:1) and 1%FA, and the resulting sample was directly injected into the instrument for the impact with oxygen gas introduced in (H0) 2 section. The oxygen gas pressure was 3.8·10⁵ mbar.

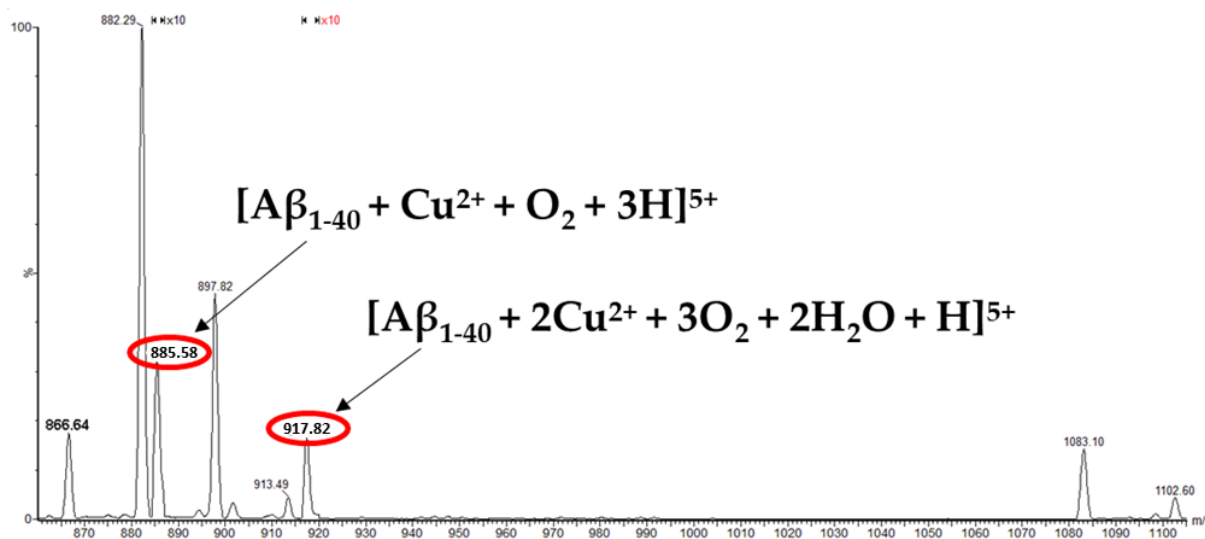


Figure 71 A β ₁₋₄₀ + CuCl₂ + O₂ mass spectrum acquired in positive mode. The setup source parameters are capillary 3.2kV, cone 40V, extractor 5V. Flow rate 10 μ l/min. Peaks at m/z 885.58 and m/z 917.82 are both magnified x10.

The analysis reveals the presence of two additional peaks: m/z 885.40 and m/z 917.82 both not present in A β ₁₋₄₀-Cu analysis (see Figure 56). The structures propose for both peaks are: [A β ₁₋₄₀ + Cu²⁺ + O₂ + 3H]⁵⁺ and [A β ₁₋₄₀ + 2Cu²⁺ + 3O₂ + 2H₂O + H]⁵⁺ respectively, where in both cases, it can be considered

the capture of oxygen molecules into the $A\beta_{1-40} - Cu$ complexes. The MS2 of: $[A\beta_{1-40} + Cu^{2+} + O_2 + 3H]^{5+}$ and $[A\beta_{1-40} + 2Cu^{2+} + 3O_2 + 2H_2O + H]^{5+}$ compounds are displayed in Fig.72.

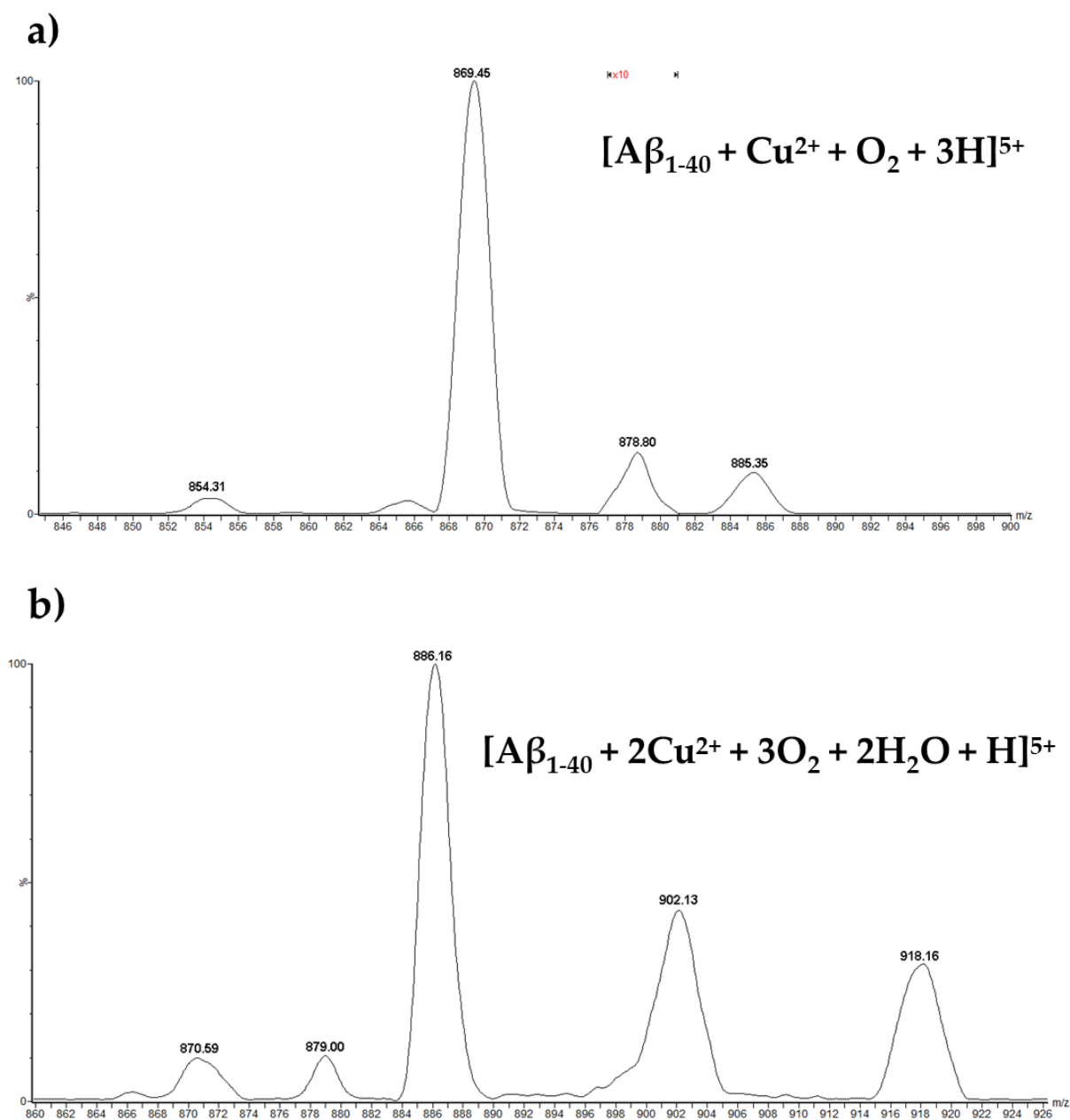


Figure 72 MS2 of **a)** $[A\beta_{1-40} + Cu^{2+} + O_2 + 3H]^{5+}$ and **b)** $[A\beta_{1-40} + 2Cu^{2+} + 3O_2 + 2H_2O + H]^{5+}$. The setup source parameters are capillary 3.2kV, cone 40V, extractor 5V in both cases. Flow rate 10 μ l/min. Acquired with ESI- Quattro II. $P_{Arg} = 1.8 \cdot 10^{-3}$ mbar. In a) the peak at m/z 878.80 is magnified x10.

The MS2 analysis of $[A\beta_{1-40} + Cu^{2+} + O_2 + 3H]^{5+}$ (Figure 72, panel a) reveals a prominent peak at m/z 878.80. This peak could correspond to the detachment of one oxygen molecule (O_2) and the subsequent formation of the $[A\beta_{1-40} + Cu^{2+} + 3H]^{5+}$ compound. Consequently, this finding would provide evidence for the presence of an oxygen adduct, suggesting that $A\beta_{1-40}$ binds to and coordinates with one oxygen molecule. On the contrary, the MS2 analysis of $[A\beta_{1-40} + 2Cu^{2+} + 3O_2$

+ 2H₂O + H]⁵⁺ uncovers two main peaks at m/z 902.13 and m/z 886.16. These peaks are due to a sequential neutral loss of 80 Da, which could be attributed to the loss of a C₄H₄N₂ molecule, indicating the removal of an aromatic compound coming from a rearrangement of methylimidazole from histidine residues. For the m/z 886.16, we have the loss of two C₄H₄N₂ molecules. Specifically, the m/z 886.16 peak corresponds to the detachment of two C₄H₄N₂ molecules. Consequently, when comparing the calculated $\Delta m/z$ between the theoretical peaks for the proposed compounds and their corresponding experimental peaks, we find the following values: *i*) $\Delta m/z = 0.40$ for m/z 878.80, *ii*) $\Delta m/z = 0.20$ for m/z 902.13, and *iii*) $\Delta m/z = 0.25$ for m/z 886.16.

As for the previous A β + O₂ experiments, we performed two additional experiments in order to better investigate the two oxygen adducts. For this purpose, He and/or O₂ gases were introduced into the mass spectrometer in (H0) 1 and (H0) 2 respectively.

Both adducts persisted even in the presence of helium gas, providing compelling evidence for their origin from the solution itself. This finding highlights that the compounds are not generated within the mass spectrometer itself but rather originate from the initial sample. Accordingly, it implies that the cooling effect of both helium and oxygen gases contributes to the preservation of these adducts throughout the experimental process.

In Table 23 the intensities of the [A β ₁₋₄₀ + Cu²⁺ + O₂ + 3H]⁵⁺ and the [A β ₁₋₄₀ + 2Cu²⁺ + 3O₂ + 2H₂O + H]⁵⁺ compounds for all three experiments are displayed.

Experiment	m/z 885.40 Intensity/ arb.u.	m/z 917.82 Intensity/ arb.u.	Pressure/ mbar
A β ₁₋₄₀ + CuCl ₂ + O ₂	7.13 · 10 ⁵	2.26 · 10 ⁵	P _{O₂} = 3.8 · 10 ⁻⁵
A β ₁₋₄₀ + CuCl ₂ + He	9.85 · 10 ⁵	6.10 · 10 ⁵	P _{He} = 4.2 · 10 ⁻⁵
A β ₁₋₄₀ + CuCl ₂ + He + O ₂	9.71 · 10 ⁵	5.31 · 10 ⁵	P _{He+O₂} = 5.3 · 10 ⁻⁵

Table 23 Intensities of [A β ₁₋₄₀ + Cu²⁺ + O₂ + 3H]⁵⁺ and [A β ₁₋₄₀ + 2Cu²⁺ + 3O₂ + 2H₂O + H]⁵⁺ from ESI- Quattro II for the three experiments performed and the value of gases pressures used. Set up source parameters are the same for all of three experiments (are capillary 3.2kV, cone 40V, extractor 5V, flow rate 10 μ l/min).

Similar to the previous case, the intensities of both peaks noticeably increase in the presence of helium, emphasizing the significant cooling effect exerted by helium. To confirm this, the intensities of DMSO adducts increase too as compared to the experiments carried out in absence of helium and/or oxygen gases.

Finally, these preliminary studies seem to suggest that copper does not play an active role in the coordination between the $A\beta_{1-40}$ and oxygen molecules. In such a scenario, the coordination would take place at a different location than the one specified for metal interaction.

Lastly, two $A\beta_{1-40}$ fragments, namely the $A\beta_{1-16}$ and the $A\beta_{25-35}$ were subjected to the treatment with oxygen gas. Samples were prepared in the same manner, i.e., 5 μ M of peptide, 15 μ M of $CuCl_2$ in acetonitrile/ water (1:1) and 0.1% of FA.

All performed experiments for both peptides do not show the appearance of oxygen adducts, whereas the intensities of DMSO adducts increase in presence of gases. This suggests that possible adducts have never formed in the solution.

This study provides further evidence supporting the capability of $A\beta_{1-40}$ to effectively coordinate oxygen molecules in solution. Furthermore, it highlights the impressive ability of helium and oxygen gases to minimize the energy stored by these species through their cooling down action, thereby facilitating their detection.

4.3. Final Remarks

In Chapter III, I reported on my research activity conducted at Université de Bretagne Occidentale in Brest (France) under the supervision of Prof. Antony Memboeuf. During this time, I had the opportunity to investigate the formation and detection of A β -oxygen adducts using a uniquely modified mass spectrometer designed specifically for this purpose.

The choice of substrate fell upon A β_{1-40} because it is easier to handle rather the more famous A β_{1-42} . I conducted an analysis of the full length A β_{1-40} both in the absence and in the presence of copper chloride to identify the amino acids involved in coordination processes.

The results suggest that the interaction between A β_{1-40} and copper chloride salt revealed the formation of Cu²⁺ complexes with the peptide, [A β_{1-40} + Cu²⁺ + 3H]⁵⁺ and [A β_{1-40} + Cu²⁺ + 2H]⁴⁺.

The results also demonstrate a preference of copper to be coordinated within the first thirty amino acids, where the hydrophilic portion of the peptide resides, demonstrating a robust coordination with the side chains of His, Arg, Lys, and the N-terminal amine residues. This was confirmed by the MS2 analysis of [A β_{1-40} + Cu²⁺ + 2H]⁴⁺ (Figure 58).

Nevertheless, certain metalloproteinases like IDE, NEP, and MMP-9 (see section 2.2) hold cleavage sites within the hydrophobic region of the full length A β_{1-40} , generating fragments whose biological role is still unknown. Therefore, I conducted a MS analysis of some A β fragments such as A β_{1-16} , A β_{12-28} , A β_{25-35} and A β_{28-35} with copper.

Shorter product ions, such as b_6^{++} (DAEFRH) and x_4^{++} (HHQK) for the [A β_{1-16} + 2Cu²⁺ -H]³⁺ fragmentation and b_6^{++} (VHHQKL) for the [A β_{12-28} + Cu²⁺ + H]³⁺ fragmentation, further confirm the high affinity of copper ions towards the hydrophilic part of the full-length A β peptide.

Based on the primary sequence of the shorter fragments obtained, Asp1, Ala2, His6, 13 and 14, turn out to be the favourite amino acid residues for copper binding, as confirmed by literature^[353-356,387].

Interestingly, the MS analysis carried out on the shorter fragments (A β_{25-35} and A β_{28-35}) localized in the hydrophobic side of the full-length A β_{1-40} reveal their capability to bind the copper when they are in their free form.

The unveiling of the copper binding site is given by the formation of the shorter product ions, i.e., b_4^+ and a_4^+ (A β_{25-35} and A β_{28-35} respectively). Both peptides share the Lys residue in 28th position, which represents a good candidate for the copper binding site.

This discovery is of paramount significance since it reveals the possibility of these fragments binding copper once they are produced by the digestion of the full length A β_{1-40} by the metalloproteases.

Consequently, the release of these fragments by metalloproteinases assumes a pivotal role at the biological level because these fragments can interact with copper ions, starting secondary and unexplored pathways, and whose biological function and impact on AD pathology have never been addressed.

The most pioneering aspect of this study revolved around the identification of A β -oxygen adducts, made only achievable by the insert of helium and oxygen gases into the mass spectrometer. This innovative step lies precisely in the capability to introduce a variety of gases, an essential advancement that rendered the detection of these compounds, otherwise nearly impossible, feasible. Indeed, detecting metastable compounds presents a challenge due to their insufficient inherent energy, which hinders them from reaching the detector successfully.

Conversely, oxygen and helium, in particular, exhibit a high cooling effect that is necessary to reduce the energy stored within molecules. This allows for the stabilization of the species and their subsequent detection.

Results demonstrated that unlike A β_{1-40} peptide, all four A β_{1-40} fragments are not capable of capturing oxygen molecules from the aqueous environment. This means that the formation of the peptide-oxygen adducts seems to be peculiar for A β_{1-40} , which would be capable of accommodating and tightly coordinating oxygen molecules within its structure. This is likely correlated with the specific A β_{1-40} structure, which adopts a distinctive conformation that integrates hydrophilic and hydrophobic components from the N-terminal and C-terminal regions, respectively.

Moreover, the detection of oxygen adducts even in the presence of helium rules out their formation within the mass spectrometer, highlighting their production in solution.

A similar scenario arises in the presence of copper, where A β_{1-40} -copper oxygen adducts were detected, while no oxygen adducts were generated with A β_{1-40} fragments. Finally, it seems that copper does not play a role in coordinating the peptide with oxygen.

It's worth noting that, although this work is promising, the research is still ongoing. Indeed, the potential significance and early positive results gave us an extra push to conduct further investigations to fully understand the research and provide a more comprehensive overview of this interesting and innovative work.

5. Conclusion and Future perspectives

In conclusion, in this thesis, I have reported the results and findings obtained in the three previous chapters regarding *i)* the amyloid catabolism *ii)* the aggregation mechanism, and *iii)* A β oxygen adducts.

In particular, in *Chapter I*, I obtained results regarding the role of metalloproteases in amyloid catabolism through an SPR analysis of the IDE-insulin interaction, chosen as model system. This analysis shed the light on the role of Car as a potent modulator of IDE activity by extracting the Hill coefficient. In this context, the use of the SPR technique is crucial for the identification of the nature of the modulators by monitoring their real-time effects on enzyme-substrate interactions.

In *Chapter II*, I have exploited the potential of CDs, using them as biosensors to monitor the early stages of insulin fibrillation and to detect and distinguish isobaric peptides. While the common belief initially regarded fibrils as the species responsible for cognitive decline, recent discoveries have identified oligomers as the most toxic species. Their formation represents the primary stage of the aggregation process. Hence, the use of CDs as biosensors allowed us to capture characteristic snapshots of the early conformations adopted by insulin over time. These impressive capabilities demonstrated by CDs will be made accessible and applied to explore the aggregation processes of other proteins prone to aggregation. Indeed, the next step involves implementing this methodology to investigate the aggregation processes that define A β , thereby uncovering the initial stages of this intricate mechanism. This has a significant impact on the AD scenario, as it overcomes detection challenges failed by other techniques, thanks to the high sensitivity of the newly proposed approach.

Lastly, Chapter III was devoted to MS investigations, which reveal *i)* the involvement of the selected A β fragments in the copper binding after digestion by the metalloproteases and, *ii)* the detection of metastable A β ₁₋₄₀-oxygen adducts. Their detection was achieved by the direct introduction of gases, namely helium and oxygen, by means of an unconventional mass spectrometer. This result has been explained by considering the cooling effect exerted by the gases used (He, O₂).

Interestingly, this thesis further demonstrates the correlation of seemingly disparate topics through the application of multi-technical approaches. Indeed, all the investigated factors contribute to the onset or worsening of AD and need to be properly addressed.

In perspective, this thesis has shed light on various intricate aspects of the catabolism, aggregation, and misfolding of the peptides involved in AD and T2DM. Through innovative methodologies and

the exploration of previously uncharted territories, it has expanded our understanding of the underlying diseases mechanisms, factors that may hold the key to more effective therapies and interventions for these complex conditions. The identification of new pathways and factors contributing to the pathologies will offer promising avenues for future research and therapeutic interventions and underscores the importance of interdisciplinary approaches in unraveling the complexities of neurodegenerative diseases and metabolic disorders.

References

- [1] W. H. Organization, *Neurological Disorders: Public Health Challenges*, World Health Organization, **2006**.
- [2] “Alzheimer’s Disease,” **n.d.**
- [3] R. Schmidt, E. Kienbacher, T. Benke, P. Dal-Bianco, M. Delazer, G. Ladurner, K. Jellinger, J. Marksteiner, G. Ransmayr, H. Schmidt, *Neuropsychiatrie* **2008**, *22*, 1–15.
- [4] W. H. Organization, *Atlas: Country Resources for Neurological Disorders 2004: Results of a Collaborative Study of the World Health Organization and the World Federation of Neurology*, World Health Organization, **2004**.
- [5] G. Deuschl, E. Beghi, F. Fazekas, T. Varga, K. A. Christoforidi, E. Sipido, C. L. Bassetti, T. Vos, V. L. Feigin, *Lancet Public Heal.* **2020**, *5*, e551–e567.
- [6] G. Livingston, J. Huntley, A. Sommerlad, D. Ames, C. Ballard, S. Banerjee, C. Brayne, A. Burns, J. Cohen-Mansfield, C. Cooper, S. G. Costafreda, A. Dias, N. Fox, L. N. Gitlin, R. Howard, H. C. Kales, M. Kivimäki, E. B. Larson, A. Ogunniyi, V. Orgeta, K. Ritchie, K. Rockwood, E. L. Sampson, Q. Samus, L. S. Schneider, G. Selbæk, L. Teri, N. Mukadam, *Lancet* **2020**, *396*, 413–446.
- [7] K. J. Barnham, C. L. Masters, A. I. Bush, *Nat. Rev. Drug Discov.* **2004**, *3*, 205–214.
- [8] B. J. Gu, X. Huang, A. Ou, A. Rembach, C. Fowler, P. K. Avula, A. Horton, J. D. Doecke, V. L. Villemagne, S. L. Macaulay, P. Maruff, E. L. Fletcher, R. Guymer, J. S. Wiley, C. L. Masters, The Australian Imaging, Biomarkers, *Acta Neuropathol.* **2016**, *132*, 377–389.
- [9] M. Smedinga, S. K. L. Darweesh, B. R. Bloem, B. Post, E. Richard, *J. Neurol.* **2021**, *268*, 724–733.
- [10] M. W. Bondi, E. C. Edmonds, D. P. Salmon, *J. Int. Neuropsychol. Soc. JINS* **2017**, *23*, 818.
- [11] C. L. Joachim, J. H. Morris, D. J. Selkoe, *Ann. Neurol. Off. J. Am. Neurol. Assoc. Child Neurol. Soc.* **1988**, *24*, 50–56.
- [12] M. G. Erkkinen, M.-O. Kim, M. D. Geschwind, *Cold Spring Harb. Perspect. Biol.* **2018**, *10*, a033118.
- [13] K. Gadhav, N. Bolshette, A. Ahire, R. Pardeshi, K. Thakur, C. Trandafir, A. Istrate, S. Ahmed, M. Lahkar, D. F. Muresanu, *J. Cell. Mol. Med.* **2016**, *20*, 1392–1407.
- [14] N. B. Nedelsky, P. K. Todd, J. P. Taylor, *Biochim. Biophys. Acta (BBA)-Molecular Basis Dis.* **2008**, *1782*, 691–699.
- [15] Q. Zeng, W. Siu, L. Li, Y. U. Jin, S. Liang, M. Cao, M. Ma, Z. Wu, *Exp. Gerontol.* **2019**, *119*, 100–110.
- [16] H. H. Jang, *J. Cancer Prev.* **2018**, *23*, 153–161.
- [17] J. Wang, M. A. Maldonado, *Cell. Mol. Immunol.* **2006**, *3*, 255–261.
- [18] J. Cao, M. B. Zhong, C. A. Toro, L. Zhang, D. Cai, *Neurosci. Lett.* **2019**, *703*, 68–78.
- [19] E. M. Hol, F. W. Van Leeuwen, D. F. Fischer, *Trends Mol. Med.* **2005**, *11*, 488–495.
- [20] G. Grasso, M. L. Giuffrida, E. Rizzarelli, *Metallomics* **2012**, *4*, 937–949.

- [21] D. J. Selkoe, M. B. Podlisny, C. L. Joachim, E. A. Vickers, G. Lee, L. C. Fritz, T. Oltersdorf, *Proc. Natl. Acad. Sci. U. S. A.* **1988**, *85*, 7341–7345.
- [22] A. Weidemann, G. König, D. Bunke, P. Fischer, J. M. Salbaum, C. L. Masters, K. Beyreuther, *Cell* **1989**, *57*, 115–126.
- [23] A. Y. Hung, D. J. Selkoe, *EMBO J.* **1994**, *13*, 534–542.
- [24] J. Walter, A. Capell, A. Y. Hung, H. Langen, M. Schnölzer, G. Thinakaran, S. S. Sisodia, D. J. Selkoe, C. Haass, *J. Biol. Chem.* **1997**, *272*, 1896–1903.
- [25] T. Oltersdorf, P. J. Ward, T. Henriksson, E. C. Beattie, R. Neve, I. Lieberburg, L. C. Fritz, *J. Biol. Chem.* **1990**, *265*, 4492–4497.
- [26] K. S. Vetrivel, G. Thinakaran, *Neurology* **2006**, *66*, S69–S73.
- [27] Y. Zhang, R. Thompson, H. Zhang, H. Xu, *Mol. Brain* **2011**, *4*, 1–13.
- [28] D. J. Selkoe, *Physiol. Rev.* **2001**.
- [29] K. G. Mawuenyega, T. Kasten, W. Sigurdson, R. J. Bateman, *Anal. Biochem.* **2013**, *440*, 56–62.
- [30] C. Patterson, J. W. Feightner, A. Garcia, G. Y. R. Hsiung, C. MacKnight, A. D. Sadovnick, *C. Can. Med. Assoc. J.* **2008**, *178*, 548–556.
- [31] C. G. Glabe, *Neurobiol. Aging* **2006**, *27*, 570–575.
- [32] C. Cheignon, M. Tomas, D. Bonnefont-Rousselot, P. Faller, C. Hureau, F. Collin, *Redox Biol.* **2018**, *14*, 450–464.
- [33] M. L. Giuffrida, F. Caraci, B. Pignataro, S. Cataldo, P. De Bona, V. Bruno, G. Molinaro, G. Pappalardo, A. Messina, A. Palmigiano, D. Garozzo, F. Nicoletti, E. Rizzarelli, A. Copani, *J. Neurosci.* **2009**, *29*, 10582–10587.
- [34] A. I. Bush, R. E. Tanzi, *Neurotherapeutics* **2008**, *5*, 421–432.
- [35] A. I. Bush, *J. Alzheimer's Dis.* **2008**, *15*, 223–240.
- [36] W. Q. Qiu, M. F. Folstein, *Neurobiol. Aging* **2006**, *27*, 190–198.
- [37] A. González, C. Calfío, M. Churrua, R. B. Maccioni, *Alzheimers. Res. Ther.* **2022**, *14*, 56.
- [38] M. Baram, Y. Miller, *ACS Chem. Neurosci.* **2020**, *11*, 445–452.
- [39] G. D. Stanciu, V. Bild, D. C. Ababei, R. N. Rusu, A. Cobzaru, L. Paduraru, D. Bulea, *J. Clin. Med.* **2020**, *9*, 1713.
- [40] K. Akter, E. A. Lanza, S. A. Martin, N. Myronyuk, M. Rua, R. B. Raffa, *Br. J. Clin. Pharmacol.* **2011**, *71*, 365–376.
- [41] L. Li, C. Hölscher, *Brain Res. Rev.* **2007**, *56*, 384–402.
- [42] J. A. Carson, A. J. Turner, *J. Neurochem.* **2002**, *81*, 1–8.
- [43] T. Matsumoto, C. D. Funk, O. Rådmark, J. O. Höög, H. Jörnvall, B. Samuelsson, *Adv. Prostaglandin. Thromboxane. Leukot. Res.* **1989**, *19*, 466–469.
- [44] K. Barnes, S. Doherty, A. J. Turner, *J. Neurochem.* **1995**, *64*, 1826–1832.
- [45] A. J. Turner, R. Elwyn Isaac, D. Coates, *BioEssays* **2001**, *23*, 261–269.

- [46] S. Howell, J. Nalbantoglu, P. Crine, *Peptides* **1995**, *16*, 647–652.
- [47] H. Kanemitsu, T. Tomiyama, H. Mori, *Neurosci. Lett.* **2003**, *350*, 113–116.
- [48] E. Hama, K. Shirotani, N. Iwata, T. C. Saido, *J. Biol. Chem.* **2004**, *279*, 30259–30264.
- [49] N. Macours, J. Poels, K. Hens, C. Francis, R. Huybrechts, *Int. Rev. Cytol.* **2004**, *239*, 47.
- [50] D. Xu, N. Emoto, A. Giaid, C. Slaughter, S. Kaw, D. deWit, M. Yanagisawa, *Cell* **1994**, *78*, 473–485.
- [51] A. J. Turner, L. J. Murphy, *Biochem. Pharmacol.* **1996**, *51*, 91–102.
- [52] M. N. Lorenzo, R. Y. Khan, Y. Wang, S. C. Tai, G. C. Chan, A. H. Cheung, P. A. Marsden, *Biochim. Biophys. Acta- Gene Struct. Expr.* **2001**, *1522*, 46–52.
- [53] K. Shimada, Y. Matsushita, K. Wakabayashi, M. Takahashi, A. Matsubara, Y. Iijima, K. Tanzawa, *Biochem. Biophys. Res. Commun.* **1995**, *207*, 807–812.
- [54] E. A. Eckman, D. K. Reed, C. B. Eckman, *J. Biol. Chem.* **2001**, *276*, 24540–24548.
- [55] J. L. Guy, D. W. Lambert, F. J. Warner, N. M. Hooper, A. J. Turner, *Biochim. Biophys. Acta - Proteins Proteomics* **2005**, *1751*, 2–8.
- [56] B. Rigat, C. Hubert, F. Alhenc-Gelas, F. Cambien, P. Corvol, F. Soubrier, *J. Clin. Invest.* **1990**, *86*, 1343–1346.
- [57] M. R. W. Ehlers, E. A. Fox, D. J. Strydom, J. F. Riordan, *Proc. Natl. Acad. Sci. U. S. A.* **1989**, *86*, 7741–7745.
- [58] L. Wei, E. Clauser, F. Alhenc-Gelas, P. Corvol, *J. Biol. Chem.* **1992**, *267*, 13398–13405.
- [59] J. Hu, A. Igarashi, M. Kamata, H. Nakagawa, *J. Biol. Chem.* **2001**, *276*, 47863–47868.
- [60] A. Papazafiropoulou, N. Tentolouris, *Hippokratia* **2009**, *13*, 76–82.
- [61] S. Rowsell, P. Hawtin, C. A. Minshull, H. Jepson, S. M. V. Brockbank, D. G. Barratt, A. M. Slater, W. L. McPheat, D. Waterson, A. M. Henney, R. A. Pauptit, *J. Mol. Biol.* **2002**, *319*, 173–181.
- [62] E.-S. Song, M. A. Juliano, L. Juliano, L. B. Hersh, *J. Biol. Chem.* **2003**, *278*, 49789–49794.
- [63] G. Grasso, in *Adv. Protein Chem. Struct. Biol.*, Elsevier, **2014**, pp. 115–142.
- [64] G. R. Tundo, D. Sbardella, C. Ciaccio, G. Grasso, M. Gioia, A. Coletta, F. Polticelli, D. Di Pierro, D. Milardi, P. Van Endert, *Crit. Rev. Biochem. Mol. Biol.* **2017**, *52*, 554–582.
- [65] S. Harada, R. M. Smith, L. Jarett, *Cell Biochem. Biophys.* **1999**, *31*, 307–319.
- [66] I. V Kurochkin, E. Guarnera, I. N. Berezovsky, *Trends Pharmacol. Sci.* **2018**, *39*, 49–58.
- [67] R. E. Hulse, L. A. Ralat, T. Wei-Jen, *Vitam. Horm.* **2009**, *80*, 635–648.
- [68] E. S. Song, D. W. Rodgers, L. B. Hersh, *PLoS One* **2010**, *5*.
- [69] C. M. González-Casimiro, B. Merino, E. Casanueva-Álvarez, T. Postigo-Casado, P. Cámara-Torres, C. M. Fernández-Díaz, M. A. Leissring, I. Cózar-Castellano, G. Perdomo, *Biomedicines* **2021**, *9*, 86.
- [70] O. Pivovarova, A. Höhn, T. Grune, A. F. H. Pfeiffer, N. Rudovich, *Ann. Med.* **2016**, *48*, 614–624.

- [71] W. Farris, M. A. Leissring, M. L. Hemming, A. Y. Chang, D. J. Selkoe, *Biochemistry* **2005**, *44*, 6513–6525.
- [72] H. Im, M. Manolopoulou, E. Malito, Y. Shen, J. Zhao, M. Neant-Fery, C. Y. Sun, S. C. Meredith, S. S. Sisodia, M. A. Leissring, W. J. Tang, *J. Biol. Chem.* **2007**, *282*, 25453–25463.
- [73] Z. Zhang, W. G. Liang, L. J. Bailey, Y. Z. Tan, H. Wei, A. Wang, M. Farcasanu, V. A. Woods, L. A. McCord, D. Lee, W. Shang, R. Deprez-Poulain, B. Deprez, D. R. Liu, A. Koide, S. Koide, A. A. Kossiakoff, S. Li, B. Carragher, C. S. Potter, W. J. Tang, *Elife* **2018**, *7*, e33572.
- [74] M. Manolopoulou, Q. Guo, E. Malito, A. B. Schilling, W. J. Tang, *J. Biol. Chem.* **2009**, *284*, 14177–14188.
- [75] G. Grasso, A. I. Bush, R. D’Agata, E. Rizzarelli, G. Spoto, *Eur. Biophys. J.* **2009**, *38*, 407–414.
- [76] R. Vassar, B. D. Bennett, S. Babu-Khan, S. Kahn, E. A. Mendiaz, P. Denis, D. B. Teplow, S. Ross, P. Amarante, R. Loeloff, Y. Luo, S. Fisher, J. Fuller, S. Edenson, J. Lile, M. A. Jarosinski, A. L. Biere, E. Curran, T. Burgess, J. C. Louis, F. Collins, J. Treanor, G. Rogers, M. Citron, *Science (80-.)*. **1999**, *286*, 735–741.
- [77] A. Mukherjee, E. S. Song, M. Kihiko-Ehmann, J. Goodman, J. St. Pyrek, S. Estus, L. B. Hersh, *J. Neurosci.* **2000**, *20*, 8745–8749.
- [78] V. Chesneau, K. Vekrellis, M. R. Rosner, D. J. Selkoe, *Biochem. J.* **2000**, *351*, 509–516.
- [79] Q. Guo, M. Manolopoulou, Y. Bian, A. B. Schilling, W.-J. Tang, *J. Mol. Biol.* **2010**, *395*, 430–443.
- [80] S. A. Hudson, H. Ecroyd, T. W. Kee, J. A. Carver, *FEBS J.* **2009**, *276*, 5960–5972.
- [81] N. Noinaj, S. K. Bhasin, E. S. Song, K. E. Scoggin, M. A. Juliano, L. Juliano, L. B. Hersh, D. W. Rodgers, *PLoS One* **2011**, *6*, e20864.
- [82] Y. Shen, A. Joachimiak, M. Rich Rosner, W.-J. Tang, *Nature* **2006**, *443*, 870–874.
- [83] G. R. Tundo, E. Di Muzio, C. Ciaccio, D. Sbardella, D. Di Pierro, F. Polticelli, M. Coletta, S. Marini, *FEBS J.* **2016**, *283*, 3755–3770.
- [84] C. Parr, N. Mirzaei, M. Christian, M. Sastre, *FASEB J.* **2015**, *29*, 623–635.
- [85] L. Zhang, M. Fiala, J. Cashman, J. Sayre, A. Espinosa, M. Mahanian, J. Zaghi, V. Badmaev, M. C. Graves, G. Bernard, *J. Alzheimer’s Dis.* **2006**, *10*, 1–7.
- [86] T. Farkhondeh, S. Samarghandian, A. M. Pourbagher-Shahri, M. Sedaghat, *J. Cell. Physiol.* **2019**, *234*, 16953–16965.
- [87] M. C. Camberos, A. A. Perez, D. P. Udrisar, M. I. Wanderley, J. C. Cresto, *Exp. Biol. Med.* **2001**, *226*, 334–341.
- [88] C. Cabrol, M. A. Huzarska, C. Dinolfo, M. C. Rodriguez, L. Reinstatler, J. Ni, L.-A. Yeh, G. D. Cuny, R. L. Stein, D. J. Selkoe, *PLoS One* **2009**, *4*, e5274.
- [89] S. F. Michael, V. J. Kilfoil, M. H. Schmidt, B. T. Amann, J. M. Berg, *Proc. Natl. Acad. Sci.* **1992**, *89*, 4796–4800.
- [90] J. K. Nyborg, O. B. Peersen, *Biochem. J.* **2004**, *381*, e3.

- [91] V. Peters, M. Kebbewar, E. W. Jansen, C. Jakobs, E. Riedl, H. Koeppel, D. Frey, K. Adelman, K. Klingbeil, M. Mack, *Amino Acids* **2010**, *38*, 1607–1615.
- [92] A. F. Mannion, P. M. Jakeman, M. Dunnett, R. C. Harris, P. L. T. Willan, *Eur. J. Appl. Physiol. Occup. Physiol.* **1992**, *64*, 47–50.
- [93] D. Finley, *Annu. Rev. Biochem.* **2009**, *78*, 477–513.
- [94] J. Myung, K. B. Kim, C. M. Crews, *Med. Res. Rev.* **2001**, *21*, 245–273.
- [95] M. J. Kunjappu, M. Hochstrasser, *Biochim. Biophys. Acta - Mol. Cell Res.* **2014**, *1843*, 2–12.
- [96] I. Sahu, M. H. Glickman, *Biomolecules* **2021**, *11*, 1–15.
- [97] D. Sbardella, G. R. Tundo, A. Coletta, J. Marcoux, E. I. Koufogeorgou, C. Ciaccio, A. M. Santoro, D. Milardi, G. Grasso, P. Cozza, *Cell. Mol. Life Sci.* **2018**, *75*, 3441–3456.
- [98] G. C. Lander, E. Estrin, M. E. Matyskiela, C. Bashore, E. Nogales, A. Martin, *Nature* **2012**, *482*, 186–191.
- [99] A. R. Hipkiss, J. E. Preston, D. T. Himsforth, V. C. Worthington, M. Keown, J. Michaelis, J. Lawrence, A. Mateen, L. Allende, P. A. Eagles, *Ann NY Acad Sci* **1998**, *854*, 37–53.
- [100] T. Matsukura, H. Tanaka, *Biochem. C/C BIOKHIMIA* **2000**, *65*, 817–823.
- [101] T. MATSUKURA, T. TAKAHASHI, Y. NISHIMURA, T. OHTANI, M. SAWADA, K. SHIBATA, *Chem. Pharm. Bull.* **1990**, *38*, 3140–3146.
- [102] G. I. Grasso, F. Bellia, G. Arena, G. Vecchio, E. Rizzarelli, *Inorg. Chem.* **2011**, *50*, 4917–4924.
- [103] G. Grasso, A. Pietropaolo, G. Spoto, G. Pappalardo, G. R. Tundo, C. Ciaccio, M. Coletta, E. Rizzarelli, *Chem. Eur. J.* **2011**, *17*, 2752–2762.
- [104] E. J. Baran, *Biochem. C/C BIOKHIMIA* **2000**, *65*, 789–797.
- [105] P. Umadevi, L. Senthikumar, *RSC Adv.* **2014**, *4*, 49040–49052.
- [106] L. Chen, T. Liu, C. Ma, *J. Phys. Chem. A* **2010**, *114*, 443–454.
- [107] A. J. Sillanpää, R. Aksela, K. Laasonen, *Phys. Chem. Chem. Phys.* **2003**, *5*, 3382–3393.
- [108] A. A. Boldyrev, G. Aldini, W. Derave, *Physiol. Rev.* **2013**.
- [109] L. J. Hobart, I. Seibel, G. S. Yeorgans, N. W. Seidler, *Life Sci.* **2004**, *75*, 1379–1389.
- [110] A. Distefano, G. Caruso, V. Oliveri, F. Bellia, D. Sbardella, G. A. Zingale, F. Caraci, G. Grasso, *ACS Chem. Neurosci.* **2022**, DOI 10.1021/acchemneuro.2c00201.
- [111] L. A. McCord, W. G. Liang, E. Dowdell, V. Kalas, R. J. Hoey, A. Koide, S. Koide, W. J. Tang, *Proc. Natl. Acad. Sci. U. S. A.* **2013**, *110*, 13827–13832.
- [112] G. Grasso, R. D’Agata, E. Rizzarelli, G. Spoto, L. D’Andrea, C. Pedone, A. Picardi, A. Romanelli, M. Fragai, K. J. Yeo, *J. mass Spectrom.* **2005**, *40*, 1565–1571.
- [113] Y. Teramura, H. Iwata, *Anal. Biochem.* **2007**, *365*, 201–207.
- [114] M. Piliarik, M. Bocková, J. Homola, *Biosens. Bioelectron.* **2010**, *26*, 1656–1661.
- [115] Y. Tang, X. Zeng, J. Liang, *J. Chem. Educ.* **2010**, *87*, 742–746.

- [116] C. T. Campbell, G. Kim, *Biomaterials* **2007**, *28*, 2380–2392.
- [117] A. Distefano, G. Antonio Zingale, G. Grasso, *Anal. Bioanal. Chem.* **2022**, *414*, 4793–4802.
- [118] E. S. Song, D. W. Rodgers, L. B. Hersh, *J. Biol. Chem.* **2011**, *286*, 13853–13858.
- [119] M. del Carmen Camberos, J. C. Cresto, *Exp. Biol. Med.* **2007**, *232*, 281–292.
- [120] C. H. B. da Cruz, G. Seabra, *J. Chem. Inf. Model.* **2014**, *54*, 1380–1390.
- [121] E. S. Song, M. A. Juliano, L. Juliano, M. G. Fried, S. L. Wagner, L. B. Hersh, *J. Biol. Chem.* **2004**, *279*, 54216–54220.
- [122] M. C. Garcia, *J. Chromatogr. B* **2005**, *825*, 111–123.
- [123] F. Chiti, C. M. Dobson, *Annu. Rev. Biochem.* **2017**, *86*, 27–68.
- [124] F. Chiti, C. M. Dobson, *Annu. Rev. Biochem.* **2006**, *75*, 333–366.
- [125] C. Haass, D. J. Selkoe, *Nat. Rev. Mol. cell Biol.* **2007**, *8*, 101–112.
- [126] D. Eisenberg, M. Jucker, *Cell* **2012**, *148*, 1188–1203.
- [127] J. Hardy, D. J. Selkoe, *Science (80-.)*. **2002**, *297*, 353–356.
- [128] S. Lesné, M. T. Koh, L. Kotilinek, R. Kaye, C. G. Glabe, A. Yang, M. Gallagher, K. H. Ashe, *Nature* **2006**, *440*, 352–357.
- [129] S. Campioni, B. Mannini, M. Zampagni, A. Pensalfini, C. Parrini, E. Evangelisti, A. Relini, M. Stefani, C. M. Dobson, C. Cecchi, *Nat. Chem. Biol.* **2010**, *6*, 140–147.
- [130] M. Bucciantini, E. Giannoni, F. Chiti, F. Baroni, L. Formigli, J. Zurdo, N. Taddei, G. Ramponi, C. M. Dobson, M. Stefani, *Nature* **2002**, *416*, 507–511.
- [131] L. M. Billings, S. Oddo, K. N. Green, J. L. McGaugh, F. M. LaFerla, *Neuron* **2005**, *45*, 675–688.
- [132] A. Wimo, M. Prince, *Glob. Econ. impact Dement.* **2010**, *56*.
- [133] J. N. Onuchic, Z. Luthey-Schulten, P. G. Wolynes, *Annu. Rev. Phys. Chem.* **1997**, *48*, 545–600.
- [134] C. M. Dobson, A. Šali, M. Karplus, *Angew. Chemie Int. Ed.* **1998**, *37*, 868–893.
- [135] E. Chatani, N. Yamamoto, *Biophys. Rev.* **2018**, *10*, 527–534.
- [136] C. Iannuzzi, G. Irace, I. Sirangelo, *Molecules* **2015**, *20*, 2510–2528.
- [137] P. Arosio, T. P. J. Knowles, S. Linse, *Phys. Chem. Chem. Phys.* **2015**, *17*, 7606–7618.
- [138] T. P. J. Knowles, C. A. Waudby, G. L. Devlin, S. I. A. Cohen, A. Aguzzi, M. Vendruscolo, E. M. Terentjev, M. E. Welland, C. M. Dobson, *Science (80-.)*. **2009**, *326*, 1533–1537.
- [139] M. Fändrich, *J. Mol. Biol.* **2007**, *365*, 1266–1270.
- [140] D. Polanco, A. Carrancho, P. Gracia, N. Cremades, *Biophysica* **2022**, *2*, 506–524.
- [141] A. W. P. Fitzpatrick, G. T. Debelouchina, M. J. Bayro, D. K. Clare, M. A. Caporini, V. S. Bajaj, C. P. Jaronec, L. Wang, V. Ladizhansky, S. A. Müller, *Proc. Natl. Acad. Sci.* **2013**, *110*, 5468–5473.
- [142] M. Sunde, L. C. Serpell, M. Bartlam, P. E. Fraser, M. B. Pepys, C. C. F. Blake, *J. Mol. Biol.*

1997, 273, 729–739.

- [143] J. L. Jiménez, E. J. Nettleton, M. Bouchard, C. V Robinson, C. M. Dobson, H. R. Saibil, *Proc. Natl. Acad. Sci.* **2002**, 99, 9196–9201.
- [144] R. Jakob-Roetne, H. Jacobsen, *Angew. Chemie Int. Ed.* **2009**, 48, 3030–3059.
- [145] T. C. T. Michaels, D. Qian, A. Šarić, M. Vendruscolo, S. Linse, T. P. J. Knowles, *Nat. Rev. Phys.* **2023**, 1–19.
- [146] S. I. A. Cohen, S. Linse, L. M. Luheshi, E. Hellstrand, D. A. White, L. Rajah, D. E. Otzen, M. Vendruscolo, C. M. Dobson, T. P. J. Knowles, *Proc. Natl. Acad. Sci. U. S. A.* **2013**, 110, 9758–9763.
- [147] H. Hampel, J. Hardy, K. Blennow, C. Chen, G. Perry, S. H. Kim, V. L. Villemagne, P. Aisen, M. Vendruscolo, T. Iwatsubo, *Mol. Psychiatry* **2021**, 26, 5481–5503.
- [148] J. Talafous, K. J. Marcinowski, G. Klopman, M. G. Zagorski, *Biochemistry* **1994**, 33, 7788–7796.
- [149] C. J. Barrow, M. G. Zagorski, *Science (80-.)*. **1991**, 253, 179–182.
- [150] D. J. Selkoe, *Nat. Cell Biol.* **2004**, 6, 1054–1061.
- [151] H. C. Rice, D. De Malmazet, A. Schreurs, S. Frere, I. Van Molle, A. N. Volkov, E. Creemers, I. Vertkin, J. Nys, F. M. Ranaivoson, D. Comoletti, J. N. Savas, H. Remaut, D. Balschun, K. D. Wierda, I. Slutsky, K. Farrow, B. De Strooper, J. De Wit, *Science (80-.)*. **2019**, 363, eaao4827.
- [152] D. A. Butterfield, T. Reed, S. F. Newman, R. Sultana, *Free Radic. Biol. Med.* **2007**, 43, 658–677.
- [153] V. H. Finder, R. Glockshuber, *Neurodegener. Dis.* **2007**, 4, 13–27.
- [154] K. N. Dahlgren, A. M. Manelli, W. Blaine Stine, L. K. Baker, G. A. Krafft, M. J. Ladu, *J. Biol. Chem.* **2002**, 277, 32046–32053.
- [155] J. P. Cleary, D. M. Walsh, J. J. Hofmeister, G. M. Shankar, M. A. Kuskowski, D. J. Selkoe, K. H. Ashe, *Nat. Neurosci.* **2005**, 8, 79–84.
- [156] R. Kaye, E. Head, J. L. Thompson, T. M. McIntire, S. C. Milton, C. W. Cotman, C. G. Glabe, *Science (80-.)*. **2003**, 300, 486–489.
- [157] E. Y. Hayden, D. B. Teplow, *Alzheimers. Res. Ther.* **2013**, 5, 1–11.
- [158] B. Mannini, E. Mulvihill, C. Sgromo, R. Cascella, R. Khodarahmi, M. Ramazzotti, C. M. Dobson, C. Cecchi, F. Chiti, *ACS Chem. Biol.* **2014**, 9, 2309–2317.
- [159] B. Barz, Q. Liao, B. Strodel, *J. Am. Chem. Soc.* **2018**, 140, 319–327.
- [160] G. F. Chen, T. H. Xu, Y. Yan, Y. R. Zhou, Y. Jiang, K. Melcher, H. E. Xu, *Acta Pharmacol. Sin.* **2017**, 38, 1205–1235.
- [161] S. Li, D. J. Selkoe, *J. Neurochem.* **2020**, 154, 583–597.
- [162] D. M. Walsh, I. Klyubin, J. V. Fadeeva, W. K. Cullen, R. Anwyl, M. S. Wolfe, M. J. Rowan, D. J. Selkoe, *Nature* **2002**, 416, 535–539.
- [163] P. N. Lacor, M. C. Buniel, P. W. Furlow, A. S. Clemente, P. T. Velasco, M. Wood, K. L. Viola, W. L. Klein, *J. Neurosci.* **2007**, 27, 796–807.

- [164] S. Ghosh, R. Ali, S. Verma, *Int. J. Biol. Macromol.* **2023**, 124231.
- [165] L. P. Sun, Y. Zhong, J. Gui, X. W. Wang, X. R. Zhuang, J. Weng, *Int. J. Nanomedicine* **2018**, *13*, 843–856.
- [166] J. S. H. Wang, S. N. Whitehead, K. K. C. Yeung, *J. Am. Soc. Mass Spectrom.* **2018**, *29*, 786–795.
- [167] K. Nurmakova, Z. Levine, *Biophys. J.* **2023**, *122*, 350a.
- [168] J. D. Harper, S. S. Wong, C. M. Lieber, P. T. Lansbury, *Biochemistry* **1999**, *38*, 8972–8980.
- [169] J. D. Harper, P. T. Lansbury, *Annu. Rev. Biochem.* **1997**, *66*, 385–407.
- [170] A. S. Johansson, J. Bergquist, C. Volbracht, A. Pääviö, M. Leist, L. Lannfelt, A. Westlind-Danielsson, *Neuroreport* **2007**, *18*, 559–563.
- [171] B. O’Nuallain, D. B. Freir, A. J. Nicoll, E. Risse, N. Ferguson, C. E. Herron, J. Collinge, D. M. Walsh, *J. Neurosci.* **2010**, *30*, 14411–14419.
- [172] C. Sachse, C. Xu, K. Wieligmann, S. Diekmann, N. Grigorieff, M. Fändrich, *J. Mol. Biol.* **2006**, *362*, 347–354.
- [173] T. P. J. Knowles, M. Vendruscolo, C. M. Dobson, *Nat. Rev. Mol. Cell Biol.* **2014**, *15*, 384–396.
- [174] R. Freer, P. Sormanni, G. Vecchi, P. Ciryam, C. M. Dobson, M. Vendruscolo, *Sci. Adv.* **2016**, *2*, e1600947.
- [175] C. Martínez-Cué, N. Rueda, *Int. J. Mol. Sci.* **2020**, *21*, 6906.
- [176] M. Alrouji, H. M. Al-Kuraishy, A. I. Al-Gareeb, A. Alexiou, M. Papadakis, H. M. Saad, G. E. S. Batiha, *Diabetol. Metab. Syndr.* **2023**, *15*, 1–16.
- [177] A. T. Templin, M. Mellati, R. Soininen, M. F. Hogan, N. Esser, J. J. Castillo, S. Zraika, S. E. Kahn, R. L. Hull, *Protein Eng. Des. Sel.* **2019**, *32*, 95–102.
- [178] A. Abedini, A. M. Schmidt, *FEBS Lett.* **2013**, *587*, 1119–1127.
- [179] L. Ma, C. Yang, J. Zheng, Y. Chen, Y. Xiao, K. Huang, *Eur. J. Med. Chem.* **2020**, *192*, 112197.
- [180] J. R. Sowers, E. D. Frohlich, *Med. Clin. North Am.* **2004**, *88*, 63–82.
- [181] Ej. Alyas, A. Rafiq, H. Amir, S. U. Khan, T. Sultana, A. Ali, A. Hameed, I. Ahmad, A. Kazmi, T. Sajid, A. Ahmad, *Biomed. Res. Ther.* **2021**, *8*, 4540–4561.
- [182] M. F. Dunn, *BioMetals* **2005**, *18*, 295–303.
- [183] S. Iqbal, A. A. Jayyab, A. M. Alrashdi, S. Reverté-Villarroya, *Endocr. Pract.* **2023**, *29*, 379–387.
- [184] L. Nielsen, R. Khurana, A. Coats, S. Frokjaer, J. Brange, S. Vyas, V. N. Uversky, A. L. Fink, *Biochemistry* **2001**, *40*, 6036–6046.
- [185] S. L. Aronoff, K. Berkowitz, B. Shreiner, L. Want, *Diabetes Spectr.* **2004**, *17*, 183–190.
- [186] D. D. Thomas, B. E. Corkey, N. W. Istfan, C. M. Apovian, *J. Endocr. Soc.* **2019**, *3*, 1727–1747.
- [187] M. C. Petersen, G. I. Shulman, *Physiol. Rev.* **2018**, *98*, 2133–2223.

- [188] S. J. Hunter, W. T. Garvey, *Am. J. Med.* **1998**, *105*, 331–345.
- [189] Z. Liu, E. J. Barrett, *Am. J. Physiol. - Endocrinol. Metab.* **2002**, *283*, E1105–E1112.
- [190] C. M. B. Edwards, *International Textbook of Diabetes Mellitus*, John Wiley & Sons, **2004**.
- [191] D. S. Straus, *Life Sci.* **1981**, *29*, 2131–2139.
- [192] S. Okamura, Y. Hayashino, S. Kore-Eda, S. Tsujii, *Diabetes Care* **2013**, *36*, 397–401.
- [193] B. Swift, P. N. Hawkins, C. Richards, R. Gregory, *Diabet. Med.* **2002**, *19*, 881–882.
- [194] F. E. Dische, C. Wernstedt, G. T. Westermarck, P. Westermarck, M. B. Pepys, J. A. Rennie, S. G. Gilbey, P. J. Watkins, *Diabetologia* **1988**, *31*, 158–161.
- [195] S. Okamura, Y. Hayashino, S. Kore-Eda, S. Tsujii, *Diabetes Care* **2013**, *36*, e200–e200.
- [196] R. Dec, V. Babenko, W. Dzwolak, *RSC Adv.* **2016**, *6*, 97331–97337.
- [197] M. Ziaunys, V. Smirnovas, *J. Phys. Chem. B* **2019**, *123*, 8727–8732.
- [198] K. Iwaya, T. Zako, J. Fukunaga, K. M. Sörgjerd, K. Ogata, K. Kogure, H. Kosano, M. Noritake, M. Maeda, Y. Ando, *BMC Endocr. Disord.* **2019**, *19*, 1–6.
- [199] J. Brange, L. Andersen, E. D. Laursen, G. Meyn, E. Rasmussen, *J. Pharm. Sci.* **1997**, *86*, 517–525.
- [200] M. Mauro, E. F. Craparo, A. Podestà, D. Bulone, R. Carrotta, V. Martorana, G. Tiana, P. L. San Biagio, *J. Mol. Biol.* **2007**, *366*, 258–274.
- [201] A. Das, M. Shah, I. Saraogi, *ACS bio med Chem Au* **2022**, *2*, 205–221.
- [202] P. D. Jeffrey, *Diabetologia* **1982**, *23*, 381–385.
- [203] D. Lin, Z. Qian, M. Bagnani, M. A. Hernández-Rodríguez, J. Corredoira-Vázquez, G. Wei, L. D. Carlos, R. Mezzenga, *ACS Nano* **2023**, *17*, 9429–9441.
- [204] Y. Cao, R. Mezzenga, *Adv. Colloid Interface Sci.* **2019**, *269*, 334–356.
- [205] M. Akbarian, R. Yousefi, F. Farjadian, V. N. Uversky, *Chem. Commun.* **2020**, *56*, 11354–11373.
- [206] D. Kurouski, T. Deckert-Gaudig, V. Deckert, I. K. Lednev, *Biophys. J.* **2014**, *106*, 263–271.
- [207] Y. Hong, L. Meng, S. Chen, C. W. T. Leung, L.-T. Da, M. Faisal, D.-A. Silva, J. Liu, J. W. Y. Lam, X. Huang, *J. Am. Chem. Soc.* **2012**, *134*, 1680–1689.
- [208] B. Vestergaard, M. Groenning, M. Roessle, J. S. Kastrop, M. van de Weert, J. M. Flink, S. Frokjaer, M. Gajhede, D. I. Svergun, *PLoS Biol.* **2007**, *5*, e134.
- [209] O. M. Selivanova, S. Y. Grishin, A. V Glyakina, A. S. Sadgyan, N. I. Ushakova, O. V Galzitskaya, *Biochem.* **2018**, *83*, S146–S162.
- [210] W. D. Loughheed, H. Woulfe-Flanagan, J. R. Clement, A. M. Albisser, *Diabetologia* **1980**, *19*, 1–9.
- [211] C. M. Yip, M. L. Brader, M. R. DeFelippis, M. D. Ward, *Biophys. J.* **1998**, *74*, 2199–2209.
- [212] H. Klostermeyer, R. E. Humbel, *Angew. Chemie Int. Ed. English* **1966**, *5*, 807–822.
- [213] T. Blundell, G. Dodson, D. Hodgkin, D. Mercola, *Adv. Protein Chem.* **1972**, *26*, 279–286.

- [214] C. P. Hill, E. J. Dodson, G. G. Dodson, Z. Dauter, Z. Dauter, M. F. Dunn, *Biochemistry* **1991**, *30*, 917–924.
- [215] M. C. Lee, W. C. Yu, Y. H. Shih, C. Y. Chen, Z. H. Guo, S. J. Huang, J. C. C. Chan, Y. R. Chen, *Sci. Rep.* **2018**, *8*, 4772.
- [216] J. Zou, K. Kajita, N. Sugimoto, *Angew. Chemie - Int. Ed.* **2001**, *40*, 2274–2277.
- [217] D. P. Smith, G. D. Ciccotosto, D. J. Tew, M. T. Fodero-Tavoletti, T. Johanssen, C. L. Masters, K. J. Barnham, R. Cappai, *Biochemistry* **2007**, *46*, 2881–2891.
- [218] Y. Bin, X. Li, Y. He, S. Chen, J. Xiang, *Acta Biochim. Biophys. Sin. (Shanghai)*. **2013**, *45*, 570–577.
- [219] F. Hane, G. Tran, S. J. Attwood, Z. Leonenko, *PLoS One* **2013**, *8*, e59005.
- [220] M. F. M. Sciacca, I. Naletova, M. L. Giuffrida, F. Attanasio, *ACS Chem. Neurosci.* **2022**, *13*, 486–496.
- [221] M. G. M. Weibull, S. Simonsen, C. R. Oksbjerg, M. K. Tiwari, L. Hemmingsen, *J. Biol. Inorg. Chem.* **2019**, *24*, 1197–1215.
- [222] D. F. Waugh, D. F. Wilhelmson, S. L. Commerford, M. L. Sackler, *J. Am. Chem. Soc.* **1953**, *75*, 2592–2600.
- [223] C. Bryant, A. Miller, D. L. Bakaysa, D. N. Brems, *Protein Eng. Des. Sel.* **1993**, *6*, 8.
- [224] E. N. Baker, T. L. Blundell, J. F. Cutfield, S. M. Cutfield, E. J. Dodson, G. G. Dodson, D. M. Hodgkin, R. E. Hubbard, N. W. Isaacs, C. D. Reynolds, *Philos. Trans. R. Soc. Lond. B. Biol. Sci.* **1988**, *319*, 369–456.
- [225] A. Kurek-Górecka, A. Rzepecka-Stojko, M. Górecki, J. Stojko, M. Sosada, G. Swierczek-Zieba, *Molecules* **2014**, *19*, 78–101.
- [226] D. Raederstorff, *Int. J. Vitam. Nutr. Res.* **2009**, *79*, 152–165.
- [227] B. Queen, T. Tollefsbol, *Curr. Aging Sci.* **2012**, *3*, 34–42.
- [228] V. Mayakrishnan, P. Kannappan, N. Abdullah, A. B. A. Ahmed, *Trends Food Sci. Technol.* **2013**, *30*, 98–104.
- [229] F. Yang, G. P. Lim, A. N. Begum, O. J. Ubeda, M. R. Simmons, S. S. Ambegaokar, P. P. Chen, R. Kayed, C. G. Glabe, S. A. Frautschy, *J. Biol. Chem.* **2005**, *280*, 5892–5901.
- [230] I. Hafner-Bratkovič, J. Gašperšič, L. M. Šmid, M. Bresjanac, R. Jerala, *J. Neurochem.* **2008**, *104*, 1553–1564.
- [231] A. Rabiee, A. Ebrahim-Habibi, L. Navidpour, D. Morshedi, A. Ghasemi, M. Sabbaghian, M. Nemati-Lay, M. Nemat-Gorgani, *Chem. Biol. Drug Des.* **2011**, *78*, 659–666.
- [232] M. Stefani, S. Rigacci, *Int. J. Mol. Sci.* **2013**, *14*, 12411–12457.
- [233] A. Arora, C. Ha, C. B. Park, *Protein Sci.* **2004**, *13*, 2429–2436.
- [234] V. Banerjee, R. K. Kar, A. Datta, K. Parthasarathi, S. Chatterjee, K. P. Das, A. Bhunia, *PLoS One* **2013**, *8*, e72318.
- [235] B. N. Ratha, A. Ghosh, J. R. Brender, N. Gayen, H. Ilyas, C. Neeraja, K. P. Das, A. K. Mandal, A. Bhunia, *J. Biol. Chem.* **2016**, *291*, 23545–23556.

- [236] M. H. Viet, S. T. Ngo, N. S. Lam, M. S. Li, *J. Phys. Chem. B* **2011**, *115*, 7433–7446.
- [237] A. J. Doig, *Curr. Opin. Drug Discov. Dev.* **2007**, *10*, 533–539.
- [238] M. Ouberai, P. Dumy, S. Chierici, J. Garcia, *Bioconjug. Chem.* **2009**, *20*, 2123–2132.
- [239] M. N. Shinde, R. Khurana, N. Barooah, A. C. Bhasikuttan, J. Mohanty, *J. Phys. Chem. C* **2017**, *121*, 20057–20065.
- [240] B. Ren, B. Jiang, R. Hu, M. Zhang, H. Chen, J. Ma, Y. Sun, L. Jia, J. Zheng, *Phys. Chem. Chem. Phys.* **2016**, *18*, 20476–20485.
- [241] H. Skaat, R. Chen, I. Grinberg, S. Margel, *Biomacromolecules* **2012**, *13*, 2662–2670.
- [242] S. Palmal, N. R. Jana, N. R. Jana, *J. Phys. Chem. C* **2014**, *118*, 21630–21638.
- [243] Q. Q. Yang, J. C. Jin, Z. Q. Xu, J. Q. Zhang, B. B. Wang, F. L. Jiang, Y. Liu, *J. Mater. Chem. B* **2017**, *5*, 2010–2018.
- [244] X. Zhang, Z. Fu, L. Meng, M. He, Z. Zhang, *Front. Aging Neurosci.* **2018**, *10*, 359.
- [245] P. Calabresi, A. Mechelli, G. Natale, L. Volpicelli-Daley, G. Di Lazzaro, V. Ghiglieri, *Cell Death Dis.* **2023**, *14*, 176.
- [246] V. N. Sivanandam, M. Jayaraman, C. L. Hoop, R. Kodali, R. Wetzels, P. C. A. van der Wel, *J. Am. Chem. Soc.* **2011**, *133*, 4558–4566.
- [247] E. Pryor, J. A. Kotarek, M. A. Moss, C. N. Hestekin, *Int. J. Mol. Sci.* **2011**, *12*, 9369–9388.
- [248] E. Chatani, R. Inoue, H. Imamura, M. Sugiyama, M. Kato, M. Yamamoto, K. Nishida, T. Kanaya, *Sci. Rep.* **2015**, *5*, 15485.
- [249] G. A. Zingale, A. Distefano, I. Pandino, N. Tuccitto, V. Oliveri, M. Gaeta, A. D’Urso, A. Arcoria, G. Grasso, *Anal. Bioanal. Chem.* **2023**, *415*, 1829–1840.
- [250] V. Mishra, A. Patil, S. Thakur, P. Kesharwani, *Drug Discov. Today* **2018**, *23*, 1219–1232.
- [251] A. Verhagen, A. Kellarakis, *Nanomaterials* **2020**, *10*, 1535.
- [252] S. N. Baker, G. A. Baker, *Angew. Chemie - Int. Ed.* **2010**, *49*, 6726–6744.
- [253] V. Perumal, U. Hashim, *J. Appl. Biomed.* **2014**, *12*, 1–15.
- [254] N. Chauhan, T. Maekawa, D. N. S. Kumar, *J. Mater. Res.* **2017**, *32*, 2860–2882.
- [255] C. Ji, Y. Zhou, R. M. Leblanc, Z. Peng, *ACS Sensors* **2020**, *5*, 2724–2741.
- [256] S. Beack, W. H. Kong, H. S. Jung, I. H. Do, S. Han, H. Kim, K. S. Kim, S. H. Yun, S. K. Hahn, *Acta Biomater.* **2015**, *26*, 295–305.
- [257] M. Zheng, S. Liu, J. Li, D. Qu, H. Zhao, X. Guan, X. Hu, Z. Xie, X. Jing, Z. Sun, *Adv. Mater.* **2014**, *26*, 3554–3560.
- [258] S. Ghosh, B. Sachdeva, P. Sachdeva, V. Chaudhary, G. M. Rani, J. K. Sinha, *Carbon Lett.* **2022**, *32*, 1381–1394.
- [259] M. Zheng, S. Ruan, S. Liu, T. Sun, D. Qu, H. Zhao, Z. Xie, H. Gao, X. Jing, Z. Sun, *ACS Nano* **2015**, *9*, 11455–11461.
- [260] S. Lu, G. Li, Z. Lv, N. Qiu, W. Kong, P. Gong, G. Chen, L. Xia, X. Guo, J. You, Y. Wu, *Biosens. Bioelectron.* **2016**, *85*, 358–362.

- [261] Y. Guo, R. Liu, Y. Liu, D. Xiang, Y. Liu, W. Gui, M. Li, G. Zhu, *Sci. Total Environ.* **2018**, 613–614, 783–791.
- [262] H. Wu, H. Li, F. Z. H. Chua, S. F. Y. Li, *Sensors Actuators, B Chem.* **2013**, 178, 541–546.
- [263] K. Mintz, E. Waidely, Y. Zhou, Z. Peng, A. O. Al-Youbi, A. S. Bashammakh, M. S. El-Shahawi, R. M. Leblanc, *Anal. Chim. Acta* **2018**, 1041, 114–121.
- [264] S. Mohammadi, A. Salimi, *Microchim. Acta* **2018**, 185, 1–10.
- [265] Q. X. Hua, M. A. Weiss, *J. Biol. Chem.* **2004**, 279, 21449–21460.
- [266] T. L. Blundell, J. F. Cutfield, S. M. Cutfield, E. J. Dodson, G. G. Dodson, D. C. Hodgkin, D. A. Mercola, M. Vijayan, *Nature* **1971**, 231, 506–511.
- [267] J. Shen, Y. Zhu, X. Yang, C. Li, *Chem. Commun.* **2012**, 48, 3686–3699.
- [268] Z. Zhang, J. Zhang, N. Chen, L. Qu, *Energy Environ. Sci.* **2012**, 5, 8869–8890.
- [269] Y. Choi, Y. Choi, O. Kwon, B. Kim, *Chem. Asian J.* **2018**, 13, 586–598.
- [270] H. Khojasteh, M. Salavati-Niasari, H. Safajou, H. Safardoust-Hojaghan, *Diam. Relat. Mater.* **2017**, 79, 133–144.
- [271] M. Jorns, D. Pappas, *Nanomaterials* **2021**, 11, 1448.
- [272] J. Bart, R. Tiggelaar, M. Yang, S. Schlautmann, H. Zuilhof, H. Gardeniers, *Lab Chip* **2009**, 9, 3481–3488.
- [273] M. J. E. Fischer, *Surf. plasmon Reson. methods Protoc.* **2010**, 55–73.
- [274] A. Distefano, F. Cali, M. Gaeta, N. Tuccitto, A. Auditore, A. Licciardello, A. d’Urso, K.-J. Lee, O. Monasson, E. Peroni, *J. Colloid Interface Sci.* **2022**, 625, 405–414.
- [275] A. Mazumdar, Y. Haddad, V. Milosavljevic, H. Michalkova, R. Guran, S. Bhowmick, A. Moulick, *Nanomaterials* **2020**, 10, 325.
- [276] Y. Lin, Y. Zheng, Y. Guo, Y. Yang, H. Li, Y. Fang, C. Wang, *Sensors Actuators, B Chem.* **2018**, 273, 1654–1659.
- [277] H. Basiri, A. Abouei Mehrizi, A. Ghaee, M. Farokhi, M. Chekini, E. Kumacheva, *Langmuir* **2020**, 36, 2893–2900.
- [278] Y. Niu, H. Tan, X. Li, L. Zhao, Z. Xie, Y. Zhang, S. Zhou, X. Qu, *ACS Appl. Mater. Interfaces* **2020**, 12, 3445–3452.
- [279] W. Wang, B. Wang, H. Embrechts, C. Damm, A. Cadranel, V. Strauss, M. Distaso, V. Hinterberger, D. M. Guldi, W. Peukert, *RSC Adv.* **2017**, 7, 24771–24780.
- [280] A. Sharma, T. Gadly, S. Neogy, S. K. Ghosh, M. Kumbhakar, *J. Phys. Chem. Lett.* **2017**, 8, 5861–5864.
- [281] J. Liu, R. Li, B. Yang, *ACS Cent. Sci.* **2020**, 6, 2179–2195.
- [282] S. Pandit, P. Behera, J. Sahoo, M. De, *ACS Appl. Bio Mater.* **2019**, 2, 3393–3403.
- [283] C. Dingwall, I. Ernberg, M. J. Gait, S. M. Green, S. Heaphy, J. Karn, A. D. Lowe, M. Singh, M. A. Skinner, R. Valerio, *Proc. Natl. Acad. Sci. U. S. A.* **1989**, 86, 6925–6929.
- [284] P. A. Osmulski, P. Karpowicz, E. Jankowska, J. Bohmann, A. M. Pickering, M. Gaczynska, *Molecules* **2020**, 25, 1439.

- [285] E. S. Chocron, E. Munkácsy, H. S. Kim, P. Karpowicz, N. Jiang, C. E. Van Skike, N. DeRosa, A. Q. Banh, J. P. Palavicini, P. Wityk, L. Kalinowski, V. Galvan, P. A. Osmulski, E. Jankowska, M. Gaczynska, A. M. Pickering, *Sci. Adv.* **2022**, *8*, eabk2252.
- [286] S. Futaki, T. Suzuki, W. Ohashi, T. Yagami, S. Tanaka, K. Ueda, Y. Sugiura, *J. Biol. Chem.* **2001**, *276*, 5836–5840.
- [287] M. Zhao, R. Weissleder, *Med. Res. Rev.* **2004**, *24*, 1–12.
- [288] J. Xie, Y. Bi, H. Zhang, S. Dong, L. Teng, R. J. Lee, Z. Yang, *Front. Pharmacol.* **2020**, *11*, 697.
- [289] A. Ferrari, V. Pellegrini, C. Arcangeli, A. Fittipaldi, M. Giacca, F. Beltram, *Mol. Ther.* **2003**, *8*, 284–294.
- [290] B. Janssen, D. Hohenadel, P. Brinkkoetter, V. Peters, N. Rind, C. Fischer, I. Rychlik, M. Cerna, M. Romzova, E. De Heer, H. Baelde, S. J. L. Bakker, M. Zirie, E. Rondeau, P. Mathieson, M. A. Saleem, J. Meyer, H. Koppel, S. Sauerhoefer, C. R. Bartram, P. Nawroth, H. P. Hammes, B. A. Yard, J. Zschocke, F. J. Van Der Woude, *Diabetes* **2005**, *54*, 2320–2327.
- [291] P. L. Hall, *Q. Rev. Biol.* **1979**, *54*, 73–74.
- [292] E. Reynaud, *Nat. Educ.* **2010**, *3*, 28.
- [293] E. Tönnies, E. Trushina, *J. Alzheimer's Dis.* **2017**, *57*, 1105–1121.
- [294] C. Angeloni, M. Malaguti, C. Prata, M. Freschi, M. C. Barbalace, S. Hrelia, *Antioxidants* **2023**, *12*, 94.
- [295] G. Cecil, A. Mucherinol, M. D'apuzzo, D. Di Serafino, S. Costantini, A. Facchiano, G. Colonna, *Springer Optim. Its Appl.* **2007**, *7*, 391–424.
- [296] D. Harman, *Proc. Natl. Acad. Sci. U. S. A.* **1991**, *88*, 5360–5363.
- [297] J. Zhang, X. Wang, V. Vikash, Q. Ye, D. Wu, Y. Liu, W. Dong, *Oxid. Med. Cell. Longev.* **2016**, *2016*, DOI 10.1155/2016/4350965.
- [298] J. Checa, J. M. Aran, *J. Inflamm. Res.* **2020**, 1057–1073.
- [299] D. A. Patten, M. Germain, M. A. Kelly, R. S. Slack, *J. Alzheimer's Dis.* **2010**, *20*, S357–S367.
- [300] F. Collin, *Int. J. Mol. Sci.* **2019**, *20*, 2407.
- [301] S. I. Liochev, I. Fridovich, *Redox Rep.* **2002**, *7*, 55–57.
- [302] M. D. Brand, *Free Radic. Biol. Med.* **2016**, *100*, 14–31.
- [303] M. Sharifi-Rad, N. V. Anil Kumar, P. Zucca, E. M. Varoni, L. Dini, E. Panzarini, J. Rajkovic, P. V. Tsouh Fokou, E. Azzini, I. Peluso, A. Prakash Mishra, M. Nigam, Y. El Rayess, M. El Beyrouthy, L. Polito, M. Iriti, N. Martins, M. Martorell, A. O. Docea, W. N. Setzer, D. Calina, W. C. Cho, J. Sharifi-Rad, *Front. Physiol.* **2020**, *11*, 694.
- [304] G. Pizzino, N. Irrera, M. Cucinotta, G. Pallio, F. Mannino, V. Arcoraci, F. Squadrito, D. Altavilla, A. Bitto, *Oxid. Med. Cell. Longev.* **2017**, *2017*, DOI 10.1155/2017/8416763.
- [305] A. K. Aranda-Rivera, A. Cruz-Gregorio, Y. L. Arancibia-Hernández, E. Y. Hernández-Cruz, J. Pedraza-Chaverri, *Oxygen* **2022**, *2*, 437–478.

- [306] B. L. Tan, M. E. Norhaizan, W. P. P. Liew, H. S. Rahman, *Front. Pharmacol.* **2018**, *9*, 1162.
- [307] E. B. Kurutas, *Nutr. J.* **2016**, *15*, 1–22.
- [308] T. R. Klran, O. Otlu, A. B. Karabulut, *J. Lab. Med.* **2023**, *47*, 1–11.
- [309] I. N. Zelko, T. J. Mariani, R. J. Folz, *Free Radic. Biol. Med.* **2002**, *33*, 337–349.
- [310] H. N. Kirkman, G. F. Gaetani, *Proc. Natl. Acad. Sci. U. S. A.* **1984**, *81*, 4343–4347.
- [311] W. Dröge, *Exp. Gerontol.* **2002**, *37*, 1333–1345.
- [312] R. Masella, R. Di Benedetto, R. Vari, C. Filesi, C. Giovannini, *J. Nutr. Biochem.* **2005**, *16*, 577–586.
- [313] M. Marlatt, H. G. Lee, G. Perry, M. A. Smith, X. Zhu, *Acta Neurobiol. Exp. (Wars)*. **2004**, *64*, 81–87.
- [314] P. Youssef, B. Chami, J. Lim, T. Middleton, G. T. Sutherland, P. K. Witting, *Sci. Rep.* **2018**, *8*, 11553.
- [315] C. Cheignon, F. Collin, L. Sabater, C. Hureau, *Antioxidants* **2023**, *12*, 472.
- [316] J. Näslund, A. Schierhorn, U. Hellman, L. Lannfelt, A. D. Roses, L. O. Tjernberg, J. Silberring, S. E. Gandy, B. Winblad, P. Greengard, C. Nordstedt, L. Terenius, *Proc. Natl. Acad. Sci. U. S. A.* **1994**, *91*, 8378–8382.
- [317] S. P. Gabbita, M. A. Lovell, W. R. Markesbery, *J. Neurochem.* **1998**, *71*, 2034–2040.
- [318] M. A. Lovell, S. Soman, M. A. Bradley, *Mech. Ageing Dev.* **2011**, *132*, 443–448.
- [319] S. Takahashi, I. Takahashi, H. Sato, Y. Kubota, S. Yoshida, Y. Muramatsu, *Biol. Trace Elem. Res.* **2001**, *80*, 145–158.
- [320] C. J. Maynard, R. Cappai, I. Volitakis, R. A. Cherny, A. R. White, K. Beyreuther, C. L. Masters, A. I. Bush, Q.-X. Li, *J. Biol. Chem.* **2002**, *277*, 44670–44676.
- [321] M. A. Lovell, J. D. Robertson, W. J. Teesdale, J. L. Campbell, W. R. Markesbery, *J. Neurol. Sci.* **1998**, *158*, 47–52.
- [322] P. S. Donnelly, Z. Xiao, A. G. Wedd, *Curr. Opin. Chem. Biol.* **2007**, *11*, 128–133.
- [323] F. Bellia, G. Grasso, *J. mass Spectrom.* **2014**, *49*, 274–279.
- [324] G. Grasso, H. Komatsu, P. H. Axelsen, *J. Inorg. Biochem.* **2017**, *174*, 130–136.
- [325] W. R. Markesbery, M. A. Lovell, *Neurobiol. Aging* **1998**, *19*, 33–36.
- [326] A. J. Gow, D. Duran, S. Malcolm, H. Ischiropoulos, *FEBS Lett.* **1996**, *385*, 63–66.
- [327] J. Thome, G. Münch, R. Müller, R. Schinzel, J. Kornhuber, D. Blum-Degen, L. Sitzmann, M. Rösier, A. Heidland, P. Riederer, *Life Sci.* **1996**, *59*, 679–685.
- [328] G. Münch, R. Schinzel, C. Loske, A. Wong, N. Durany, J. J. Li, H. Vlassara, M. A. Smith, G. Perry, P. Riederer, *J. Neural Transm.* **1998**, *105*, 439–461.
- [329] V. Prakash Reddy, M. E. Obrenovich, C. S. Atwood, G. Perry, M. A. Smith, *Neurotox. Res.* **2002**, *4*, 191–209.
- [330] C. R. Harrington, C. A. L. S. Colaco, *Nature* **1994**, *370*, 247–248.

- [331] M. P. Vitek, K. Bhattacharya, J. M. Glendening, E. Stopa, H. Vlassara, R. Bucala, K. Manogue, A. Cerami, *Proc. Natl. Acad. Sci. U. S. A.* **1994**, *91*, 4766–4770.
- [332] R. H. Swerdlow, *Int. Rev. Neurobiol.* **2020**, *154*, 207–233.
- [333] E. Ferreira, C. R. Oliveira, C. M. F. Pereira, *Neurobiol. Dis.* **2008**, *30*, 331–342.
- [334] A. M. Isaacs, D. B. Senn, M. Yuan, J. P. Shine, B. A. Yankner, *J. Biol. Chem.* **2006**, *281*, 27916–27923.
- [335] N. Pierrot, P. Ghisdal, A. S. Caumont, J. N. Octave, *J. Neurochem.* **2004**, *88*, 1140–1150.
- [336] M. R. Broadley, P. J. White, J. P. Hammond, I. Zelko, A. Lux, *New Phytol.* **2007**, *173*, 677–702.
- [337] M. Araya, F. Pizarro, M. Olivares, M. Arredondo, M. González, M. Méndez, *Biol. Res.* **2006**, *39*, 183–187.
- [338] R. A. DiSilvestro, **2004**, DOI 10.1201/9780203489673.
- [339] G. Cereda, V. Ciappolino, A. Boscutti, F. Cantù, P. Enrico, L. Oldani, G. Delvecchio, P. Brambilla, *Adv. Nutr.* **2022**, *13*, 66–79.
- [340] J. Salvo, C. Sandoval, *Burn. Trauma* **2022**, *10*, tkab047.
- [341] D. Strausak, J. F. B. Mercer, H. H. Dieter, W. Stremmel, G. Multhaup, *Brain Res. Bull.* **2001**, *55*, 175–185.
- [342] H. W. Ejaz, W. Wang, M. Lang, *Int. J. Mol. Sci.* **2020**, *21*, 1–33.
- [343] H. Kozłowski, M. Luczkowski, M. Remelli, D. Valensin, *Coord. Chem. Rev.* **2012**, *256*, 2129–2141.
- [344] A. S. Prasad, *Curr. Opin. Clin. Nutr. Metab. Care* **2009**, *12*, 646–652.
- [345] N. Kim, H. J. Lee, *Int. J. Mol. Sci.* **2021**, *22*, 7697.
- [346] D. Strozyk, L. J. Launer, P. A. Adlard, R. A. Cherny, A. Tsatsanis, I. Volitakis, K. Blennow, H. Petrovitch, L. R. White, A. I. Bush, *Neurobiol. Aging* **2009**, *30*, 1069–1077.
- [347] S. Noël, S. Bustos Rodriguez, S. Sayen, E. Guillon, P. Faller, C. Hureau, *Metallomics* **2014**, *6*, 1220–1222.
- [348] B. Alies, A. Conte-Daban, S. Sayen, F. Collin, I. Kieffer, E. Guillon, P. Faller, C. Hureau, *Inorg. Chem.* **2016**, *55*, 10499–10509.
- [349] C. Hureau, *Coord. Chem. Rev.* **2012**, *256*, 2164–2174.
- [350] M. Manea, G. Schlosser, M. Murariu, *Int. J. Pept. Res. Ther.* **2015**, *21*, 125–131.
- [351] V. Tõugu, A. Tiiman, P. Palumaa, *Metallomics* **2011**, *3*, 250–261.
- [352] C. Talmard, A. Bouzan, P. Faller, *Biochemistry* **2007**, *46*, 13658–13666.
- [353] P. Dorlet, S. Gambarelli, P. Faller, C. Hureau, *Angew. Chemie - Int. Ed.* **2009**, *48*, 9273–9276.
- [354] S. C. Drew, K. J. Barnham, *Acc. Chem. Res.* **2011**, *44*, 1146–1155.
- [355] S. C. Drew, C. L. Masters, K. J. Barnham, *J. Am. Chem. Soc.* **2009**, *131*, 8760–8761.

- [356] S. C. Drew, C. J. Noble, C. L. Masters, G. R. Hanson, K. J. Barnham, *J. Am. Chem. Soc.* **2009**, *131*, 1195–1207.
- [357] A. Conte-Daban, V. Borghesani, S. Sayen, E. Guillon, Y. Journaux, G. Gontard, L. Lisnard, C. Hureau, *Anal. Chem.* **2017**, *89*, 2155–2162.
- [358] C. Hureau, Y. Coppel, P. Dorlet, P. L. Solari, S. Sayen, E. Guillon, L. Sabater, P. Faller, *Angew. Chemie - Int. Ed.* **2009**, *48*, 9522–9525.
- [359] S. López-Ortiz, J. Pinto-Fraga, P. L. Valenzuela, J. Martín-Hernández, M. M. Seisdedos, O. García-López, N. Toschi, F. Di Giuliano, F. Garaci, N. B. Mercuri, R. Nisticò, E. Emanuele, S. Lista, A. Lucia, A. Santos-Lozano, *Int. J. Mol. Sci.* **2021**, *22*, 1–29.
- [360] B. Halliwell, Jm. Gutteridge, *Biochem. J.* **1984**, *219*, 1.
- [361] S. Scarpa, A. Fuso, F. D'Anselmi, R. A. Cavallaro, *FEBS Lett.* **2003**, *541*, 145–148.
- [362] M. Govindaraju, H. S. Shekar, S. B. Sateesha, P. V. Raju, K. R. S. Rao, K. S. J. Rao, A. J. Rajamma, *J. Pharm. Anal.* **2013**, *3*, 354–359.
- [363] H. Fritzsche, C. Zimmer, *Eur. J. Biochem.* **1968**, *5*, 42–44.
- [364] M. N. Dehkordi, A.-K. Bordbar, P. Lincoln, V. Mirkhani, *Spectrochim. Acta Part A Mol. Biomol. Spectrosc.* **2012**, *90*, 50–54.
- [365] W. Förster, E. Bauer, H. Schütz, H. Berg, N. M. Akimenko, L. E. Minchenkova, Y. M. Evdokimov, Y. M. Varshavsky, *Biopolym. Orig. Res. Biomol.* **1979**, *18*, 625–661.
- [366] Y. K. Al-Hilaly, T. L. Williams, M. Stewart-Parker, L. Ford, E. Skaria, M. Cole, W. G. Bucher, K. L. Morris, A. A. Sada, J. R. Thorpe, *Acta Neuropathol. Commun.* **2013**, *1*, 1–17.
- [367] W. M. Kok, J. M. Cottam, G. D. Ciccotosto, L. A. Miles, J. A. Karas, D. B. Scanlon, B. R. Roberts, M. W. Parker, R. Cappai, K. J. Barnham, *Chem. Sci.* **2013**, *4*, 4449–4454.
- [368] C. S. Atwood, G. Perry, H. Zeng, Y. Kato, W. D. Jones, K.-Q. Ling, X. Huang, R. D. Moir, D. Wang, L. M. Sayre, *Biochemistry* **2004**, *43*, 560–568.
- [369] V. A. Streltsov, S. J. Titmuss, V. C. Epa, K. J. Barnham, C. L. Masters, J. N. Varghese, *Biophys. J.* **2008**, *95*, 3447–3456.
- [370] K. J. Barnham, F. Haeffner, G. D. Ciccotosto, C. C. Curtain, D. Tew, C. Mavros, K. Beyreuther, D. Carrington, C. L. Masters, R. A. Cherny, *FASEB J.* **2004**, *18*, 1427–1429.
- [371] S. A. James, I. Volitakis, P. A. Adlard, J. A. Duce, C. L. Masters, R. A. Cherny, A. I. Bush, *Free Radic. Biol. Med.* **2012**, *52*, 298–302.
- [372] F. Peng, O. Muzik, J. Gatson, S. G. Kernie, R. Diaz-Arrastia, *J. Nucl. Med.* **2015**, *56*, 1252–1257.
- [373] P. Wang, Z.-Y. Wang, *Ageing Res. Rev.* **2017**, *35*, 265–290.
- [374] J. M. Kim, U. Lee, J. Y. Kang, S. K. Park, E. J. Shin, H. J. Kim, C. W. Kim, M. J. Kim, H. J. Heo, *Antioxidants* **2020**, *9*, 1–24.
- [375] Q. Lu, Y. Zhang, C. Zhao, H. Zhang, Y. Pu, L. Yin, *J. Appl. Toxicol.* **2022**, *42*, 694–705.
- [376] N. Doreulee, Y. Yanovsky, H. L. Haas, *Hippocampus* **1997**, *7*, 666–669.
- [377] N. L. Salazar-Weber, J. P. Smith, *Int. J. Alzheimers. Dis.* **2011**, *2011*, DOI 10.4061/2011/864753.

- [378] E. Nam, G. Nam, M. H. Lim, *Biochemistry* **2019**, *59*, 15–17.
- [379] P. K. Stys, H. You, G. W. Zamponi, *J. Physiol.* **2012**, *590*, 1357–1368.
- [380] Q. Xue, R. Kang, D. J. Klionsky, D. Tang, J. Liu, X. Chen, *Autophagy* **2023**, 1–21.
- [381] D. G. Smith, R. Cappai, K. J. Barnham, *Biochim. Biophys. Acta (BBA)-Biomembranes* **2007**, *1768*, 1976–1990.
- [382] T. A. Enache, A. M. Oliveira-Brett, *Bioelectrochemistry* **2017**, *114*, 13–23.
- [383] A. Carrano, J. J. M. Hoozemans, S. M. van der Vies, A. J. M. Rozemuller, J. van Horsen, H. E. de Vries, *Antioxid. Redox Signal.* **2011**, *15*, 1167–1178.
- [384] S. Nishino, Y. Nishida, *Inorg. Chem. Commun.* **2001**, *4*, 86–89.
- [385] A. Maroto, D. Jeanne Dit Fouque, A. Memboeuf, *J. Mass Spectrom.* **2020**, *55*, e4478.
- [386] K. P. Wanczek, B. Kanawati, *Mass Spectrom. Rev.* **2022**, *41*, 338–351.
- [387] B. Alies, C. Hureau, P. Faller, *Metallomics* **2013**, *5*, 183–192.

Appendix

Instrumental techniques' overview

SPR Theory and Instrumentation

The attractiveness of gold nanomaterials has exponentially grown, spreading across numerous and diverse research fields. The appealing aspect is linked to their flexibility in various applications where gold plays a prominent role, particularly in the biomedical field. These applications include cellular imaging, drug delivery, disease therapy, and sensing. The latter is one of the most intriguing fields concerning gold nanomaterials. By exploiting on their optical characteristics, it becomes possible to investigate biological interactions and shed light on a deeper understanding of conformational diseases.

In 1902, the SPR phenomenon was first observed by Woods, who noticed a pattern of light and dark lines when p-polarized light was incident on the surface of a diffraction grating. Then, in 1957, R. H. Ritchie theoretically confirmed the presence of metal surface plasma excitations (SPE), which was subsequently demonstrated by C.H. Powell. However, it wasn't until 1983 that the application of SPR-based sensors in biomolecular interaction monitoring, label-free and in real-time, was demonstrated by Liedberg, Nylander, and Lundström at the Institute of Technology in Sweden.

SPR theory relies on two main physical phenomena occurring simultaneously: total internal reflection (TIR) and evanescent wave. The total internal reflection (TIR) occurs when an incident light beats a surface with an incident angle greater than the critical angle. To ensure that this phenomenon happens, the second medium must have an index of refraction less than the first medium, as in the case of gold and water respectively.

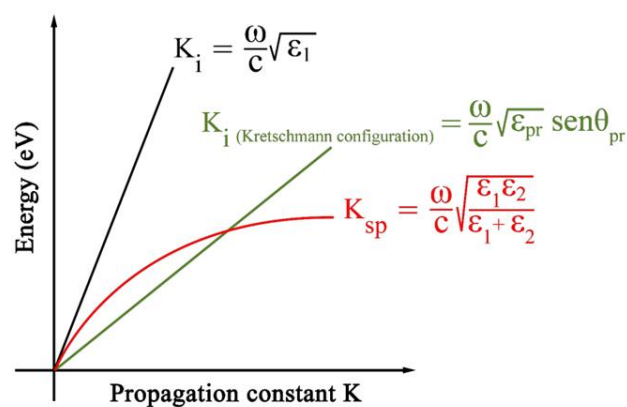


Figure 73 Overlaying the wave vector equations for the incident light (K_i), the surface plasmon (K_{sp}), and the Kretschmann configuration.

In resonance conditions, the energy of the electric field of photons can interact with the outer layer of gold and with the conduction band electrons called free electrons. Consequently, the absorption of photons from the incident light causes a transfer of energy to the free electrons, generating surface plasmons. As a result, under total internal reflection circumstances, the absorption of photons leads to a decrease in the intensity of the reflected light, which is recorded by the detector.

Simultaneously, on the opposite side of the interface, under TIR conditions, a discontinuity in the electric and magnetic field on the surface arises. However, this is overpassed by the formation of an evanescent wave. The term “evanescent” refers to the exponential decrease in wave intensity as a function of the distance from the gold surface (Figure 74).

If the material with the higher refractive index is gold, this evanescent wave could excite the free electrons present on the metal surface, inducing a charge separation from the ionic lattice and the formation of a dipole along the electric field of the light.

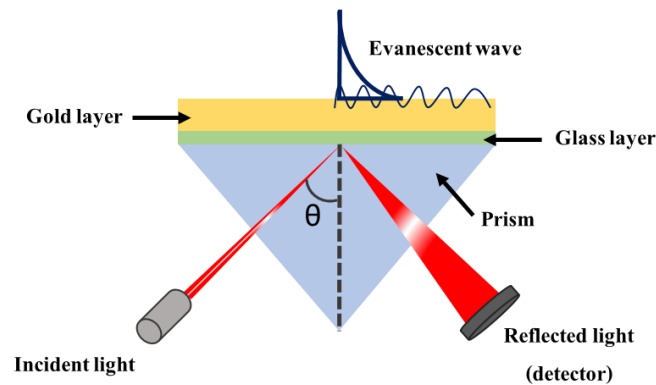


Figure 74 Schematic representation of the Kretschmann configuration.

The field produced by the evanescent wave matches the one generated by the plasmons. The attainment of a maximum in the amplitude of the oscillation is called SPR. The intensity and wavelength of the SPR band depend on factors such as metal type, particle size, shape, structure, composition, and the dielectric constant of the surrounding medium which can manipulate the electron charge density of the gold surface.

The SPR technique finds its theories on the modulation of the collective coherent oscillation of free electrons, called *surface plasmon*, which exists at the interface between two materials with different refractive indices.

To generate and sustain SPR, the wave vector of the surface plasmon (K_{sp}) and the wave vector of the incident light (K_i) need to coincide. However, when observing both math formulas of K_i and K_{sp} , there is no single point at which both relationships can be equal except for Energy (ev) = 0. Fig.73 illustrates the mathematical expression related to K_i and K_{sp} , where ω represents the incident

frequency, c is the velocity of light, ϵ_1 , and ϵ_2 are the dielectric constants of the medium and the metal film, respectively.

Nevertheless, the issue is overcome through the Kretschmann configuration (Figure 74), where the introduction of a high-refractive glass prism enables the alignment between the function of the surface plasmon and that of the incident light. The new wave vector of the incident light K_i (Kretschmann configuration), shown in Fig.73 in green, intersects the wave vector of the surface plasmon (K_{sp}) at a non-zero point, resulting in wave resonance.

$$\frac{\omega}{c} \sqrt{\epsilon_{pr}} \sin\theta_{pr} = \frac{\omega}{c} \sqrt{\frac{\epsilon_1 \epsilon_2}{\epsilon_1 + \epsilon_2}} \quad (4)$$

Equation 4 shows that the resonance condition is fulfilled when the laser beam hits the surface with a specific incident angle. In this condition, a minimum of reflectance is observed, meanwhile, by varying θ , it is observable how the angular distribution of reflectance changes at the metal-prism edge.

The resonance condition can change whenever something is anchored at the metal surface. Indeed, the most common and spreading application of this technique is the studying of binding interaction between biological molecules.

When a molecule, called *ligand*, is immobilized on the gold surface, the resonance condition changes due to an alteration of the environment, thus causing a change in the average refractive index of the region within which the evanescent field penetrates. This will result in a gradual shift of the resonance angle (the minimum in Figure 75).

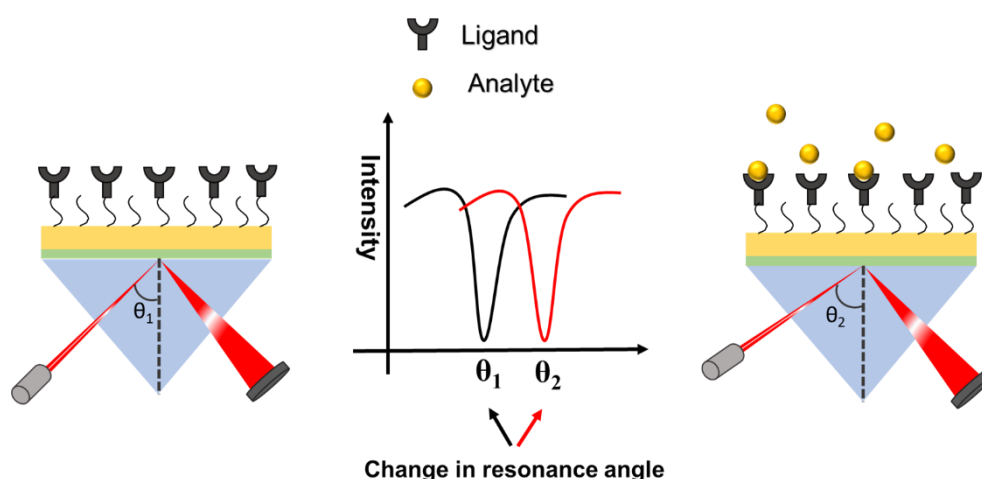


Figure 75 Graphic illustration of resonance angle change in the absence (on the left, black curve) and in the presence of the analyte (on the right, red curve).

The presence of an analyte interacting with the immobilized ligand on the surface induces an additional modification in the near bulk close to the metal surface. This leads to a shift in the angle required for the new resonance condition when the analyte is present ($\theta_1 \neq \theta_2$).

The shift is converted by the instrument in a SPR response versus time and the resulting graph, called sensorgram, allows a kinetic analysis between the analyte and the ligand.

Noteworthy, one of the most meaningful advantages of the SPR technique is the possibility to investigate the molecular interaction occurring on the surface in real-time and label-free.

As explained above, the interaction between the analyte and the ligand is recorded by the instrument. The result is a variation of the SPR response over time (Figure 76).

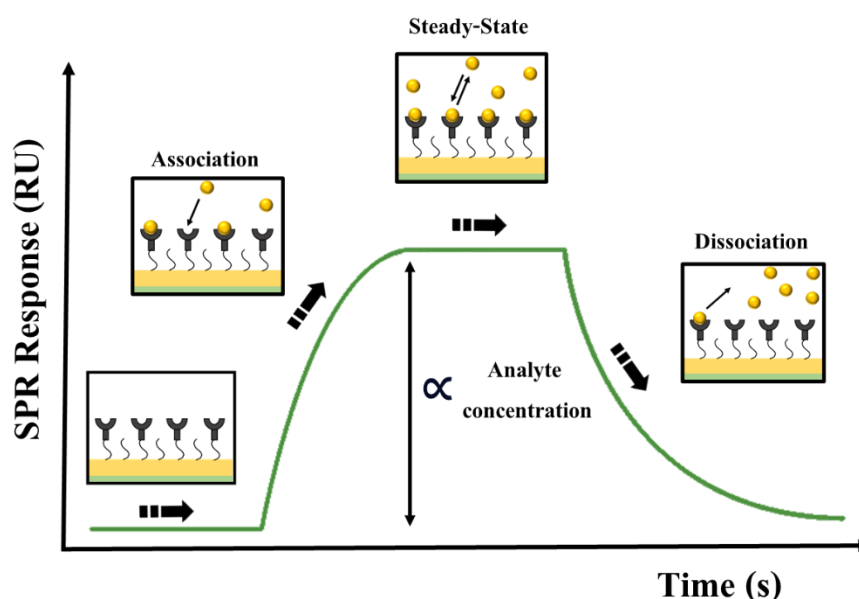


Figure 76 Sensorgram profile illustrating an analyte-ligand interaction alongside the characteristic phases of SPR. Additionally, the correlation between the SPR response and the analyte concentration is exhibited.

The sensorgram provided above, describing the interaction between an analyte and a ligand, is characterized by the presence of three phases: the association phase, the steady state, and the dissociation phase. During the *association phase*, the analyte reaches the surface and interacts with the ligand, resulting in an increase in the SPR response over time.

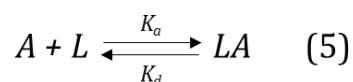
Following this, the *steady state* is the phase where an equilibrium between the analyte and the ligand is achieved. Here, the SPR response reaches its maximum value and remains almost constant over time.

Lastly, the *dissociation phase* begins with the introduction of the buffer. The buffer, free of the analyte, sweeps the analyte molecules away from the surface, and the SPR response gradually returns to the baseline, following an exponential function.

Since the SPR response is directly proportional to the concentration of the analyte, one limitation could be the failure to return to the baseline due to incomplete washing and removal of the analyte from the surface. However, this issue and the reusability of the sensor are overcome by treating the surface with various regeneration solutions depending on pH and ionic force.

From a kinetic standpoint, it is possible to extrapolate kinetic parameters from the three phases that can provide significant information about the type of interaction occurring between the ligand and the analyte.

The simplest model is described by a 1:1 interaction: the molecule binding from the solution (analyte, A) and the species immobilized on the sensor surface (ligand, L) interact with each other according to the following dynamic equilibrium.



The forward and the reverse reactions are in turn described by the adsorption (association) rate constant (k_a) and the desorption (dissociation) rate constant (k_d), respectively. The association process results in the formation of the complex [LA] on the sensor surface:

$$\frac{d [LA]}{dt} = K_a [A][L] \quad (6)$$

Whereas the dissociation constant is given by the disappearance of the complex LA and the return to the reagents:

$$-\frac{d [LA]}{dt} = K_d [LA] \quad (7)$$

The association constant K_a corresponds to the reaction rate of the complex (LA) formation, indicating the number of complexes formed per unit time at unit concentrations of L and A. On the other hand, the dissociation rate constant (K_d) expresses the number of LA complexes dissociating per unit time. Furthermore, the unit dimensions for K_a and K_d are different. Indeed, K_a is described as $L \text{ mol}^{-1} \text{ s}^{-1}$, and K_d is s^{-1} .

Dynamic equilibrium is reached (at the steady state) when the rates of the association and dissociation reactions are equal, i.e.,

$$K_a [A][L] = K_d [LA] \quad (8)$$

Hence, the equilibrium constant it can be expressed as both affinity constant K_A (Eq. 9) and equilibrium dissociation constant K_D (Eq. 10)

$$K_A = \frac{[LA]}{[A][L]} = \frac{K_a}{K_d} \quad (9) \quad K_D = \frac{[L][A]}{[LA]} = \frac{K_d}{K_a} \quad (10)$$

However, K_A and K_D do not share the same dimension; indeed, K_A is $L \text{ mol}^{-1}$, while K_D is mol L^{-1} (M). Because K_D has the dimensions of concentration (moles per Liter) and it correlates to the amount that has been bound in relation to the concentration of free analyte, it is recommended to employ K_D rather than K_A .

The rate constants and equilibrium constants of interactions between two or more biomolecules provide insight into the association strength and the propensity for dissociation. Moreover, the K_D provides an implicit indication of the affinity between the ligand and the analyte.

The amount, i.e., the concentration, of the complex formed by the analyte-ligand interaction can be determined by the following differential equation:

$$\frac{d [LA]}{dt} = K_a [L][A] - K_d [LA] \quad (11)$$

By integrating the equation 11, the equation 12 describes the complete interaction curve as opposed to the differential rate equation, which describes the slope of the curve:

$$R_t = R_{eq} [1 - e^{-(K_a C + K_d)(t-t_0)}] \quad (12)$$

Where R_t is the response at time t and R_{eq} is the response at equilibrium achievable with the injected analyte concentration C . The term $t-t_0$ denotes the time interval since the start of the analyte injection. The R_{eq} value corresponds to the reaction of the injected analyte concentration as the injection period extends sufficiently to achieve equilibrium. It can be calculated by considering R_{max} , the kinetic constant (K_a , K_d) and the analyte concentration C .

In SPR analysis, measuring the change in the refractive index provides a precise assessment of molecule absorption on the metal surface. This sensitivity to SPR is widely used in many biological applications, rendering it an increasingly employed and sophisticated diagnostic method.

Beyond the real-time monitoring and measurement of the ligand-analyte interaction, the employment of the SPR technique includes the screening of compounds in the pharmaceutical industry, molecular recognition of specific molecules from biological fluid, measurement of DNA hybridization, detection of microRNAs, polyclonal antibody characterization, and label-free immunoassays.

Mass Spectrometry

MS is a mainstream chemical analysis technique in the twenty-first century. It has contributed to numerous discoveries in chemistry, physics, and biochemistry. Hundreds of research laboratories scattered all over the world use MS every day to investigate fundamental phenomena on the molecular level. MS is also widely used by industry—especially in drug discovery, quality control and food safety protocols. In some cases, mass spectrometers are indispensable and irreplaceable by any other metrological tools.

The uniqueness of MS is due to the fact that it enables direct identification of molecules based on the mass-to-charge ratios as well as fragmentation patterns. The charged species (ions) are produced in the ion source and then transported in gas-phase.

The gas-phase ions subsequently are transferred into the mass analyser which sorts the ions—in space or time—according to the mass-to-charge ratios (m/z). The separated ions are detected by an ion detector in the space or time domain. Electric signals, produced by the ion detector, are subsequently processed to produce mass spectra. MS enables direct identification of molecules based on the mass-to-charge ratio as well as fragmentation patterns. Thus, it fulfils the role of a qualitative and quantitative analytical technique with high selectivity.

Hence, from an instrumental point of view, the MS is composed of three important parts: the ionic source, the analyser, and the detector, which are all under vacuum. Moreover, in tandem MS two analyzers are interspersed with a collision cell used to induce the fragmentation of ions.

Ionic sources can vary in type based on the amount of energy they intend to impart to induce sample ionization. This aspect, in turn, depends on the type of sample (proteins, organic molecules, etc) and on their physical properties (volatile and non-volatile compound). For this reason, the ionic sources are divided into two categories: Hard and Soft, depending on whether the energy transfer is high or low, respectively.

In biological field, to preserve the molecular structure as much as possible, soft ion sources are preferred, since are less destructive, such as ESI and MALDI.

The basic principle of electrospray ionization (ESI) involves two steps: *i*) the electrospraying, which leads to the formation of charged droplets, and *ii*) the desolvation, where the dramatic reduction of droplet's size, results in the emission of ions from the droplets.

Specifically, the sample solution is channelled inside a capillary with a variable diameter and is pushed away by a carrier gas until it emerges from the needle. In this set-up, a voltage difference is applied, creating an electric field between the capillary and the counter electrode.

The application of a high voltage to the fine capillary needle forms a so-called Taylor cone, which ejects a fine jet of liquid from its apex towards the counter electrode.

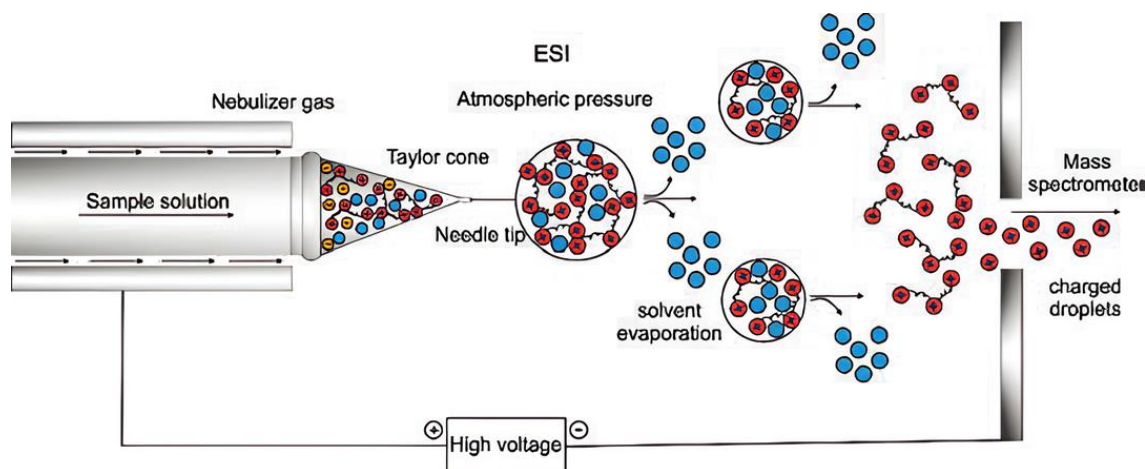


Figure 77 Schematic representation of the ESI process.

Small, charged droplets are emitted from the Taylor cone, and they will move toward the analyser due to the applied voltage difference. Electrosprayed droplets will possess an excess of positive or negative charges depending on the capillary bias polarity. During their passage, the presence of gas and the application of high temperature within the ESI chamber, determine the intensive reduction in droplet size through solvent evaporation. In this context, the choice of the type of solvent is crucial and significantly impact the efficiency and quality of the ionization process. For obtaining naked ions without solvent, it is necessary that the solvent is polar enough to dissolve and stabilize polar (bio)analytes, and also volatile. Volatility is fundamental as the solvent should have a relatively low boiling point and high vapor pressure. This is important for efficient desolvation of the droplets during the ionization process, allowing the generation of analyte ions in the gas phase.

The continuous reduction in droplet size increases the repulsive forces between the excess charges in the droplet, promoting electrohydrodynamic disintegration into many smaller droplets. The inevitable asymmetry in the distribution of charge on the droplet's surface may trigger a 'coulombic explosion' of the droplet before it reaches the Rayleigh limit. This threshold value is the point at which repulsive forces between similar charges in an electrolytic solution overcome the cohesive forces of the solvent, ensuring the stability of a spherical charged droplet. After this step, the emission of ions from the droplets occurs, followed by their entrance into the analyser.

The employment of ESI offers several advantages. Noteworthy, it enables the analysis of large biomolecules because ESI can produce multiple-charge ions, overcoming the limitations of the mass analyser's resolution and accuracy and placing the mass-to-charge (m/z) value of ions within the range of most commonly used mass spectrometers.

Once ions reach the analyser, they will be analyzed in accordance with their mass to charge ratio. Mass analyzers are categorized into various types based on their operational modes and separation principles, which for example time-based and space-based. Below two examples are shown.

Ion trap (Figure 78, panel A) employs a three-dimensional electric field to trap and separate ions based on their mass-to-charge ratio. Specifically, ion traps use electromagnetic fields to confine ions within a specific region of space. These fields can be generated using a combination of radiofrequency (RF) and direct current (DC) voltages. The interaction between these fields creates a stable region where ions can be trapped. The behaviour of ions within an ion trap is governed by mathematical equations that describe their motion under the influence of the applied electromagnetic fields. Such an example, the equations for the ion trap involve the stability of ions in the presence of RF and DC fields. In an ion trap, RF voltage is applied to the end-cap electrodes, creating a time-varying electric field. This RF field confines ions in the axial direction and causes them to oscillate in the radial direction. The DC voltage applied to the ring electrodes maintains a static electric field that helps to confine ions radially. By altering the radiofrequency potential, the trajectories of ions become unstable, and they are expelled from the trap, subsequently being captured by the detector.

Ion traps offer several advantages in the field of MS including high sensitivity, multiple scan modes, and the possibility to be coupled with ESI for the analysis of fragile biomolecules, minimizing the fragmentation.

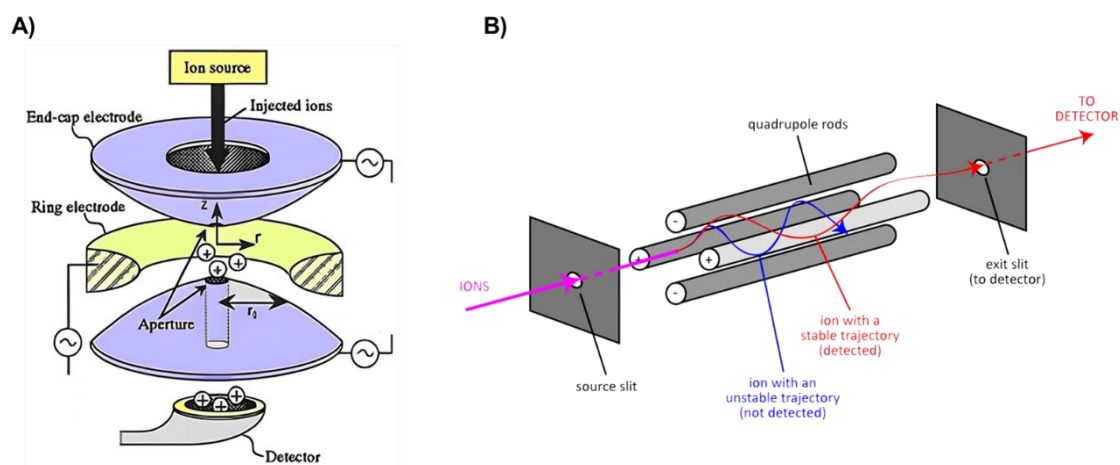


Figure 78 Simplified schematic representation of **A)** a portion of an ion trap and **B)** the four rods of the quadrupole.

A quadrupole analyser (Figure 78, panel B) works by applying a combination of RF and DC voltages to a set of four rod-shaped electrodes, forming a quadrupole configuration. These voltages create a stable region in which ions with specific m/z ratios can pass through without colliding with the electrodes. The RF voltage oscillates at a specific frequency, causing ions to oscillate within the quadrupole along the central axis. The DC voltage creates a pseudo-potential that guides ions towards the center of the quadrupole or pushes them away from it. Indeed, by adjusting the RF and DC voltage

settings, a specific range of m/z values can pass through the quadrupole, while ions with other m/z ratios will be unstable and collide with the rods, leading to their ejection from the analyser. The analyser can be operated in two modes: scanning mode and selected ion monitoring (SIM) mode. In the scanning mode, a range of m/z values is scanned, allowing for a full mass spectrum. In SIM mode, specific m/z values are chosen to monitor, enhancing sensitivity for targeted compounds. The quadrupole analyser is known for its simplicity, versatility, and widespread use in various analytical applications. Beside the versatility, quadrupole is low cost, and can scan a wide range of m/z quickly. Furthermore, it can be easily coupled with other quadrupoles to construct a tandem mass analyser, facilitating fragmentation, and offering valuable structural information.

Fluorescence Spectroscopy

Fluorescence spectroscopy is an emission phenomenon where an energy transition from a higher to a lower state is accompanied by radiation. Only molecules in their excited forms are able to emit fluorescence; thus, they have to be brought into a state of higher energy prior to the emission phenomenon. For a better comprehension of the phenomenon, we need to observe the following diagram in Fig.79 also called *Jablonski's diagram*.

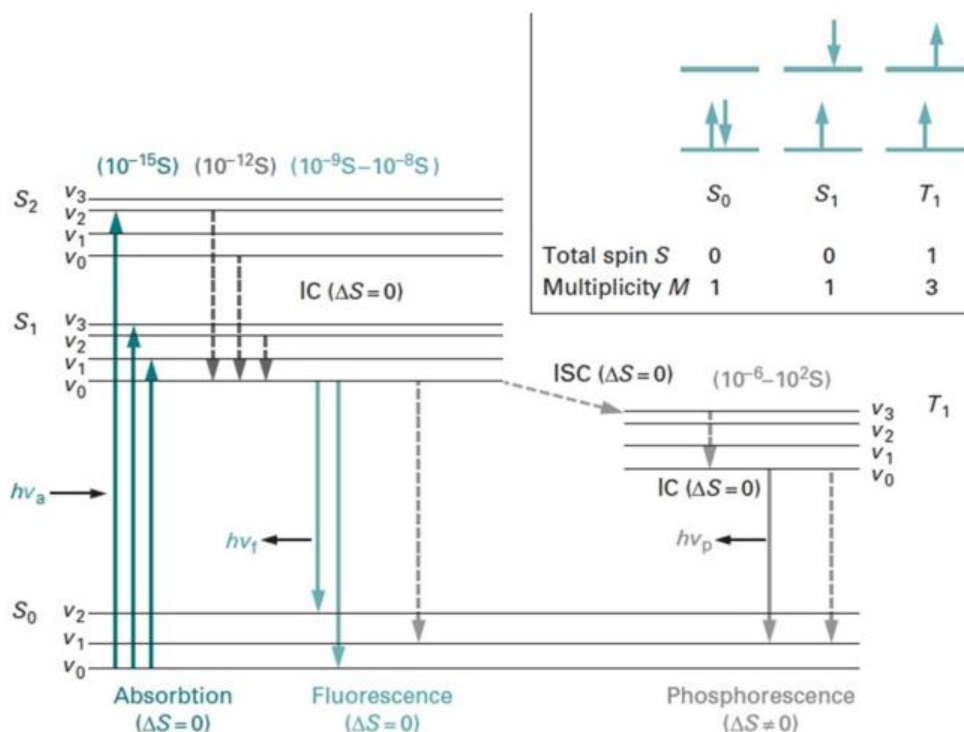


Figure 79 Jablonski's Diagram- In the diagram are shown: the electronic ground state (S_0), two excited singlet states (S_1 , S_2) and a triplet state (T_1). Vibrational level (V) are only illustrated exemplarily. Solid vertical lines indicate radiative transitions, dotted-lines show non-radiative transitions (i.e., Internal Conversion, IC). The inset shows the relationship between electron configurations, total spin number S and multiplicity M .

In these diagrams, energy transitions are indicated by vertical lines. Not all transitions are possible: allowed transitions are defined by the selection rules of quantum mechanics.

A molecule in its electronic and vibrational ground state (S_{1V0}) can absorb photons matching the energy difference of its various discrete states. The required photon energy has to be higher than that required to reach the vibrational ground state of the first electronic excited state (S_{1V0}). The excess energy is absorbed as vibrational energy ($V > 0$), and quickly dissipated as heat by collision with solvent molecules. The molecule, thus, returns to the vibrational ground state of the first electronic excited state (S_{1V0}). These relaxation processes are non-radiating transitions from one energetic state to another with lower energy and are called internal conversion (IC). From the lowest level of the first electronic excited state, the molecule returns to the ground state (S_0) either by emitting light (fluorescence) or by a non-radiative transition. Upon radiative transition, the molecule can end up in any of the vibrational states of the electronic ground state (as per quantum mechanical rules). If the vibrational levels of the ground state overlap with those of the electronic excited state, the molecule will not emit fluorescence, but rather revert to the ground state by non-radiative internal conversion. This is the most common way for excitation energy to be dissipated and is why fluorescent molecules are rather rare. Most molecules are flexible and thus have very high vibrational levels in the ground state. Indeed, most fluorescent molecules possess fairly rigid aromatic rings or ring systems. The fluorescent group in a molecule is called a fluorophore. Since radiative energy is lost in fluorescence as compared to absorption, the fluorescent light is always at a longer wavelength than the exciting light (namely, Stokes shift). The emitted radiation appears as a band spectrum because there are many closely related wavelength values dependent on the vibrational and rotational energy levels attained. However, the fluorescence spectrum of a molecule is independent of the wavelength of the exciting radiation and has a mirror-image relationship with the absorption spectrum.

In addition, the probability of the transition from the electronic excited to the ground state is proportional to the intensity of the emitted light.

In this context, an associated phenomenon is the *phosphorescence* due to the transition from a triplet state (T_1) to the electronic singlet ground state (S_0). The molecule gets into the triplet state from an electronic excited singlet state (S_1) by a process called intersystem crossing (ISC). Noteworthy, the transition from singlet state to triplet state is quantum-mechanically not allowed (i.e., happens with very low probability) and thus only in certain molecules where the electronic structure is favourable, such as heavy atoms. The rate constants for phosphorescence are much longer, as a consequence, phosphorescence occurs with a long delay and persists even when the exciting energy is no longer applied. The fluorescence properties of a molecule are determined by properties of the molecule itself

(internal factors), as well as the environment (external factors). The fluorescence intensity emitted by a molecule is dependent on the lifetime of the excited state. The transition from the excited to the ground state can be treated like a decay process of first order, i.e., the number of molecules in the excited state decreases exponentially with time. The ratio between photons emitted and photons absorbed by a fluorophore is called *quantum yield* Φ . The quantum yield is a dimensionless quantity, and most importantly, the only absolute measure of fluorescence for a molecule. Measuring the quantum yield is a difficult process and requires comparison with a fluorophore of known quantum yield.

Fluorescence spectroscopy works most accurately at very low concentrations of emitting fluorophores. One major factor adding to the high sensitivity of fluorescence applications is the spectral selectivity. Due to the Stokes shift, the wavelength of the emitted light is different from that of the exciting light. Another feature makes use of the fact that fluorescence is emitted in all directions. By placing the detector perpendicular to the excitation pathway, the background of the incident beam is reduced. In a typical spectrofluorometer two monochromators are used, one for tuning the wavelength of the exciting beam and a second one for analysis of the fluorescence emission. Due to the emitted light always having a lower energy than the exciting light, the wavelength of the excitation monochromator is set at a lower wavelength than the emission monochromator. The better fluorescence spectrometers in laboratories have a photon-counting detector yielding very high sensitivity. Temperature control is required for accurate work as the emission intensity of a fluorophore is dependent on the temperature of the solution. Optical geometries with 90° arrangement are commonly used. Pre- and post-filter effects can arise owing to the absorption of light prior to reaching the fluorophore and the reduction of emitted radiation. These phenomena are also called inner filter effects and are more evident in solutions with high concentrations.

Optical Properties of Carbon Dots

Fluorescence CDs including graphene quantum dots (GQDs), carbon nanodots (CNDs), and carbon quantum dots (CQDs) own relevant advantages in terms of low toxicity, small size, easy functionalization, resistance to photobleaching, and eco-friendly synthesis.

The optical properties of CDs lie in both the core state, which is provoked by perfect carbon crystals characterized by modified groups and few defects, and the surface state, which depends on the type of functional groups coated on the surfaces and the hybridization of the carbon backbone.

CDs display strong optical absorption in the UV region ranging from visible to NIR region. Fig.80 depicts the correlation between the absorption spectrum and the electron transition in both the core and shell, namely the surrounded functional groups, of CDs.

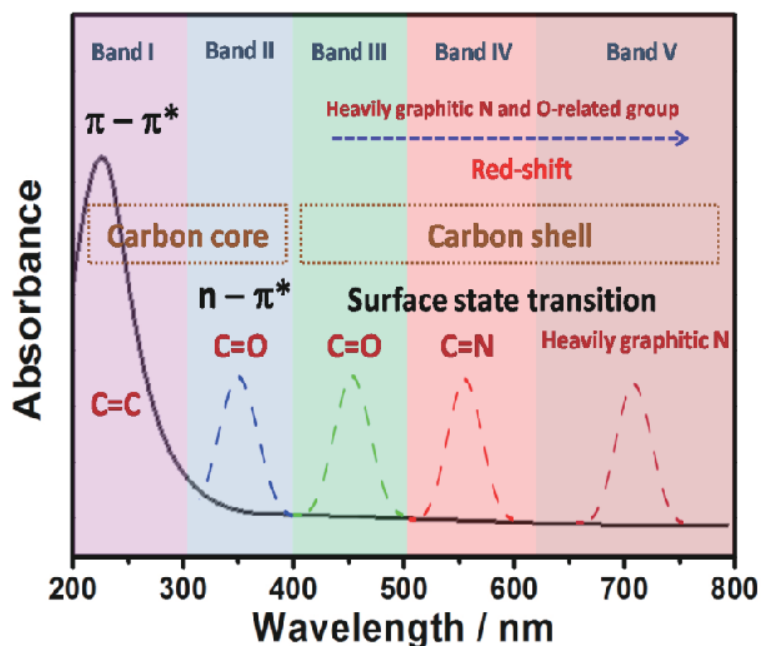


Figure 80 A graphic representation of the correlation between the absorption spectrum and electron transition of CDs.

The $\pi \rightarrow \pi^*$ transition involving aromatic sp^2 carbons like aromatic C=C bonds regards the carbon core region (Band I), as well as the $n \rightarrow \pi^*$ transition (starting from 300nm to 400 nm, Band II) assigned to the C=O bonds.

Above 400nm there are the absorption bands originating from the surface state. Being the $n \rightarrow \pi^*$ transition overlapped, the adjustment of emission does not experience significant disruption, resulting in a continuous color transition as the excitation wavelength changes.

Environmental factors, structural and energetic disorder, deprotonation, and excitonic coupling can all play a role in influencing the spectra.

The red-shifted UV-vis absorption spectrum is ascribed to the addition of graphitic nitrogen into the carbon sp^2 lattice due to the excess electron into the unoccupied π^* orbitals.

The fluorescent origins of CDs are multiple and include surface state, conjugated structure, edge defects, and many others. Moreover, this fluorescence is temperature, concentration, and pH-dependent.

The term "surface state" refers to the oxidation degree of the surface and the surface functional groups directly responsible for the fluorescence of CDs.

This surface state is caused by oxygen-based groups that create defects. These defects lead to various emission sites of the CDs, increasing their fluorescence.

Among these defects are excitons (i.e., electrons and holes), the radiation of which results in a red-shifted emission.

The different emissions (blue, green, and red) depend on various types of transitions.

For example, the blue emission stems from the transition of excited electrons from n to π^* due to the C=O group transition.

With an increase in oxygen-containing groups on the sp^2 hybridized carbons, the π^* states increase, leading to more $n \rightarrow \pi^*$ transitions. The band gap decreases as the oxygen content on the surface increases, resulting in a red shift and an increase in surface oxidation.

The conjugation system contributes to the fluorescence emission of CDs. Indeed, the progressive red-shift in the fluorescence of CDs can be attributed to the diminishing bandgap energy of CDs resulting from the augmentation of their conjugated structure.

Edge defects in CDs refer to irregularities or imperfections that occur at the edges of carbon-based nanomaterials that can arise due to various factors during their synthesis or formation. These defects can include vacancies, dangling bonds, or structural irregularities in the carbon lattice at the edges of the dots. As the oxygen content on the surface increases, the size of the defect also grows, leading to a more pronounced red shift in the fluorescence.

Lastly, parameters such as temperature, concentration, and pH can affect the intensity of CD's fluorescence.

Generally, the fluorescent intensity of CDs decreases as the increase of temperature, meanwhile, the relaxation dynamic turns faster at the higher temperature, due to non-radiative decay processes. At elevated temperatures, additional non-radiative pathways become active, leading to a greater number of excited electrons transitioning back to the ground state through non-radiative processes. This ultimately leads to a reduction in fluorescence intensity.

In many cases, an increase in the concentration of CDs leads to a proportional increase in fluorescence intensity. This is because, with more CDs present, there are more fluorophores (molecules that emit light) available to generate fluorescence.

However, at very high concentrations, a phenomenon called self-quenching can occur. When CDs are extremely close to each other, they can interact in a way that reduces the fluorescence intensity. This is often seen as a decrease in fluorescence at very high CD concentrations. Moreover, at high CD concentrations, there can also be reabsorption of emitted light by nearby CDs. This means that some of the emitted light is absorbed by other CDs, reducing the overall fluorescence intensity.

Finally, the influence of pH depends on the protonation/deprotonation of functional groups present on the surface of CDs, because pH parameters can alter the nature of the energy levels and in turn influence the type of electronic transitions involved in CDs. Indeed, at low pH values the fluorescence

intensity of CDs increases. This is due to the strong vibrational coupling of the OH groups, produced by H-bonds, which can induce an energy level broadening, improving the conformational rigidity of CDs.

On the other hand, at high pH values, deprotonation leads to reduced vibrational coupling and more discrete energy levels, which results in the decrease of fluorescence for CDs.

Cell viability: Trypan Blue and MTT assays

Cell viability refers to the measure of the health and viability of cells in a biological sample and indicates the overall health of cells within a population, their functioning properly, and the measure of cell survival following treatment with compounds, such as for instance during a drug screening.

Hence the final outcome is the percentage of viable (living) cells in a population of cells. This survival can be affected by several factors including the type of cultured or treated cells, the presence of nutrients and growth factors, exposure to toxins or stressors, and more.

Typically, cell viability provides a readout of cell health through the measurement of metabolic activity, ATP content, cell proliferation, or cell toxicity assays that provide a readout on markers of cell death, such as a loss of membrane integrity.

Herein, it will describe the two assays employed for the readout of cell viability of mixed cultures of cortical cells treated with A β ₁₋₄₂ oligomers (Chapter I): trypan blue and MTT assays.

The trypan blue (Figure 81, panel A) forecasts determine the percentage of cells that have clear cytoplasm (viable cells) versus cells that have blue cytoplasm (non-viable cells). Indeed, trypan blue is a dye used to stain non-viable cells, which have compromised cell membranes. Viable cells exclude the dye and remain unstained, otherwise, the cells (non-viable cells) appear with a distinct blue color visible when observed under the microscope. This leads to the capacity for simple differentiation between living and non-living cells, as the former appear unstained, small, and round, while the latter are stained and swollen.

The MTT assay (Figure 81, panel B) is utilized to measure mitochondrial activity. Specifically, it involves the conversion of the water-soluble yellow dye MTT [3-(4,5-dimethylthiazol-2-yl)-2,5-diphenyltetrazolium bromide] into an insoluble purple formazan through the action of mitochondrial reductase. The mitochondrial succinate dehydrogenase (reductase) is active only within viable cells, leading to the cleavage of the MTT ring and the formation of formazan. Consequently, viable cells will exhibit a purple color, while non-viable cells will remain yellow due to the enzyme's inability to perform its function.

The MTT assay finds application in assessing cell viability, measuring the cytotoxicity of therapeutic agents, and evaluating the cytostatic activity of potential medicinal or toxic substances.

The reaction is followed by the spectrophotometric readout at the wavelength of 570 nm.

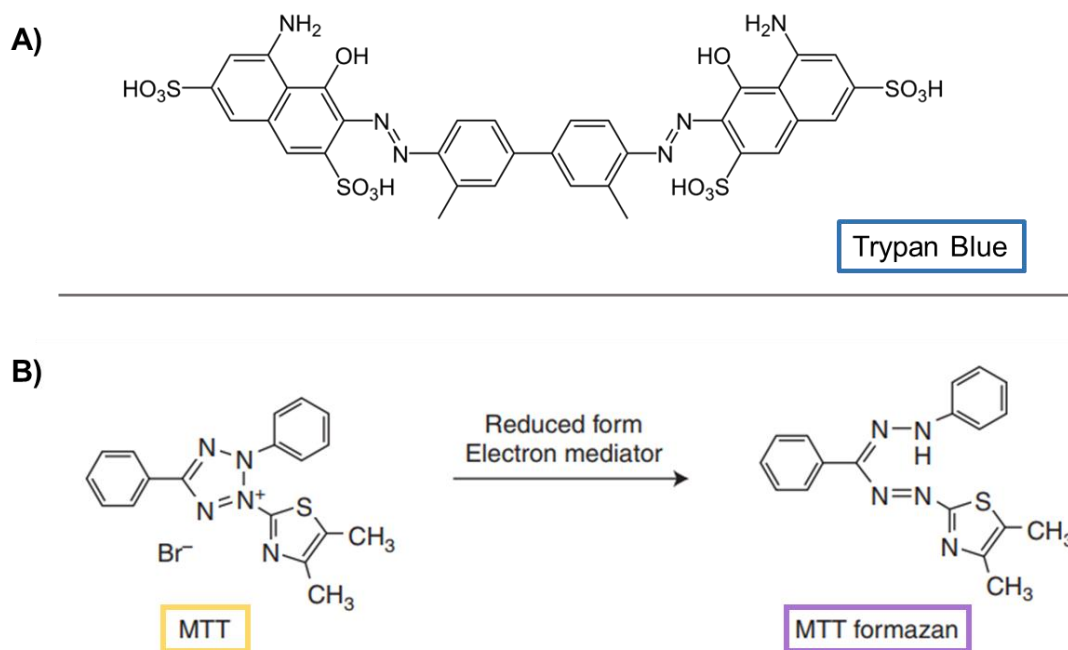


Figure 81 The chemical structures of **A)** Trypan blue and **B)** MTT and Formazan are illustrated. Additionally, the reaction responsible for the conversion of MTT to formazan in viable cells is depicted. Conversely, non-viable cells will retain their yellow coloration.

Dynamic Light Scattering

DLS is a non-invasive analytical technique used to determine the size of particles in solution in the sub-micron region. DLS measures the Brownian motion exhibited by particles and correlates it with their size. Brownian motion is characterized by a random movement of particles caused by the constant collisions with solvent molecules that surround them. Smaller particles exhibit faster Brownian motion compared to larger particles. The velocity of the Brownian motion is defined by a property known as the translational diffusion coefficient (usually indicated with the symbol D). The size of particles, expressed as hydrodynamic diameter $d(H)$ is extrapolated by the application of the Stokes-Einstein equation (13):

$$d(H) = \frac{kT}{3\pi\eta D} \quad (13)$$

Where D is the translational diffusion coefficient, K is the Boltzmann's constant, T the absolute temperature, and η the viscosity of the solution. The translational diffusion coefficient will depend

not only on the size of the particle “core”, but also on any surface structure, as well as the concentration and type of ions in the medium.

In DLS analysis, the sample is hit by a monochromatic light source, usually a laser, the light scatters in all direction according to the Rayleigh scattering. The incident light is polarized perpendicular to the scattering plane, and the scattered light has the same polarization. The diffracted light from all the molecules can either interfere constructively (generating light region) or destructively (forming dark regions).

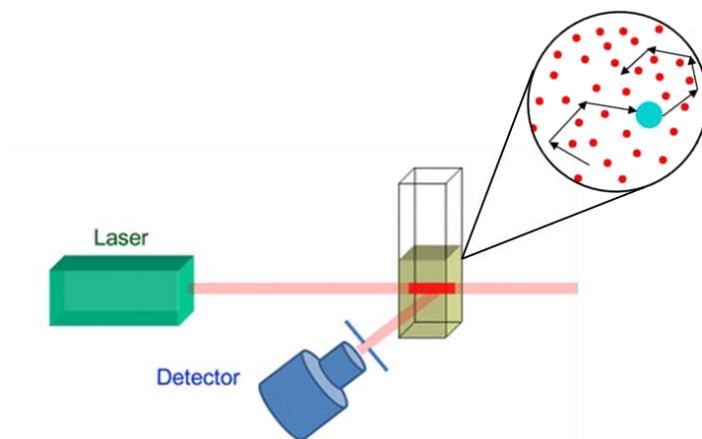


Figure 82 *Illustration of DLS experiment featuring a laser source, the sample, and the detector. The inset displays the Brownian motion of particles.*

The "scattering" of the light is produced by the interaction of electrons with the incident radiation. However, since electrons are mobile sources (due to Brownian motion), the frequency of the resulting "scattering" radiation will be shifted to higher or lower values depending on the direction of motion and the relative velocity with respect to the detector (Doppler effect).

Molecules in solution move in all directions with equal probability, and since they have a continuous distribution of velocities, a broadening of the continuous spectrum will be observed compared to the frequency of the incident radiation. The extent of this spectrum broadening is related to the Brownian motion of molecules and, therefore, to the diffusion coefficients.

However, in a non-ideal sample, multiple populations of particles with different sizes are often present simultaneously. DLS analysis can reveal distinct populations with varying sizes, resulting in multiple Gaussian distributions corresponding to the different populations in the sample. However, if there are substantial discrepancies between the sizes of larger particles and smaller ones, the light diffracted by the larger particles could eclipse the smaller particles, potentially causing them to go undetected.

Advantages of DLS include its non-invasiveness, ability to measure a wide range of particle sizes, and suitability for analyzing fragile biomolecules. However, DLS has limitations, such as difficulty

in measuring very small or very large particles accurately and sensitivity to particle concentration and interactions.

Circular Dichroism Spectroscopy

Circular dichroism spectroscopy, or simply CD, is strictly allied to chirality, because it is a manifestation of diastereomer discrimination. CD may be regarded as one of the most powerful techniques for stereochemical analysis: it is sensitive to the absolute configuration as well as to conformational features, which are often completely obscured in the ordinary absorption spectrum. The CD spectroscopy is based on the fact that the plane-polarized light wave can be obtained as a superposition of a left circularly polarized light and a right circularly polarized light, whose amplitude and wavelength are identical, see the schematic Fig. 83 below.

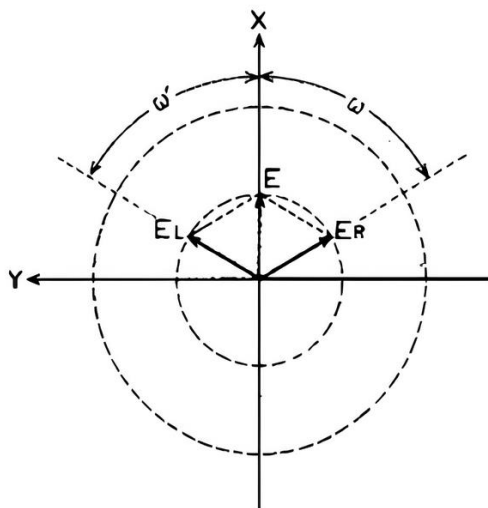


Figure 83 *The superposition between the electric field vector's left circularly polarized light EL.*

Any chiral non-racemic sample adsorbs left circularly polarized light to a different extent than right circularly polarized light: this phenomenon is called Circular Dichroism. In other words, CD is the difference:

$$CD = A_l - A_r \quad (14)$$

where A_l and A_r are the absorptions of left and right circularly polarized light, respectively. The definition of the equation immediately tells us that CD can be measured only in correspondence to absorption bands; a dichroic peak is also called a Cotton effect, on account of the discoverer of the phenomenon. Moreover, it is easy to show that for each absorption band, the CD of two enantiomers are always exactly opposite. As illustrated in Fig.84, the superposition of the two components is no longer a linearly polarized wave when CD occurs. The resulting electric field vector does not oscillate

along a straight line, but it rotates along and ellipsoid path. In other terms, such light wave is called an elliptically polarized light.

For this reasons, the output of CD instruments is usually measured as ellipticity Θ (in mdeg), related to CD through Θ (mdeg) = 33000 CD.

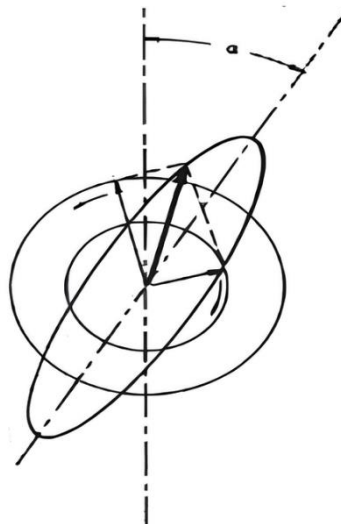


Figure 84 *Illustration of the elliptically polarized light.*

The basic instrumentation for CD measurement is the conventional spectropolarimeter. In the most common setup, there is a device between the monochromator and the sample compartment, called photoelastic modulator (PEM), which alternatively furnishes left and right circularly polarized light. It is based on a piezoelectric quartz crystal typically oscillating with a frequency in the 50 kHz range: during each cycle the light polarization changes, while the intensity remains constant. After passing through a chiral non-racemic sample, because the two circularly polarized light components become absorbed to a different extent, the light reaching the detector is time-modulated with the same frequency as the PEM. Phase-locked amplification of this signal can provide simultaneously absorbance, and circular dichroism. Theoretically, a baseline correction should not be required for CD, since the baseline is expected to be 0. In real life, on the contrary, it is strongly recommended that any CD spectrum is corrected by baseline subtraction obtained from a measurement ideally of the racemic compound at the same concentration and in the same cell; as a common alternative, a blank of the same solvent provides acceptable results.

Curriculum Vitae

Alessia Distefano was born on January 31st, 1992, in Catania (Italy).

She attained her MSc in Biomolecular Chemistry with full marks (110/110 cum laude) in 2020 discussing an experimental work about functionalized cyclodextrin nanoparticles as drug carriers.

In the same year, she started her PhD course in Chemical Sciences where she worked in the Laboratory of Bioinorganic Chemistry in Neurodegenerative Pathologies under the supervision of Prof. Giuseppe Grasso.



She spent part of her PhD course (8 months) at Université de Bretagne Occidentale (Brest, France), under the supervision of Prof. Antony Memboeuf, to acquire skills in the employment and handling of unconventional application of the Mass Spectrometry technique.

During her PhD period, the candidate Alessia Distefano worked on the research project *“Unveiling the biomolecular mechanisms of Alzheimer's disease: A multi-technical investigation of chemical factors involved in amyloid β peptide dyshomeostasis.”*

The main scientific interests are focused on neurodegenerative diseases, especially Alzheimer's and diabetes with particular attention to biomolecular interactions through the use of the SPR and Mass Spectrometry techniques.

Another significant development in the field of neurodegeneration is the utilization of carbon dots as novel biosensors for diagnostic purposes.

Over these three years, she has acquired skills in *i)* the study of biomolecular interactions, *ii)* synthesis, and covalent binding approaches of CDs with different analytes through spectroscopic characterizations, and *iii)* spectrometric analyses of A β -oxygen adducts.

At the University of Catania, she attended numerous lectures kept by Italian and international scientists. Furthermore, the candidate joined several schools, including:

- “25° CORSO DI SPETTROMETRIA DI MASSA 2021” Certosa di Pontignano (Siena, Italy) from 27th September – 1st October 2021.

- “1st ISMEC – NECTAR Training School on the Determination, Analysis and Use of Thermodynamic Data SOLvE – Advances in Solution Equilibria”, University of Catania, July 26th – 28th, 2021.

- “European School of Medicinal Chemistry” kept by Prof. Lucia Bedini, (online) June 28th - 30th, 2021, and July 1st, 2021.

As tutorship activities, she gave lessons (subject: General and Inorganic Chemistry) to undergraduates of chemistry, pharmacy biology, and natural sciences degree courses (University of Catania).

During the PhD course she presented the results of her research activity, giving both oral and poster contributions, at several conferences.

She won the Best Flash Presentation Prize at the 2021 “XX Edition of Merck Young Chemist’s Symposium” organized by Italian Chemical Society (SCI) in Rimini (Italy) in 2021.

Alessia Distefano has co-authored several articles, published in international refereed scientific journals. She is also member of the Italian Chemical Society (SCI).

Detailed description of her research activities is reported in the following paragraph “List of publications and proceedings”.

List of Publications and Proceedings

- Publications

1. *Neuroprotective Effect of Carnosine Is Mediated by Insulin-Degrading Enzyme.*

A. Distefano, G. Caruso, V. Oliveri, F. Bellia, D. Sbardella, G.A. Zingale, F. Caraci, and G. Grasso.
ACS Chem. Neurosci. 2022, 13, 10, 1588–1593

2. *An SPR-based method for Hill coefficient measurements: the case of insulin-degrading enzyme.*

A. Distefano, G.A. Zingale, and G. Grasso.
Analytical and Bioanalytical Chemistry, 2022, 414, 4793–4802.

3. *Carbon dots surface chemistry drives fluorescent properties: New tools to distinguish isobaric peptides.*

A. Distefano, F. Calì, M. Gaeta, N. Tuccitto, A. Auditore, A. Licciardello, A. D'Urso, K.J. Lee, O. Monasson, E. Peroni, and G. Grasso.
Journal of Colloid and Interface Science, 2022, 625, 405-414.

4. *The use of Surface Plasmon Resonance to Study the Interactions of Proteins Involved in Conformational Diseases: Experimental Approaches for New Therapeutical Perspectives.*

G.A. Zingale, A. Distefano, G. Grasso.
Current Medicinal Chemistry, 2023, 30 (36), 4072-4095.

5. *Carbon dots as a versatile tool to monitor insulin aggregation.*

G.A. Zingale, A. Distefano, I. Pandino, N. Tuccitto, V. Olivieri, M. Gaeta, A. D'Urso, A. Arcoria & G. Grasso.
Analytical and Bioanalytical Chemistry, 2023, 415, 1829–1840.

6. *A novel SPR based method for measuring diffusion coefficients: From small molecules to supramolecular aggregates.*

G.A. Zingale, I. Pandino, A. Distefano, N. Tuccitto, G. Grasso.
Biosensors and Bioelectronics: X, 2023, 13, 100306.

7. *Cyclodextrin Polymers as Delivery Systems for Targeted Anti-Cancer Chemotherapy.*

N. Bognanni, M. Viale, **A. Distefano**, R. Tosto, N. Bertola, F.Loiacono, M. Ponassi, D. Spinelli, G. Pappalardo and G. Vecchio.

Molecules, 2021, 26(19), 6046.

Proceedings – oral communications

1. *From Amino Acid Recognition to Insulin Aggregation Monitoring: Unveiling the Versatile Potential of Carbon Dots' Fluorescence Properties.*

Convegno Nazionale della Divisione di Chimica dei Sistemi Biologici della Società Chimica Italiana (DCSB 2023) Milano, 2023.

Alessia Distefano, Gabriele Antonio Zingale, Nunzio Tuccitto, Giuseppe Grasso.

2. *Exploring the Amyloid- β Oxygen adduct in Alzheimer's Disease: A Mass Spectrometry Study.*

Istituto Brestois Santé-Agro-Matière (IBSAM), Brest, 2023. Flash contribution - Language: French.

Alessia Distefano, Antony Memboeuf, and Giuseppe Grasso.

3. *The search for IDE activity modulators: new perspectives for therapeutic potentials in Alzheimer's disease.*

XX Edition of Merck Young Chemist's Symposium, Società Chimica Italiana, Rimini, 2021.

Alessia Distefano, Valentina Oliveri, and Giuseppe Grasso.

4. *Searching for Small Molecules as Potential Modulator of the IDE's activity.*

Convegno Regionale della Sezione Sicilia 2021

Alessia Distefano, Valentina Oliveri and Giuseppe Grasso.

5. *A MS and SPR coupled approach to fully characterize IDE activity modulation.*

XXVII Congresso Nazionale Della Società Chimica Italiana, SCI 2021

Alessia Distefano, Damiano Calcagno, Josè Giuffrida, and Giuseppe Grasso.

Proceedings – posters

1. *Insights into A β -Oxygen-adducts formation: A breakthrough Mass Spectrometry study in Alzheimer's disease research.*

39th Informal Meeting on Mass Spectrometry, Paris, May 2023

Alessia Distefano, Antony Memboeuf, and Giuseppe Grasso.

2. *Carbon dots as a versatile tool to monitor insulin aggregation.*

Workshop: I chimici per le Biotecnologie. Società Chimica Italiana Napoli, 2023

Alessia Distefano, Gabriele Antonio Zingale, Nunzio Tuccitto, and Giuseppe Grasso.

Acknowledgments

First of all, I would like to extend my gratitude to my supervisor Prof. Giuseppe Grasso, for his support, motivation, knowledge-sharing, and guidance over the last three years.

Sincere appreciation to Prof. Valentina Oliveri and Prof. Nunzio Tuccitto for enriching my scientific knowledge and contributing to greater completeness in my thesis.

My deepest gratitude goes to Prof. Antony Memboeuf (Université de Bretagne Occidentale), Prof. Alicia Maroto, Dr. Filiz Arýö, and the SPECTRE group for the invaluable opportunity to join their research projects as a visiting PhD student, granting me access to their laboratories and research facilities. Above all, I want to convey my heartfelt appreciation for their guidance in teaching me and instilling a profound passion for mass spectrometry, their constant support, and their unwavering belief in me. Especially, I am immensely grateful for welcoming me into your team, making me feel at home, and giving me the most beautiful experience of my life, both in the realm of science and, most importantly, on a personal level.

I thank my PhD coordinator, Prof. Salvatore Sortino, for ensuring a high scientific standard for the PhD program. A special mention goes to Ms. Sabrina Tosto for consistently assisting us with our administrative matters.

I thank the “FSE – Fondo Sociale Europeo Sicilia 2020 Programma Operativo” for the financial support.

Real gratefulness to my thesis reviewers: Prof. Elisa Peroni (CY Cergy Paris University, France) and Dr. Claudio Iacobucci (University of Aquila, Italy) for improving my dissertation with their comments and suggestions.

Very genuine thanks to my labmates for having shared with me stressing laboratory sessions and the efforts of a research activity.

A special thanks goes to my colleagues and roommates in Brest, Ana and Marco, my friends Dorsaf and Mahdi, and my labmates Olivier and Léna, who made the months in Brest truly unforgettable. Thank you for sharing memorable memories with me and for turning that wonderful Breton city into a second home.

I thank my XXXVI cycle colleagues for sharing with me the joys and pains of this extraordinary journey of life that is the PhD. In particular, I would like to express my gratitude to my colleagues and friends, Claudia, Matteo, and Gabriele, for the strength and laughter you have bestowed upon me.

To all my friends, whether near or far, I extend my heartfelt gratitude for the support and affection you have showered upon me over the years.

To my family, and especially to my parents, Cinzia and Pino. I am immensely grateful for all your support, your constant encouragement to chase my dreams, the endless love you show me every day, and for always being my biggest fans. My heartfelt thanks to you.

To my guardian angels, who have been and will forever remain by my side, I extend my profound gratitude and boundless love to you, wherever you may be.

More than anyone, I want to thank my great love, Massimiliano. Your patience, your love, your smile have illuminated the toughest and darkest days of these years. You have given me strength and courage, believing tirelessly in me and my passion. You have always been by my side, supporting my choices, sharing my joys, and making me stronger day by day, piece by piece. I will never thank you enough for all the love you give me every day.

page left blank intentionally.